THE UNIVERSITY OF TEXAS AT AUSTIN
CENTER FOR TRANSPORTATION RESEARCH

TECHNICAL REPORT 0-7090-1
TxDOT PROJECT NUMBER 0-7090

Evaluate the Deployment of High Strength Reinforcing Steel in Texas

Yongjae Yu
Cheska Espanol
Dagoberto Garza
Jesse Hernandez Gonzalez
Thinh P Dinh
Jose C Rivera Aguilar
Nathnael Jia Garedew
Yousun Yi
Hansol Jang
Elias Saqan
Oguzhan Bayrak

December 2024

Published July 2025

Technical Report Documentation Page

1. Report No. FHWA/TX-25/0-7090-1	2. Government Accession No.	3. Recipient's Catalog No.

4. Title and Subtitle Evaluate the Deployment of High Strength Reinforcing Steel in Texas	5. Report Date Submitted: December 2024 6. Performing Organization Code
7. Author(s) Yongjae Yu, Cheska Espanol, Dagoberto Garza, Jesse Hernandez Gonzalez, Thinh P Dinh, Jose C Rivera Aguilar, Nathnael Jia Garedew, Yousun Yi, Hansol Jang, Elias Saqan, Oguzhan Bayrak.	8. Performing Organization Report No. 0-7090
9. Performing Organization Name and Address Center for Transportation Research The University of Texas at Austin 3925 W. Braker Lane, 4th Floor Austin, TX 78759	10. Work Unit No. (TRAIS) 11. Contract or Grant No. 0-7090
12. Sponsoring Agency Name and Address Texas Department of Transportation Research and Technology Implementation Division P.O. Box 5080 Austin, TX 78763-5080	13. Type of Report and Period Covered Technical Report September 2020 – December 2024 14. Sponsoring Agency Code

15. Supplementary Notes

Project performed in cooperation with the Texas Department of Transportation.

16. Abstract

This research addresses the application of high-strength reinforcing steel in Texas bridge construction. The project involved experimental and analytical work to evaluate the effectiveness of current design recommendations for high-strength reinforcing steel in various bridge structural components. These components include spliced beam, CIP-PCP deck, prestressed girder, bent cap, and footing.

Significant findings include the validation of the tension lap splice length equation, the effectiveness of minimum web reinforcement requirements, and the influence of reducing the reinforcement quantities by replacing normal-strength steel with high-strength steel. Structural performance, including load-carrying capacity and crack control, was comparable compared to that achieved with normal-strength steel.

The project provided design recommendations for integrating high-strength steel into various bridge components. This work offers valuable insights and guidelines for both the practical application and theoretical understanding of high-strength steel in Texas bridge construction.

17. Key Words High-strength reinforcing steel, lap splice, reinforced concrete deep beam, prestressed girder, CIP-PCP deck, finite element analysis.	18. Distribution Statement No restrictions

19. Security Classif. (of report) Unclassified	20. Security Classif. (of this page) Unclassified	21. No. of pages	22. Price

Form DOT F 1700.7 (8-72) Reproduction of completed page authorized

THE UNIVERSITY OF TEXAS AT AUSTIN
CENTER FOR TRANSPORTATION RESEARCH

Evaluate the Deployment of High Strength Reinforcing Steel in Texas

Yongjae Yu
Cheska Espanol
Dagoberto Garza
Jesse Hernandez Gonzalez
Thinh P Dinh
Jose C Rivera Aguilar
Nathnael Jia Garedew
Yousun Yi
Hansol Jang
Elias Saqan
Oguzhan Bayrak

CTR Technical Report:	0-7090
Report Date:	November, 2024
Project:	0-7090
Project Title:	Evaluate the Deployment of High Strength Reinforcing Steel in Texas
Sponsoring Agency:	Texas Department of Transportation
Performing Agency:	Center for Transportation Research at The University of Texas at Austin

Project performed in cooperation with the Texas Department of Transportation and the Federal Highway Administration.

Center for Transportation Research
The University of Texas at Austin
3925 W. Braker Lane, 4th floor
Austin, TX 78759

https://ctr.utexas.edu/

Disclaimers

Author's Disclaimer: The contents of this report reflect the views of the authors, who are responsible for the facts and the accuracy of the data presented herein. The contents do not necessarily reflect the official view or policies of the Federal Highway Administration or the Texas Department of Transportation (TxDOT). This report does not constitute a standard, specification, or regulation.

Patent Disclaimer: There was no invention or discovery conceived or first actually reduced to practice in the course of or under this contract, including any art, method, process, machine manufacture, design or composition of matter, or any new useful improvement thereof, or any variety of plant, which is or may be patentable under the patent laws of the United States of America or any foreign country.

Engineering Disclaimer

NOT INTENDED FOR CONSTRUCTION, BIDDING, OR PERMIT PURPOSES.

Project Engineer: Oguzhan Bayrak
Professional Engineer License State and Number: Texas No. 106598
P.E. Designation: Research Supervisor

Acknowledgments

The authors are grateful to the Texas Department of Transportation (TxDOT) for providing the funds to conduct this research study. The contributions of the project director Martin Dassi (RTI PM) (Bridge Division) and other members of the Project Monitoring Committee are deeply appreciated.

Table of Contents

List of Tables

List of Figures

Chapter 1. Introduction

1.1. Overview

With the rise of large infrastructure projects, the use of high-strength reinforcement in reinforced concrete (RC) structures—common in such infrastructures—has gained attention due to several benefits, such as improved performance, reduced congestion, lower reinforcement quantities, and cost savings. High-strength reinforcement typically refers to steel bars with yield strengths exceeding 80 ksi. Examples include low-carbon chromium steel bars (ASTM A1035), introduced in 2004, and high-strength grades of carbon steel standards under ASTM A615 and A706.

As a result, design codes such as AASHTO LRFD Bridge Design Specifications and ACI 318 have incorporated provisions for high-strength reinforcement. However, some design provisions still restrict its use, especially for shear reinforcement or reinforcement in the D-region, due to the lack of sufficient experimental data. This has created barriers to the application of high-strength reinforcing steel in Texas bridges, despite its development over 20 years ago. This project aims to address these challenges and overcome the limitations that hinder the implementation of high-strength reinforcing steel in Texas bridge design.

This comprehensive research project utilized both experimental and analytical approaches to validate the application of high-strength steel in bridge system. To achieve its objectives, the research team outlined four key tasks: a literature review, experimental investigations on each bridge component, finite element modeling of bridge systems, and providing design recommendations. The findings and procedures from each task are detailed in this report, collectively paving the way for more efficient Texas bridge construction through the use of high-strength reinforcement.

1.2. Project Objectives

The Texas Department of Transportation (TxDOT) Research Project 0-7090, funded by TxDOT, focuses on examining the application of high-strength reinforcing steel in Texas bridges. The primary objectives of the project are: (a) conducting large-scale structural experiments and finite element analyses to investigate the structural response of bridge systems with high-strength steel and validate its application under current design codes, and (b) Offering practical guidelines for applying high-strength reinforcing bars through example calculations based on actual bridge systems.

1.3. Project Scope

The current research project aims to address the following technical tasks:

- The literature review analyzes the limitations of implementing high-strength steel in bridges, leading to the development of an experimental program aimed at overcoming these limitations.

- An experimental investigation was conducted on various bridge components, including the deck, beam, girder, bent cap, and footing. Additionally, finite element analysis was performed to verify and supplement the experimental findings.

- Based on the research results, design recommendations were developed to guide the application of high-strength steel in bridges.

1.4. Organization

Chapter 1: Introduction
- Presents an overview of the research objectives, significance, and the necessity of investigating the applicability of high-strength steel in bridges.
- Describes the structure and organization of the report.

Chapter 2: Literature Review
- Provides a review of existing literature, including design codes related to the use of high-strength steel in bridge systems.
- Highlights significant findings and identifies knowledge gaps to be addressed in this research.

Chapter 3: Experimental Program
- Introduces the experimental program developed to assess the applicability of high-strength steel in bridge systems.
- Details the methodology, instrumentation, experimental procedures and results.
- Analyzes the experimental results for each bridge component, comparing the strength performance and serviceability of cases using high-strength steel versus those using normal-strength steel.
- Evaluates whether the current design codes based on normal-strength steel are applicable to cases using high-strength steel.

Chapter 4: Finite Element Analysis
- Presents a finite element model based on the experimental results described in the previous chapters.
- Provides numerical data to development of design recommendations.

Chapter 5: Practical Applications

- Provides example calculations illustrating the application of high-strength reinforcing bars in real bridge systems.
- Offers design recommendations for engineers and practitioners to implement the high-strength steel in bridge systems effectively.

Chapter 6: Conclusions

- Summarizes the key findings and contributions of the study.
- Highlights the significance of the research in advancing bridge construction technology.

Chapter 2. Literature Review

2.1. Overview

With the development and growing demand for high-strength steel, design provisions permitting its use have been incorporated into ACI 318-19 and AASHTO LRFD (2020), as summarized in Table 2-1. However, the criteria differ across design codes, and notably, the use of high-strength steel is restricted for shear reinforcement and reinforcement in the D-region (Disturbed or Discontinuity Region), where the strut-and-tie method is recommended. This uncertainty presents a challenge for engineers in applying high-strength steel. To address this limitation, the chapter summarizes existing studies related to the application of high-strength steel in bridge systems, organizing the information into superstructure and substructure categories.

Table 2-1. Provisions of high-strength steel in design codes

Usage	AASHTO LRFD (2020)	ACI 318-19
Flexural	• Up to 100 ksi • 75-100 ksi may be used in a seismic application with the owner’s approval, only as permitted in the AASHTO Guide Specifications for LRFD Seismic Bridge Design (2011).	• Up to 100 ksi except for special seismic system
Shrinkage and temperature	• Up to 75 ksi	• Up to 100 ksi except for special seismic system
Shear	• Up to 100 ksi	• For stirrups, up to 60 ksi (deformed bar), up to 80 ksi (welded wire)
Strut-and-tie	• Up to 75 ksi	• For longitudinal tie, up to 80 ksi, other is up to 60 ksi.

2.2. Superstructures

2.2.1. Bridge Deck

Several researchers (Solamon et al. 2014, Sim and Frosch 2020, Kareem et al. 2020) investigated the impact of various reinforcement types, including high-strength steel, on the performance of concrete deck specimens subjected to four-point bending tests. The key findings indicated that using high-strength rebar as a one-to-one replacement for normal-strength steel increased the load capacity due to its higher yield strength. However, this replacement led to a wider crack width than in specimens with normal-strength rebar. Despite this increase in crack width, Kareem et al. (2020) confirmed that the maximum crack width remained within AASHTO specifications limit (2017). Solamon et al. (2014) suggested reducing the rebar size and increasing the concrete cover thickness for high-strength rebar to meet AASHTO LRFD (2010) requirements. Additionally, the crack width model adopted by ACI 318 (2014) and AASHTO (2010) was found to be valid for high-strength rebar (ASTM A1035), with a recommendation to apply actual stress-strain relations rather than the elastic modulus when rebar stress exceeds the elastic limit.

Seliem et al. (2008) and Solamon et al. (2017) conducted field monitoring of bridge decks reinforced with high-strength bar. Seliem et al. (2008) concluded that high-strength steel could be used as flexural reinforcement in cast-in-place concrete bridge decks, requiring a reinforcement ratio 33% lower than that needed for Grade 60 steel. Additionally, Solamon et al. (2017) reported no significant serviceability issues after the deck was opened to traffic.

However, these studies have primarily focused on traditional cast-in-place (CIP) decks. In practice, precast, prestressed concrete panels (PCPs) combined with cast-in-place (CIP) concrete slabs are often used for their cost-effectiveness, accelerated construction, and enhanced safety. The CIP-PCP deck system exhibits slightly different cracking behavior compared to traditional CIP decks. Major cracks tend to form at the panel edges in CIP-PCP decks, likely due to factors such as shrinkage, edge restraints, and gaps between panels (Folliard et al., 2003 and Merrill, 2002). Additionally, the Texas Department of Transportation (TxDOT) has developed design standards for CIP-PCP decks through experimental and field studies. These standards include optimizing the top-mat reinforcement to improve crack control and adjusting the initial prestress in PCPs to minimize collinear panel cracking during fabrication and transportation (Azimov, 2012; Bayrak et al., 2013; Foreman, 2010; Foster, 2010; Kwon, 2012; TxDOT 2023; TxDOT 2024). However, compared to CIP decks, there is limited experimental data available to support the applicability of high-strength steel in CIP-PCP deck systems.

2.2.2. Prestressed Girder

ACI 318-19 and AASHTO LRFD (2020) specify a minimum amount and maximum spacing requirements for transverse reinforcement, as shown in Table 2-2. According to Bridge Design Manual-LRFD by TxDOT (2020), the required stirrup spacing for #4 Grade 60 bars in pre-tensioned concrete I-girders and Box beams should be calculated following Article 5.7 of AASTHO LRFD (2010). Since the minimum amount of transverse reinforcement is inversely proportional to the yield strength of reinforcement, using high-strength steel as transverse reinforcement could potentially reduce the reinforcement quantities.

Shahrooz et al. (2011) conducted shear tests on nine specimens, including four AASHTO Type I prestressed girders, to evaluate high-strength steel as shear reinforcement. Normal-strength steel (A615) and high-strength steel (A1035) were used as transverse reinforcement, with each specimen containing both #3 A1035 and #4 A615 bars along with 0.6-inch low-relaxation strands. The tests showed that all specimens exceeded the predicted shear capacities based on AASHTO LRFD (2007). At lower shear stress levels, crack widths were similar regardless of the reinforcement type. However, as shear stress increased, cracks widened more quickly on sides with A1035 stirrups than on those with A615 stirrups. This is because the A1035 stirrups were smaller in size than the A615 stirrups (#3 vs. #4).

Based on this results, AASHTO LRFD (2020) permit the use of high-strength steel as shear reinforcement as shown in Table 2-1. However, pre-tensioned girder was affected various factors such as support configuration and loading conditions. Therefore, it is uncertain whether the current requirement for transverse reinforcement can be applied to high-strength steel without any verification.

Table 2-2. Design codes for transverse reinforcement

	AASHTO LRFD (2020)	ACI 318-19
Minimum amount	$A_v \geq 0.0316\lambda\sqrt{f_c'}\dfrac{b_v s}{f_y}$ where, A_v: area of transverse reinforcement within distance s (in.^{2}) λ: concrete density modification factor f_c': compressive strength of concrete for use in design (ksi) b_v: width of web adjusted for the presence of ducts (in.) s: spacing of transverse reinforcement (in.) f_y: yield strength of reinforcement (ksi)	(1) Nonprestressed and prestressed with $A_{ps}f_{se} < 0.4(A_{ps}f_{pu} + A_s f_y)$ $A_{v,min}$ is determined as to be the greater of the followings: $(a)0.75\sqrt{f_c'}\dfrac{b_w}{f_{yt}} \quad (b)50\dfrac{b_w}{f_{yt}}$ (2) Prestressed with $A_{ps}f_{se} \geq 0.4(A_{ps}f_{pu} + A_s f_y)$ $A_{v,min}$ is determined as to be the greater of the followings: Greater of (c) or (d) vs. (e) $(c)0.75\sqrt{f_c'}\dfrac{b_w}{f_{yt}} \quad (d)50\dfrac{b_w}{f_{yt}}$ $(e)\dfrac{A_{ps}f_{pu}}{80f_{yt}d}\sqrt{\dfrac{d}{b_w}}$ where, A_{ps}: area of prestressed longitudinal tension reinforcement (in.^{2}) f_{se} : effective stress in prestressed reinforcement, after allowance for all prestress losses (psi) f_{pu}: specified tensile strength of prestressing reinforcement (psi) A_s: area of nonprestressed longitudinal tension reinforcement, (in.^{2}) f_y: specified yield strength for nonprestressed reinforcement (psi) $A_{v,min}$: minimum area of shear reinforcement within distance s (in.^{2}) f_c': specified compressive strength of concrete (psi) b_w: web width or diameter of circular section (in.) s : center-to-center spacing of transverse reinforcement (in.) f_{yt} : specified yield strength of transverse reinforcement (psi) d: distance from extreme compression fiber to centroid of longitudinal tension reinforcement (in.)
Maximum spacing	If $v_u < 0.125f_c'$, then $s_{max} = 0.8d_v \leq 24.0\ in.$ If $v_u \geq 0.125f_c'$, then $s_{max} = 0.4d_v \leq 12.0\ in.$ where, v_u: sheaer stress (ksi) d_v: effective shear depth (in.)	

2.3. Substructures

2.3.1. Bent Cap and Drilled Shaft Footing

One of the major safety concerns in substructures, such as bent cap and drilled shaft footing, is preventing failure near the load point, identified as a diagonal crack issues in bent caps in Texas (Birrcher et al. 2009). The region near the loading points, known as the D-regions (disturbed or discontinuity region), does not conform to traditional section design assumptions. AASHOTO LRFD (2020) and ACI 318-19 recommended using the strut-and-tie method for designing members in D-regions. As shown in Table 2-1, AASHTO LRFD (2020) and ACI 318-19 limits the yield strength of reinforcement under 80 ksi when using the strut-and-tie method. Additionally, for crack control, AASHTO LRFD (2020) and ACI 318-19 specify minimum requirements for crack control reinforcement and shrinkage and temperature reinforcement, as listed in Table 2-3. However, these specifications include strength limitations, which make it challenging to apply high-strength steel.

Table 2-3. Design codes for crack control reinforcement in D-region and shrinkage and temperature reinforcement

	AASHTO LRFD (2020)	ACI 318-19
Crack control reinforcement in D-region	$\frac{A_v}{b_w s_v} \geq 0.003 \quad \frac{A_h}{b_w s_h} \geq 0.003$ where, A_v : total area of vertical crack control reinforcement within spacing s_v (in.^{2}) A_h : total area of horizontal crack control reinforcement within spacing s_h (in.^{2}) b_w: width of member's web (in.) s_v, s_h: spacing of vertical and horizontal crack control reinforcement, respectively (in.) The spacing of the bars in these grids shall not exceed the smaller of d/4 and 12 in.	Minimum distributed reinforcement ratio shall be provided as follows: (1) Not restrained - Orthogonal grid: 0.0025 in each direction - Reinforcement in one direction crossing strut at angle $\alpha_1 = \frac{0.0025}{sin^2\alpha_1}$ (2) Restrained - Distributed reinforcement not required Distributed reinforcement shall satisfy (a) Spacing shall not exceed 12 in., (b) Angle α_1 shall not be less than 40 degrees.
Shrinkage and temperature reinforcement	For bars or welded wire reinforcement, the area of reinforcement per foot, on each face and in each direction, shall satisfy the following: $A_s \geq \frac{1.30bh}{2(b+h)f_y}$ except that: $0.11 \leq A_s \leq 0.60$ where, A_s: area of reinforcement in each direction and each face (in.^{2}/ft) b: least width of component section (in.) h: least thickness of component section (in.) f_y : specified minimum yield strength of reinforcement ≤ 75 ksi	The ratio of deformed shrinkage and temperature reinforcement area to gross concrete area shall be greater than or equal to 0.0018. The spacing of deformed shrinkage and temperature reinforcement shall not exceed the lesser of 5h and 18 in.

Several studies have conducted shear tests on beams to investigate the impact of high-strength reinforcement, including longitudinal reinforcement (de Dios Garay-Moran, J. and Lubell, A.S., 2016; Desalegne, A.S. and Lubell, A.S., 2010; Hassan, T.K et al., 2008), transverse reinforcement (Munikrishna, A et al., 2011; Lee, J.Y et al., 2011; Lee, J.Y et al., 2018; Ou, Y.C. and Bui, C.T., 2024; Shin, D et al., 2019; Sumpter, M.S et al., 2009), or both types of reinforcement (Desalegne, A.S. and Lubell, A.S., 2015). These studies generally indicate that the use of high-strength steel enhances the shear capacity. Additionally, transverse reinforcement was found to be key parameter in controlling diagonal crack widths. When the spacing of the transverse reinforcement was maintained, similar crack widths were observed regardless of the strength of transverse reinforcement at the same load level. However, only a small proportion of these studies (8%) conducted tests using deep beams, where shear span-to-depth ratio less than 2.0. Furthermore, high-strength steel was not used as transverse reinforcement in the tests involving deep beams.

Yi et al. (2022) carried out an extensive study that involved 19 large-scale experiments and numerical analyses. The tests were designed with various parameters and loading scenarios, including vertical compression and uniaxial bending, while the numerical analyses were used to address additional design parameters that could not be considered in the experiments. Based on the findings, 3D strut-and-tie modeling guidelines for drilled shaft footings are suggested. These guidelines include a definition of the 3D nodal geometry at bearing faces, refinements for strength modification factors, critical section definitions for development of horizontal and vertical ties, and recommendations for bottom mat reinforcement configuration. For shrinkage and temperature reinforcement, a minimum requirement of 0.18% is proposed, which aligns with the requirements in AASHTO LRFD (2020) and ACI 318-19. However, since only normal-strength reinforcement (Grade 60) is used in this study, the applicability of high-strength reinforcement remains limited.

2.4. Supplementary Topics

2.4.1. Tension Lap Splice

Table 2-4 provides a comparison of provisions on development length and tension lap splice requirements in AASHTO LRFD (2020) and ACI 318-19. As shown, all the codes calculate development and splice lengths similarly, taking into account factors such as reinforcement location and size, coating, and confinement effects. Additionally, both codes permit the use of high-strength reinforcing bars with a yield strength of up to 100 ksi for development applications.

Table 2-4. Design codes for tension development length and lap splice

	AASHTO LRFD (2020)	ACI 318-19
Tension development length	1) f_y: up to 100 ksi 2) d_b: up to No.11 bar 3) f'_c: up to 15 ksi for normal up to 10 ksi for lightweight 4) Equation $l_d = l_{db}\left(\frac{\lambda_{rl}\lambda_{cf}\lambda_{rc}\lambda_{er}}{\lambda}\right)$	1) f_y:up to 100 ksi 2) d_b: Not limited, reinforcement size is considered by using ψ_s 3 $\sqrt{f'_c}$ up to 100 psi 4) Equation

	AASHTO LRFD (2020)	**ACI 318-19**
	$l_{db} = 2.4 d_b \frac{f_y}{\sqrt{f'_c}}$ $\lambda_{rc} = \frac{d_b}{c_b+k_{tr}}, k_{tr} = 40\frac{A_{tr}}{sn}$ shall not be less than 12 in. where, l_{db}: basic development length (in.) λ_{rl}: reinforcement location factor λ_{cf}: coating factor λ_{rc}: reinforcement confinement factor λ_{er}: excess reinforcement factor λ : concrete density modification factor f_y : specified minimum yield strength of reinforcement (ksi) d_b: nominal diameter of reinforcing bar or wire (in.) f'_c: compressive strength of concrete for use in design (ksi) c_b: the smaller of distance from center of bar or wire being developed to the nearest concrete surface and one-half the center-to-center spacing of the bars or wires being developed (in.) k_{tr}: transverse reinforcement index A_{tr} : total cross-sectional area of all transverse reinforcement that is within the spacing s and that crosses the potential plane of splitting through the reinforcement being developed (in.^{2}) s : maximum center-to-center spacing of transverse reinforcement within l_d (in.) n: number of bars or wires developed along plane of splitting	$l_d = \frac{3}{40}\frac{f_y}{\lambda\sqrt{f'_c}}\frac{\psi_t\psi_e\psi_s\psi_g}{\left(\frac{c_b+k_{tr}}{d_b}\right)} d_b$ shall not be less than 12 in. where, l_d : development length in tension of deformed bar (in.) ψ_t : factor used to modify development length for casting location in tension ψ_e factor used to modify development length based on reinforcement coating ψ_s : factor used to modify development length based on reinforcement size ψ_g : factor used to modify development length based on grade of reinforcement d_b: modification factor to reflect the reduced mechanical properties of lightweight concrete relative to normal-weight concrete of the same compressive strength
Tension lap splice	1) f_y: up to 100 ksi 2) d_b: up to No.11 bar 3) f'_c: up to 15 ksi for normal up to 10 ksi for lightweight 4) Class A splice: $1.0l_d$ Class B splice: $1.3l_d$ Shall not be less than 12 in. For splices whose specified yield strength is larger than 75 ksi, transverse reinforcement satisfying the requirements shall be provided over the required lap splice length.	1) f_y:up to 100 ksi 2) d_b: Not limited, reinforcement size is considered by using ψ_s 3 $\sqrt{f'_c}$up to 100 psi 4) Class A splice: $1.0l_d$ Class B splice: $1.3l_d$ Shall not be less than 12 in. Class A or B is determined considering $A_{s,provided}/A_{s,required}$ over length of splice and maximum percentage of A_s spliced within required lap length.

The ACI committee 408, “Bond and Development of Steel Reinforcement”, provides a tension lap splice database. This database includes 27 experimental studies, encompassing a total of 609 tension lap splice tests. Additionally, Frosch et al. (2020) and Rulon et al. (2022) conducted beam splice tests using high-strength steel. Frosch et al. (2020) tested beam spliced with No. 8 high-strength reinforcement, varying the rebar type (ASTM A615 and ASTM A1035), transverse reinforcement, and splice length. The results indicated that transverse reinforcement enhances bond strength, particularly when placed at the splice ends. Additionally, failure occurred within the linear elastic range, suggesting that the type of high-strength rebar (ASTM A615 or ASTM A1035) had a minimal effect on performance. Concrete crack widths showed a relatively linear relationship with rebar stress. Rulon et al. (2022) conducted beam splice test using large size rebar (No. 14 and No. 18). It was found that the development length equations in ACI 318-19 and ACI 408R-03 become less conservative as bar size increases. They observed that concrete crack width tends to increase with increasing bar stress. All test database is summarized in Table 2-5. The database analysis highlighted a substantial gap in experimental data for large-diameter high-strength rebars, particularly those of size No. 11 or larger. Among the 609 tests, 15 involved high-strength steel (Grade 100), and only nine of these specimens were longer than 30 inches in depth, limiting their relevance for practical applications.

Table 2-5. Summary of tension lap splice database

References	No. tests	Beam height, in.	Bar diameter, in.	Bar yield stress, ksi
Azizinamini et al. (1993)	13	14−18	1.00−1.41	71−78
Azizinamini et al. (1995)	7	16−18	1.41	70−74
Azizinamini et al. (1999)	57	14−18	1.00−1.41	71−78
Chamberlin (1958)	6	6	0.50	50
Chinn et al. (1955)	32	Not provided	0.38−1.41	57−79
Choi et al. (1990, 1991)	8	14−16	0.63−1.41	64−71
Darwin et al. (1996)	73	15−17	0.63−1.41	62−81
DeVries et al. (1991)	10	16	0.75−1.13	66−77
Ferguson and Breen (1965)	35	15−18	1.00−1.41	64−99
Frosch et al. (2020)	34	20	1.00	108−120
Hamad and Itani (1998)	8	12	0.98	62
Hasan et al. (1996)	2	8−12	0.88−1.41	43
Hegger et al. (2015)	13	14−24	1.10−1.97	78−84
Hester et al. (1991, 1993)	17	16	1.00	64−71
Hwang et al. (1994, 1996)	18	10	1.13	69, 75
Kadoriku (1994)	34	10−13	0.75	64−122
Rezansoff et al (1991, 1993)	49	13−20	0.77−1.41	61−73
Rulon et al. (2022)	11	32−36	1.69−2.26	52−109
Seliem et al. (2009)	64	10−36	0.63−1.41	100
Thompson et al. (1975)	15	13−16	0.75−1.69	59−67
Zekany et al. (1981)	12	16	1.13−1.41	60−63
Zuo and Darwin (1998)	91	15−16	0.63−1.41	63−81
Overall	609	8−36	0.38−2.26	43−122

2.5. Summary

This literature review encompasses a broad range of design codes, researches and projects concerning the implementation of high-strength steel in bridge systems, including both superstructures and substructures. From this review, the following key findings can be drawn:

- The use of high-strength steel as flexural reinforcement in bridge decks has been shown to be effective in terms of load performance and serviceability, but this applies primarily to traditional CIP decks. Therefore, a practical review is needed to assess the applicability of high-strength steel in CIP-PCP decks, which are widely used in the field.

- In prestressed girders, high-strength steel has been considered as a shear reinforcement, with AASHTO LRFD (2020) allowing its use, while ACI 318-19 does not permit high-strength steel for this purpose. Moreover, the behavior of prestressed girders varies significantly depending on factors such as cross-sectional details, a/d ratio, and strand configuration. Therefore, further review is necessary to assess its practical application.

- Although high-strength rebar is permitted for tension lap splice by AASHTO LRFD (2020) and ACI 318-19, an analysis of the relevant studies reveals that the use of large-diameter high-strength rebar is extremely limited. Therefore, the needs for verification of its applicability are crucial.

- The application of high-strength steel reinforcement in bent cap and drilled shaft footing is challenging due to design code restrictions, such as those in AASHTO LRFD (2020) and ACI 318-19. Additionally, while studies on the use of high-strength reinforcement have been conducted, they are very limited in the context of deep beams, and there are no confirmed cases of high-strength reinforcement being applied to drilled shaft footings.

Chapter 3. Experimental Program

This chapter presents a comprehensive experimental program designed to assess the applicability of high-strength steel in bridge systems. The program consists of 44 large-scale structural tests on various bridge components, along with 20 concrete prism tests aimed at examining cracking behavior in detail. The following chapters outline the testing matrix, specimen design, fabrication of specimens, test setup, and instrumentation, and results.

3.1. Superstructures

3.1.1. CIP-PCP Deck

3.1.1.1 Specimen Design

The deck specimens were designed to evaluate the applicability of high-strength reinforcement in CIP-PCP concrete slabs. The deck specimens simulate the details of transverse and longitudinal panel joints in CIP-PCP bridge decks (Refer to Figure 3-1).

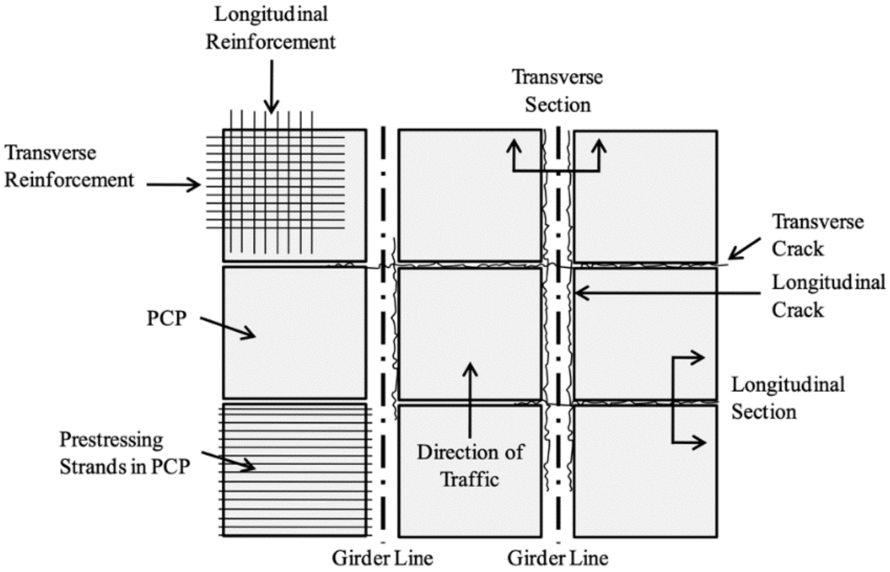

Figure 3-1. CIP-PCP Bridge Deck Terminology (Foster, 2010)

A total of six deck specimens were designed, divided into two groups, each consisting of three specimens. One group simulated transverse panel joints, while the other group simulated longitudinal panel joints. Each group featured three specimens with different reinforcement arrangements, varying in rebar grade and spacing. The control specimen used the current TxDOT rebar layout with normal-strength steel. The remaining two specimens incorporated high-strength rebars: one maintained the same rebar layout as the control specimen, while the other reduced the reinforcement ratio by approximately 40%, while maintaining the theoretical load capacity as the control specimen. The test matrix is shown in Table 3-1. In the table, the first letter of each ID represents the type of deck specimen: "T" denotes transverse deck strip specimens, while "L" indicates longitudinal deck specimens. The second letter indicates the rebar grade, with "N" representing normal-strength reinforcing bars and "H" indicating high-strength rebars. The following number specifies the rebar layout, as detailed in the table.

In the table, the first letter of each ID represents the type of deck specimen: "T" denotes transverse deck strip specimens, while "L" indicates longitudinal deck specimens. The second letter indicates the rebar grade, with "N" representing normal-strength reinforcing bars and "H" indicating high-strength rebars. The following number specifies the rebar layout, as detailed in the table.

Table 3-1. Test matrix of CIP-PCP deck specimen

Specimen ID	Top mat reinforcement		Remark
	Longitudinal	Transverse	
TN	Gr.60 @ 9 in.	Gr.60 @ 9 in.	Current TxDOT standard
TH1	Gr 60 @ 9 in.	Gr.100 @ 9 in.	One-to-one replacement
TH2	Gr.60 @ 9 in.	Gr.100 @ 15 in.	40% reduction
LN	Gr.60 @ 9 in.	Gr.60 @ 9 in.	Current TxDOT standard
LH1	Gr.100 @ 9 in.	Gr.60 @ 9 in.	One-to-one replacement
LH2	Gr.100 @ 15 in.	Gr.60 @ 9 in.	40% reduction

Each specimen consisted of two layers: a PCP layer and a CIP layer. Two standard PCPs, each measuring 8'-0"x8'-0"x0'-4", were used to simulate panel placement along the girder line or girder. The transverse specimens included a 7-inch gap between PCPs to allow space for shear connectors, aligning with typical construction practices. Longitudinal specimens, which represented panel joints in the longitudinal direction, included a 1.5-inch gap to account for minor imperfections on the side surfaces. The CIP panel, with a depth of 4.5-inch, was positioned above the PCPs, spanning two PCPs and the gaps between them as shown in Figure 3-2. The PCPs were manufactured by fabricator to meet the TxDOT standards, using Class H concrete with a release strength is 3,500 psi and a minimum 28-day strength is 5,000 psi. The CIP concrete mix targeted Class S, with a 28-day strength of 4000 psi. The compressive strength, splitting tensile strength, and modulus of elasticity were tested in accordance with ASTM standards: ASTM C39, ASTM C496, and ASTM C469, respectively. The properties of rebars were obtained through rebar tension test following ASTM A370. (Refer to Figure 3-3).

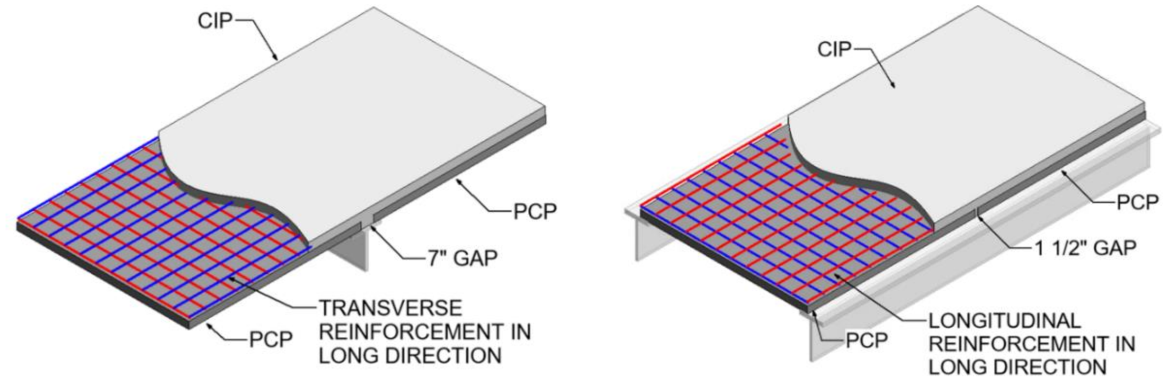

(a) Transverse specimen (b) Longitudinal specimen

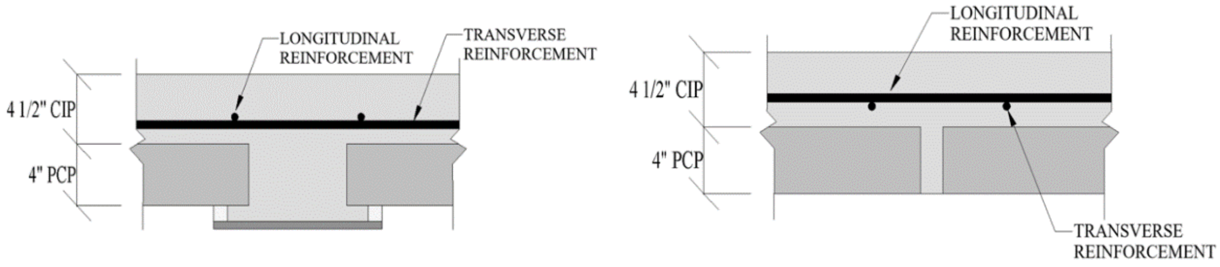

(c) Transverse panel joint (d) Longitudinal panel joint

Figure 3-2. Detail of specimens

(a) Compression (b) Splitting tension (c) Modulus of elasticity (d) Rebar tension

Figure 3-3. Material testing setup

3.1.1.2. Fabrication

3.1.1.2.1. PCPs (Precast, prestressed concrete panels)

Twelve PCPs with were constructed by Valley Prestressed Product Inc. The concrete panels were constructed following TxDOT standard. Prestressed strands were used as transverse reinforcement spaced at 6-inch with a tension force of 14.4 kips per strand. No.3 steel reinforcing bars used as longitudinal reinforcement at 6-inch. Precast panels were broom-finished to assist in composite action with the CIP layer of concrete. After stressing the strands and curing the concrete, the strands were cut with 3 inches projecting from each side of the panel. Panels were demolded from the formwork after a day of being moist-cured. The PCP reinforcement and finished PCPs are shown in Figure 3-4.

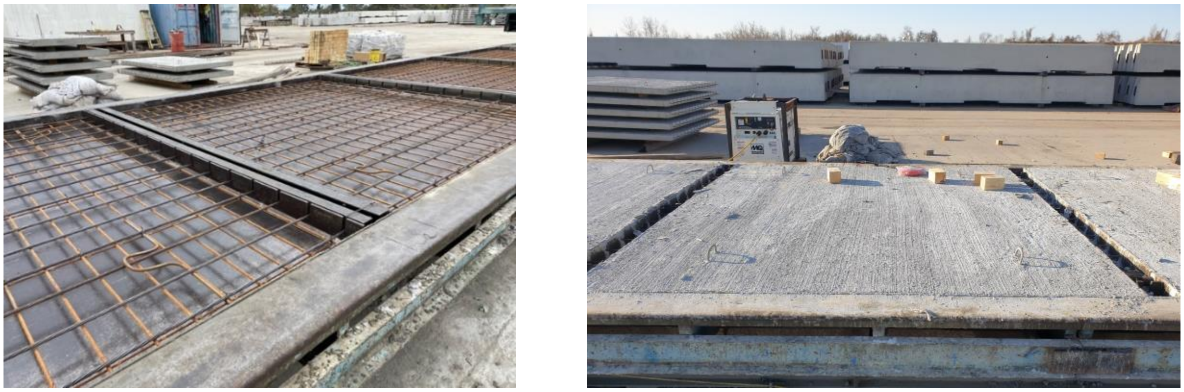

(a) PCP reinforcement (b) Finished PCPs

Figure 3-4. Fabrication of PCPs

3.1.1.2.2. CIP (Cast-in-Place) Panels

For the CIP fabrication, the PCPs were first positioned. For the transverse specimens, a simulated girder line made of a 12"x96"x1/2" steel plate with 7/8" diameter shear studs spaced at 12 inches interval was placed on the soffit. Bedding strips were glued to the simulated girder line to serve as the placement base. Once the PCPs were in place, the transverse and longitudinal reinforcement were arranged. Strain gauges (120-ohm, 5 mm gauge length) were applied to the reinforcement at critical locations following the procedure described in Chapter 3.1. Subsequently, steel formwork was assembled. Prior to casting the CIP, the surface of the PCPs was sprayed with water to achieve a saturated surface dry condition. During the CIP cast, concrete was initially placed at the panel joint to ensure proper filling of the joint, followed by the placement of the entire CIP layer. Concrete vibrators were used to achieve proper consolidation, and the top layer was screeded to create a flat surface. After casting, the specimen was covered with plastic sheeting to allow for curing. The details of fabrication process are shown in Figure 3-5.

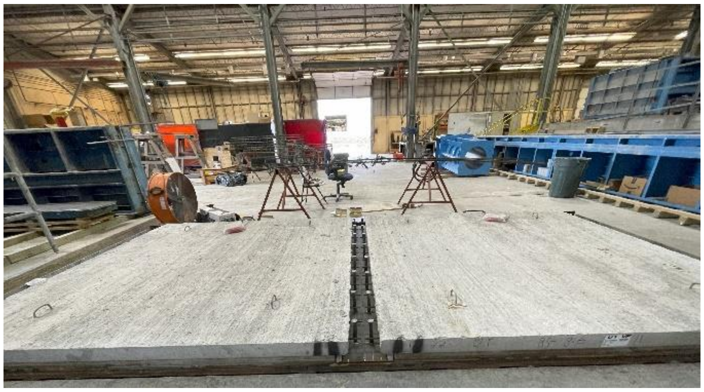

(a) Placement of PCPs

(b) Assembly of reinforcement and steel formwork

(c) Concrete casting

Figure 3-5. Fabrication of CIP panels

3.1.1.3. Test Setup

3.1.1.3.1. Loading Frame

The four-point bending test was selected to secure cracking at the panel joints. The testing setup is shown in Figure 3-6. The specimen was placed on pin-roller steel beams, supported by four hydraulic rams. The support system included reaction beams, pin and roller supports, load cells, and rods with reaction nuts was placed on the specimen. The load was applied through the rods from the hydraulic rams. Each end of the specimen was supported by a pin at one end and a roller at the other. The pin support featured a 2-inch diameter welded rod attached to a steel plate, while the roller support, also 2 inches in diameter, allowed for lateral translation. Two 100-kip load cells, anchored with rods and reaction nuts, were mounted on each reaction beam.

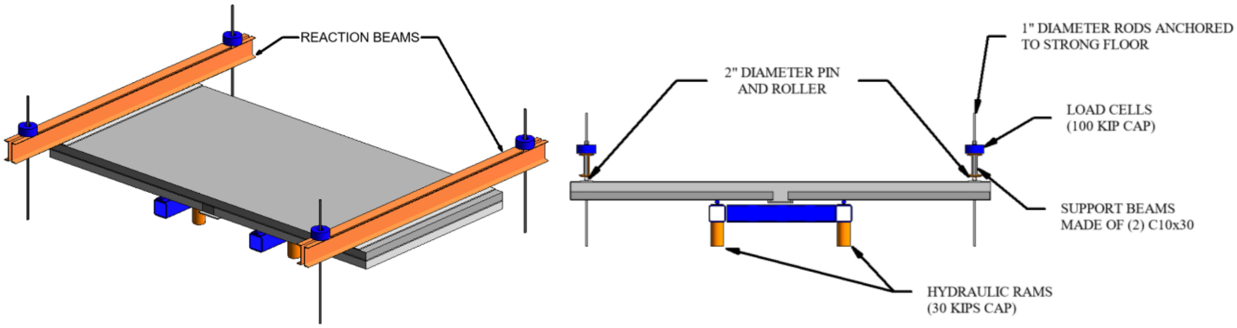

(a) Isometric view (b) Elevation view

Figure 3-6. CIP-PCP deck testing setup

3.1.1.3.2. Instrumentation

The reactions, displacement of specimen, rebar strain and crack widths were all extensively measured during the experiment.

- Load and displacement measurements

Four 100-kip capacity load cells, mounted on the reaction beams, measured the applied loads. Six LPOTs were used to monitor displacement. Two LPOTs were placed at the center of the specimen on each side, while the remaining four LPOTs were positioned at each end of the reaction beams to capture rigid body motion, as shown in Figure 3-7.

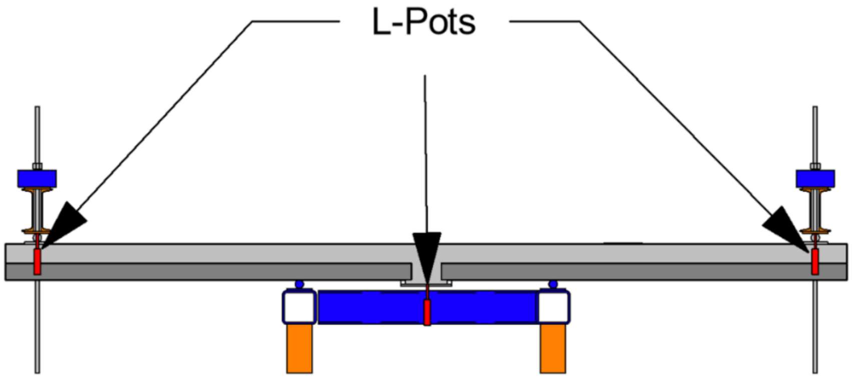

Figure 3-7. Location of linear potentiometers for deck test

- Strain measurements for reinforcing bars

Electrical resistance strain gauges were attached to the flexural rebars in the CIP portion of the deck covering the panel joint within the test region. Strain gauges on the rebars near the center of the specimen were spaced 9 inches apart, while those on the remaining rebars were spaced 18 inches apart. The specific locations of the strain gauges are shown in Figure 3-8.

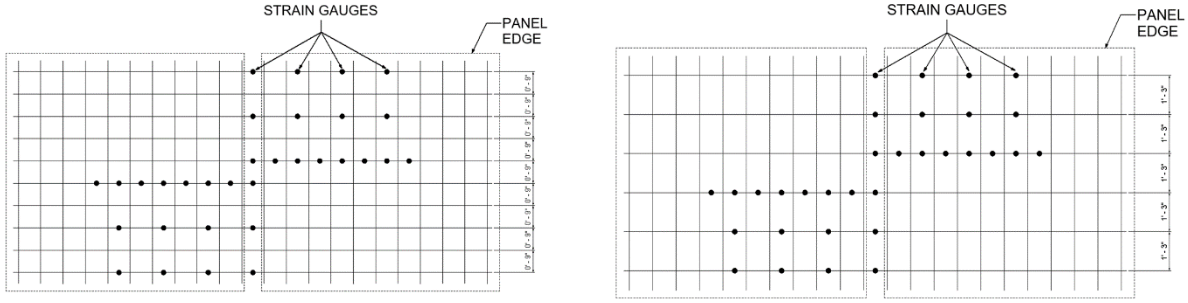

(a) Specimen with normal-strength steel (b) Specimen with high-strength steel

Figure 3-8. Strain gauge locations of CIP-PCP deck specimen

- Crack widths

During the test, cracks were marked, and crack widths were measured using a crack comparator at each load step. All measurements were taken by the same student to secure consistency. Furthermore, the Optotrak Certus System was used to measure crack widths. This optical system included a camera and markers, which were arranged in an orthogonal grid pattern across the center of the specimen, with a 6-inch spacing in each direction, as shown in Figure 3-9. The system recorded the positions of the markers in three-dimensional coordinates throughout the test, enabling the calculation of relative displacement between markers to determine the crack width.

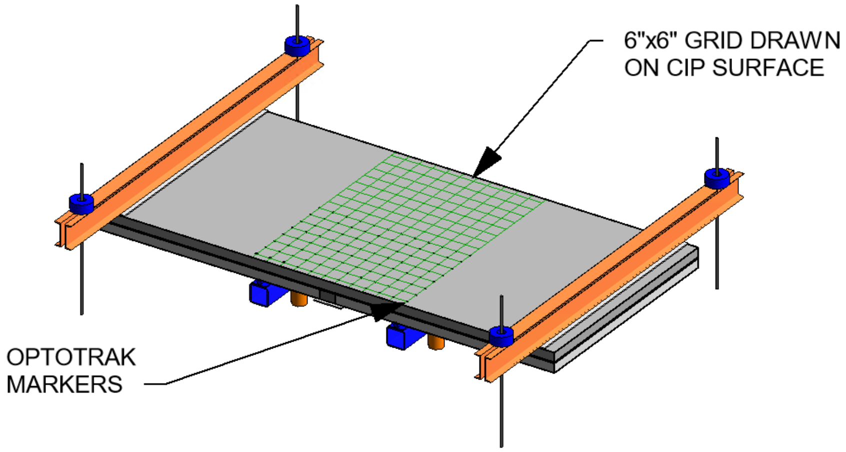

Figure 3-9. Optotrak marker location

3.1.1.4. Test Procedure

After the test setup was installed, the load was applied incrementally in 3-kip increments until excessive crack widths, approximately 0.04 inches, were observed. At this point, cracks were marked, and crack widths were measured using a crack card at each load interval. Afterwards, the load was increased until failure occurred.

3.1.1.5. Experimental Results and Discussion

3.1.1.5.1. Overview

This chapter provides a thorough analysis of experimental results, including crack patterns, load-displacement behavior, measured rebar strain, and an evaluation of serviceability based on crack width. Table 3-2 summarizes the material properties obtained from laboratory testing. Particularly, the yield strength of the high-strength steel used in the deck test was calculated using the 0.2% offset method, due to the absence of a clear yield plateau, as shown in Figure 3-10.

Table 3-2. Material properties used in deck test

Specimen ID	**Type**	**Concrete**			**Top mat reinforcement**	
		Compressive strength (psi)	**Splitting tensile strength (psi)**	**Modulus of elasticity (psi)**	**Yield strength (ksi)**	**Tensile strength (ksi)**
TN	CIP	6516	436	4553	63.9	104.3
	PCP	9784	456	6321		
TH1	CIP	4898	442	5019	136.9	172
	PCP	9347	488	6505		
TH2	CIP	5539	628	5304		
	PCP	8782	615	6572		
LN	CIP	6098	617	5919	73.8	114.3
	PCP	8323	748	6779		
LH1	CIP	6795	429	5315	136.9	172
	PCP	9409	490	6103		
LH2	CIP	5440	453	5980		
	PCP	9193	600	7360		

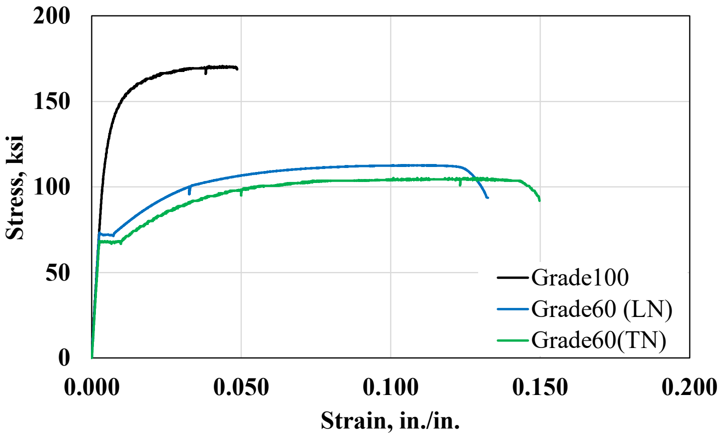

Figure 3-10. Rebar stress-strain curve (Deck specimen)

3.1.1.5.2. Crack Pattern

Figure 3-11 illustrate the crack patterns observed in each specimen. Since the self-weight of the specimen opposed the applied loads during testing, initial cracks appeared near the loading points, where the moment was highest, rather than at the midpoint. These cracks propagated transversely but not uniformly across the specimen. The extent of propagation along each crack and the crack width measured with the Optotrak system varied at different measurement locations along the same crack, confirming an uneven progression of cracking.

Following this, cracks developed near the panel joint and then spread throughout the test region. In specimens with high-strength rebars, additional cracks formed between the loading points and end supports, resulting in more cracks overall than in those reinforced with normal-strength rebars. This behavior is attributed to the higher strength of high-strength rebar. Unlike normal-strength rebar, which has a distinct yield plateau, high-strength rebar follows a parabolic stress-strain curve (see Figure 3-10), allowing it to resist loads progressively as strength increases. This gradual resistance enables the load to transfer more effectively from the center toward the supports, promoting crack propagation along the specimen. In contrast, normal-strength rebar, with its defined yield plateau, undergoes concentrated deformation near the joint once yielding occurs, causing cracks to localize and intensify in this area. This observation is further supported by stress distribution analysis from strain gauges attached to the rebar, as will be discussed in a later section.

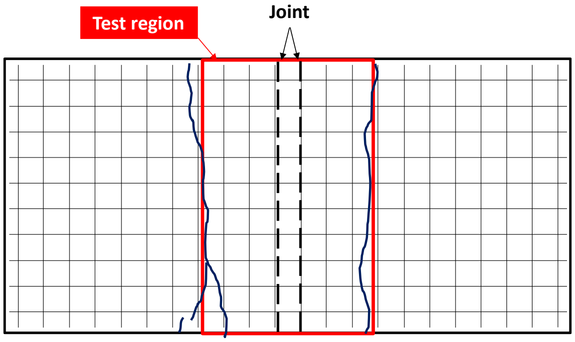

Initial cracking

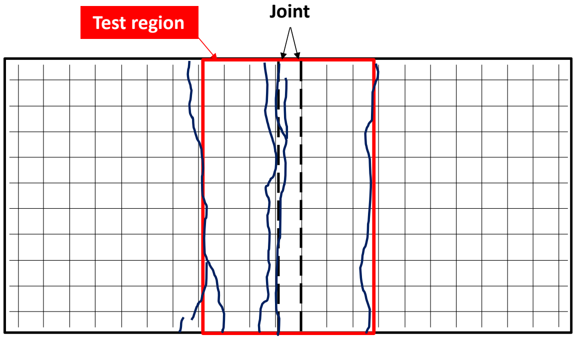

Joint cracking

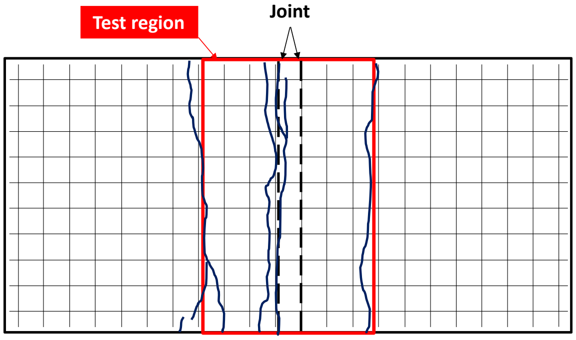

Failure

(a) TN

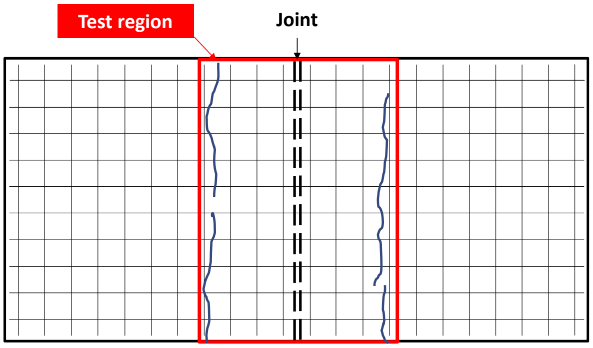

Initial cracking

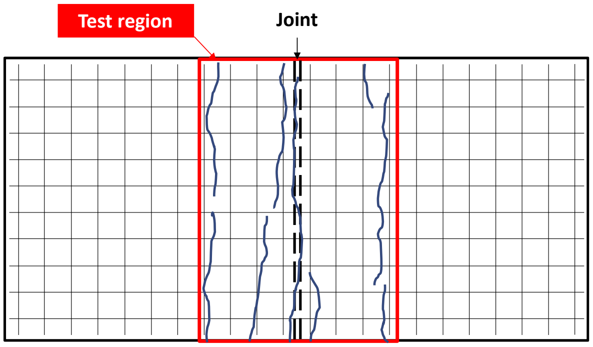

Joint cracking

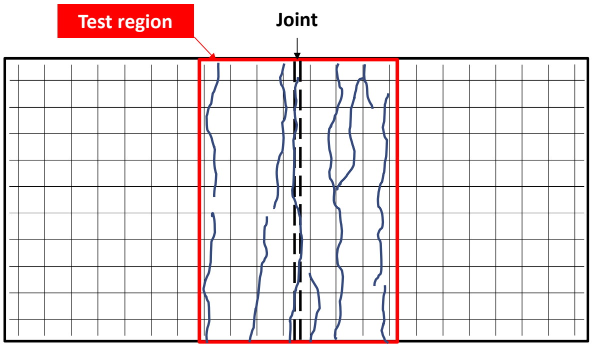

Failure

(b) LN

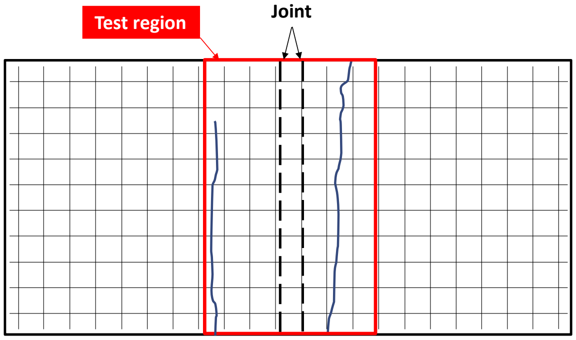

Initial cracking

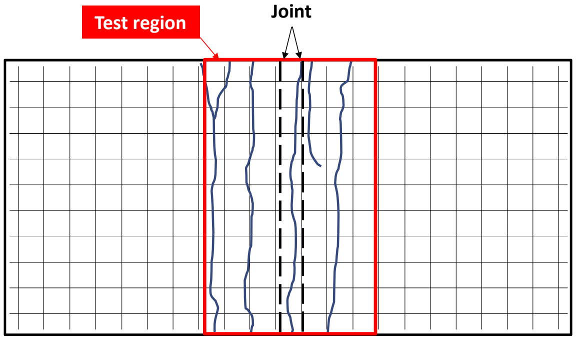

Joint cracking

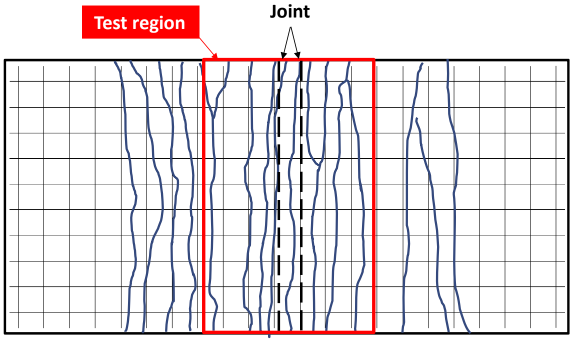

Failure

(c) TH1

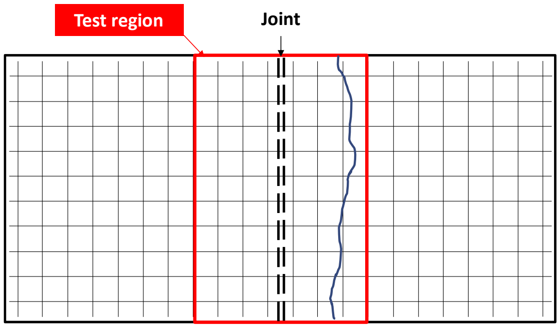

Initial cracking

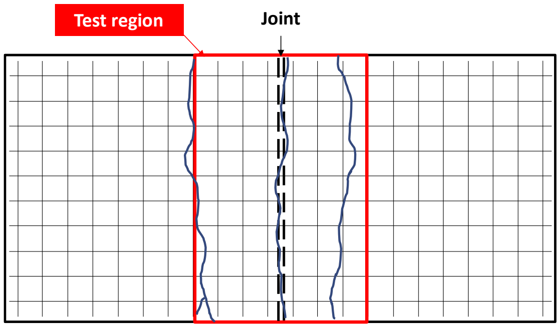

Joint cracking

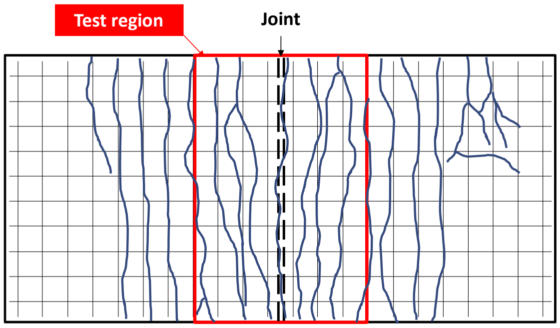

Failure

(d) LH1

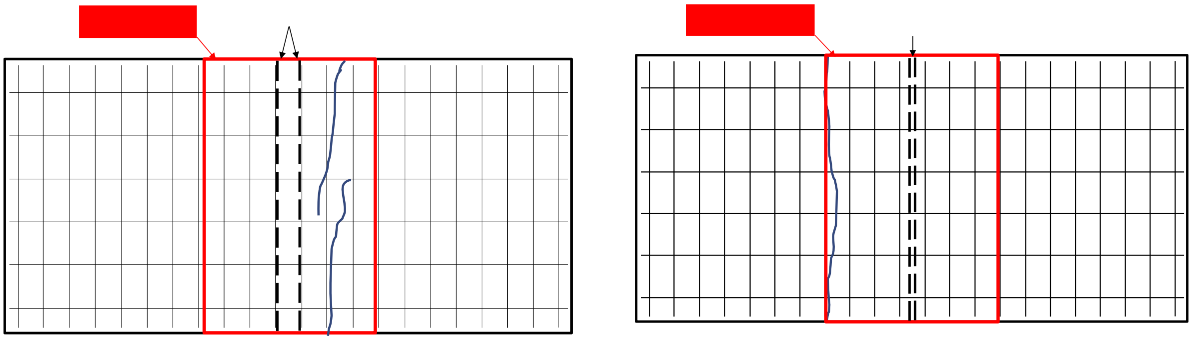

Initial cracking Initial cracking

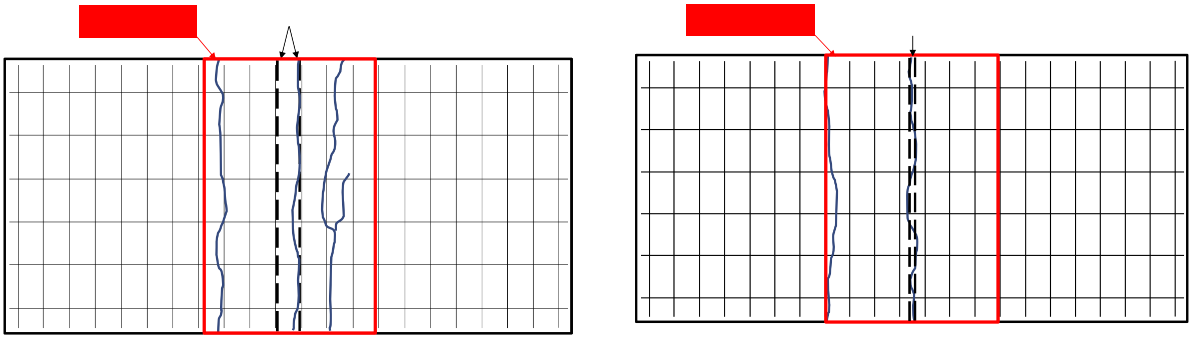

Joint cracking Joint cracking

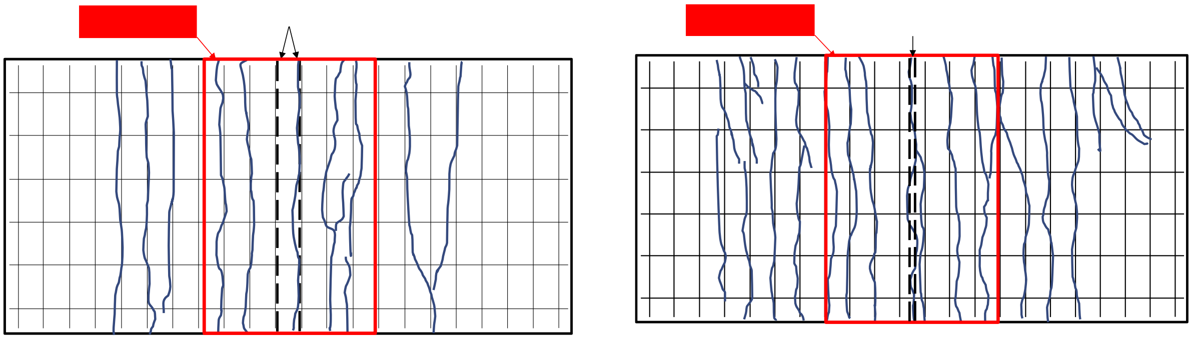

Failure Failure

(e) TH2 (f) LH2

Figure 3-11. Crack patterns of deck specimens

3.1.1.5.3. Load-Displacement Behavior

Figure 3-12 shows the load-displacement relationships with respect to type of specimen and rebar layouts. This graph uses the applied load data from the load cells and the deflection measurements at the midpoint of the specimens. Displacement values were adjusted to exclude rigid body motion effects by using two LPOTs positioned at the ends of the reaction beam. Several load drops and increases, due to crack formation, were observed, though all specimens overall exhibited similar load-displacement behavior.

In LH1 and LH2 specimens, localized cracking near the support caused a sudden load drop, resulting in an abrupt test termination. This phenomenon was attributed from excessive rotation of the support due to insufficient resistance, likely from an improper support system setup, resulting in failure at lower load levels than TH1 and TH2 specimens. Nonetheless, LH1 and LH2 specimens achieved maximum load capacities higher than LN1, which was reinforced with normal-strength rebar. Moreover, strain measurements indicated that bar stress exceeded the design yield strength of 100 ksi, verifying the suitability of these test data for further crack behavior analysis.

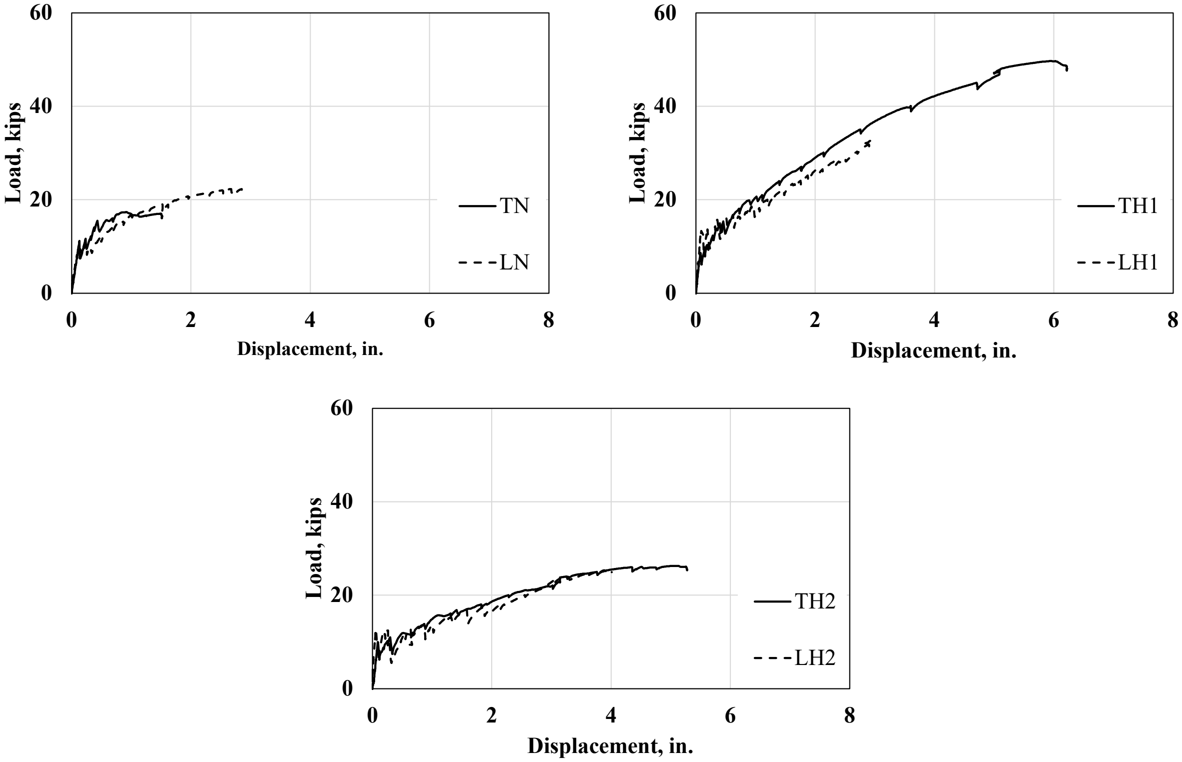

(a) Type of specimen

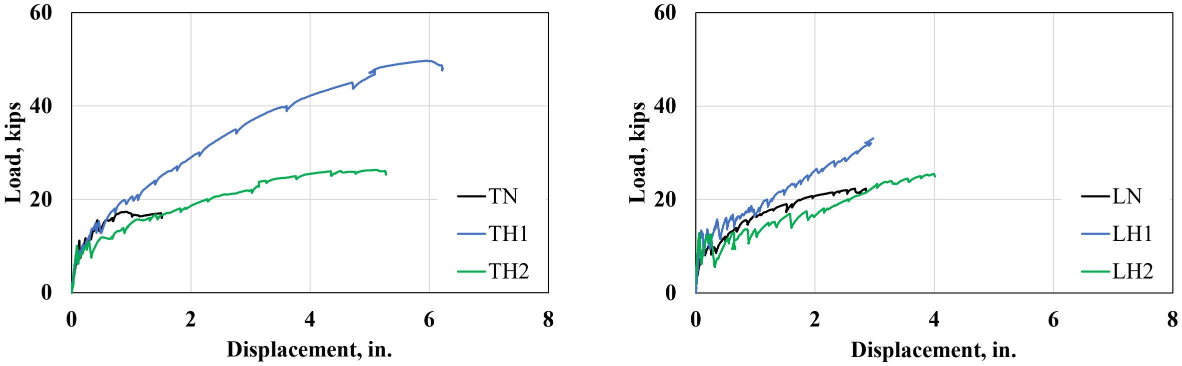

(b) Rebar layout

Figure 3-12. Load-displacement curve of deck test

3.1.1.5.4. Rebar stress distribution

Rebar stress was converted from strain gauge measurements using the stress-strain relationship obtained from material test data. Figure 3-13 presents the stress distribution at each gauge location, along with observed crack patterns. The contour values denote the percentage of stress relative to the specified yield strengths of 60 ksi for normal-strength rebar and 100 ksi for high-strength rebar, respectively. Certain gauges were damaged during testing and ceased functioning; these are marked with an "X" at their respective locations in the Figure.

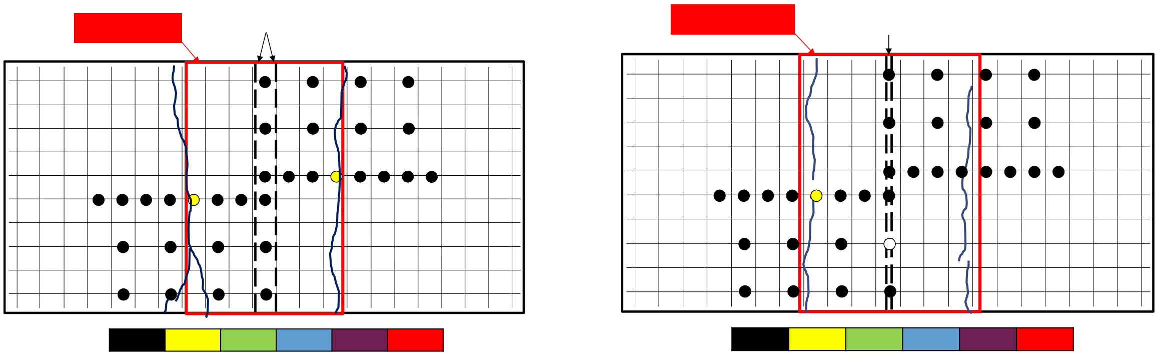

Initial cracking

Initial cracking

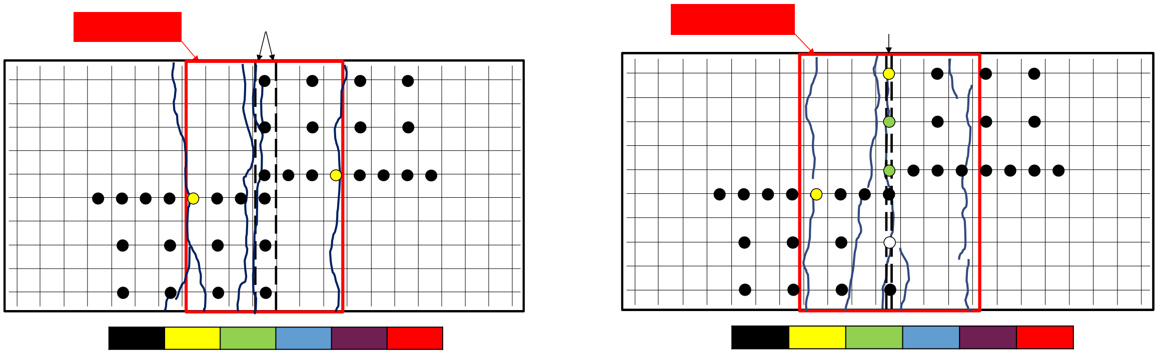

Joint cracking

Joint cracking

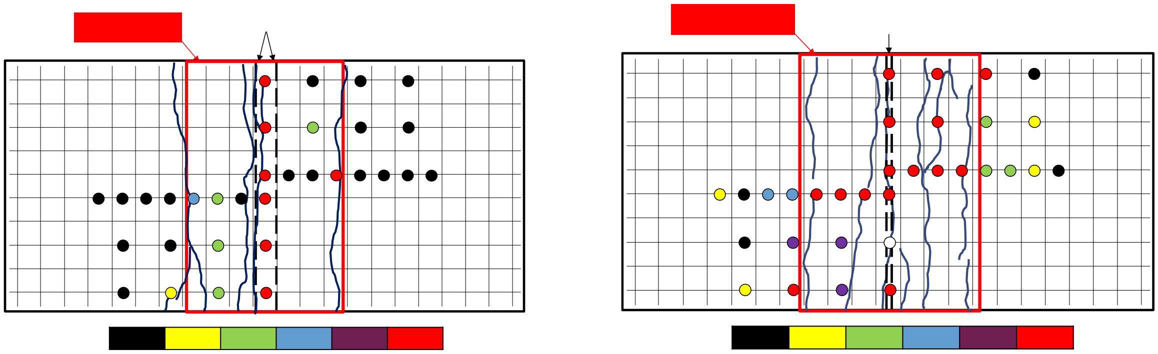

Failure

Failure

(a) TN

(b) LN

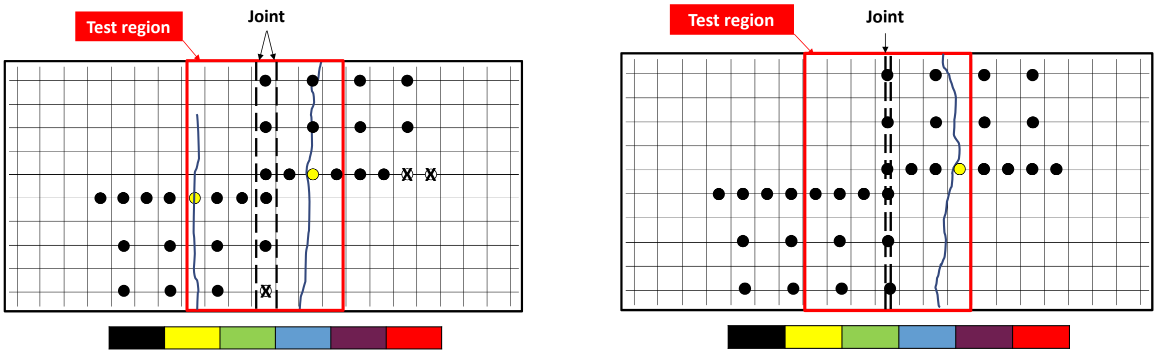

Initial cracking

Initial cracking

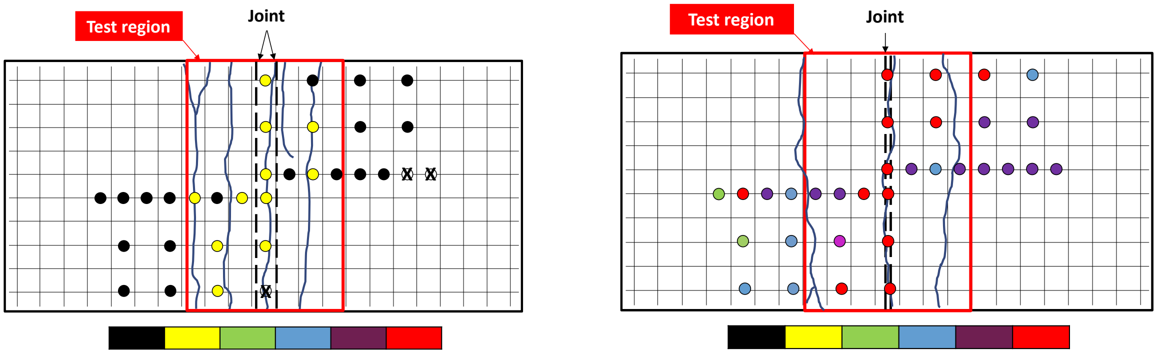

Joint cracking

Joint cracking

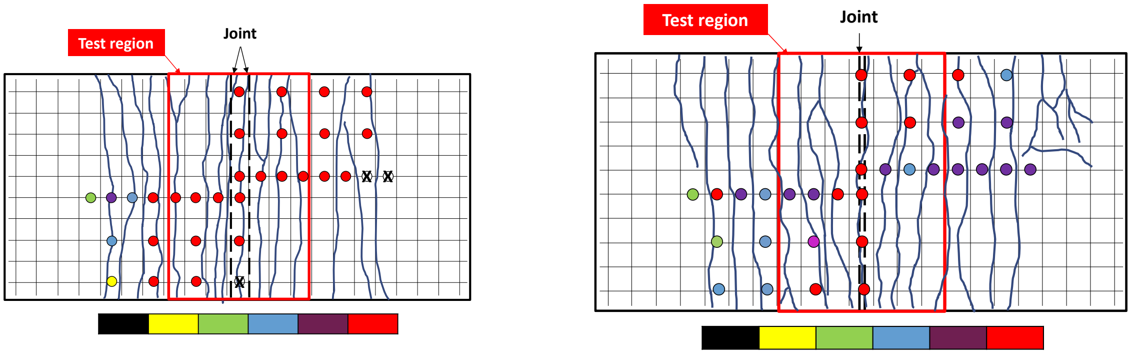

Failure

Failure

(c) TH1

(d) LH1

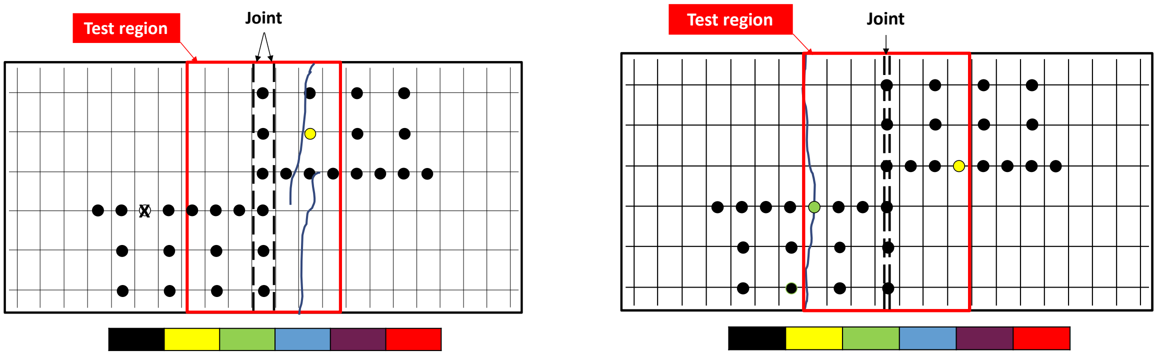

Initial cracking Initial cracking

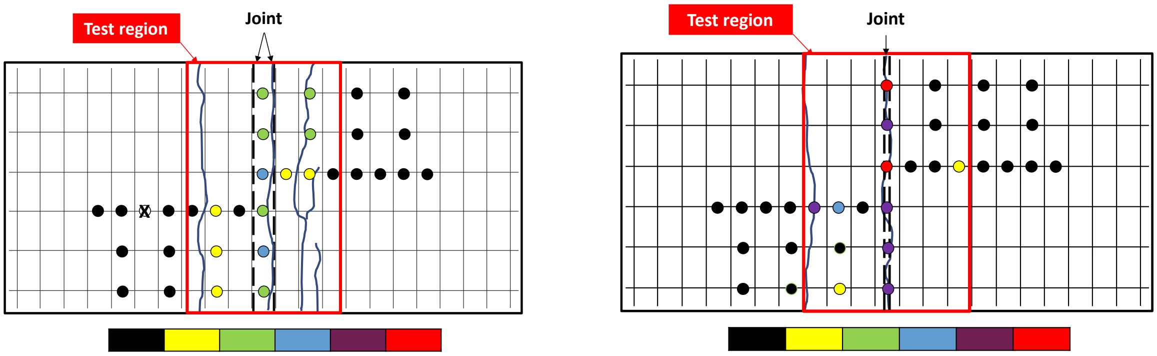

Joint cracking Joint cracking

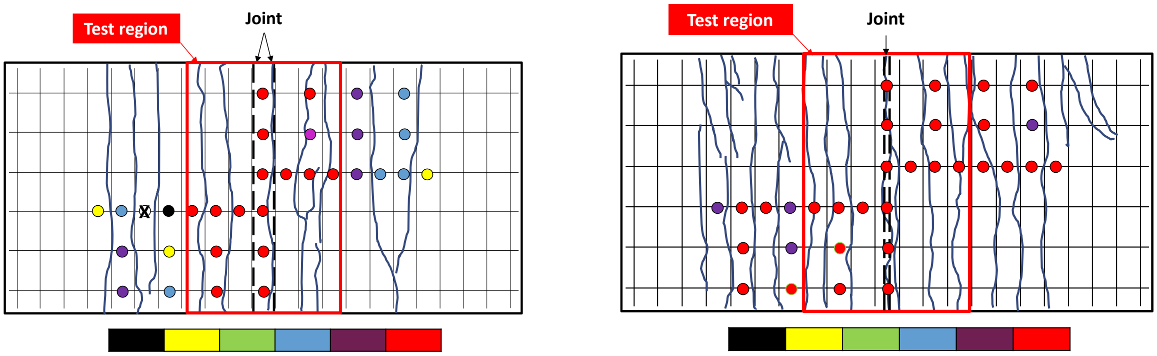

Failure Failure

(e) TH2 (f) LH2

Figure 3-13. Rebar stress distribution with crack patterns of deck specimens

As applied loads increased, bar stress increased correspondingly, with uneven stress distribution along the longitudinal axis with localized concentrations near the joint. This finding aligns with prior observations, where cracks near the joint played a dominant role in overall crack behavior. Therefore, it is crucial to recognize that joint-adjacent cracks are key factors in controlling cracking and assessing serviceability.

3.1.1.5.5. Crack widths

As described in previous chapter, the crack width was derived from Optotrak system, specifically calculated based on changes in distance between paired markers. Given the significant deflection observed during testing, the relative distance between markers accounted for coordinates in both the z- and x-directions, as shown in Figure 3-14. In the absence of cracking, measurements L_1 and L_2 would remain equal. However, any detected difference in length indicated the presence of a crack, with the resulting crack width recorded accordingly.

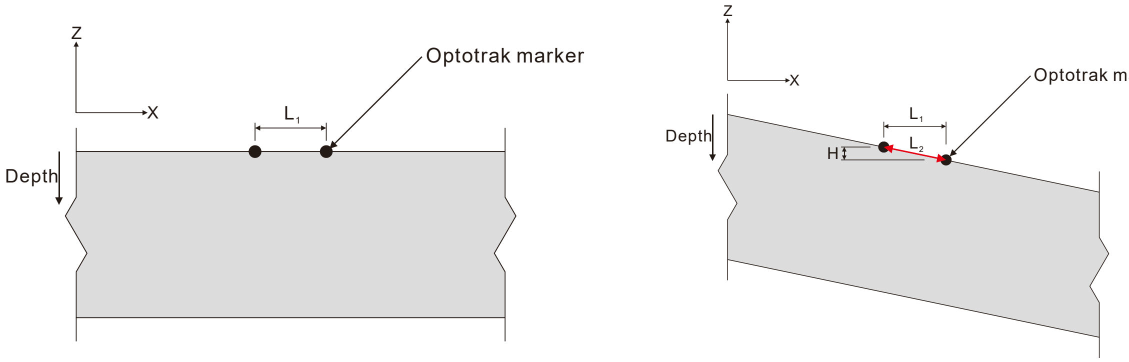

(a) Inital condition (b) After deforation

Figure 3-14. Methodology of crack width calculation with Optotrak system

The relationship between crack width and rebar stress was analyzed as shown in Figure 3-15 and Figure 3-16. Given that cracks near the joint are the primary concern and that rebar stress is highly sensitive to the distance between the gauge and crack, crack width measured using the Optotrak markers closest to the strain gauge location near the joint was used in the analysis.

The stress-crack width curve typically followed a proportional trend, with similar behavior within each specimen. However, in certain cases, crack width did not change even as rising of rebar stress, likely due to the relative positions of crack width measurement and rebar gauges; these cases were excluded from further analysis. Generally, crack width remained relatively stable with increasing rebar stress but showed a sharp increase at a specific stress level. This suggests that crack width near the joint did not increase gradually but surged suddenly at a certain stress level due to unevenly concentrated joint cracking.

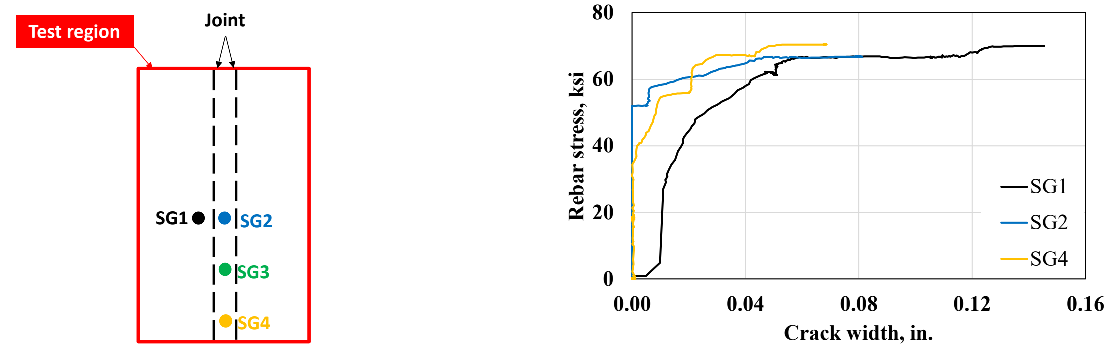

(a) Gauge location (Transverse specimen)

(b) TN

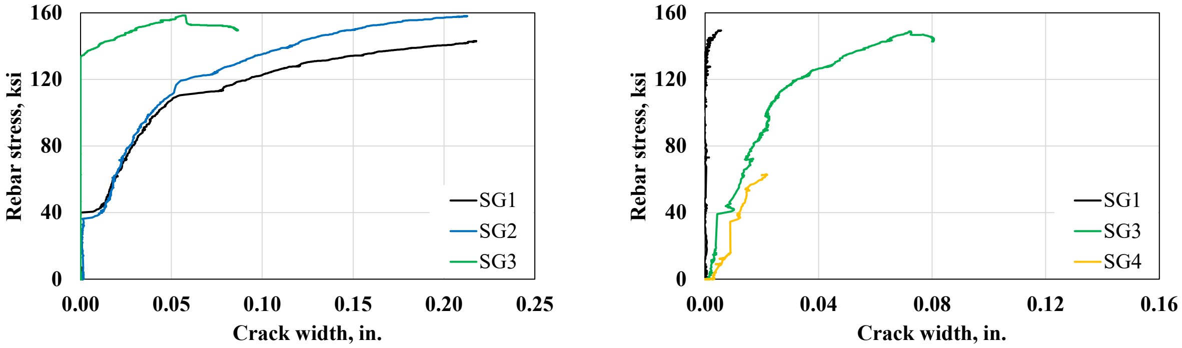

(c) TH1

(d) TH2

Figure 3-15. Crack width according to rebar stress near joint in transverse deck specimen

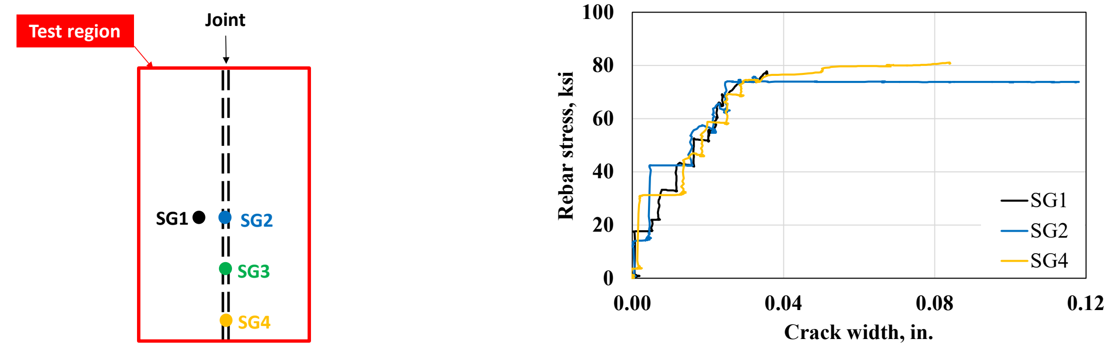

(a) Gauge location (Longitudinal specimen)

(b) LN

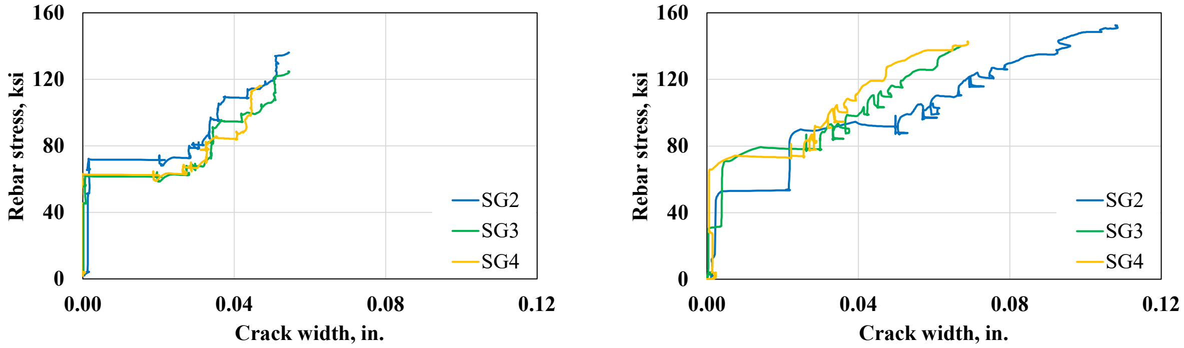

(c) LH1

(d) LH2

Figure 3-16. Crack width according to rebar stress near joint in longitudinal deck specimen

ACI 318-19 and AASHTO LRFD (2020) establish limits on the spacing of flexural rebars to control crack widths, as specified in Equations (3-1) and (3-2), respectively. Since the service limit state is determined by the yield strength of the rebar, the relationship between rebar stress and crack width is commonly used to assess serviceability.

However, as the rebar stress was measured locally and does not always correspond to the crack location, the validity of the relationship between rebar stress and crack width was examined prior to evaluating the serviceability. The rebar spacing requirements are based on a crack model proposed by Frosch (1999, 2001), from which Equation (3-3) was developed to predict crack width. Therefore, the Frosch model was compared with the experimental results, as illustrated in Figure 3-17. In some test cases, including TN, LN, and TH1 specimens, behavior closely aligned with the crack model; however, the remaining cases showed substantial variants. Consequently, these inconsistent trends compromised the reliability even though rebar stress was measured at locations closest to the crack width measurement locations.

$$s_{max} = Lesser\ of: 15\left(\frac{40000}{f_{s,ACI318}}\right) - 2.5c_c\ , 12\left(\frac{40000}{f_{s,ACI318}}\right) \qquad \text{Units: psi and in.} \tag{3-1}$$

$$s_{max} = \frac{700\gamma_e}{\beta_s f_{s,AASHTO}} - 2d_c \qquad \text{Units: ksi and in.}$$

$$\beta_s = 1 + \frac{d_c}{0.7(h - d_c)} \tag{3-2}$$

$$w_c = 2\frac{f_s}{E_s}\beta\sqrt{d_s^2 + (s/2)^2} \qquad \text{Units: ksi and in.}$$

$$\beta = 1 + 0.08d_c \tag{3-3}$$

where,

s_{max}= maximum spacing of flexural reinforcement in the layer closest to the tension side

$f_{s,ACI318}$=tensile stress in the reinforcement at service loads $\left(\leq 2/3\, f_y\right)$

c_c=clear cover of reinforcement

β_s=ratio of flexural strain at the extreme tension face to the strain at the centroid of the reinforcement layer nearest the tension face

$f_{s,AASHTO}$= calculated tensile stress in nonprestresssed reinforcement at the service limit state not to exceed $0.6f_y$

γ_e=exposure factor: 1.0 for Class 1 exposure condition and 0.75 for Class 2 exposure condition

d_c=thickness of concrete cover measured from extreme tension fiber to center of the flexural reinforcement located closest thereto

h=overall thickness or depth of the component

w_c=crack width

E_s=modulus of elasticity of reinforcement

s =center-to-center spacing of tensile reinforcement

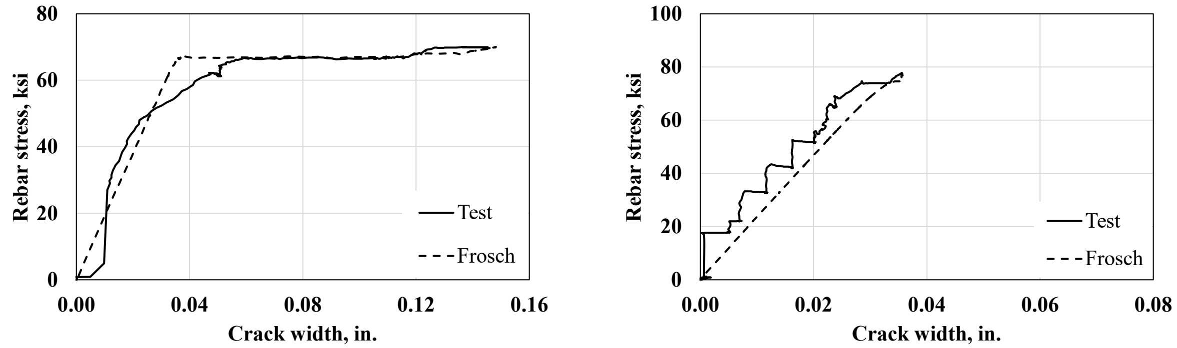

(a) TN (b) LN

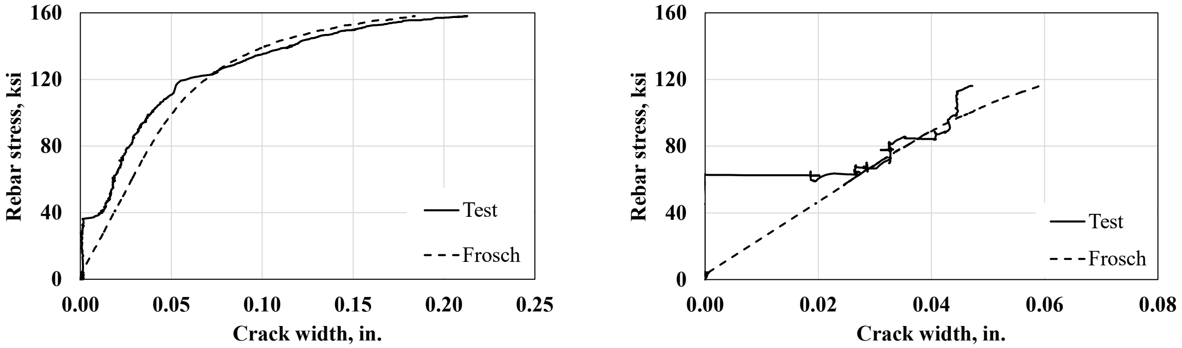

(c) TH1 (d) LH1

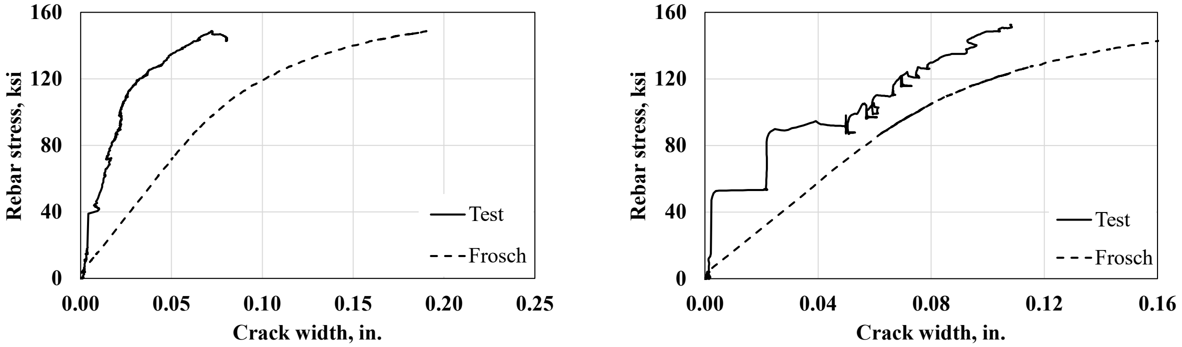

(e) TH2 (f) LH2

Figure 3-17. Comparison crack width measured in deck test and predicted by Frosch model

Alternatively, the behavior of crack width in relation to the moment, calculated from the measured load during testing, was analyzed and is shown Figure 3-18. To determine the moments in service state, load combinations and deck slab design tables in in AASHTO LRFD (2020). Specifically, the Service I load combination was used. The dead load was calculated by considering the weight of the deck and wear surface with reference to the geometry of the Tx-girder to consider the actual bridge deck conditions, and the live load was determined using the deck slab design tables in Appendix A4 of AASHTO LRFD (2020). The crack width limits specified by AASHTO and ACI are included to assess the serviceability. The crack width limit recommended by AASHTO LRFD (2020) is 0.017 in., while ACI 224R-01 specifies a limit of 0.016 in.

The crack width remains stable up to a certain moment level, after which it increases sharply. With the same rebar layout, similar behavior was observed across different specimen types. In specimens with regular rebars (TN and LN), the moment increases only slightly as the crack width grows. In contrast, when high-strength reinforcing bars are used with the same layout (TH1 and LH1), the moment increases more gradually alongside the crack width. Additionally, specimens with high-strength rebars and wider spacing show greater crack widths at the same moment level compared to the other cases, highlighting the importance of bar spacing in crack control. However, all cases were found to meet serviceability requirements.

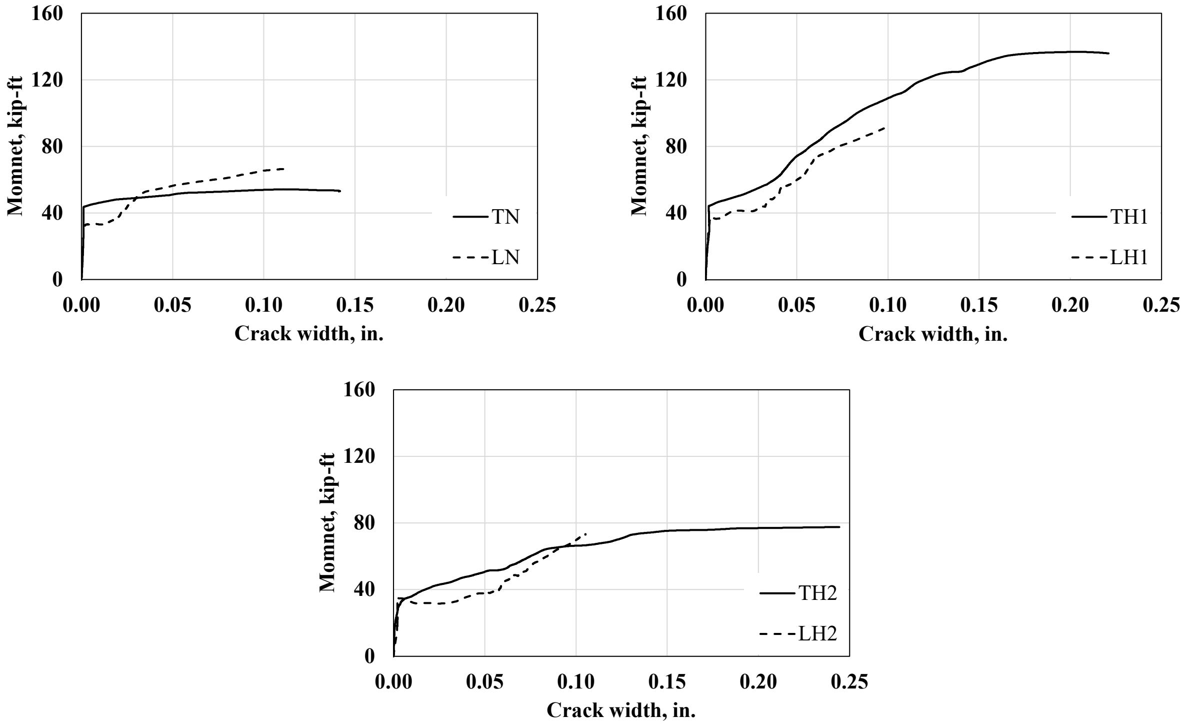

(a) Type of specimen

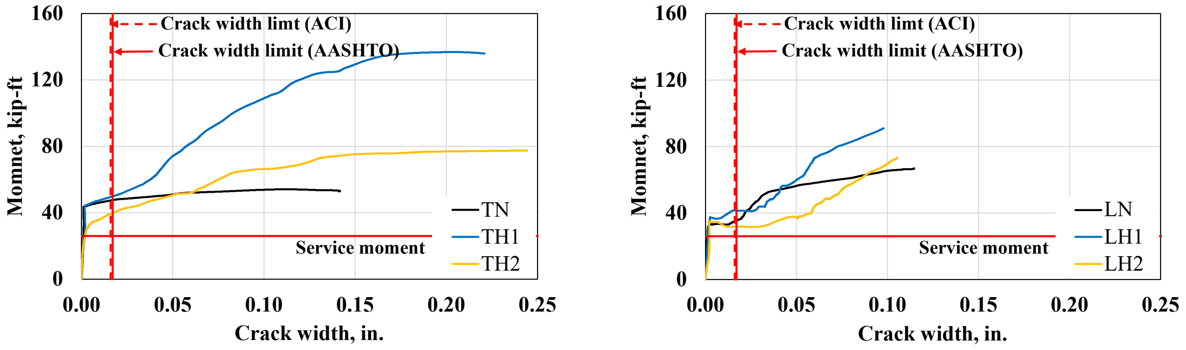

(b) Rebar layout

Figure 3-18. Crack width with respect to moment in deck test

3.1.1.6. Conclusions

Six CIP-PCP deck with normal- and high-strength rebars were tested. The study primarily focused on the overall behavior related to cracking in the joint area due to bond effects and assessed the impact of using high-strength rebar. The main conclusions are as follows:

- Depending on the differences in the yield plateau of rebars, cracks in specimen with normal-strength rebar did not propagate uniformly along the longitudinal axis, while high-strength rebar led to more extensive crack propagation. However, it is noted that cracks adjacent joints emerged as the major cracks with the widest widths.
- High-strength rebar, arranged in the same layout as normal-strength rebar, enhanced load capacities. Additionally, when rebar spacing was increased according to the specified yield strength ratio between normal- and high-strength rebar, comparable load capacities were attained.
- Rebar spacing proved to be a crucial factor in controlling crack width. At the same moment level, wider crack widths were observed with increased rebar spacing. However, crack width limits specified by ACI 224R-01 and AASHTO LRFD (2020) at the service moment level were satisfied, ensuring compliance with serviceability requirements.

3.1.2. Prestressed Girder

3.1.2.1. Specimen Design

A total of eight prestressed beams are fabricated; four beams are Tx-girder, and the remaining beams are box beams. In order to study the serviceability performance and structural capacity, each beam will be tested twice, once on each side of the beam. Variables for the Tx-girder include shear span, strand pattern, yield strength of the shear reinforcement, and spacing of the end region confinement and shear reinforcement. On the other hand, for the box beam, four separate factors are chosen, including the number of supports, the spacing of the shear reinforcement, the yield strength, and the shear span. According to the TxDOT bridge design document, all strands for prestressed beam specimens are 0.6 in. in diameter with low relaxation, and the ultimate prestress for the strand is 270 ksi. The anticipated concrete strength at 28-days (f'_c) and at release day (f'_{ci}) is 8.5 ksi and 6.0 ksi, respectively, for both types of prestressed girder.

Rebar cage congestion is a common issue in prestressed bridge members. Using high-strength rebar as shear reinforcement can help reduce shear rebar congestion in Texas standard prestressed girders. In this study, the spacing of high-strength shear rebar was increased to achieve shear strength similar to that of existing Texas standard prestressed girders. The amount of shear reinforcement, excluding the end region rebar, is compared across all specimens based on the grade of shear rebar, as shown in Table 3-3. The results indicate that the reduction ratio in rebar quantity does not vary significantly with the loading location, generally showing a reduction of about 33%.

Table 3-3. Amount of shear rebar differences

Type	a/d_v	Number of shear rebar (ea)		Percent decrease
		Grade 60	Grade 100	
Tx-girder	2.95	19	13	32%
	1.44	7	5	29%
Box beam	1.43	19	12	37%
	2.95	11	7	36%
	Average			33.5%

3.1.2.1.1. Tx-girder

The impact of shear reinforcement in the end region is analyzed previously to determine the test matrix for the Tx-girder type specimen. The closely spaced reinforcements are placed in the end region of the Tx-girders web to prevent the spalling cracks that may occur during the transfer of the prestress. The stress in the steel to prevent the splitting resistance cannot exceed 20.0 ksi to control the crack at the end region in accordance with O'Callaghan (2007) and AASHTO LRFD (2020). Therefore, the quantity of reinforcing steel to prevent splitting cracks cannot be reduced due to the stress limit even if the high-strength steel is applied.

To thoroughly investigate the performance of high-strength reinforcement in pretensioned Tx-girder, the Tx-62, which is the largest size among the Tx-girder provided in the Texas standard drawing, is chosen for this experimental program. These specimens follow the geometry and reinforcement details listed in the TxDOT Bridge Design Manual (2024), as shown in Figure 3-19. The specimens for Tx-62 are 45 ft long, and each specimen contains 28 bonded strands with an 8-inch thick composite deck cast on top. These strands are spaced at 2 in., with one row positioned 2.5 in. from the bottom. This strand layout ensured sufficient flexural capacity for shear testing in both D-region and B-region while mitigating other types of potential issues related to prestressing strands, such as bursting and splitting stress in the end region. Also, the selection of the total number of strands considers the longitudinal reinforcement limit according to AASHTO LRFD (2020).

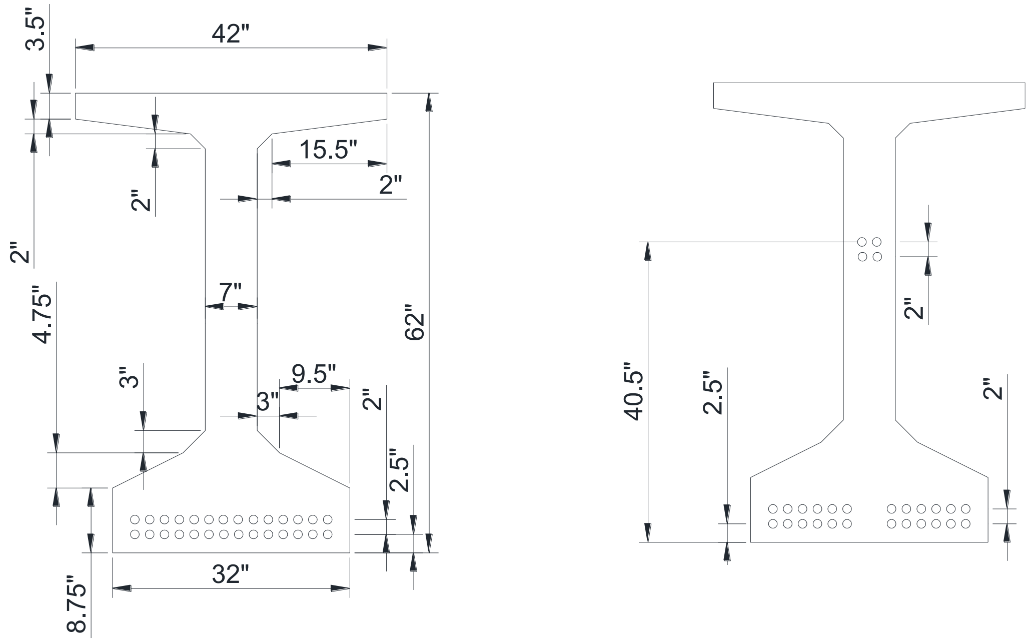

(a) Straight strand (b) Harped strand

Figure 3-19. Cross-section of Tx-62

The strand pattern is one of the variables for the specimens in this research. For Tx-62, two different types of strand patterns will be tested and compared, as shown in Figure 3-20. Only straight strands are placed in the two test specimens, but the harped strands are considered in the other specimens with the same number of total strands. Finally, 28 straight strands will be placed on two Tx-62 specimens, and two other specimens will contain four harped strands and 24 straight strands.

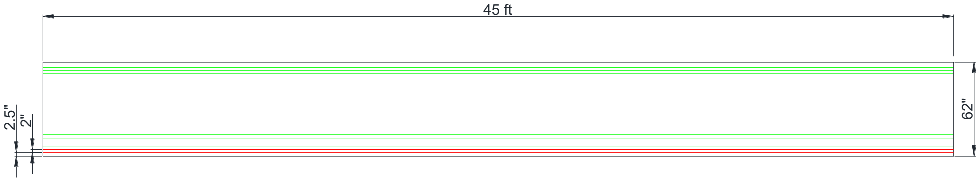

(a) Straight strand

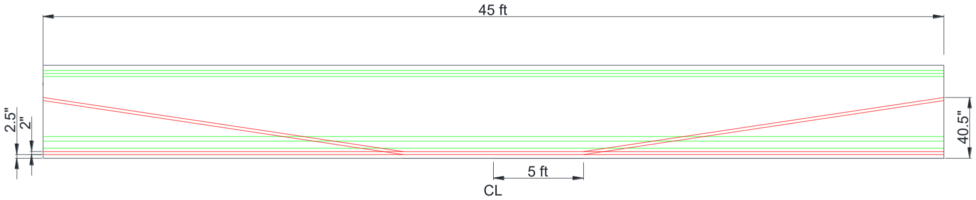

(b) Harped strand

Figure 3-20. Strand layout for Tx-62 specimens

In standard Tx-62 with Grade 60 shear reinforcement, the spacing is set at 8 inches in accordance with TxDOT Bridge Design Manuel. The spacing of the shear reinforcement for Grade 100 was chosen based on similar shear capacity instead of using Grade 60. The sectional design method in AASHTO LRFD is utilized to obtain the equivalent shear failure load. The contribution of concrete remained consistent among specimens due to their shared cross-sectional geometry and prescribed concrete strength. By equating the shear contribution of steel of Grade 100 to that of Grade 60, the spacing in high-strength shear reinforcement is established to the 13-inch in the shear region. However, the maximum shear reinforcement spacing by AASHTO LRFD (2020) is 12 inches, so the spacing of the shear reinforcement when using Grade 100 is set as 12 inches. These minor differences should not have an effect on the shear behavior of the specimens using high-strength shear reinforcement.

As illustrated in Figure 3-21, the shear reinforcement in Tx-62 is composed of double layer #4 reinforcements labeled R bar. With this reinforcement configuration, all specimens satisfied the minimum shear reinforcement requirement in AASHTO LRFD (2020). The spacing of the confinement reinforcement placed in the end region of the bottom flange is also increased when using Grade 100. From the TxDOT design manual (2024) and AASHTO LRFD (2020), the maximum spacing for confinement is limited to 6 in. However, there is no specific suggestion for selecting the confinement spacing based on the strengths approach. Accordingly, the serviceability and ultimate strength of the beam when using the 6 in. maximum confinement spacing suggested in the provisions are compared with the increased confinement spacing. In order to develop the same confinement strength as when the Grade 60 reinforcement is paced at 6 in. spacing, the increased confinement spacing by using Grade 100 is set to 10 in. The safety of confinement under loading conditions is confirmed using cross-section STM, which has been applied in previous research (Ross et al. 2013; Shahrooz et al. 2017). Additionally, it is important to mention that other types of reinforcement remained the same across all Tx-girder specimens, following the reinforcement details outlined for Tx-62 in the TxDOT Bridge Design Manual. In conclusion, each specimen contains a different strand pattern, shear reinforcement spacing, and yield strength of the reinforcing steel. Detailed specimen drawings are shown in Appendix A.

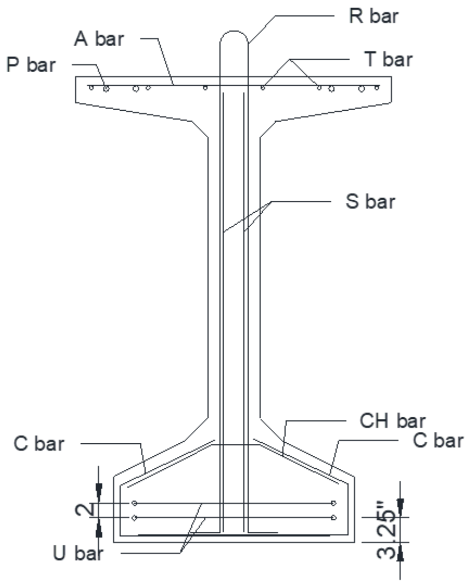

Figure 3-21. Rebar layout for Tx-62

Selecting the shear span is essential for isolating the shear behavior of beams and examining their response under shear stress. Therefore, the shear span of the specimen is the additional variable of the test specimens. Each specimen underwent two different shear regions: The D-region at one end and the B-region at the other end. The shear-span-to-effective-depth ratio, denoted as a/d_v, is chosen as 1.4 for the D-region and 3.0 for the B-region. These values are determined considering available resources at FSEL, with the aim of ensuring the specimens would primarily fail in shear.

Given the presence of various experimental factors, differentiation between specimens is crucial to make appropriate comparisons. Specimens are named to reflect these factors, facilitating their categorization based on the topic of interest. The rationale behind the naming process for the Tx-62 specimens can be found in the figure below.

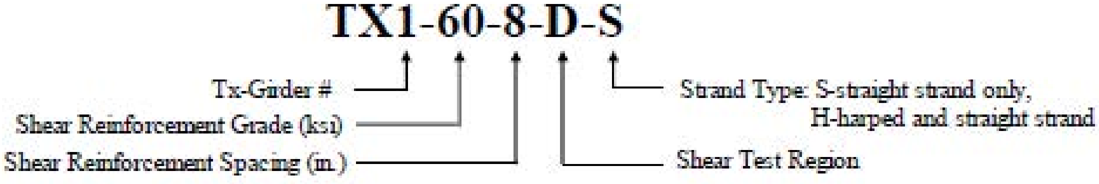

Figure 3-22. Tx-62 specimen identification details

Eight structural tests are conducted on four Tx-62 at FSEL. The research objective is to investigate the structural capacity and serviceability performance when applying high-strength shear reinforcement under the shear load with different experimental variables in a pretensioned I-girder. The description of each specimen is presented in Table 3-4.

Table 3-4. Tx-62 specimen test matrix

Specimen ID	Shear reinforcement grade	Shear reinforcement spacing (in.)	a/d_v	Strand layout
TX1-60-8-B-S	Grade 60	8	2.95	28-straight
TX1-60-8-D-S	Grade 60	8	1.44	28-straight
TX2-100-12-D-S	Grade 100	12	1.54	28-straight
TX2-100-12-B-S	Grade 100	12	3.05	28-straight
TX3-60-8-D-H	Grade 60	8	1.43	24-straight + 4-harped
TX3-60-8-B-H	Grade 60	8	2.95	24-straight + 4-harped
TX4-100-12-B-H	Grade 100	12	3.05	24-straight + 4-harped
TX4-100-12-D-H	Grade 100	12	1.54	24-straight + 4-harped

3.1.2.1.2. Box Beam

In addition to the Tx-girder, experiments are conducted on a 5B40-type box beam, representing one of the largest Texas standard prestressed box beams. This subsection provides a description of the specimens used in the experimental program of this study, with detailed design drawings available in Appendix B. The tested 5B40 beam measured 40 feet in length and 40 inches in height, featuring an 8-inch thick composite deck cast on top. Notably, the box beam's end block and void region showed significant volume differences, which can result in cracks due to temperature differentials during concrete curing (Avendano et al., 2013). To mitigate crack formation resulting from volume differences in the specimen region, the fabrication of the box beam accounted for block-out regions in the end block. The block out depth is 7 inches, adhering to the Texas standard design specifications at 12 inches in length (TxDOT, 2020). Figure 3-23 presents a cross-section of 5B40.

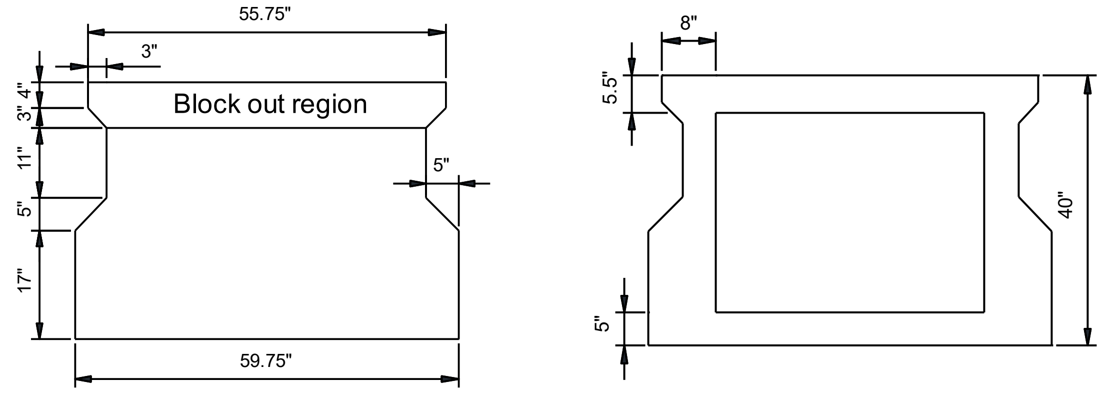

(a) End region (b) Void region

Figure 3-23. Cross-section geometry of 5B40

For each specimen, a total of 26 strands, each with a diameter of 0.6 inches and perfectly bonded, are employed, as illustrated in Figure 3-24. The centroid of all strands is situated 2.5 inches away from the bottom of the beam. Additionally, the strands are horizontally and vertically spaced two inches apart. Grade 270 prestressing strands with low relaxation properties are utilized. The selection of the number of strands takes into account the longitudinal tie capacity and a flexure strength higher than the shear strength. Furthermore, the concrete strength on the day of strand release is designed to be 6 ksi. The number of strands is determined to ensure compliance with the concrete stress limits at the beam's top and bottom extreme fibers when the concrete strength is 6 ksi, per Article 5.9.2.3 of AASHTO LRFD (2020).

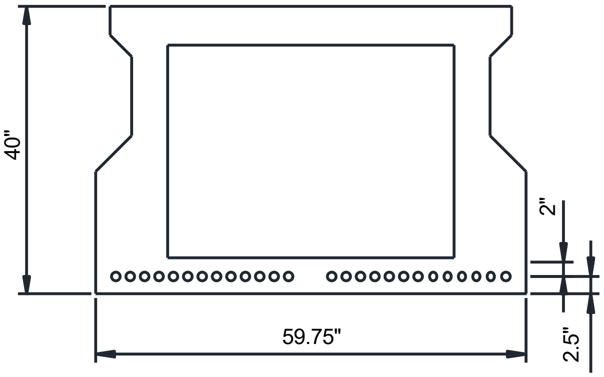

Figure 3-24. Strand layout for 5B40 specimens

Various types of reinforcements are used in the fabrication of the box beam (Avendano et al., 2013; TxDOT, 2024). Standard TxDOT shear reinforcement details are used to fabricate 5B40 specimens tested in this research (Refer to Figure 3-25). 5B40 uses two types of shear reinforcement, spliced vertically within the web. One type of shear reinforcement is Bar C, which extends 36 inches up through the web from the bottom of the strands. The other is Bar A, which extends 22 inches down from the top of the longitudinal reinforcement. The size of both shear reinforcements is #4.

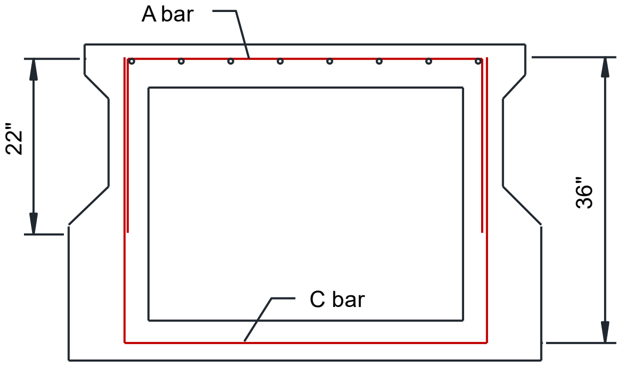

Figure 3-25. Shear reinforcement for 5B40

The spacing of the shear reinforcement is selected to ensure that shear failure governs the failure mechanism of the specimens. In this research, two different grades of shear reinforcement, Grade 60 and Grade 100, are used for the specimens with different spacings. The spacing of the shear reinforcement for high-strength reinforcing steel is calculated based on the shear strength of the box beam. According to the TxDOT drawing (TxDOT 2024), the spacing of the shear reinforcement of 5B40 is 6 inches when using Grade 60 steel. The spacing of the shear reinforcement with similar force capacity, even if Grade 100 steel is used instead of Grade 60, is calculated. As a result, the high-strength shear reinforcement spacing is chosen as 10 inches. Additionally, the minimum shear reinforcement requirement and the maximum shear reinforcement spacing by AASHTO LRFD (2020) are also considered when determining the spacing of the shear reinforcement.

The two different types of reinforcement, such as Bar M and Bar N, are placed in the end block of the box beams, as shown in Figure 3-26. The layout for the reinforcement placed in the end block follows the standard reinforcement details currently used in TxDOT (2024). The purpose of the reinforcement placed in the end region of the prestressed girder is to prevent the spalling cracks that may occur during the transfer of the prestress. However, reinforcement placed in the end block might have some impact on the shear strength of the box beam end region. The stress in the steel to prevent the splitting resistance cannot exceed 20.0 ksi to control the crack at the end region in accordance with O’Callaghan (2007) and AASHTO LRFD (2020). Therefore, the quantity of reinforcing steel to prevent splitting cracks cannot be reduced due to the stress limit even if the high-strength steel is applied.

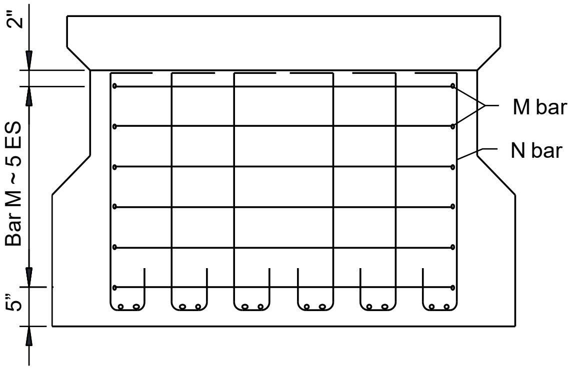

Figure 3-26. End region reinforcement for 5B40

In conclusion, when high-strength rebars are used, the reinforcement layout in the end block maintains consistent spacing, unlike the increased spacing observed in the shear reinforcement layout. Consequently, variations in the strength of the reinforcement within the end block can be compared to differences in the shear strength of the end region of the box beam.

This section aims to analyze the box beam's shear mechanism under simply supported conditions. To support a box beam with a relatively wide width compared to an I-girder, two bearing plates support one end, while the other end is supported by one, ensuring balance. To examine how the effect of high-strength rebar on the shear mechanism varies with different support conditions, the number of supports is specified as a variable in this project.

To comprehend the shear mechanism of the box beam, the shear span-to-depth ratio is designed to fall between 1.5 and 1.7 for the D-region and 2.5 and 3.4 for the B-region. Three main variables are established in alignment with the experimental goals: the rebar strength of the shear reinforcement, the number of supports, and the loading region. Therefore, a total of eight experiments are conducted by combining these three variables, as shown in Table 3-5, and the description of each specimen's ID is provided in Figure 3-27.

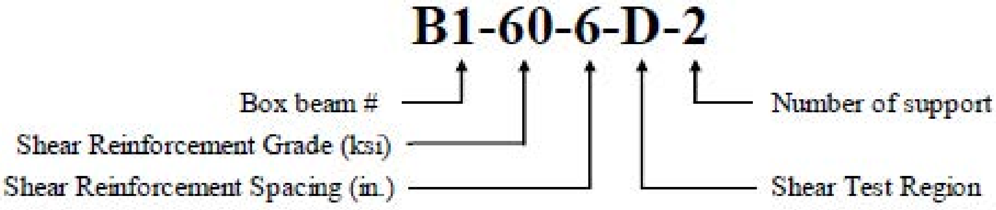

Figure 3-27. 5B40 specimen identification details

Table 3-5. 5B40 specimen test matrix

Specimen ID	Shear reinforcement grade	Shear reinforcement spacing (in.)	a/d_v	No. of supports (ea)
B1-60-6-B-2	Gr. 60	6	2.63	2
B1-60-6-D-1	Gr. 60	6	1.53	1
B2-60-6-D-2	Gr. 60	6	1.69	2
B2-60-6-B-1	Gr. 60	6	3.5	1
B3-100-10-D-1	Gr. 100	10	1.53	1
B3-100-10-B-2	Gr. 100	10	2.63	2
B4-100-10-B-1	Gr. 100	10	2.63	1
B4-100-10-D-2	Gr. 100	10	1.53	2

3.1.2.2. Fabrication

A total of eight specimens—four Tx-girders and four box beams—were provided by Valley Prestress Products Inc. (VPP), a local precast plant in Texas. Collaborating closely with the VPP construction team involved supplying detailed drawings (as shown in the Appendix), attaching instrumentation on-site, and ensuring that fabrication practices met precast bridge element requirements. The Tx-girder specimens were constructed following the TxDOT Tx-62 design with variations in shear reinforcement details, while the box beam specimens followed the 5B40 standard design with varying shear reinforcement details.

The prestressed specimens undergo various processes during fabrication (Refer to Figure 3-28). Before commencing the rebar caging work at the local prestressing yard, strain gauges must be attached to the reinforcement. The attachment of strain gauges to the appropriate positions of the reinforcement is carried out at FSEL, and after attaching the gauges to the reinforcements, they are packed and shipped to Valley Prestress Products.

At Valley Prestress Products, the initial phase of the fabrication process involved prestressing strands in accordance with the acceptable method outlined in TxDOT Bridge Design Manuel. Subsequently, rebar caging, sensor wiring, and concrete casting work for prestressed girders are carried out. As illustrated in Figure 3-28 (d-2), rectangular styrofoam is placed in the void region of the box beam instead. However, due to the significantly lower elastic modulus and strength of styrofoam compared to concrete, it can be assumed to serve the same role as the void region. The steel forms for casting were removed a day after casting the concrete, and the prestressing strands were released when the concrete strength exceeded 6 ksi on the same day.

(a) Strain gage installation (b) Rebar packing & delivering

(c) Prestressing (d-1) Rebar caging for Tx-62

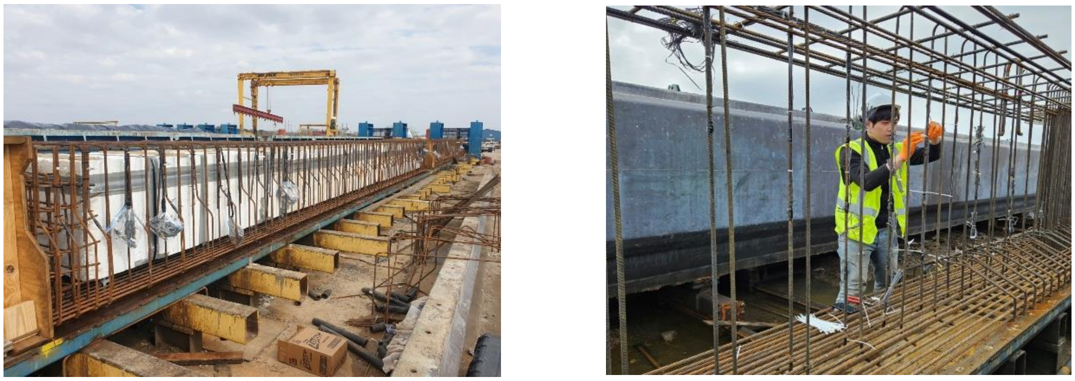

(d-2) Rebar caging for 5B40 (e) Sensor wiring

(f) Concrete casting (g) Form removal

(h) Prestress releasing

Figure 3-28. Fabrication procedure for the prestressed girder

The test specimens are also fabricated using self-consolidating concrete (SCC), following the accepted method for constructing Texas bridges. The average slump flow for the mixtures is 23.5 inches, falling within the acceptable range for SCC (TxDOT, 2020). Moreover, 70 concrete cylinder samples are cast for material tests of each type of prestressed girder at four different stages (prestressing release and structural testing). After the fabrication, cylinder samples and eight prestressed girders produced at Valley are shipped to FSEL, and the test specimens are fabricated by casting the composite deck on top of the girder at FSEL. 20-cylinder samples for the composite deck are prepared for testing days.

(a) Cylinder deliver (b) Girder deliver

(c) Deck casting

Figure 3-29. Following the procedure after fabricating the girder

3.1.2.3. Test Setup

3.1.2.3.1. Loading Frame

The test setup for conducting prestressed girder experiments in this study is established based on the setups utilized in TxDOT projects 0-6652 and 0-5831, as shown in Figure 3-30. The distance from the edge of the beam to the centroid of the support, denoted as *Oh*, remains constant at 6.5 inches for all specimens. The shear span varies depending on the target test region, as shown in Table 3-4 and Table 3-5.

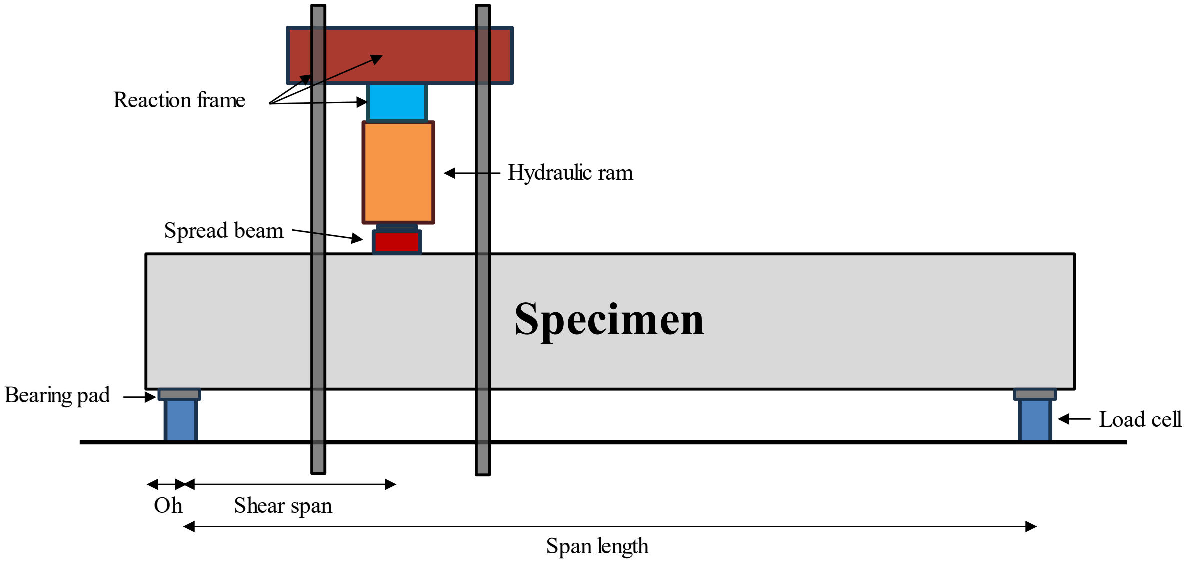

Figure 3-30. Side elevation view of the test setup of the prestressed girder

The support region comprises four distinct components, as shown in Figure 3-31. Firstly, a 0.5-inch-thick steel plate is affixed to the strong floor, and the load cell is attached to the top to prevent independent movement. Hydrostone is cast around the steel plate to stabilize the support condition to ensure the load cell remains stationary when loads are applied. Atop the 1000 kips load cell, a 3-inch blue steel plate is mounted to ensure a flat contact surface with the support plate. Additionally, a socket matching the load cell's shape is fashioned on the upper steel plate to secure both the load cell and the blue steel plate. Elastomeric laminated bearing plates are positioned on the blue steel plate, with the specimens placed atop them, simulating real bridge conditions.

Figure 3-31. Support setup in prestressed girder

For the Tx-girder, one large support is placed at the center of the girder for both ends. However, to support a box beam with a relatively wide width compared to an I-girder, two bearing plates support one end, while the other end is supported by one, ensuring balance. When using two bearing plates, each plate's size is approximately half the size compared to when using a single plate, with a longitudinal length of 9 inches in both cases, as shown in Figure 3-32.

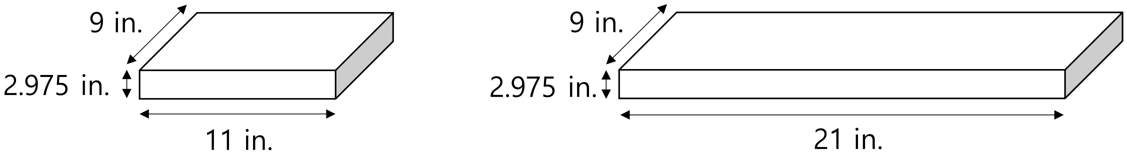

(a) For two supports (b) For one support

Figure 3-32. Size of the bearing plates in prestressed girder test

In the experiments, a single large bearing support is positioned at the center of the Tx-girder and box beam to support the specimen. Conversely, two small bearing plates align with the web region to ensure direct transmission of stress from the loading ram through the web to the bearing plate (refer to Figure 3-33). Through experiments conducted under these two different support conditions, the comparison and analysis reveal the effect of high-strength reinforcement of the end block for the box beam, depending on the support condition.

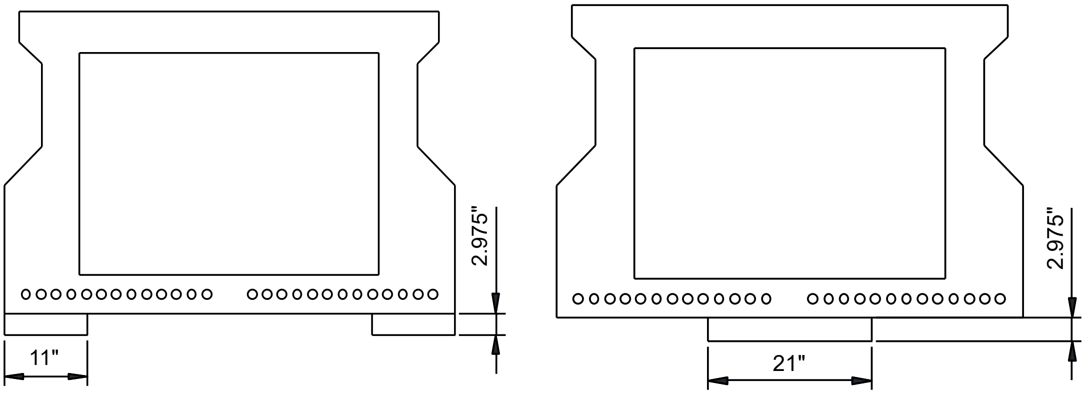

(a) Two supports (b) One support

Figure 3-33. Support locations of prestressed girder

The loading setup for applying load to the specimens comprises a total of five components for the Tx-girder and six components for the box beam, as illustrated in Figure 3-34. The difference in the loading setup between the two types of specimens is the presence or absence of a spreader beam. Since the Tx-girder has a single web, shear stress is directly applied from the loading ram placed at the center of the beam to the support. However, the box beam has a central void region, and shear stress is transmitted to support through the webs on both sides. Therefore, a spreader beam loading system is implemented to ensure the smooth transmission of shear stress from the loading point to the support, in line with the methodology used in previous research studies (Avendano et al., 2013; Chamberlain, 1997; Schnittker and Bayrak, 2008).

The reaction frame is initially established to install the loading ram. Steel rods are utilized to secure both the laboratory floor and frames, and a reaction frame capable of accommodating a hydraulic ram is constructed using vertical and longitudinal steel frames. The hydraulic ram is positioned at the center of the specimen to prevent eccentric loading, and a tilted saddle is affixed to the ram base to mitigate the risk of torsional loads. The spreader beam is installed under the loading ram to make the force act directly above the web. Furthermore, two 0.5-inch-thick steel plates are employed to connect the spread steel beam to the specimen, aligning the centroids of the steel plates with the centers of the specimen's two webs.

(a) Tx-girder (b) Box beam

Figure 3-34. Loading setup of prestressed girder

3.1.2.3.2. Instrumentation

Hydraulic rams were used to apply load to the specimens. Given that the expected failure load of the specimens was below 1,000 kips, a ram with a 2,000-kip capacity was employed. The load applied to the specimens was measured using four load cells installed at the support positions, each with a capacity of 1,000 kips. When only one large-size bearing support was used, two load cells were placed at the center of the beam. Load cells were positioned beneath each bearing plate for setups with two supports. Additionally, two linear potentiometers (LPOTs) were installed at the loading points to monitor the reactions while verifying the applied loads. The load cells worked in conjunction with the LPOTs to record deflections at each applied load throughout the test. Multiple PODs were used to connect the LPOTs and load cells to the DAQ system for data recording. Furthermore, four LPOTs are strategically placed around the bearing plates to monitor the deformation of the plates under the applied load. The measured deformation of the bearing plates enables the calculation of their elastic modulus, which is then utilized in the development of the finite element model. Moreover, this external instrumentation serves to measure strand slip by being affixed to the end of the strands. The deformation of a total of four strands is recorded, with measurements taken at the midpoint and edge point of the bottom flange. Figure 3-35 displays the load and displacement instrumentation used in experiments.

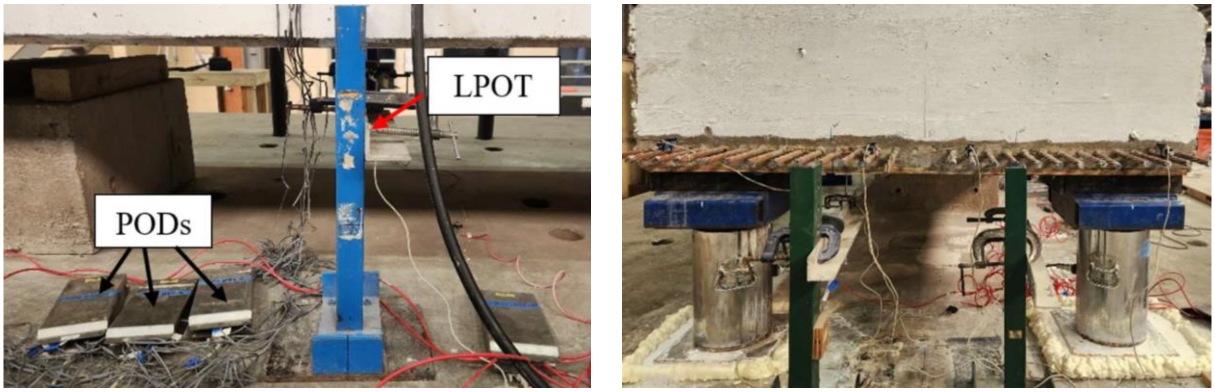

(a) LPOT and PODs (b) Load cells

(c) LPOT for strand slip

Figure 3-35. Measurements for prestressed girder test

3.1.2.4. Test Procedure

The load was applied from the hydraulic rams incrementally in 50 to 100-kip increments. Cracks were marked at each load interval, and crack widths were measured using a crack card. The test was terminated when the load decreased by more than 10% from the peak value.

3.1.2.5. Experimental Results and Discussion

3.1.2.5.1. Overview

This chapter provides experimental results and comprehensive comparisons with design methodologies to validate the strength and service limit state of high-strength prestressed reinforced specimens. The shear load, deflection, and crack patterns at the ultimate stages in the main test region of all tested specimens are presented. Discussion regarding the results is also included.

Table 3-6 summarizes the general information and the test results of all Tx-62 specimens. The findings from the experimental program are presented alongside the AASHTO LRFD General Procedure (2020) for comparative analysis. This method utilizes the Modified Compression Field

Theory (MCFT) principle to estimate the reinforced concrete section's nominal shear resistance, denoted as V_{AASHTO} in Table 3-6. The shear capacity of each specimen was estimated by combining the contribution of concrete and reinforcing steel.

Table 3-6. Test results for Tx-62 specimens

Test results	**Straight strand only**				**Straight and harped strand**			
	Tx1-60-8		**Tx2-100-12**		**Tx3-60-8**		**Tx4-100-12**	
	B-S	**D-S**	**D-S**	**B-S**	**D-H**	**B-H**	**B-H**	**D-H**
Beam-f'c (ksi)	10	9.5	10.3	10.4	9.2	9.4		
Rebar grade	60	60	100	100	60	60	100	100
Deck-(ksi)	6.8	5.4	5.6	5.8	6.9	6.9		
f_y (ksi)	67	67	137	137	67	67	137	137
Spacing (in.)	8	8	12	12	8	8	12	12
A_{ps} (in^2)	6.076	6.076	6.076	6.076	6.076	6.076	6.076	6.076
$f_{p,jack}$ (ksi)	202.5	202.5	202.5	202.5	202.5	202.5	202.5	202.5
Shear span, a (ft)	186	90	90	186	96	193	186	90
d_v (in)	63.0	62.9	63.6	64.1	63.1	63.1	63.6	63.6
a/d_v	2.95	1.43	1.42	2.9	1.51	3.05	2.93	1.42
$V_{n(AASHTO)}$ (kip)	402	477	580	438	533	396	448	596
$P_{n,shear}$ (kip)	663	578	704	721	651	623	700	721
$P_{n,flexural}$ (kip)	883	1146	1364	912	1297	852	957	1490
P_{max} (kip)	750	972	1052	762	1006	756	768	1092
V_{max} (kip)	454	801	870	463	829	464	474	900
V_{max}/V_{AASHTO}	1.13	1.68	1.5	1.06	1.56	1.17	1.06	1.51
$P_{n,shear}$ / P_{max}	0.88	059	0.67	0.95	0.65	0.82	0.91	0.66
$P_{n,flexural}$/ P_{max}	1.18	1.18	1.3	1.2	1.29	1.13	1.25	1.36

Table 3-7 summarizes the general information and the test results of all 5B40 specimens. The findings from the experimental program are presented alongside the AASHTO LRFD General Procedure (2020) for comparative analysis. This method utilizes the Modified Compression Field Theory (MCFT) principle to estimate the reinforced concrete section's nominal shear resistance, denoted as V_{AASHTO} in Table 3-7. An equivalent I-beam cross-section with a single web whose thickness is twice that of the 5B40 box beam's web was used to simplify the calculation process. The shear capacity of each specimen was estimated by combining the contribution of concrete and reinforcing steel.

Table 3-7. Test results for 5B40 specimens

Test results	**Normal Strength Rebar**				**High Strength Rebar**			
	B1-60-6		**B2-60-6**		**B3-100-10**		**B4-100-10**	
	B-2	**D-1**	**D-2**	**B-1**	**D-1**	**B-2**	**B-1**	**D-2**
Beam-f'c (ksi)	10.4	10.4	9.1	9.2	11.3	11.5	11.1	10.6
No. Support	2	1	2	1	1	2	1	2
Deck-(ksi)	6.6	5.8	5.4	7.0	6.7	7.2	10.2	9.5
f_{yt} (ksi)	82	82	82	82	140	140	140	140
Spacing (in.)	6	6	6	6	10	10	10	10
A_{ps} (in^2)	5.64	5.64	5.64	5.64	5.64	5.64	5.64	5.64
f_{pjack} (ksi)	202.5	202.5	202.5	202.5	202.5	202.5	202.5	202.5
Shear span, a (ft)	113.5	65.5	72	155	65.5	113.5	113.5	65.5
d (in)	45.5	45.5	45.5	45.5	45.5	45.5	45.5	45.5
a/d	2.49	1.44	1.58	3.41	1.44	2.49	2.49	1.44
$V_{n\ (AASHTO)}$ (kip)	406	506	483	353	511	410	414	515
$P_{n,shear}$ (kip)	554	588	571	555	595	560	565	600
$P_{n,flexural}$ (kip)	762	1117	1026	647	1128	767	784	1154
P_{max} (kip)	646	678	635	676	723	650	680	718
V_{max} (kip)	507	584	529	431	616	469	501	616
V_{max}/V_{AASHTO}	1.25	1.15	1.10	1.22	1.20	1.14	1.21	1.20
$P_{n,shear}$ / P_{max}	0.86	0.87	0.90	0.82	0.82	0.86	0.83	0.84
$P_{n,flexural}$/ P_{max}	1.18	1.65	1.62	0.96	1.56	1.18	1.15	1.61

3.1.2.5.2. Crack Pattern

Tx-girder

The crack propagation maps serve as visual indicators of the distress level experienced by specimens as the applied load increases. Two maps are included for each test to evaluate the effect of high-strength rebars with increased spacing on crack propagation. One crack map represents the load step for the first crack issued, while another represents the crack at the ultimate stages.

The crack propagation maps in D-region shear tests are presented with two sets of specimens of similar experimental variables, allowing for a direct comparison of the crack-control performance between Grade 60 and Grade 100 reinforcing steel as shear reinforcement in prestressed box beam, as shown in Figure 3-36 to Figure 3-39. Specifically, all specimens had the same formation of diagonal cracks, emerging in the web and propagating from the point load to the support.

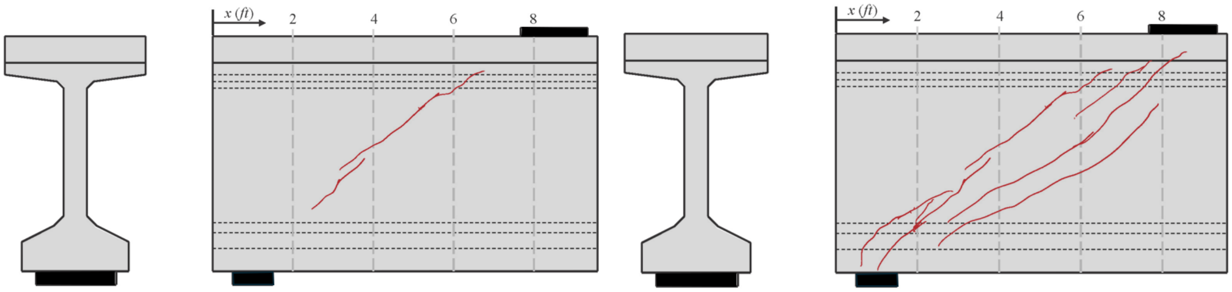

V=375 kips	V/Vu=0.47	V/V_{AASHTO}=0.79

V=801 kips	V/Vu=1.0	V/V_{AASHTO}=1.68

Figure 3-36. Crack progression maps of TX1-60-8-D-S

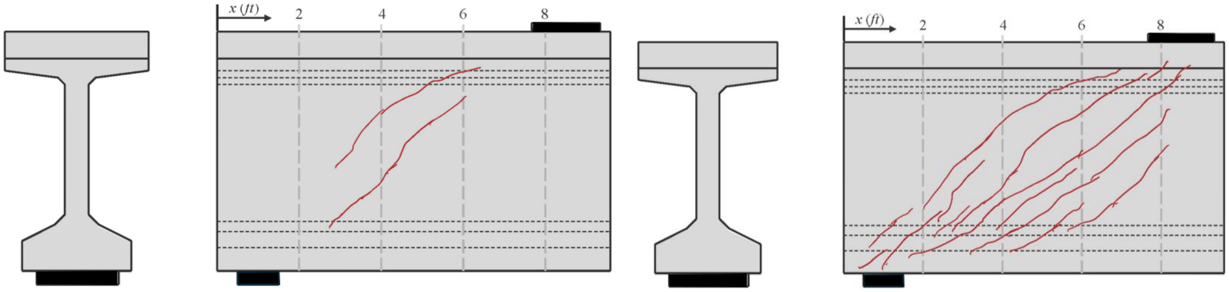

V=375 kips	V/Vu=0.43	V/V_{AASHTO}=0.65

V=870 kips	V/Vu=1.0	V/V_{AASHTO}=1.5

Figure 3-37. Crack progression maps of TX2-100-12-D-S

Specimen TX1-60-8-D-S and TX2-100-12-D-S contain only a straight strand on the bottom flange with the same shear span to depth ratio of 1.4. However, specimen TX2-100-12-D-S contained less stirrups because this specimen utilized high-strength shear reinforcement with larger spacing, while TX1-60-8-D-S uses normal-strength rebar. The initial crack in both specimens occurred at around 45% of the shear strength of the specimen. The initial crack always formed in the web near the center of the test region, and as the applied load increased, it spread toward the loading point and the support location. In both specimens, multiple cracks formed near the web at the ultimate stage, and the crack with the widest width reached the support. Additionally, in the specimen with high-strength shear reinforcement placed at wider spacing, the crack distribution was observed to be wider across the test region compared to the specimen without such reinforcement.

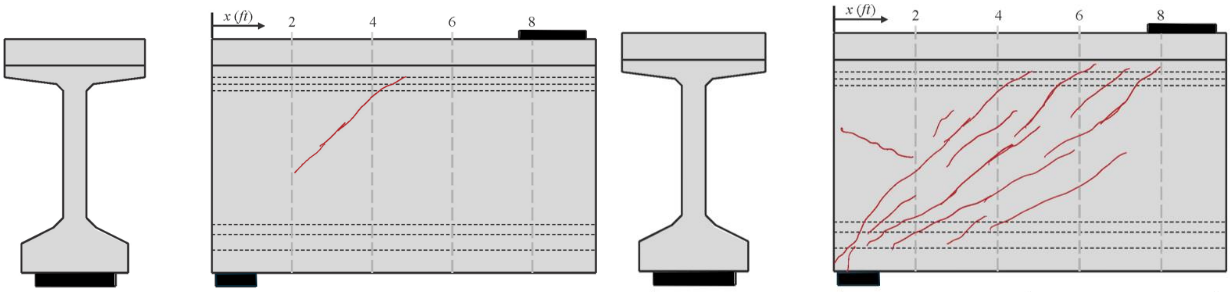

V=325 kips	V/Vu=0.40	V/V_{AASHTO}=0.61

V=829 kips	V/Vu=1.0	V/V_{AASHTO}=1.56

Figure 3-38. Crack progression maps of TX3-60-8-D-H

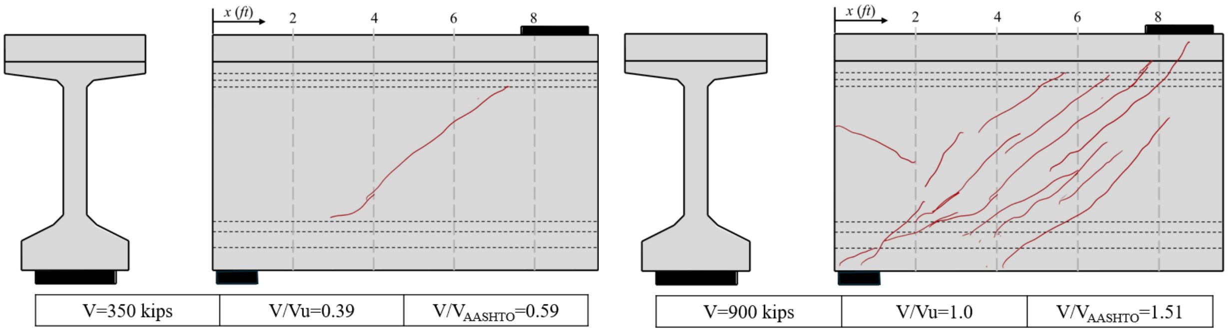

Figure 3-39. Crack progression maps of TX4-100-12-D-H

When harped strands are used, the initial crack occurs under the same load regardless of the strength of the shear reinforcement, and this load is approximately 40% of the ultimate strength. Furthermore, the crack patterns at the ultimate stage are also nearly identical. In other words, it can be seen that the strength of the shear reinforcement does not influence the crack pattern of I-girders containing harped strands.

Similarly, to explore how cracks progressed during the B-region shear test, the crack propagation maps are presented in the order that allows for a direct comparison, considering similar a/d_v ratio and strand layout, as shown in Figure 3-40 to Figure 3-43.

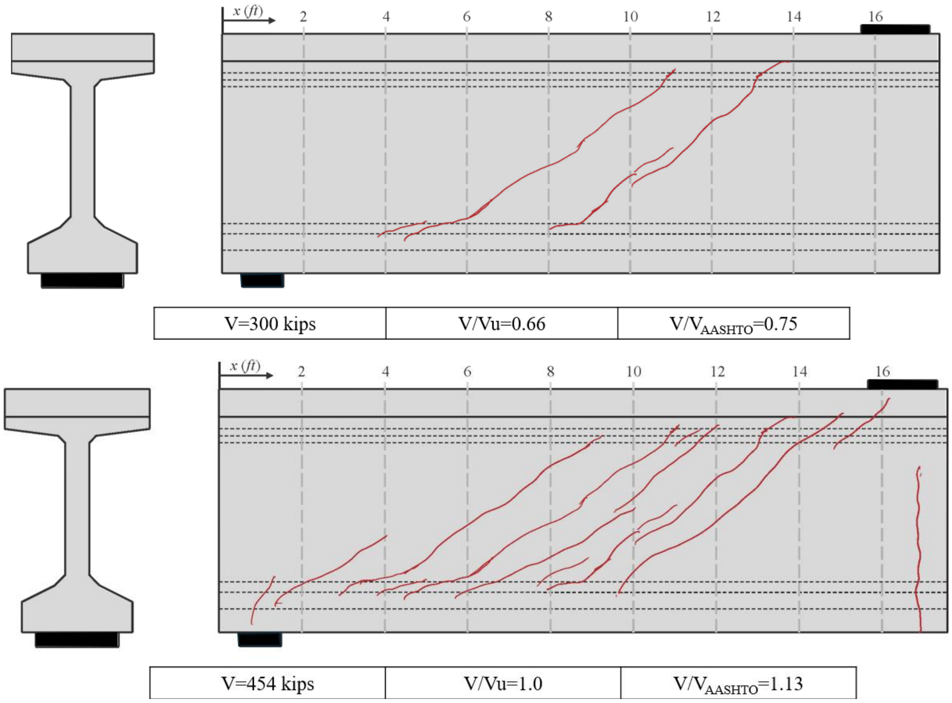

Figure 3-40. Crack progression maps of TX1-60-8-B-S

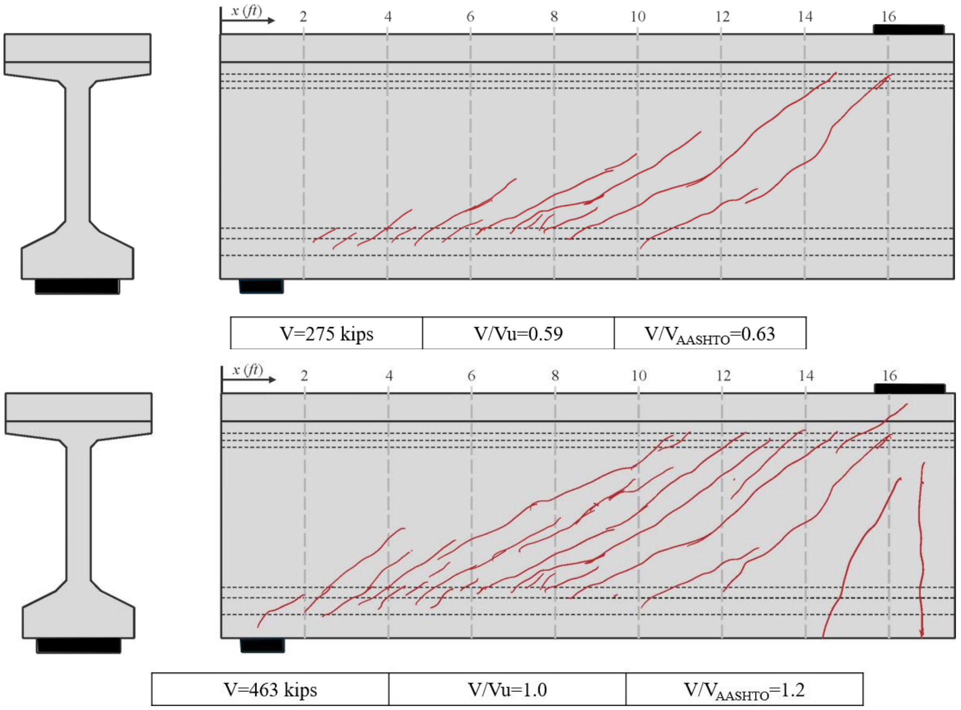

Figure 3-41. Crack progression maps of TX2-100-12-B-S

Figure 3-40 and Figure 3-41 illustrate the progression of cracks in specimens TX1-60-8-B-S and TX2-100-12-B-S, respectively. Given the same shear span of 2.9, specimen TX2-100-12-B-S contained high-strength shear reinforcement with larger spacing compared to another specimen. Unlike the results in the D-region, the initial cracks in both specimens occurred at around 60% of the specimen's shear strength, which is higher than the D-region result. Additionally, the initial crack always formed in the web near the center of the test region, and as the applied load increased, it spread toward the loading point and the support location. In both specimens, diagonal cracks spread throughout the entire test region, and the width of the crack that appeared first was wider than that of the other cracks in the ultimate stages. Furthermore, it was observed that at both the initial and ultimate stages, high-strength reinforcement resulted in more cracks forming over a wider area.

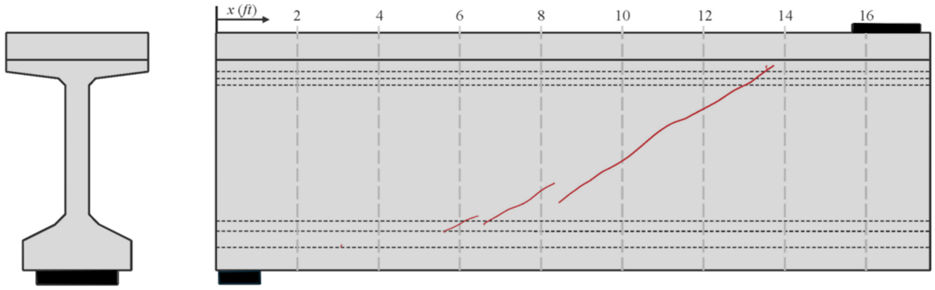

V=275 kips	V/Vu=0.59	V/V_{AASHTO}=0.69

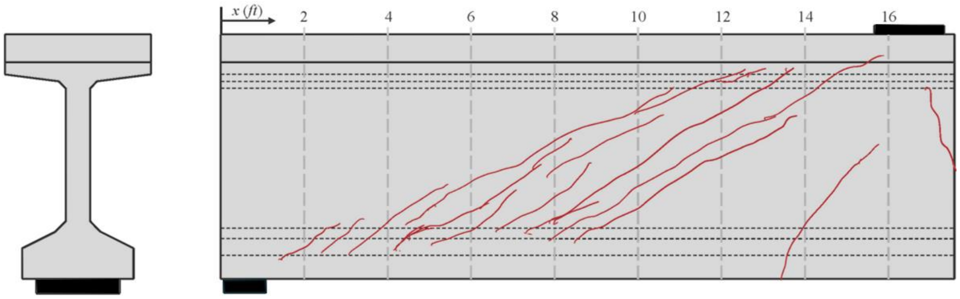

V=464 kips	V/Vu=1.0	V/V_{AASHTO}=1.13

Figure 3-42. Crack progression maps of TX3-60-8-B-H

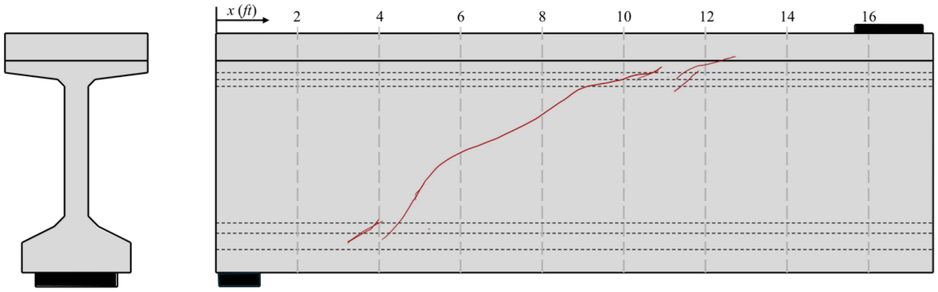

V=300 kips	V/Vu=0.63	V/V_{AASHTO}=0.67

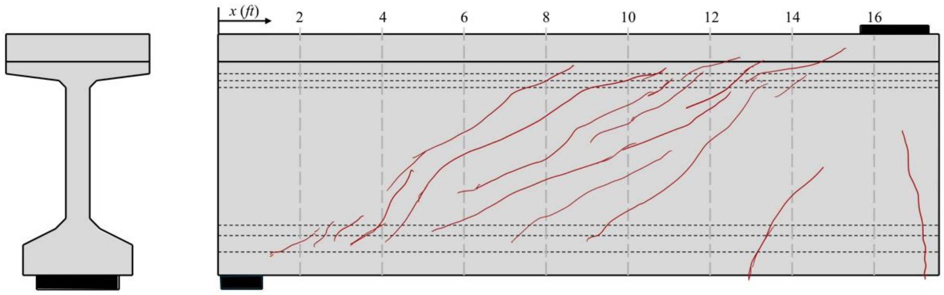

V=474 kips	V/Vu=1.0	V/V_{AASHTO}=1.06

Figure 3-43. Crack progression maps of TX4-100-12-B-H

The crack progression maps of the specimens with harped strands are shown in Figure 3-42 and Figure 3-43. When harped strands are used, the initial crack occurs under the same load regardless of the strength of the shear reinforcement, and this load is approximately 60% of the ultimate strength. Furthermore, the crack patterns at the ultimate stage are also nearly identical. In other words, it can be seen that the strength of the shear reinforcement does not influence the crack pattern of I-girders containing harped strands. However, in the B-region, unlike the D-region, cracks did not occur at locations corresponding to the position of the harped strands. Additionally, it was observed that using high-strength reinforcement resulted in more cracks forming over a wider area under ultimate load.

Box Beams

The crack propagation maps in D-region shear tests are presented with two sets of specimens of similar experimental variables, allowing for a direct comparison of the crack-control performance between Grade 60 and Grade 100 reinforcing steel as shear reinforcement in prestressed box beam, as shown in Figure 3-44 and Figure 3-45. Specifically, these specimens had the same formation of diagonal cracks, emerging in the web and propagating from the point load to the support.

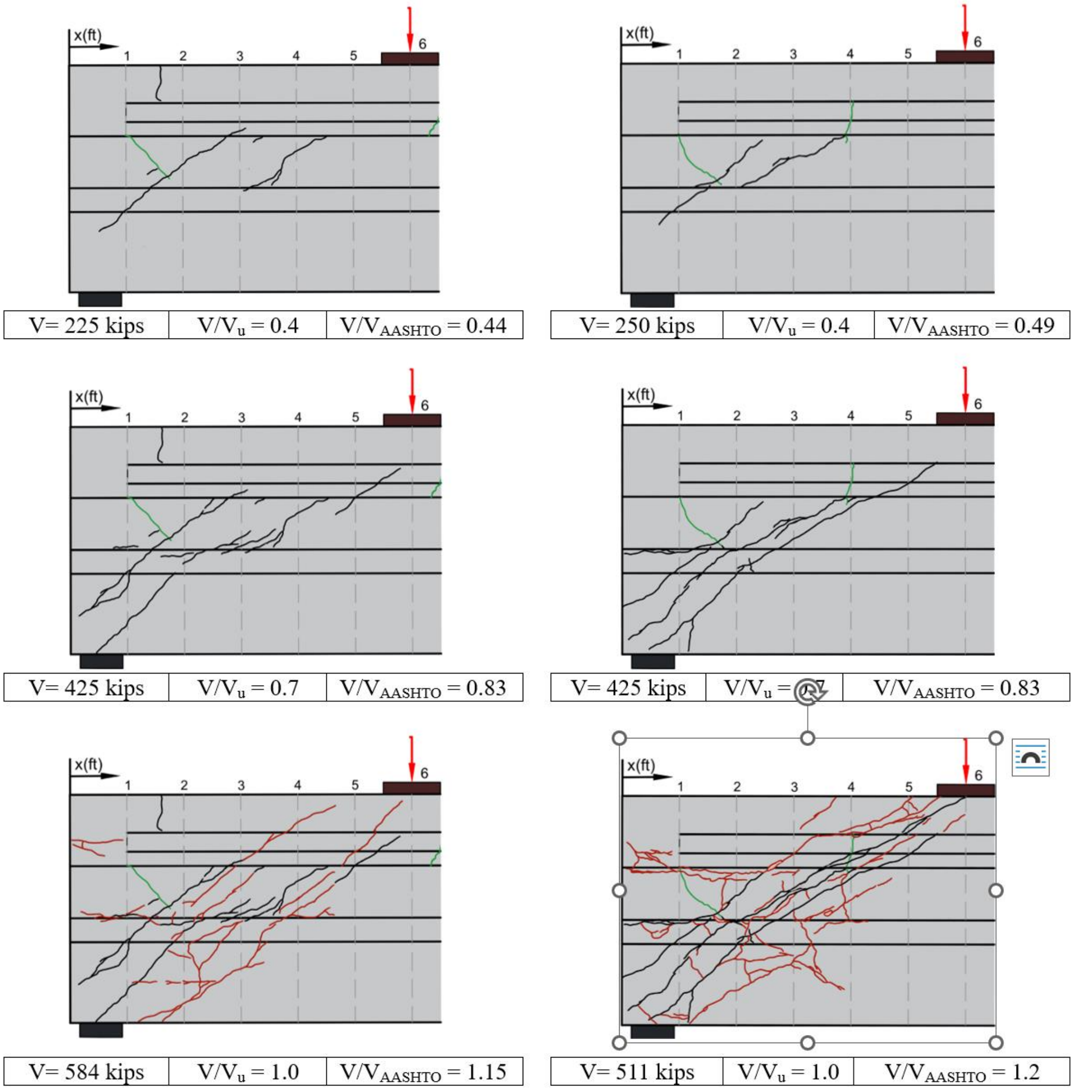

Figure 3-44. Crack progression maps of B1-60-6-D-1 (left) and B3-100-10-D-1 (right)

Specimen B1-60-6-D-1 and B3-100-10-D-1 contain one support at the center of the girder with the same shear span to depth ratio of 1.4. However, specimen B3-100-10-D-1 contained four more stirrups because high-strength shear reinforcement with larger spacing is utilized, while B1-60-6-D-1 uses normal-strength rebar. The dominant shear cracks formed and extended into the bottom flange, while other shear cracks concentrated within the web region in both specimens when the shear force reached approximately 40% of the specimen's shear capacity. Also, all the shear cracks extended into the bottom flanges towards support, with one reaching the end block, under 70% of the specimen's shear capacity is loaded. These shear cracks also propagated into the top flange towards the point load. Finally, at the ultimate stages, more diagonal shear cracks emerged, spanning through the deck from the point load to the support, accompanied by other cracks.

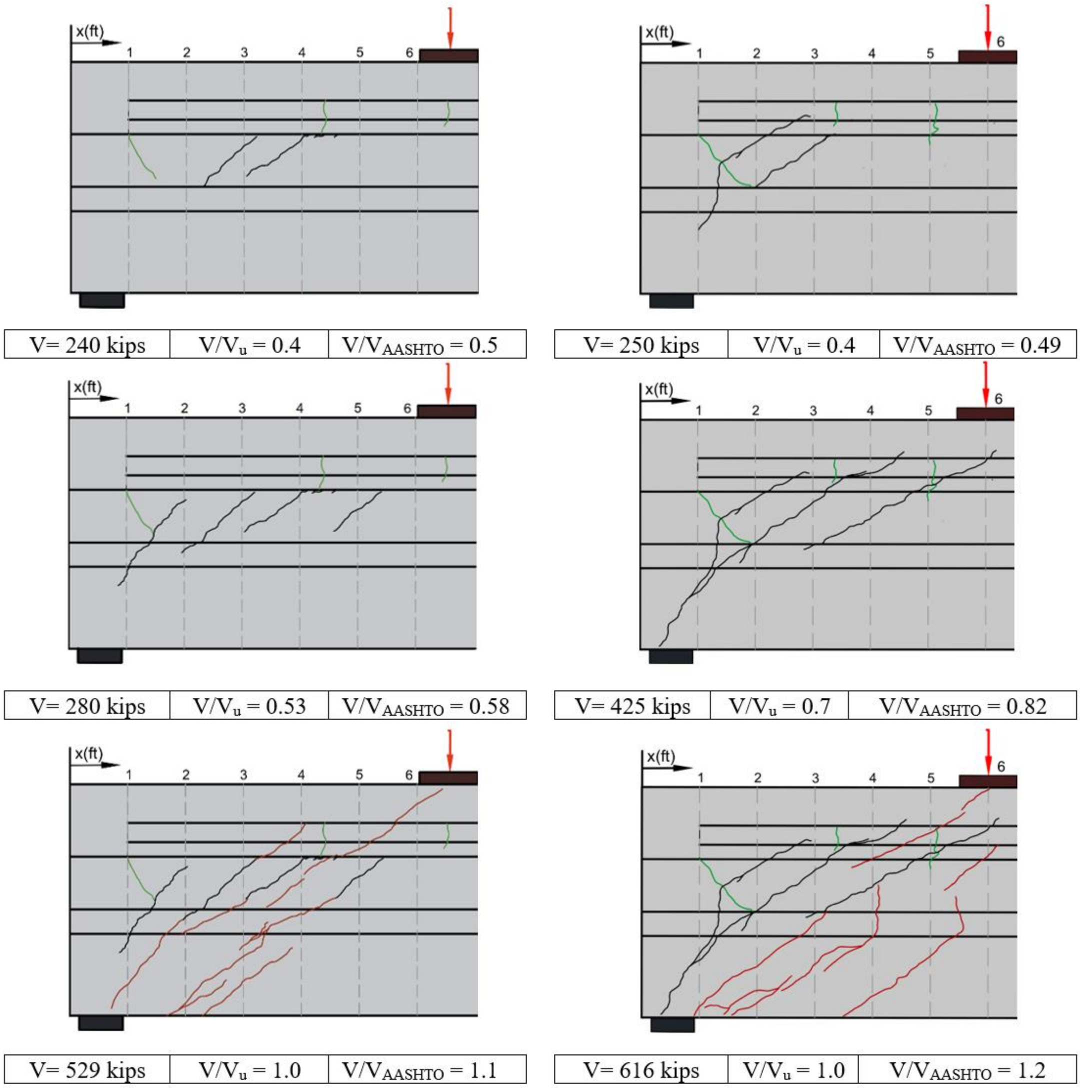

Figure 3-45. Crack progression maps of B2-60-6-D-2 (left) and B4-100-10-D-2 (right)

It is important to mention that both specimens have two supports under the web and a similar shear span-to-depth ratio, but the strength of shear reinforcement and spacing is different. The comparison for the crack propagation shows that shear cracks within the web emerged in both specimens as the load reached 40 % of shear capacity. In addition, at the second intermediate load step, the diagonal cracks in specimen B4-100-10-D-2 propagate rapidly towards the support, while cracks in specimen B2-60-6-D-2 remained mostly within the web. At the ultimate shear capacity, both specimens displayed inclined cracks that span from the point load across the deck and the specimen to the support. These cracks are observed to be widely spaced in specimen B4-100-10-D-2.

Similarly, to explore how cracks progressed during the B-region shear test, the crack propagation maps are presented in the order that allows for a direct comparison, considering similar a/d_v ratio and the number of supports.

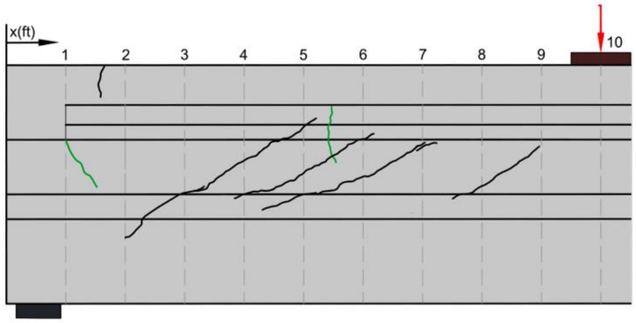

V= 225 kips	$V/V_u = 0.4$	$V/V_{AASHTO} = 0.48$

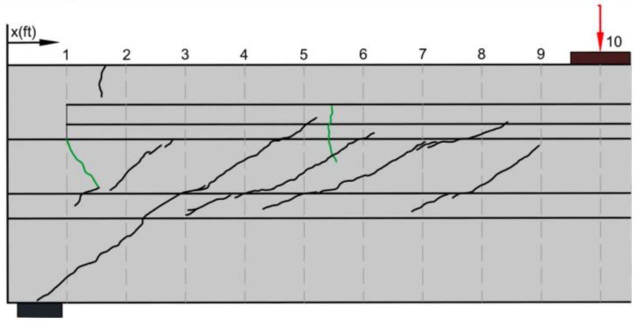

V= 400 kips	$V/V_u= 0.7$	$V/V_{AASHTO} = 0.85$

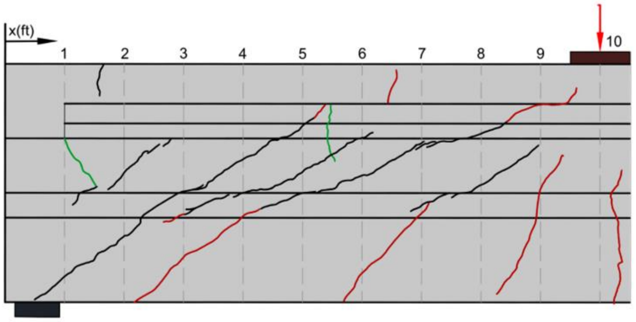

V= 507	$V/V_u = 1$	$V/V_{AASHTO} = 1.25$

Figure 3-46. Crack propagation maps of B1-60-6-B-2

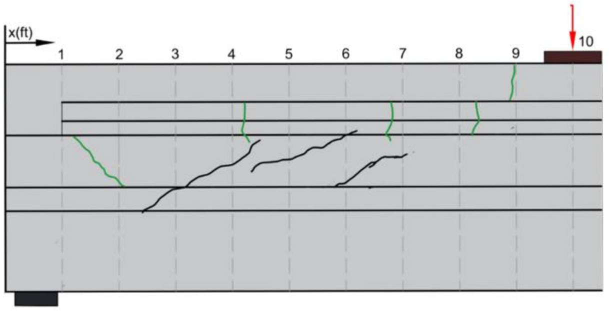

V= 225 kips	V/V$_u$ = 0.4	V/V$_{AASHTO}$ = 0.47

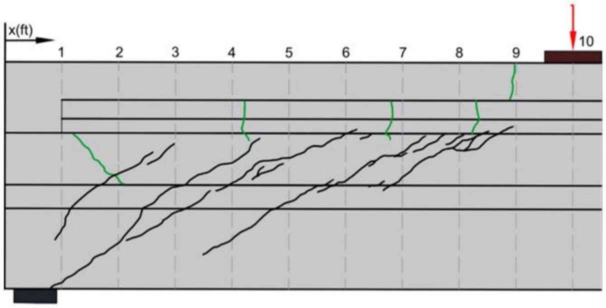

V= 375 kips	V/V$_u$ = 0.7	V/V$_{AASHTO}$ = 0.8

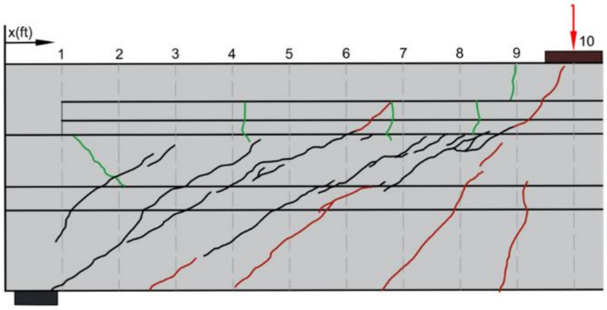

V= 469 kips	V/V$_u$ = 1.0	V/V$_{AASHTO}$ = 1.14

Figure 3-47. Crack propagation maps of B3-100-10-B-2

Figure 3-46 and Figure 3-47 illustrate the progression of cracks in specimens B1-60-6-B-2 and B3-100-10-B-2, respectively, in two intermediate load increments. Given the same shear span of 2.5, specimen B3-100-10-B-2 contained high-strength shear reinforcement with larger spacing compared to another specimen. The shear cracks emerged within the web region, with a predominant shear crack expanding to the bottom flange for both specimens upon reaching 40% of the ultimate shear capacity. As the load reached approximately 70% of the shear capacity, additional diagonal cracks formed and extended into both specimens' top and bottom flange. These cracks moved in two directions, towards the loading plate and the support, respectively. Finally, both specimens exhibited shear cracks with minor flexural cracks beneath the loading plate, primarily concentrated in the bottom flange region under the ultimate shear force.

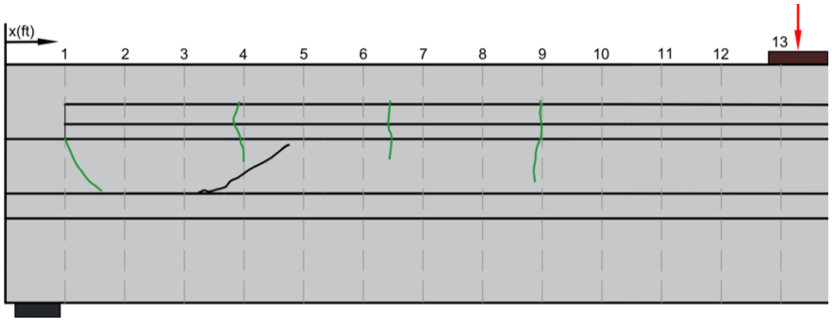

V= 175 kips	$V/V_u = 0.4$	$V/V_{AASHTO} = 0.5$

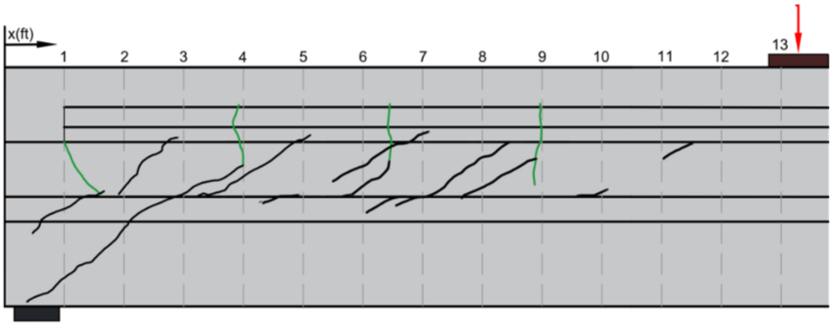

V= 300 kips	$V/V_u = 0.7$	$V/V_{AASHTO} = 0.85$

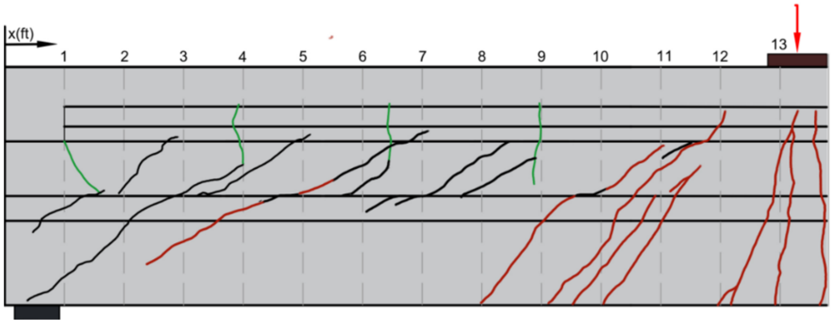

V= 431 kips	$V/V_u = 1.0$	$V/V_{AASHTO} = 1.22$

Figure 3-48. Crack propagation maps of B2-60-6-B-1

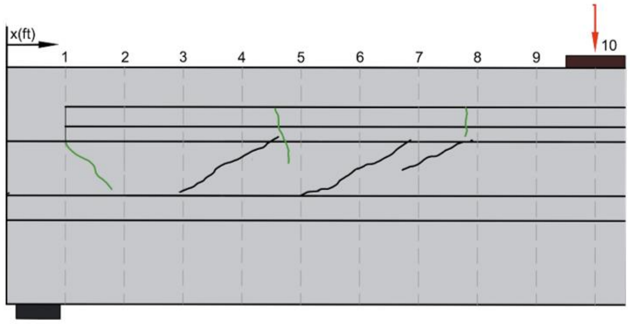

V= 200 kips	$V/V_u = 0.4$	$V/V_{AASHTO} = 0.48$

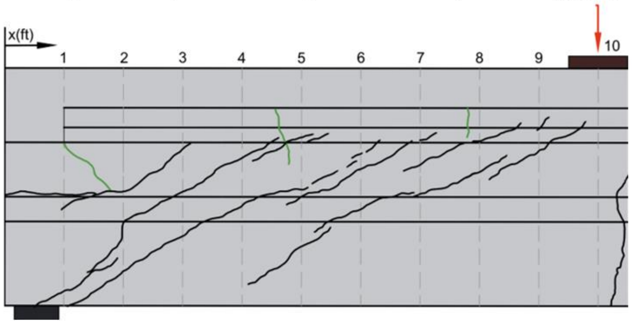

V= 350 kips	$V/V_u = 0.7$	$V/V_{AASHTO} = 0.86$

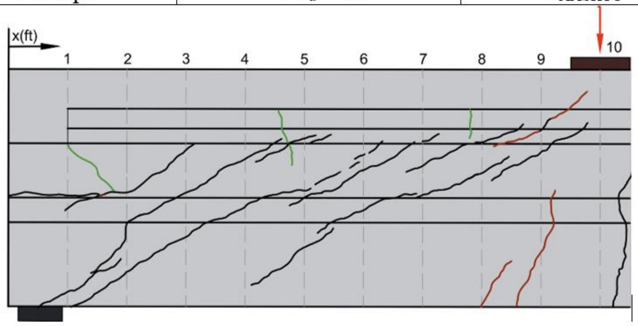

V= 501 kips	$V/V_u = 1.0$	$V/V_{AASHTO} = 1.21$

Figure 3-49. Crack propagation maps of B4-100-10-B-1

From the comparison between Figure 3-48 and Figure 3-49, the number of cracks is different from each specimen after the force reaches 40% of the failure capacity. However, the maximum length of the crack is similar. At 70 % of the failure load, additional shear cracks formed, but most cracks remained within the web while the dominant shear crack extended into the bottom flange for both specimens. However, the shear cracks formed in the B4-100-10-B-1 specimen were more dispersed compared to those in the B2-60-6-B-1 specimen. The crack trend is slightly different at the ultimate stages because the shear span to depth ratio of 3.4 in specimen B2-60-6-B-1 is noticeably larger than that of specimen B4-100-10-B-1, in which the shear span to depth ratio is 2.5. In B4-100-10-B-1, most shear cracks tend to connect between the loading plate and the support, with some minor flexural cracks. Conversely, specimen B2-60-6-B-1 has an unexpected emergence of dominant flexural cracks along with shear cracks concentrated beneath the loading plate.

Summary

For Tx-girders, it was observed that even with the use of high-strength shear reinforcement and increased shear reinforcement spacing, there is no difference in deflection due to the applied load in both the D-region and B-region. Additionally, regardless of the strength of the reinforcement used, the shear cracks in Tx-girders always first occur in the web in both the D-region and B-region, spreading toward the support and the loading plate. However, when high-strength reinforcement is used and the shear reinforcement spacing is increased, more cracks form compared to regular reinforcement, and the region where cracks form also becomes wider.

For Box beams, specimens tested in the D-region exhibited a consistent crack propagation pattern, with concrete cracking along the straight line connecting the point load and the support. Also, the specimens using high-strength shear reinforcement with wider spacing showed no differences in the shear capacity. In B-region shear tests, three specimens, B1, B3, and B4, sharing the same shear span-to-depth ratio of 2.5, displayed comparable shear strength and crack propagation pattern despite variations in rebar grade and spacing of shear reinforcement and the number of supports. Specimen B2-60-6-B-1 presents a unique case with a crack pattern indicative of flexural failure. First observed at 70% of the shear capacity, the majority of shear cracks in this specimen remained within the web region, while in the other three specimens, these diagonal cracks tended to align along the line connecting the support and the point load. The subsequent appearance of vertical cracks confirmed the flexural failure mode of specimen B2-60-6-B-1.

3.1.2.5.3. Load-Displacement Behavior

To illustrate the behavior of specimens during the structural test, the deflection, calculated by taking the average of both LPOT readings under the loading region, is plotted against the corresponding shear load.

Tx-girder

According to Figure 3-50, the experimental results for the D-region, which has a short shear span-to-depth ratio, show that the response is almost linear up to the ultimate load, followed by a brittle failure. In contrast, the B-region experiments demonstrate that after reaching a certain load, the slope of the shear-force deflection curve decreases before reaching the ultimate load, after which failure occurs.

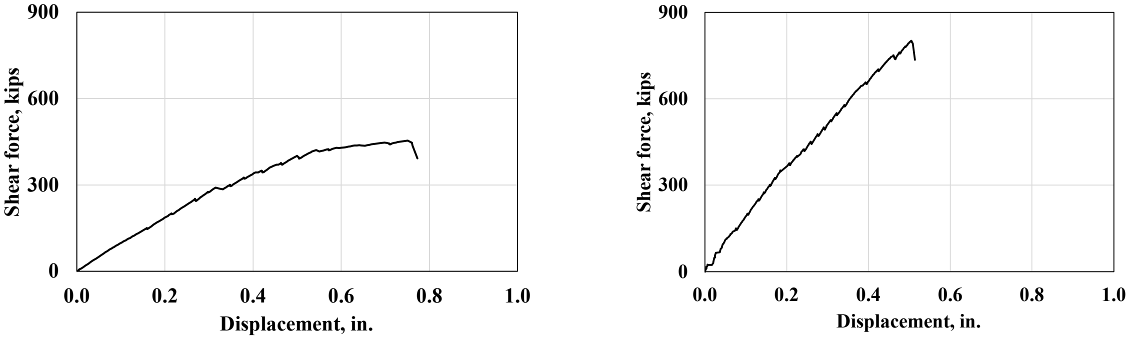

(a) TX1-60-8-B-S (b) TX1-60-8-D-S

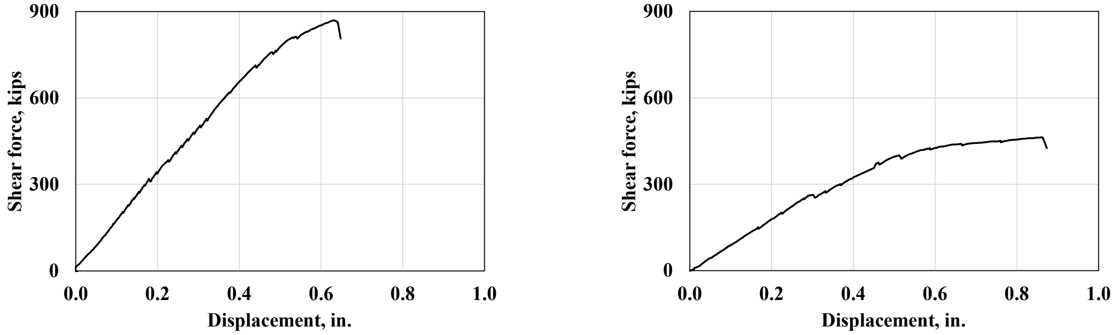

(c) TX2-100-12-D-S (d) TX2-100-12-B-S

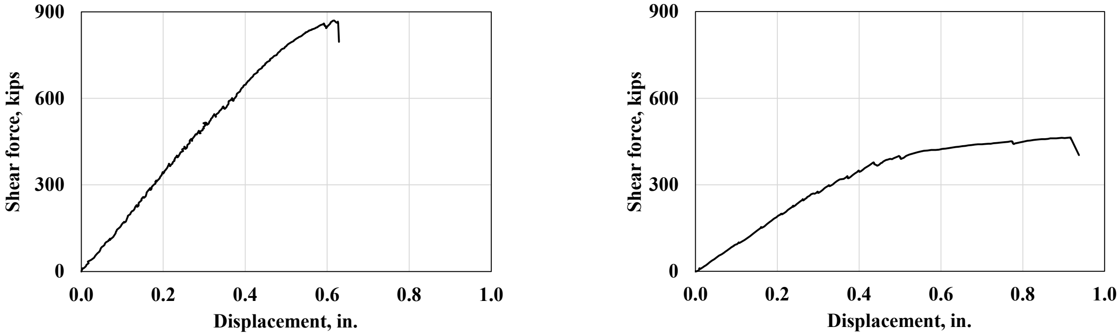

(e) TX3-60-8-D-H (f) TX3-60-8-B-H

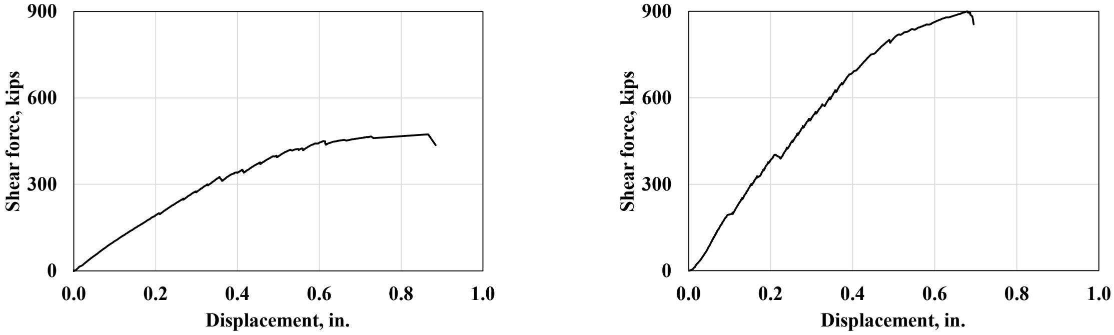

(g) TX4-100-12-B-H (h) TX4-100-12-D-H

Figure 3-50. Shear force-displacement curve for Tx-62 specimens

Box Beams

According to Figure 3-51, the experimental results for the D-region, which has a short shear span-to-depth ratio, show that the response is almost linear up to the ultimate load, followed by a brittle failure. In contrast, the B-region experiments demonstrate that after reaching a certain load, the slope of the shear-force deflection curve decreases before reaching the ultimate load, after which failure occurs. Furthermore, the data from the LPOT for detecting the strand slip shows that no slips were issued for every specimen until loading. Therefore, the slip of the strand has no impact on the capacity of the specimens.

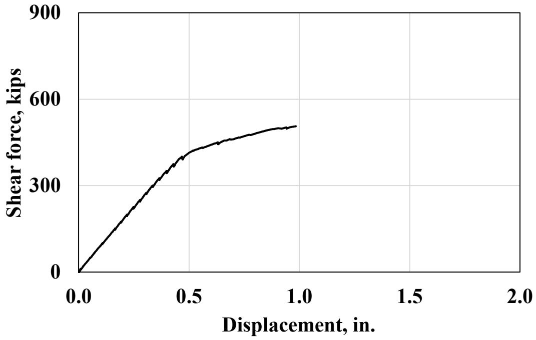

(a) B1-60-6-B-2

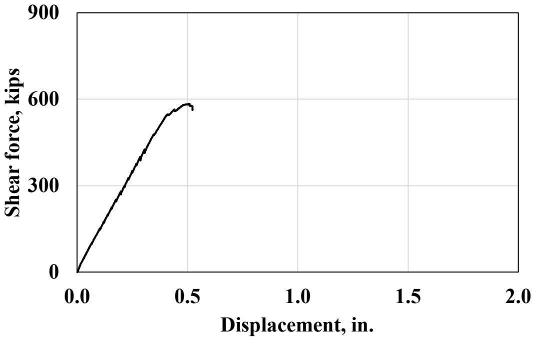

(b) B1-60-6-D-1

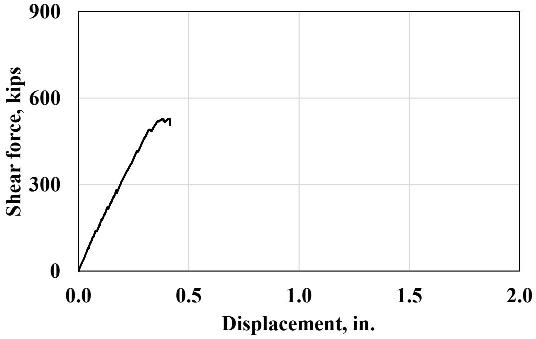

(c) B2-60-6-D-2

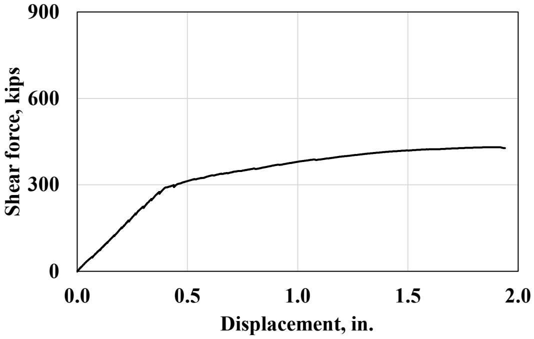

(d) B2-60-6-B-1

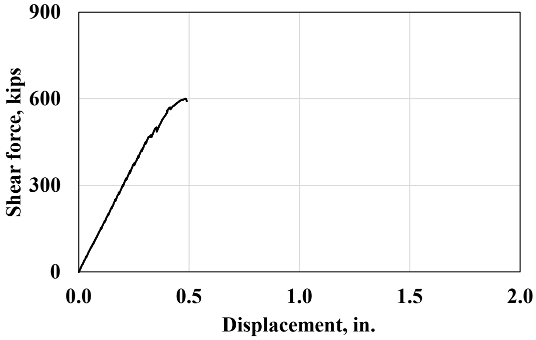

(e) B3-100-10-D-1

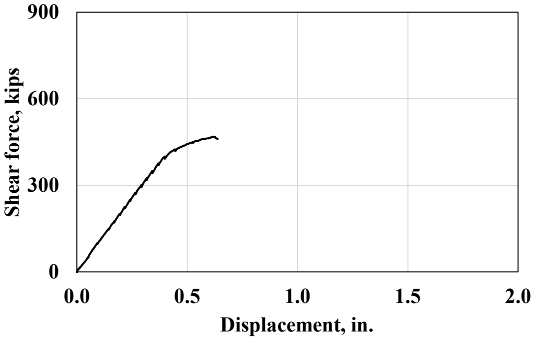

(f) B3-100-10-B-2

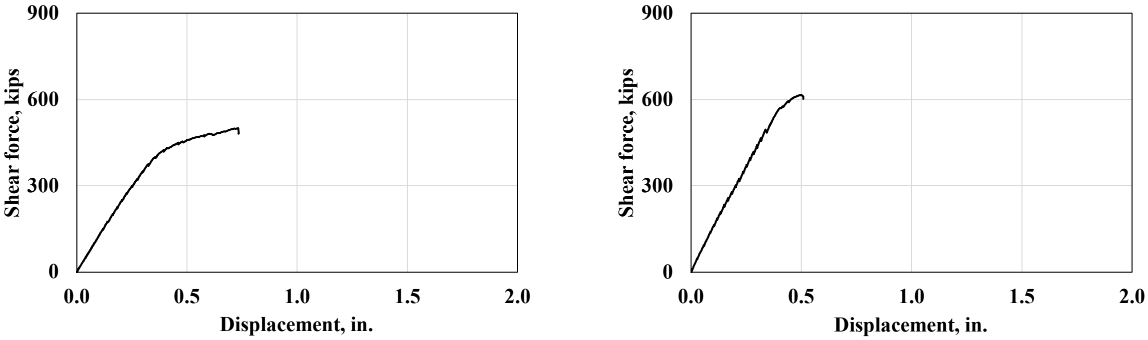

(g) B4-100-10-B-1 (h) B4-100-10-D-2

Figure 3-51. The shear force-displacement curve for 5B40 specimens

3.1.2.5.2. Load Capacity

The shear load versus deflection curve provides insight into the behavior of specimens throughout the structural test. This subchapter compares these curves to analyze how shear reinforcement strength and spacing variations affect prestressed girders' shear behavior. The influence of different strand layouts in prestressed I-girder and the impact of different support conditions in prestressed box beams on the shear performance are examined.

Tx-girder

Rebar grade and spacing

To analyze the impact of different rebar grades and spacing of the shear reinforcement, two specimens with similar shear span-to-depth ratios and the number of supports are compared.

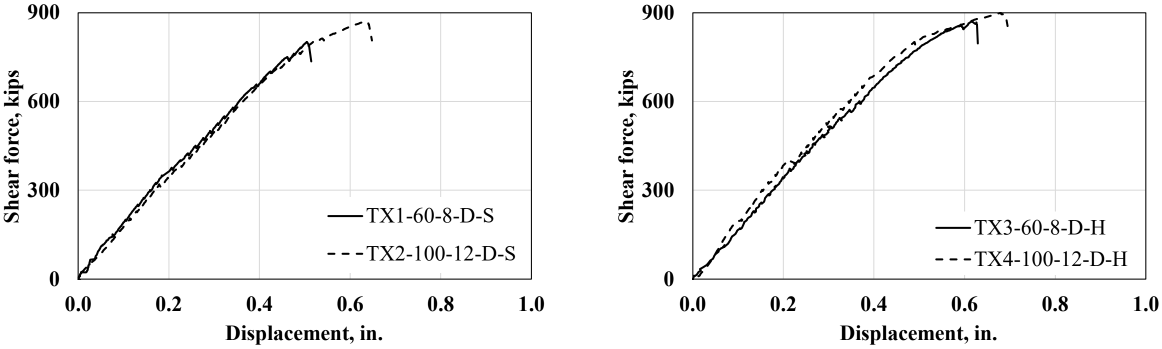

(a) Straight strand only (b) Straight & harped strands

Figure 3-52. Shear force-displacement in D-region with same strand layout (Tx-girder)

Experiencing the same shear failure mode, two specimens in Figure 3-52 exhibit a similar behavior, with deflection increasing linearly as the applied shear load increases. Also, it is observed that the specimens using Grade 100 shear reinforcement display a slightly higher shear capacity (nearly 8%) and larger deflection at the ultimate compared to those in specimens using Grade 60 shear reinforcement, which is a constant result for the design strength differences for the specimens, even though specimen with Grade 100 uses larger spacing. Additionally, the stiffness of specimens with different strengths of the shear reinforcement is almost the same from the initial stage to the ultimate stage. This means that the spacing of the shear reinforcement does not impact the specimens' stiffness when the rebar is applied at a higher strength.

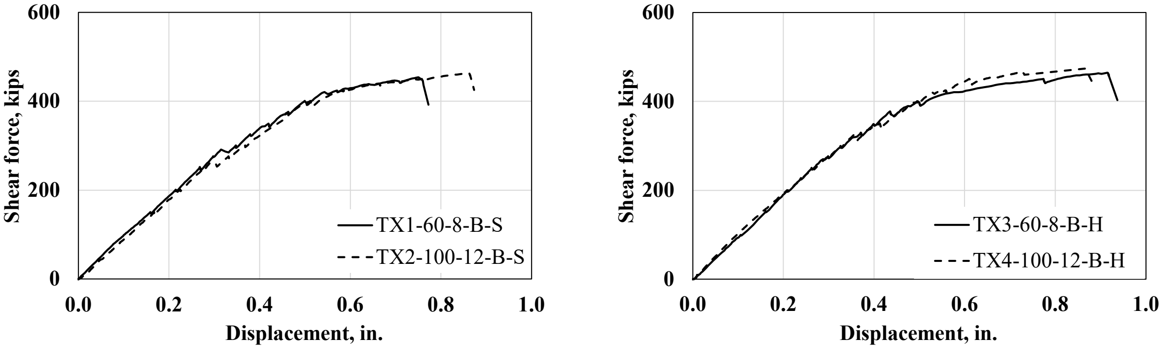

(a) Straight strand only (b) Straight & harped strands

Figure 3-53. Shear force-displacement in B-region with same strand layout (Tx-girder)

Upon visual examination of Figure 3-53, all the specimens failed in flexure shear and displayed a similar plot pattern with similar ultimate strength. The deflection exhibits a linear relationship with the shear load, yet the shape becomes curved as it reaches failure. The final deflection at the ultimate stage when using high-strength shear reinforcement with wider spacing is slightly higher than that of normal-strength shear reinforcement.

Overall, it is evident that the prestressed I-beam using high-strength shear reinforcement with increased spacing demonstrates comparable shear capacity as Grade 60 specimens in both B and D-region shear tests. This finding stemmed from the equivalent shear contribution of steel, leading to the same ratio of stirrups to spacing. As the shear capacity in Grade 100 specimens is not compromised, shear reinforcement spacing can be increased in proportion to the Grade to alleviate congestion.

The comparison results also concluded that Grade 100 specimen plots generally display higher deflection but have similar stiffness compared to those in Grade 60 specimens. This trend also shows up in both the D-region and B-region shear tests.

Strand layout

To analyze the impact of different rebar grades and spacing of the shear reinforcement, two specimens with similar shear span-to-depth ratios and the number of supports are compared.

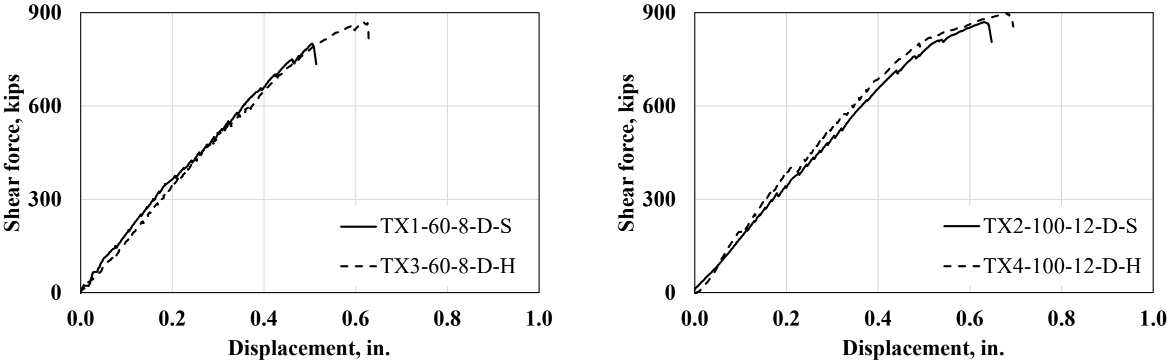

(a) Grade 60 (b) Grade 100

Figure 3-54. Shear force-displacement in D-region with same shear rebar grade (Tx-girder)

Experiencing the same shear failure mode, two specimens in Figure 3-54(a) exhibit similar behavior, with deflection increasing linearly as the applied shear load increases. Also, it is observed that the specimens containing harped strands display a slightly higher shear capacity (30 kips) compared to those in specimens using straight strands only in the bottom flange. The increased shear capacity based on the harped strands is higher than the expected increased value from AASHTO LRFD (V_p), which is 24 kips. Additionally, the stiffness of specimen TX1, which has normal-strength shear reinforcement with straight strands, is similar to specimen TX3, which contains harped strands.

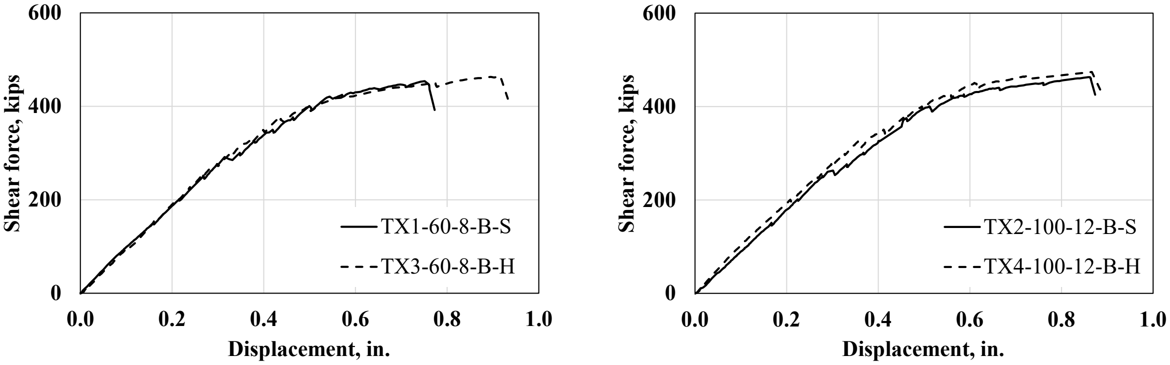

(a) Grade 60 (b) Grade 100

Figure 3-55. Shear force-displacement in B-region with same shear rebar grade (Tx-girder)

As shown in Figure 3-55, the final deflection at the ultimate stage when using harped strands is higher than when using only straight strands. In addition, the stiffness of the specimens is the same as the specimens that don’t apply harped strand when using normal-strength shear reinforcement under the B-region shear test. Also, it is observed that the specimens containing harped strands display a slightly higher shear capacity (10 kips) compared to those in specimens using straight strands. The value is less than the expected V_p from AASHTO LRFD (2020).

In conclusion, the harped strand application can increase the shear strength of the prestressed I-girder, and the increased value is near the expected value calculated based on AASHTO LRFD (2020). Additionally, the harped strand application shows no correlation with the stiffness of the prestressed I-girder. However, using only straight strands instead of considering harped strands results in a reduction in deflection under ultimate conditions under both test regions.

Box Beams

Rebar grade and spacing

To analyze the impact of different rebar grades and spacing of the shear reinforcement, two specimens that have similar shear span-to-depth ratios and the number of supports are compared.

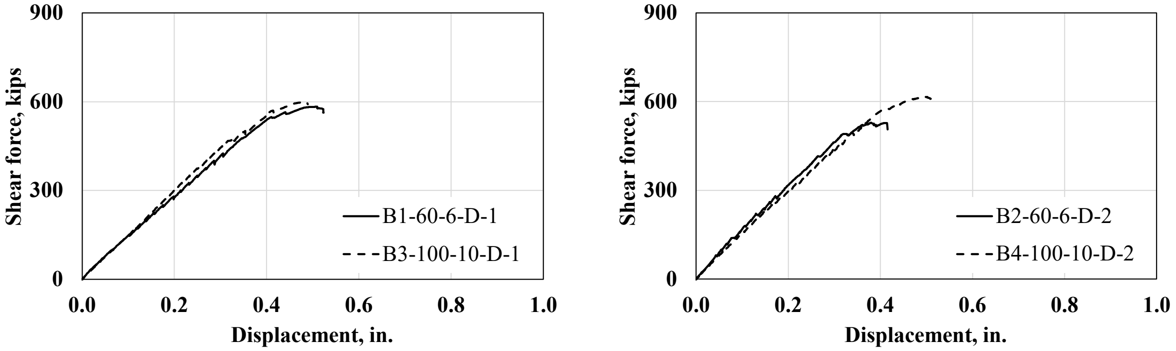

(a) One support (b) Two supports

Figure 3-56. Shear load-deflection in the D-region with the same number of supports (Box beams)

Experiencing the same shear failure mode, four specimens in (a) and (b) in Figure 3-56 exhibit a similar behavior, with deflection increasing linearly as the applied shear load increases. Also, it is observed that the specimens using Grade 100 shear reinforcement display a consistent shear capacity compared to those in specimens using Grade 60 shear reinforcement with narrower spacing. Additionally, the stiffness of specimens B2 and B4 are similar, but the stiffness of specimen B3, which has high-strength shear reinforcement, is higher than that of specimen B1.

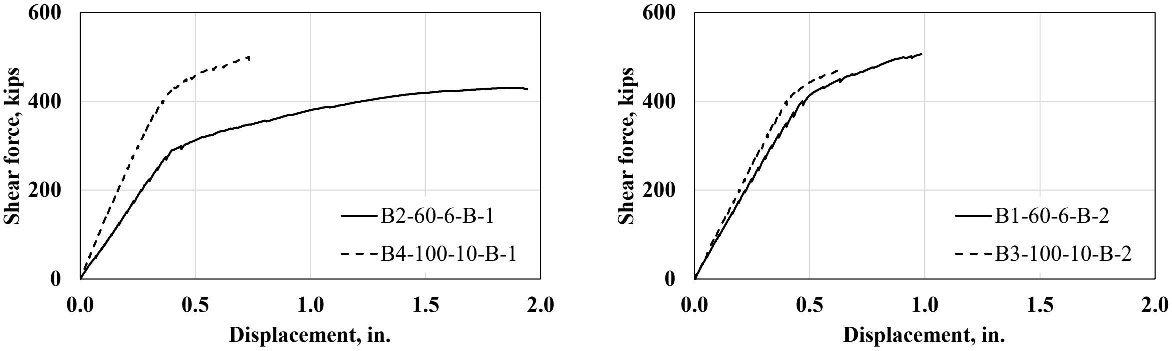

(a) One support (b) Two supports

Figure 3-57. Shear load-deflection in the B-region with the same number of supports (Box beams)

Upon visual examination of Figure 3-57 three specimens that failed in flexural shear, B4-100-10-B-1, B1-60-6-B-2, and BB3-100-10-B-2, display a similar plot pattern. The deflection exhibits a linear relationship with the shear load, yet the shape becomes curved as it reaches failure. Conversely, specimen B2-60-6-B-1 presents a typical plot pattern of flexural failure, characterized by a large range of deflection before reaching failure. The final deflection at the ultimate stage when using high-strength shear reinforcement with wider spacing is lower than those using normal-strength shear reinforcement.

Overall, it is evident that the prestressed box beam using high-strength shear reinforcement with increased spacing demonstrates comparable shear capacity as Grade 60 specimens in both B and D-region shear tests. This finding stemmed from the equivalent shear contribution of steel, leading to the same ratio of stirrups Grade to spacing, set at 10. As the shear capacity in Grade 100 specimens is not compromised, shear reinforcement spacing can be increased in proportion to the Grade to alleviate congestion. The comparison results also concluded that Grade 100 specimen plots generally display lower deflections and steeper initial slope trends, indicating higher stiffness, compared to those in Grade 60 specimens. However, the difference in deflection between the two grades is minimal in the D-region shear test.

Support Conditions

To analyze the impact of different numbers of supports, two specimens that have similar shear span-to-depth ratio and the strength of shear reinforcements are compared.

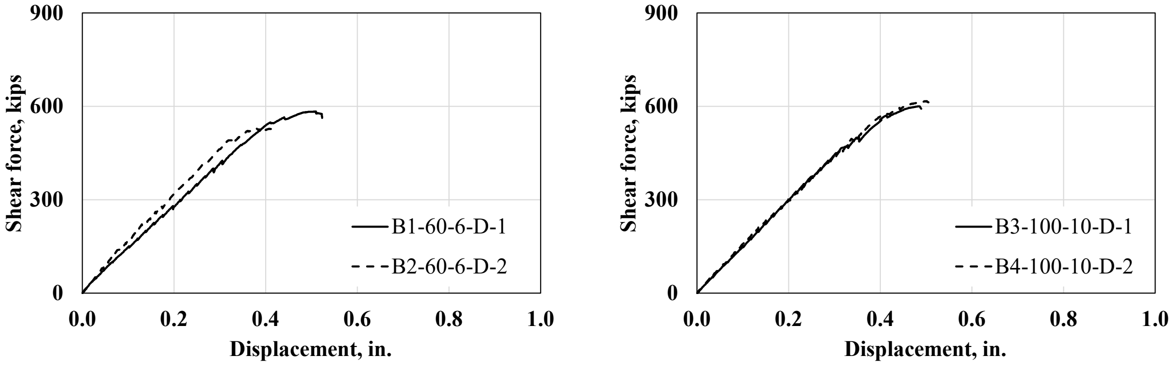

(a) Grade 60 (b) Grade 100

Figure 3-58. Shear load-deflection in the D-region with the same shear reinforcement grade (Box beams)

Experiencing the same shear failure mode, four specimens in Figure 3-58 exhibit a similar behavior, with deflection increasing linearly as the applied shear load increases. Also, it is observed that the specimen's two supports display a consistent shear capacity compared to those in specimens using one support placed in the center of the beam. Additionally, the stiffness of the specimens using high-strength rebars are similar, but the stiffness of specimen B1, which has normal-strength shear reinforcement with one support, is lower than that of specimen B2, which contains two supports.

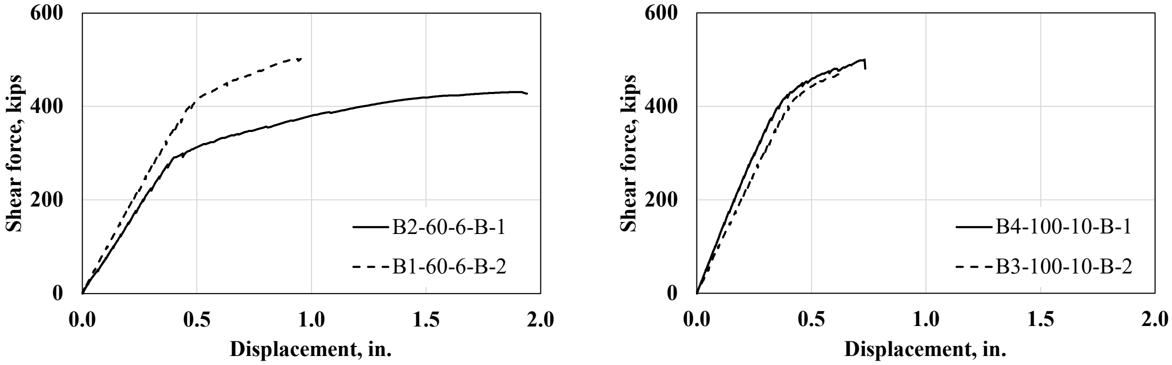

(a) Grade 60 (b) Grade 100

Figure 3-59. Shear load-deflection in B-region with the same shear reinforcement grade (Box beams)

As shown in Figure 3-59, the final deflection at the ultimate stage when using two supports is lower than that using one support. Also, the stiffness of the specimens supported by one support is higher than those supported by two supports when using high-strength shear reinforcement, which is the opposite of normal-strength shear reinforcement.

In conclusion, the support condition does not affect the shear strength of prestressed box beams. Additionally, the number of supports shows no correlation with the stiffness of the box beam. However, using two supports instead of one reduces deflection under ultimate conditions, with this effect being more pronounced in the B-region, where the shear span-to-depth ratio is larger.

3.1.2.5.3. Crack widths

Comparing the patterns of maximum crack width between conventional reinforcement and high-strength reinforcement is prudential to assess the serviceability of specimens with increased rebar spacing. The crack width on both sides of the specimen was visually measured with a crack card at every 25-kip loading increment until a dominant shear crack connecting the loading plate to the support was developed. The maximum crack width measurements on both sides are then averaged, and this value is plotted against the ratio of applied shear to failure shear.

Tx-girder

In Figure 3-60, the crack width in both Grade 60 and Grade 100 specimens is observed to follow a consistent pattern in respective shear region tests as the applied load increased. Under similar experimental conditions, Grade 100 specimens with increased spacing consistently exhibited wider crack widths compared to Grade 60 specimens. The initial crack typically emerged at around 43% of the failure load in D-region tested specimens, while the initial crack for B-region tested specimens is issued at around 60% of the failure load.

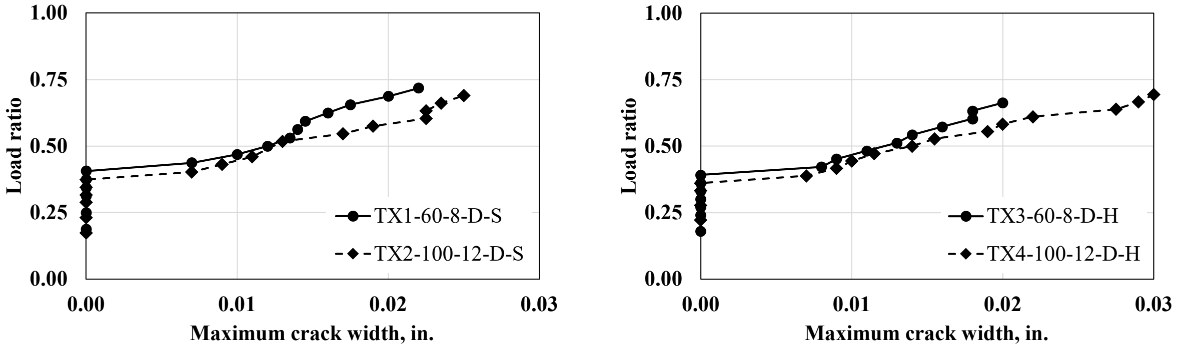

(a) Straight strand (D-region) (b) Strand and harped strand (D-region)

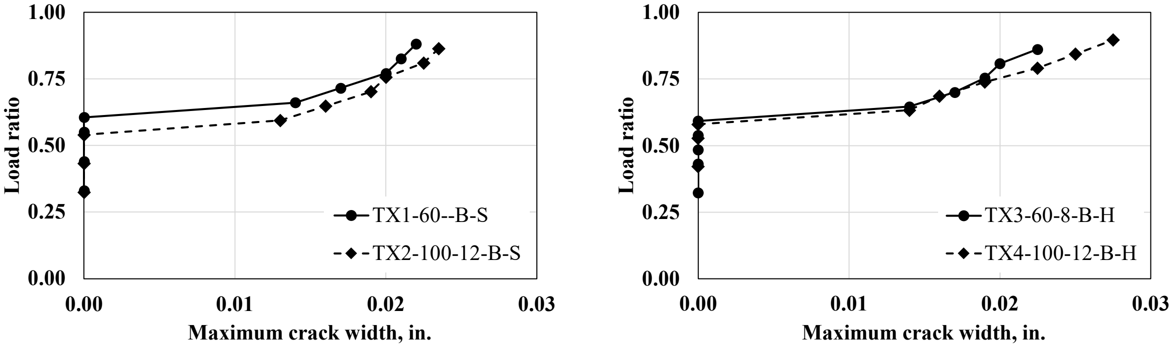

(c) Straight strand (B-region) (d) Strand and harped strand (B-region)

Figure 3-60. Maximum crack width versus load ratio (Tx-girder)

Box Beams

In Figure 3-61, the crack width in both Grade 60 and Grade 100 specimens is observed to follow a consistent pattern in respective shear region tests as the applied load increased. Under similar experimental conditions, Grade 100 specimens with increased spacing consistently exhibited wider crack widths compared to Grade 60 specimens. The initial crack typically emerged at around 33% of the failure load in all specimens. However, B2-60-6-B-1, with the highest shear span, developed the first shear cracks at 25% of the failure load, preceding other specimens. At 80% of the failure load, the widest shear crack measured in the Grade 100 specimen is 0.025 in., whereas 0.019 in. in the Grade 60 specimen.

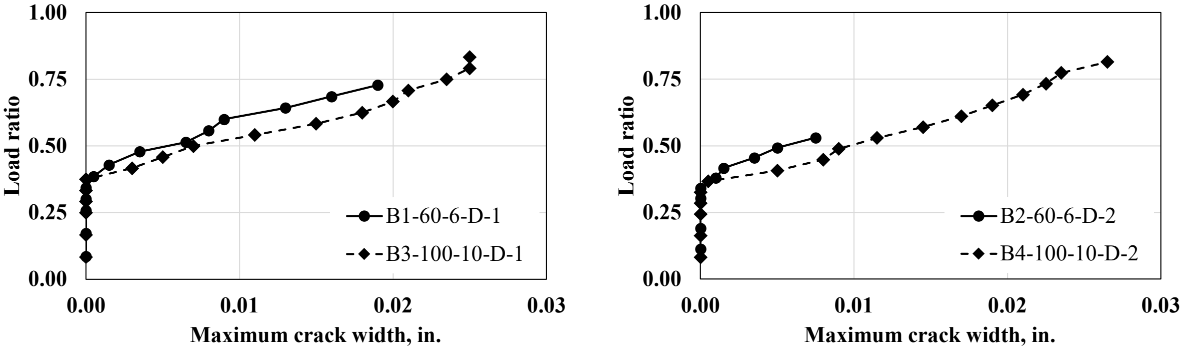

(a) One support (D-region) (b) Two supports (D-region)

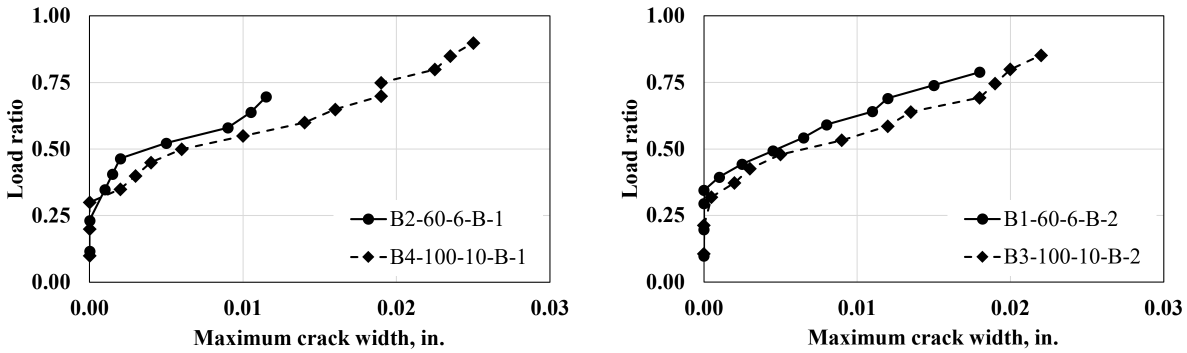

(c) One support (B-region)

(b) Two supports (B-region)

Figure 3-61. Maximum crack width versus load ratio (Box beam)

The benchmark for service loading conditions is established following the approach adopted by TxDOT project 0-5831. However, the ratio of the failure shear ($V_{failure}$) to the design shear capacity (V_n) and the selection of the load factors are modified to align with the current experimental program. Table 3-7 displays the ratio of failure shear to design shear capacity of specimens. By averaging these ratios, a relationship is derived to represent the shear behavior of TX-girder and box beams, as presented in Equation (3-4).

In addition, AASHTO LRFD (2020) assigns a resistance factor of 0.9 for the shear of reinforced normal-weight concrete section and a reinforcement yield strength of up to 100 ksi. The specimens meet AASHTO LRFD (2020) requirements for prestressed sections; therefore, the relationship between the ultimate load and nominal capacity is expressed as the equation below.

$$\begin{gathered} V_{failure} = 1.34 \times V_n \text{ for TX-girder} \\ V_{failure} = 1.22 \times V_n \text{ for Box Beams} \end{gathered} \tag{3-4}$$

Dividing both sides of Equation (3-5) by Equation (3-4) respectively results in another ratio of shear capacity that can be calculated as shown in Equation (3-14). The load factor represents the ratio of the design strength to the nominal capacity, accommodating any variability in loadings. In the experimental program, the dead load constitutes the self-weight of the specimen. In contrast, the live load refers to the applied load when the specimen reaches failure. In this research, the standard load combination with a factor of 1.25 for dead load and 1.75 for live load, as follows, is the AASHTO Strength I load factor. This combination refers to the member's typical vehicular usage without wind load considerations. As a result, the average load factor is computed by combining the weighted contributions of the self-weight (with a dead load factor of 1.25) and the failure load (with a live load factor of 1.75). The average load factor across eight shear tests is established by Equation (3-15).

$$V_u = 0.9 \times V_n \tag{3-5}$$

$$\begin{gathered}\frac{V_u}{V_{failure}} = \frac{0.9\times V_n}{1.34\times V_n} = 0.67 \text{ for TX-girder} \\ \frac{V_u}{V_{failure}} = \frac{0.9\times V_n}{1.22\times V_n} = 0.74 \text{ for Box beams}\end{gathered} \tag{3-6}$$

$$V_u = 1.71 \times V_{service} \tag{3-7}$$

By substituting Equation (3-15) to Equation (3-6), a service level for the prestressed box beam can be estimated from the ratio of the shear failure load as described in Equations (3-8) and (3-9).

$$\frac{V_u}{V_{failure}} = \frac{1.71 \times V_{service}}{V_{failure}} = 0.67 \text{ for TX-girder, } 0.74 \text{ for Box beams} \tag{3-8}$$

$$\frac{V_{service}}{V_{failure}} = 0.39 \text{ for TX-girder, } 0.43 \text{ for Box beams} \tag{3-9}$$

AASHTO LRFD (2020) suggested a reasonable crack width benchmark of 0.017-in. if corrosion is not a concern. Figure 3-62 illustrates width crack measurements of all shear tests alongside 0.017 in. benchmark limit and service level limit at 0.39 to explore the effect of high-strength rebar on serviceability. From the eight shear test results in this project, thirty data points in Grade 60 specimens and forty-six data points in Grade 100 specimens are obtained.

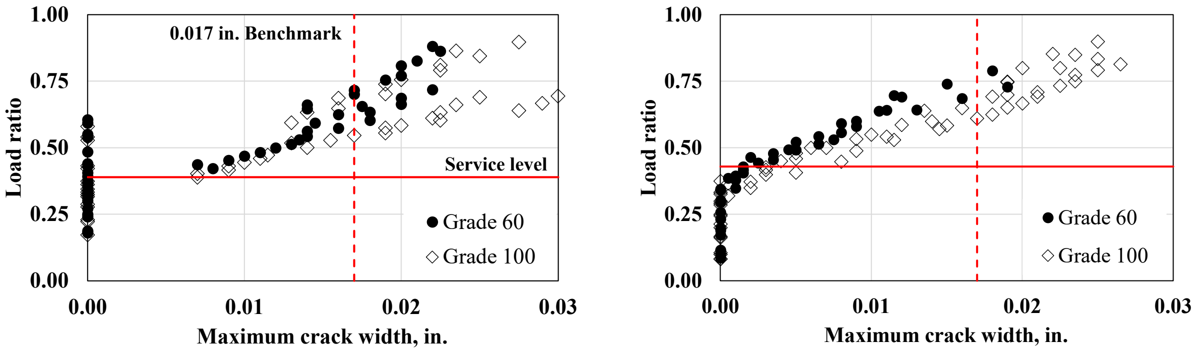

(a) TX-girder (b) Box beams

Figure 3-62. Crack width distributions of Grade 60 and Grade 100 specimens

Upon visual inspection, both Grade 60 and Grade 100 specimens exhibited similar cracking behavior, with cracking steadily increasing as the applied load increased. However, at equivalent load levels, cracks in Grade 100 specimens tend to be wider than those in Grade 60 specimens. The maximum observed differences are approximately 0.005 inch at around 70% of the failure load for the box beam and 0.01 inch at around 80% of the failure load for the TX-girder. Despite the wider crack widths in Grade 100 specimens, all crack widths remain below the 0.017-inch limit until 53% of the failure load for the box beam and 57% of the failure load for the Tx-girder.

Notably, all shear cracks in Grade 100 specimens remain below the crack limit benchmark around the service level line. Grade 100 shear reinforcement with increased spacing does affect the serviceability, yet it remains within the acceptable limits outlined by AASHTO LRFD under the service conditions. In other words, high-strength shear rebars have the potential to replace conventional shear rebars in both the prestressed box beam and Tx-girder.

3.1.2.6. Conclusions

Tx-girder

The analysis of eight shear tests was conducted on four Tx-62 girders. The shear failure mode is governed for all the specimens, while shear-tension failure is issued in the D-region test, and flexure-shear failure is issued in the B-region test. Upon analyzing the test results, several key observations are made:

- The shear strength of prestressed girders using Grade 100 shear reinforcement can be conservatively predicted using the design method introduced in AASHTO LRFD (2020), regardless of the loading region or the presence of harped strands.
- When high-strength reinforcement is used and the shear reinforcement spacing is increased, more cracks form compared to normal reinforcement, and the region where cracks form also becomes wider.
- In the shear test, Grade 100 specimens with increased spacing in each region carry a shear capacity comparable to that of Grade 60 specimens.
- Increasing the stirrup spacing proportionally with the Grade leads to a wider crack width.
- The presence of different strand layouts, such as applying harped strands, did not affect strength and serviceability.

Box Beams

The analysis of eight shear tests was conducted on four 5B40 box beams. While seven specimens exhibited experienced shear failure, one failed in flexure. Upon analyzing the test results, several key observations are made:

- The shear strength of prestressed girders using Grade 100 shear reinforcement can be conservatively predicted using the design method introduced in AASHTO LRFD (2020), regardless of the loading region or the support configuration.
- Specimens with high-strength shear reinforcement exhibited a consistent crack propagation pattern, with concrete cracking along the straight line connecting the point load and the support, compared to the specimens using normal-strength shear rebar.

- Grade 100 specimens with increased spacing generally demonstrate a lower deflection than Grade 60 specimens.
- In the shear test, Grade 100 specimens with increased spacing in each region carry a shear capacity comparable to that of Grade 60 specimens.
- Increasing the stirrup spacing proportionally with the Grade leads to a wider crack width. However, crack widths measured under the service condition for all specimens remain below the limit specified by AASHTO LRFD (2020).
- The presence of different support conditions did not affect the strength and serviceability.

3.2. Substructures

3.2.1. Deep Beam

3.2.1.1. Specimen Design

A total of eight RC deep beams were designed replicate on those in previous studies (Birrcher et al, 2009), as shown in Table 3-8. Two cross-section types were utilized: rectangular and inverted T cross-section, with four beams of each type. Each beam contains two test regions, resulting in a total of 16 tests. To assess the applicability of high-strength rebar in deep beams, longitudinal reinforcement was employed using both normal-strength and high-strength steel, while web reinforcement consisted exclusively of high-strength steel with two reinforcement ratios: 0.2% and 0.3%. Additionally, beams with heights of 42 inches and 75 inches were utilized. The test identification in the table sequentially denotes the cross-section type, grade of longitudinal reinforcement, web reinforcement grade, web reinforcement ratio, and beam height. For example, "R-L60-W100-0.2-45" refers to a rectangular beam with Grade 60 longitudinal reinforcement, Grade 100 web reinforcement, a 0.2% web reinforcement ratio, and a beam height of 45 inches. The concrete mix was designed to achieve a target 28-day compressive strength of 4,000 psi.

Table 3-8. Test matrix of deep beam test

Specimen ID	Cross-section		Reinforcement grade		Web reinforcement ratio (%)
	Type	Dimension (in.)	Long.	Web	
R-L60-W100-0.2-42	Rectangular	21×42	Gr.60	Gr.100	0.2
R-L60-W100-0.3-42			Gr.100	Gr.100	0.3
R-L100-W100-0.2-42			Gr.60	Gr.100	0.2
R-L100-W100-0.3-42			Gr.100	Gr.100	0.3
R-L60-W100-0.2-75		21×75	Gr.60	Gr.100	0.2
R-L60-W100-0.3-75			Gr.100	Gr.100	0.3
R-L100-W100-0.2-75			Gr.60	Gr.100	0.2
R-L100-W100-0.3-75			Gr.100	Gr.100	0.3
IT-L60-W100-0.2-42	Inverted T	21×42	Gr.60	Gr.100	0.2
IT-L60-W100-0.3-42			Gr.100	Gr.100	0.3
IT-L100-W100-0.2-42			Gr.60	Gr.100	0.2
IT-L100-W100-0.3-42			Gr.100	Gr.100	0.3
IT-L60-W100-0.2-75		21×75	Gr.60	Gr.100	0.2
IT-L60-W100-0.3-75			Gr.100	Gr.100	0.3
IT-L100-W100-0.2-75			Gr.60	Gr.100	0.2
IT-L100-W100-0.3-75			Gr.100	Gr.100	0.3

The geometry of the deep beam specimens was based on the previous research (Birrcher et al. 2009) as shown in Figure 3-63. Each beam featured web reinforcement ratios of 0.2% and 0.3% applied to both sides. Furthermore, the amount of high-strength longitudinal rebars was reduced to achieve the same load capacity as the normal-strength longitudinal bars.

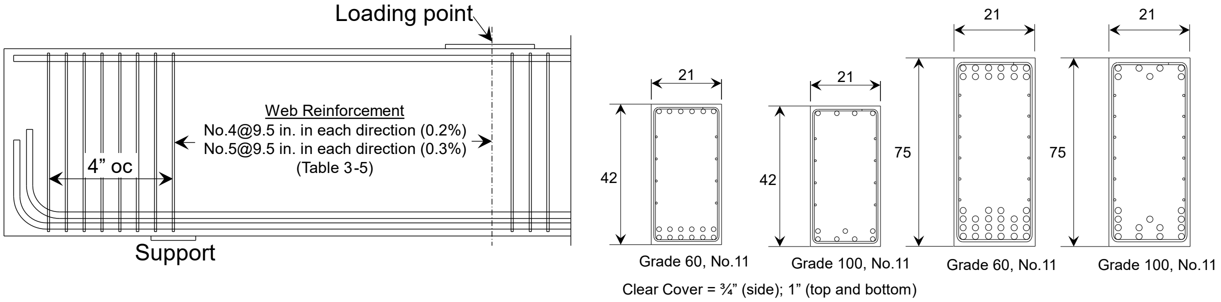

(a) Rectangular beam

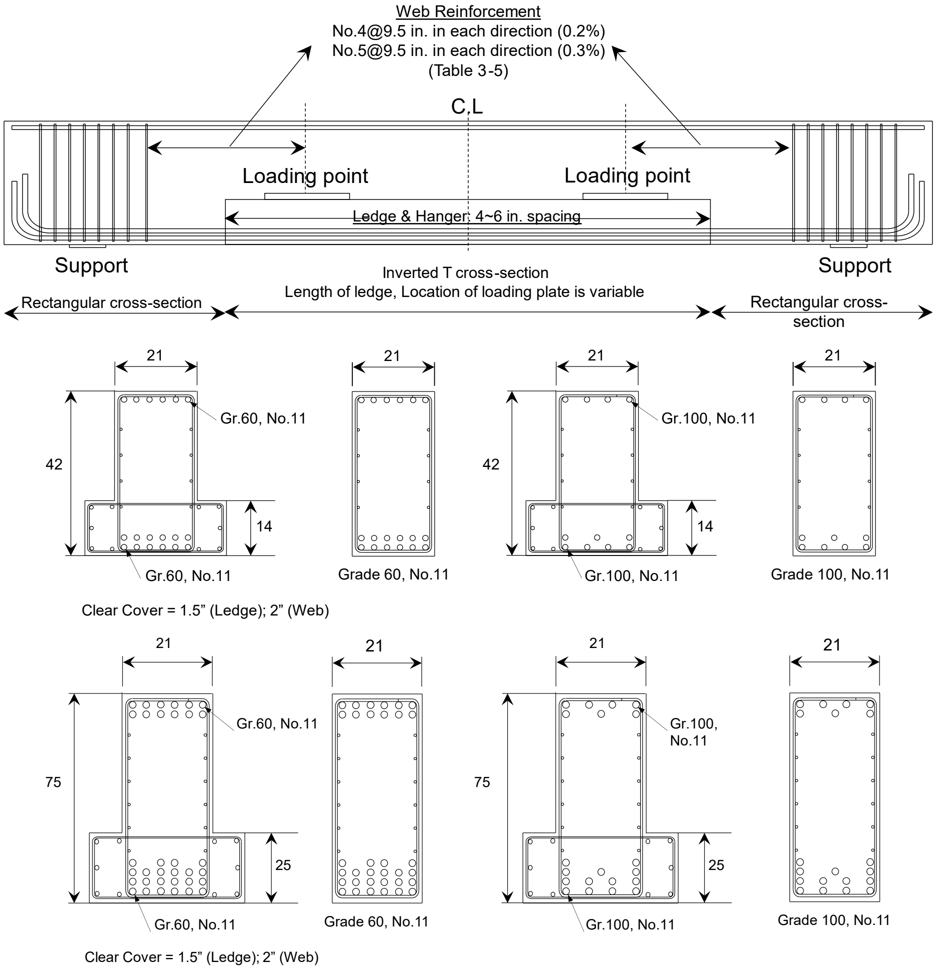

(b) Inverted T beam

Figure 3-63. Deep beam specimen configuration

3.2.1.2. Fabrication

The fabrication of deep beams followed the sequence: assembly of reinforcement cage, installation of rebar strain gauges, assembly of steel formwork, concrete casting, and formwork removal, as shown in Figure 3-64. Notably, steel formwork was used to ensure precise dimensions. Concrete was supplied by a local ready-mix provider, with workability ensured by achieving an adequate slump, considering the beam height and rebar spacing. This was verified through slump tests performed according to ASTM C143 before casting. For the 75-inch beams, two ready-mix trucks were required, both supplied from the same batch, with no more than 30 minutes between deliveries to prevent cold joints. During casting, the research team operated an external pneumatic vibrator attached to brackets along the steel formwork and portable vibrators at the top of the beam to compact the concrete. After casting, the beams were covered with plastic sheeting and allowed to cure in the laboratory.

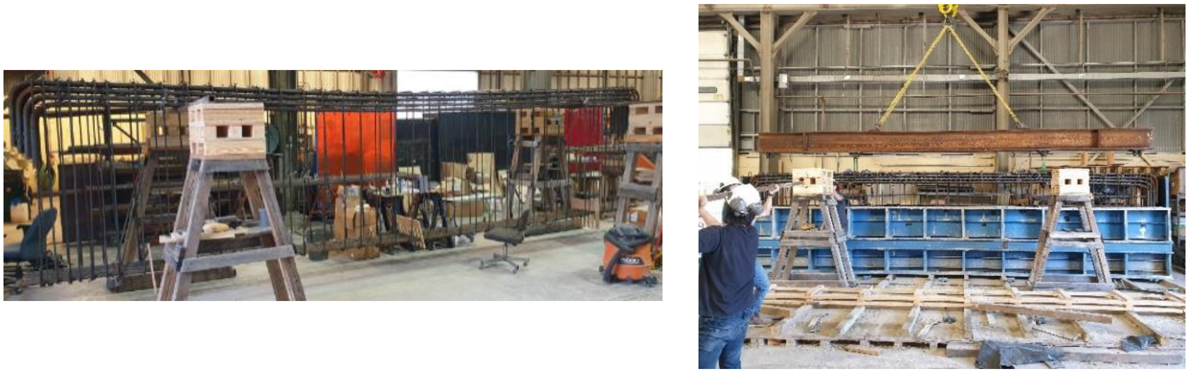

(a) Assembly of rebar cage (b) Assembly of steel formwork

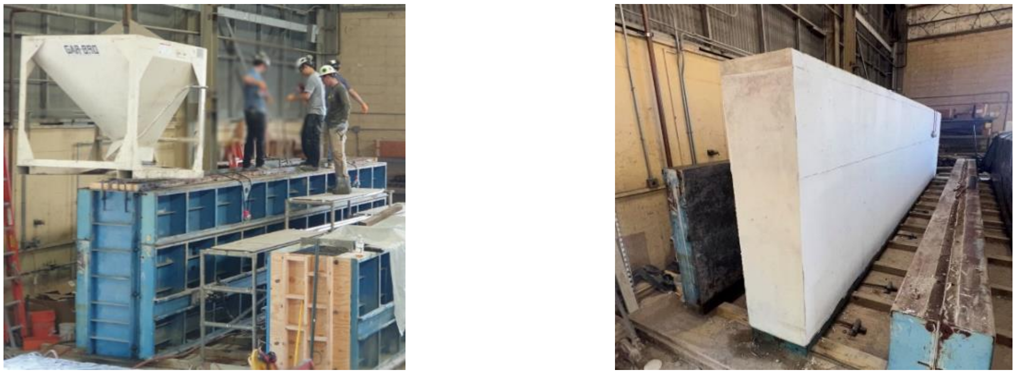

(c) Concrete casting (d) Removal formwork

Figure 3-64. Fabrication of deep beam specimens

3.2.1.3. Test Setup

3.2.1.3.1. Loading Frame

The loading frame used in beam splice test was used for deep beam test (Refer to Chapter 3.1.2.3). The details are shown in Figure 3-65. Especially, for inverted T beams U-shaped frames were used to apply loads evenly to the ledges on both sides of the beams.

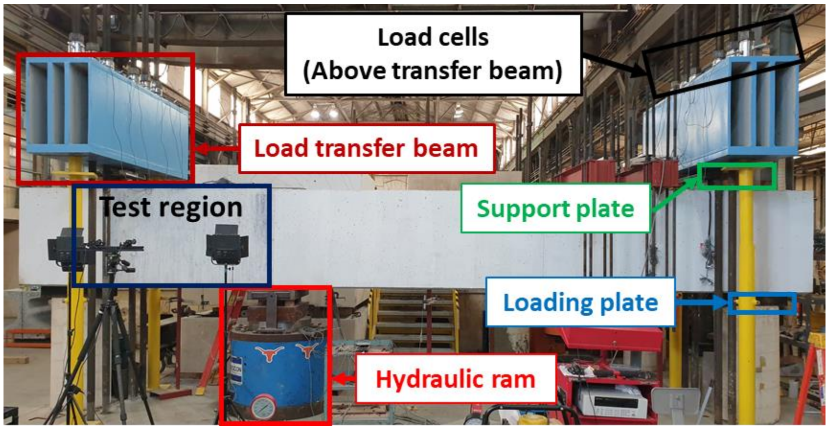

(a) Rectangular beam

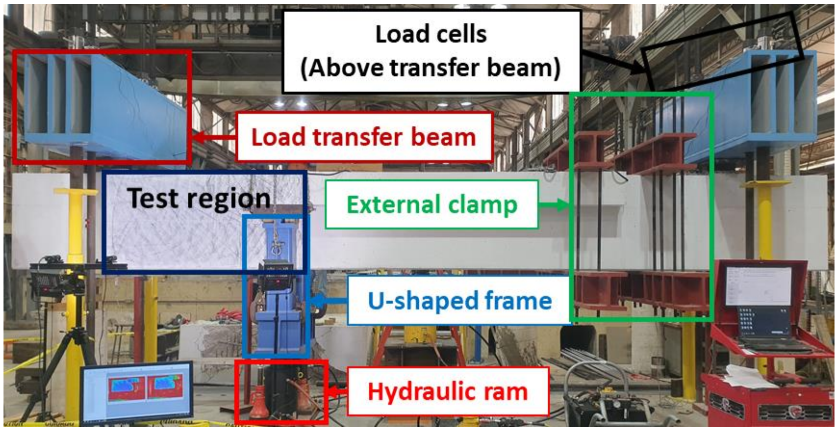

(b) Inverted T beam

Figure 3-65. Test setup of deep beams

3.2.1.3.2. Instrumentation

The reactions, displacement of specimen, rebar strain and crack widths were all extensively measured during the experiment.

- Load and displacement measurements

500-kip capacity load cells measured the applied load during the test. Four 4-inch linear potentiometers were placed at the supports, loading point, and center of the beam. To avoid overestimation of displacement from the rigid body motion, the displacements recorded at the supports were used to account for the effect of rigid body motion on the displacement readings. Assuming that the rigid body motion-induced displacement varies linearly along the beam's length, the displacement at the load point due to the rigid motion was determined from the displacement readings at the supports. This value was then subtracted from the displacement recorded at the loading point to isolate the pure beam displacement.

- Strain measurements for reinforcing bars

Electrical resistance strain gauges were mounted on the surfaces of both longitudinal and web reinforcements. The gauges on the longitudinal reinforcement were attached on the bar in the outmost layer. The placement of gauges on the web reinforcement were determined along the assumed strut line. Detailed location of the gauges is illustrated in Figure 3-66.

- Crack widths

Crack widths were measured visually using a crack comparator and digitally using a DIC system, similar to the beam splice test (Refer to Chapter 3.1.2.3). The DIC system was employed for the 42-inch beam; however, it could not be used for the 75-inch beam because the test region extended beyond its coverage area. Instead, for the 75-inch beam, crack patterns were monitored between load steps, and crack widths were measured manually using a crack comparator card.

3.2.1.4. Test Procedure

Two tests were conducted on each beam. For the 42-inch beams, to prevent pre-cracking of the second test region, it was strengthened with external post-tensioned clamps. The first test was then carried out in several load steps, each approximately 10% of the expected ultimate load capacity. The first test terminated when failure was observed, and then the failed region was strengthened with external post-tensioned clamps. The hydraulic ram was repositioned for the second test, and the beam was reloaded until the second test region failed. For the 75-inch beams, the loading point was positioned at the center of the beam, allowing the shear-span to depth ratio of both 42-inch and 75-inch beams were the identical. Therefore, two tests for the 75-inch beams were conducted simultaneously. Both test regions were monitored at the first test, with crack widths measured on both sides. Once the first test region failed, the load was removed, and failed region was strengthened using external post-tensioned clamps. The load was then reapplied at the same location for the second test, continuing until the second test region reached failure.

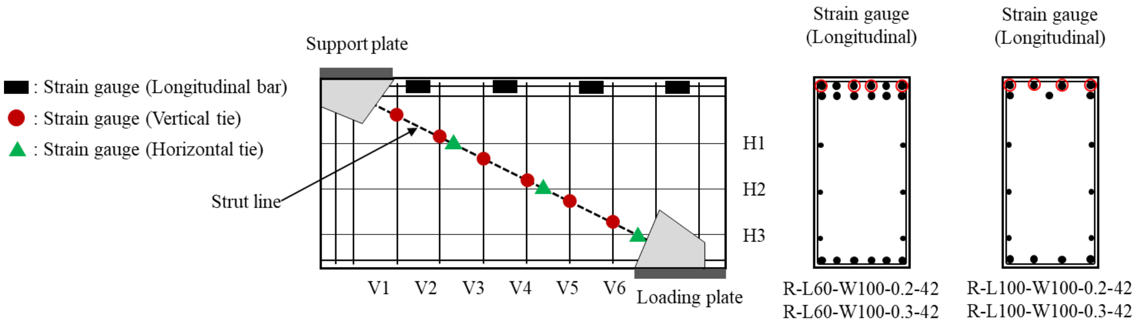

(a) Rectangular 42-inch beam

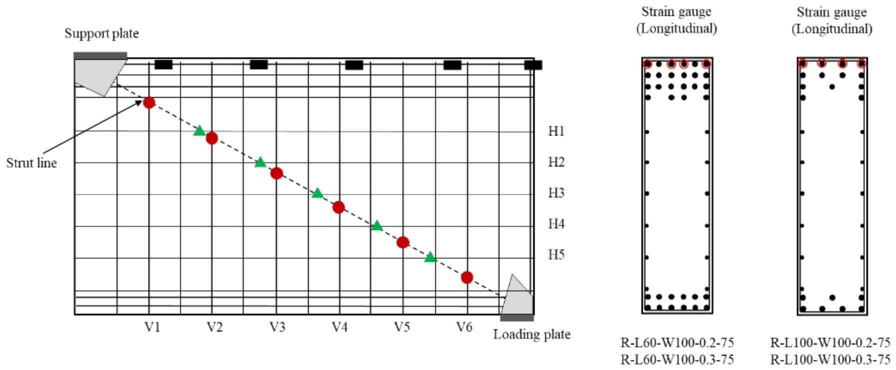

(b) Rectangular 75-inch beam

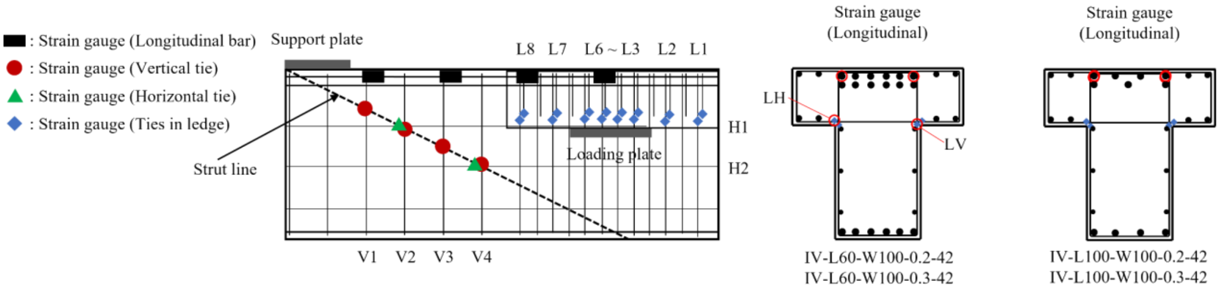

(c) Inverted T 42-inch beam

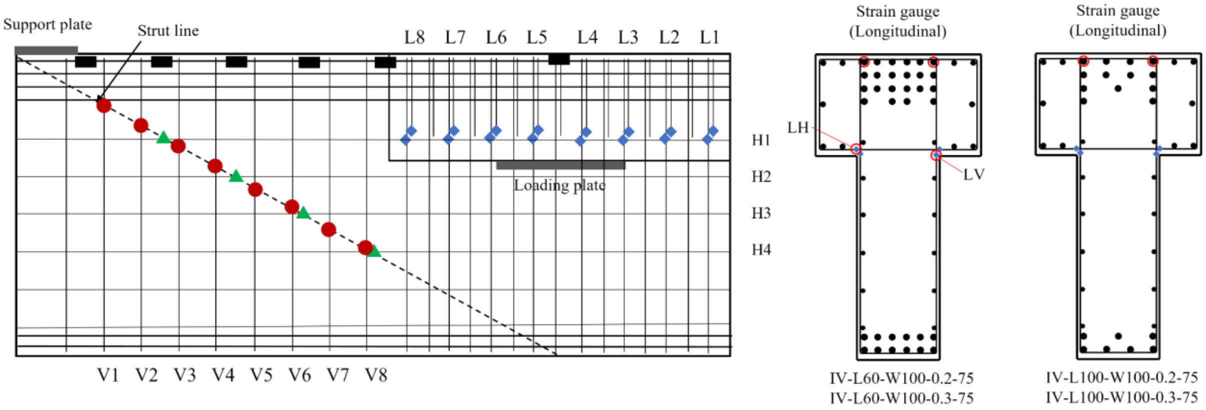

(d) Inverted T 75-inch beam

Figure 3-66. Strain gauge location of deep beams

3.2.1.5. Experimental Results and Discussion

3.2.1.5.1. Overview

This chapter presents a detailed summary of the experimental results, including load-displacement behavior, rebar strain distribution, and cracking patterns, as well as an assessment of serviceability through crack width evaluation. The material properties obtained from laboratory testing are listed in Table 3-9, Table 3-10 and Figure 3-67.

Table 3-9. Concrete properties of deep beams

Specimen ID	Compressive strength (psi)	Splitting tensile strength (psi)	Modulus of elasticity (ksi)
R-L60-W100-0.2-42	6215	525	4264
R-L60-W100-0.3-42	5578	450	4154
R-L100-W100-0.2-42	6218	598	4225
R-L100-W100-0.3-42	6325	497	4510
R-L60-W100-0.2-75	4678	422	4173
R-L60-W100-0.3-75	5062	436	4283
R-L100-W100-0.2-75	5530	454	4067
R-L100-W100-0.3-75	5861	504	4485
IT-L60-W100-0.2-42	6192	490	4324
IT-L60-W100-0.3-42	6211	478	4301
IT-L100-W100-0.2-42	6297	480	4348
IT-L100-W100-0.3-42	6400	515	4486
IT-L60-W100-0.2-75 **IT-L60-W100-0.3-75**	6656	553	4728
IT-L100-W100-0.2-75 **IT-L100-W100-0.3-75**	5691	521	4510

Table 3-10. Rebar properties of deep beams

Rebar	Yield strength (ksi)	Ultimate strength (ksi)
Grade 60 (#11)	65.7	100.9
Grade 100 (#4)	135.9	172.1
Grade 100 (#5)	136.9	173.9
Grade 100 (#11)	112.9	128.8

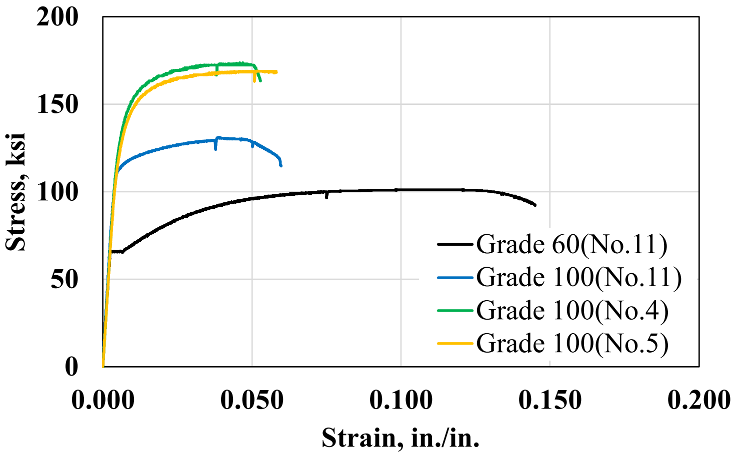

Figure 3-67. Rebar stress-strain curves (Deep beam test)

3.2.1.5.2. Crack pattern

Rectangular Beam

During the initial loading stage, flexural cracks were observed on the tension side of the beam. As the load increased, diagonal cracks developed at the tips of the flexural cracks, preventing their further propagation. These diagonal cracks continued to extend, with additional parallel diagonal cracks appearing within the shear span, indicating that the web reinforcement effectively distributed the cracking. The failure occurred with an abrupt decrease in load as the concrete fractured near the loading point, a failure mode consistently observed across all test cases.

Figure 3-68 illustrates the progression of these crack patterns, with load levels expressed as a percentage of the maximum shear capacity at the critical section, defined as the midsection of the test area. In the 42-inch beam, the main diagonal crack extended from the edges of both plates, while in the 75-inch beam, it extended from the loaded plate at a slightly larger angle. This difference suggests that the relatively larger amount of web reinforcement in the shear span may have influenced the load transfer mechanism.

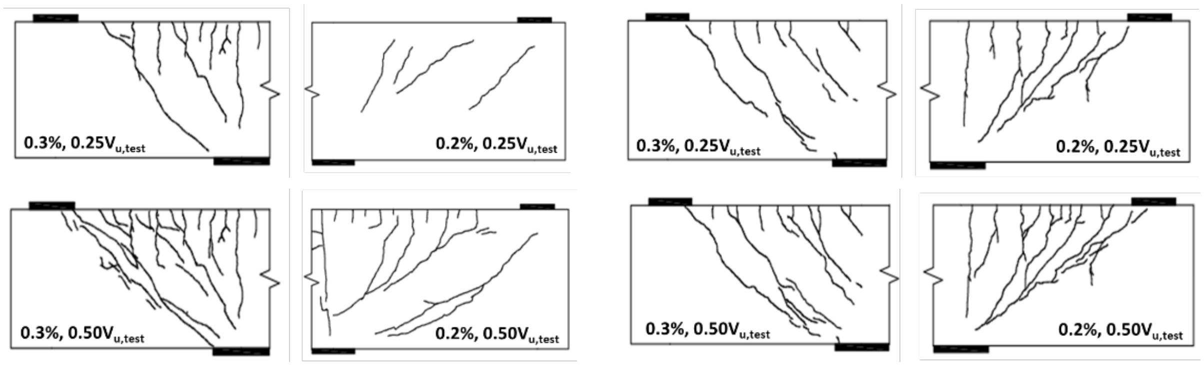

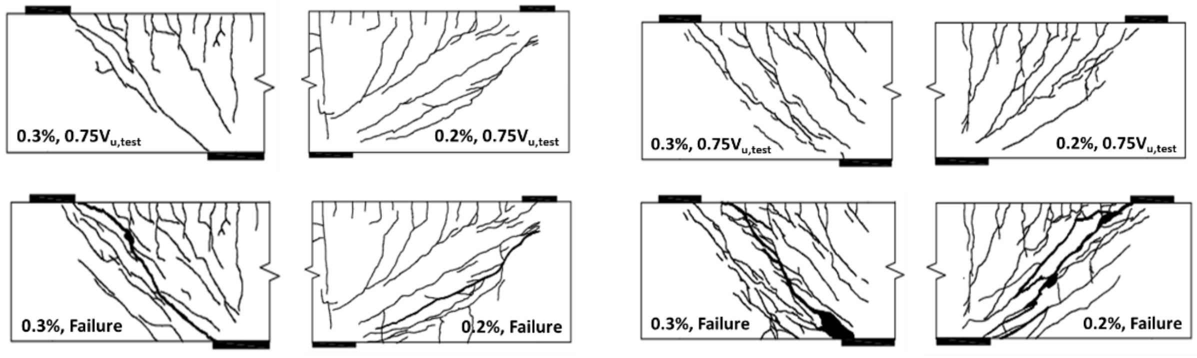

(a) R-L60-W100-42 (b) R-L100-W100-42

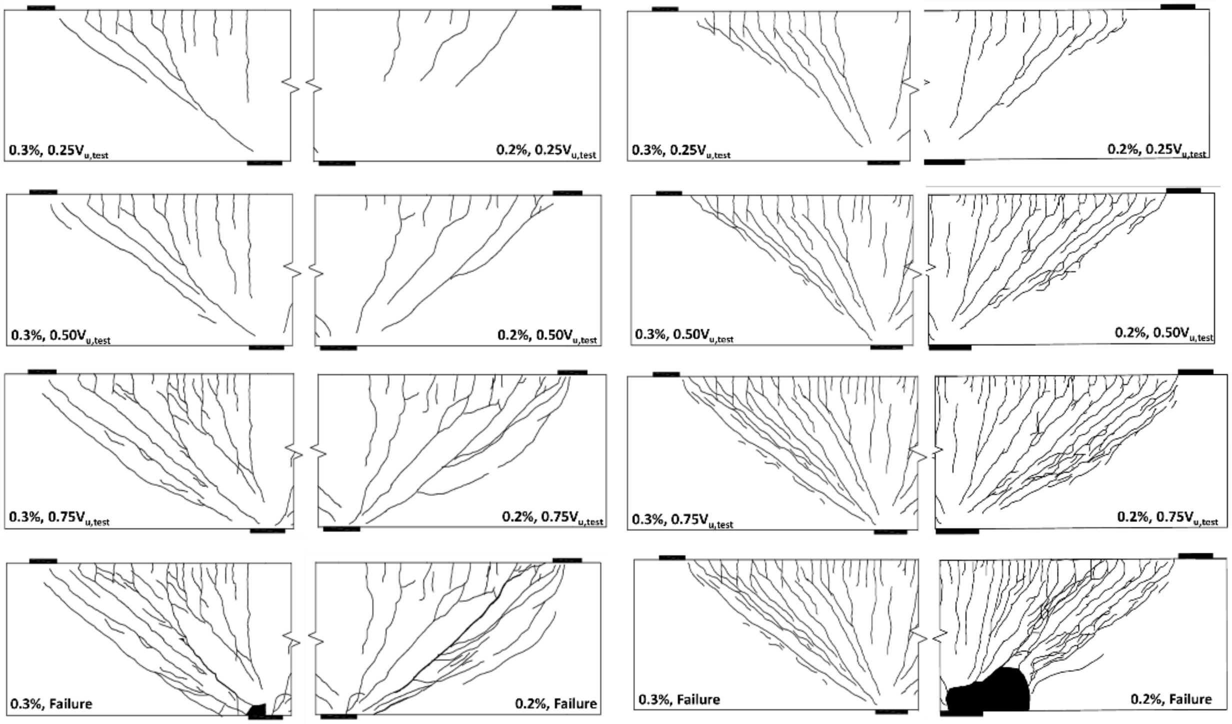

(c) R-L60-W100-75 (d) R-L100-W100-75

Figure 3-68. Crack patterns in rectangular deep beams

Inverted T Beam

Figure 3-69 illustrates the crack patterns observed in inverted T deep beams. Initially, flexural cracks formed near the ledge on the tension side of the rectangular section. Subsequently, diagonal cracks developed at the tips of the flexural cracks, extending toward the middle of the ledge and the compression side of the beam. Following this, additional diagonal cracks developed parallel to the initial cracks, forming between the support and the ledge. Cracks were also appeared on the side surface of the ledge. Near failure, crack patterns and failure modes distinct from those observed in the rectangular deep beams. First, the initially developed diagonal cracks extended the lower part of the ledge transversely. In the final stage, a complex crack pattern emerged. Cracks formed at the edge between the ledge and rectangular sections and diagonal cracks propagating across rectangular section toward the strut node under the loading point rapidly extended and widened. These resulted in a sharp decrease in load, ultimately leading to the termination of the experiments.

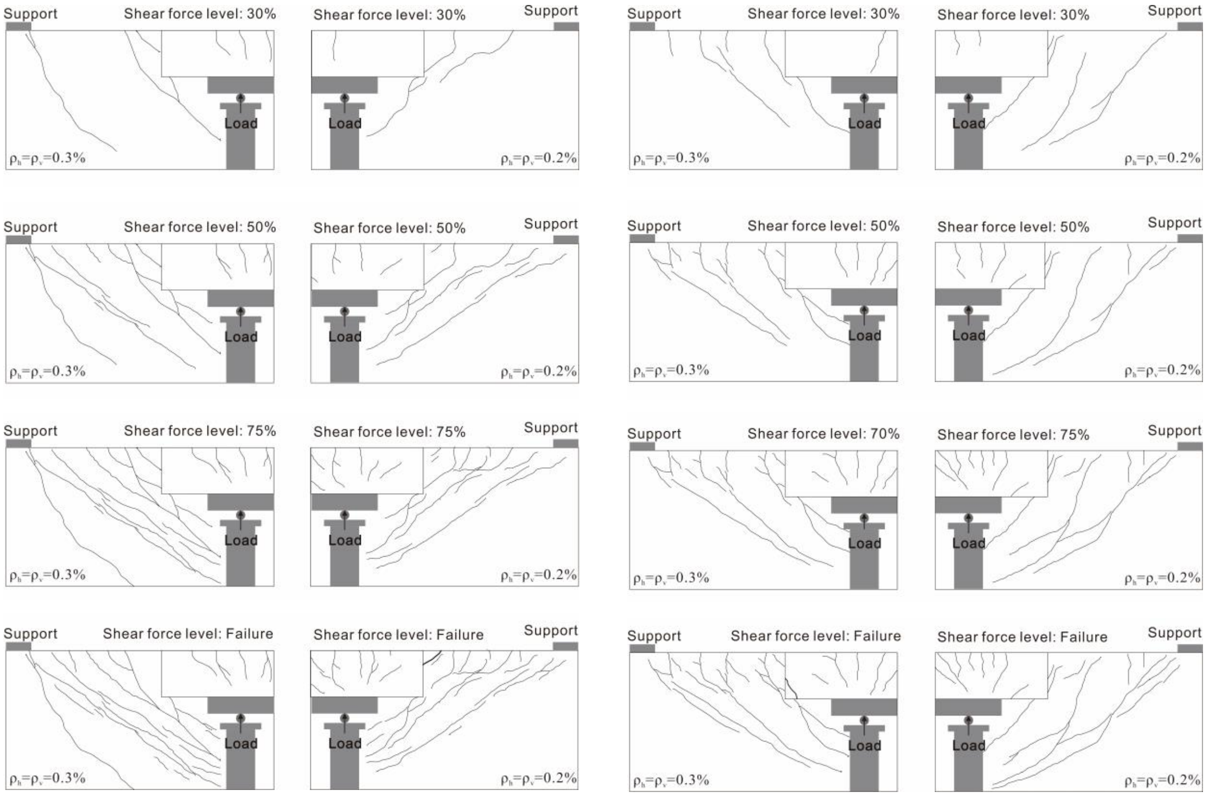

(a) IT-L60-W100-42 (b) IT-L100-W100-42

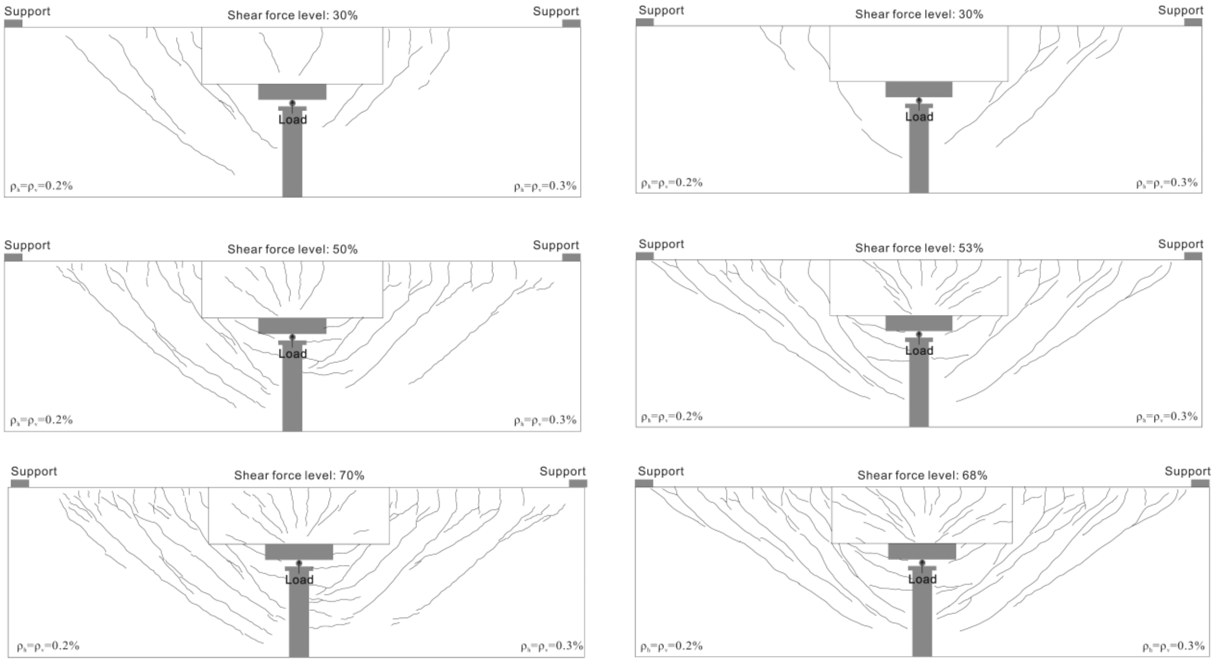

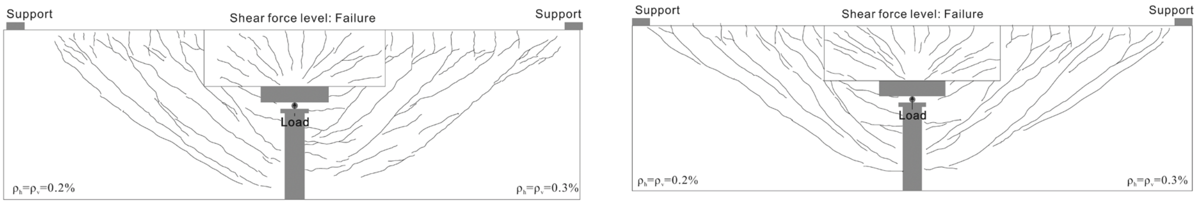

(c) IT-L60-W100-75 (d) IT-L100-W100-75

Figure 3-69. Crack patterns in inverted T deep beams

3.2.1.5.3. Load Capacity

For deep beams, the shear strength at the critical section was calculated and compared to evaluate the load capacity. The critical section was defined as the point halfway between the support and loading point. The shear strength considered self-weight of the beam and load transferred beam, and the shear force calculation detail is illustrated in Figure 3-70. In the figure, W_{DL} represents portion of the beam's weight. P_{TR} denotes the weight of each load transfer beam, and P_D represents the weight of the beam. R_A and R_B are the reaction forces measured by the load cells. V_{test} is the shear strength in the test.

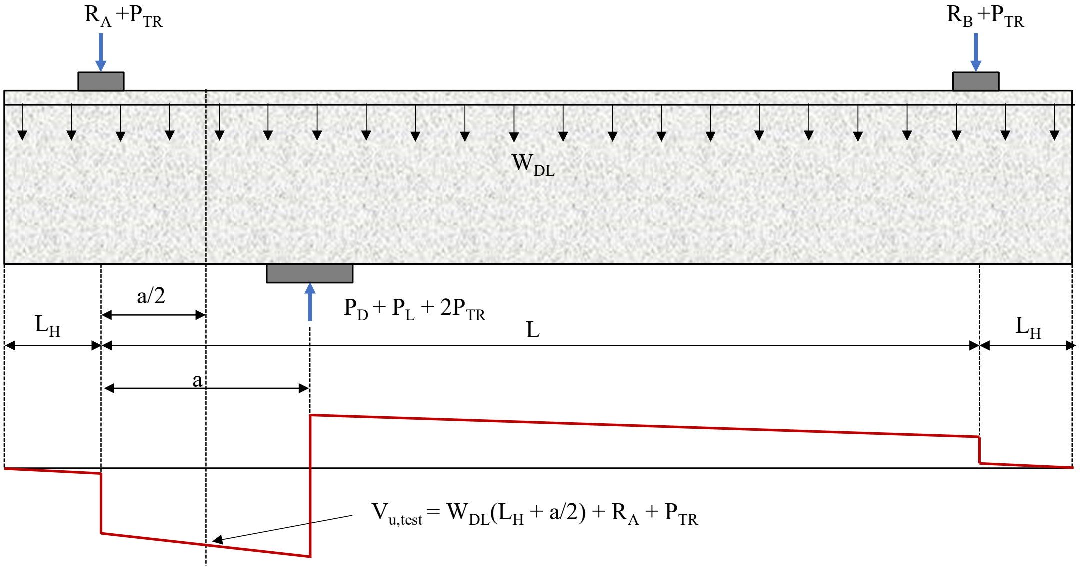

Figure 3-70. Shear strength calculation for deep beams

Rectangular Beam

Three values of shear strength were calculated to normalize shear strength by dividing the test value by the calculated value. The calculated values were based on the STM from AASHTO LRFD (2020) and the sectional methods from ACI 318-19 and AASHTO LRFD (2020). The shear strength and normalized values are summarized in Table 3-11. Figure 3-71 shows the normalized shear strength for rectangular beams.

Table 3-11. Shear strength of rectangular deep beams

Test ID	Shear strength (kip)				Normalized ratio		
	Test$^{(1)}$	STM$^{(2)}$	$\text{SM}_{\text{ACI}}^{(3)}$	$\text{SM}_{\text{AASHTO}}^{(4)}$	(1)/(2)	(1)/(3)	(1)/(4)
R-L60-W100-0.2-42	567	304	368	418	1.86	1.54	1.36
R-L60-W100-0.3-42	536	358	479	528	1.50	1.12	1.01
R-L100-W100-0.2-42	537	289	344	364	1.85	1.56	1.48
R-L100-W100-0.3-42	479	346	456	457	1.38	1.05	1.05
R-L60-W100-0.2-75	711	326	629	789	2.18	1.13	0.90
R-L60-W100-0.3-75	938	446	850	1026	2.10	1.10	0.91
R-L100-W100-0.2-75	743	355	612	719	2.09	1.21	1.03
R-L100-W100-0.3-75	915	454	830	921	2.01	1.10	0.99

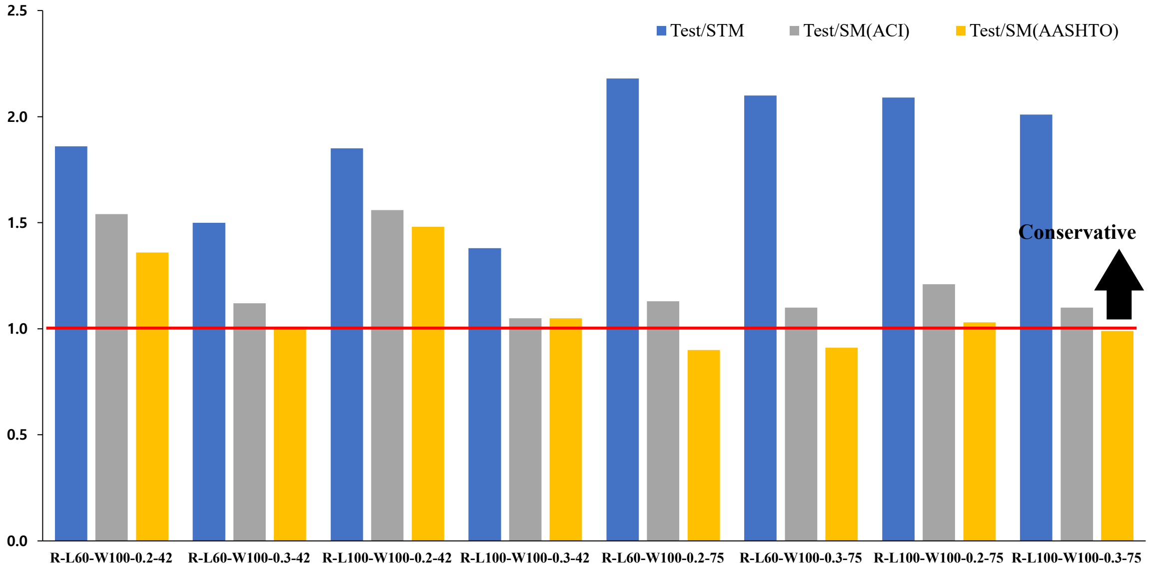

Figure 3-71. Normalized shear strength of rectangular beams

For the 42-inch beam, shear strength was higher with a web reinforcement ratio of 0.2% compared to 0.3%. However, the difference in shear strength for the 42-inch beam was relatively small, approximately within 10%. Moreover, a previous study (Birrcher et al., 2009) indicated that the web reinforcement ratio does not consistently influence shear strength; in some cases, shear strength was greater with a ratio of 0.3% than 0.2%. This suggests that for the 42-inch beam, the web reinforcement ratios of 0.2% and 0.3% do not significantly impact shear strength, and both ratios were sufficient for the structure to achieve its intended strength. Conversely, in the 75-inch beam, shear strength increased with a web reinforcement ratio of 0.3% compared to 0.2%. This means that the reinforcing bar can affect the strength of the 75-inch beam, possibly due to the presence of more web reinforcement compared to the 42-inch beam.

The normalized value is the ratio between the experimental value and the estimated value using various methods. Therefore, a value greater than 1.0 indicates a conservative and safe design, while a value less than 1.0 suggests an unconservative and potentially unsafe design. The normalization results for shear strength show that the sectional method generally predicts shear strength more accurately than the STM. However, in some cases, it predicts a strength lower than the experimental values or yields a normalized value very close to 1.0, which could lead to an unsafe design. Conversely, it was confirmed that using the STM consistently ensures safety across all cases.

For the 42-inch beam, the single-panel method consistently predicted strut failure, while the two-panel method predicted vertical tie failure in all cases. This suggests that the two-panel method provides significantly more conservative strength estimation than the single-panel method. In conclusion, the single-panel STM is a reasonable design approach for a 42-inch beam, aligning with the failure mode observed in the crack pattern. Meanwhile, for the 75-inch beam, both methods predicted the same failure mode: strut failures. This change in expected failure mode is attributed to the increased web reinforcement in the shear span compared to the 42-inch beam. Consequently, the stress flow of the 75-inch beam differed from that in the 42-inch beam, consistent with the observed crack patterns and longitudinal strain profiles. Nonetheless, experimental results confirm that the STM remains a reasonable design method for rectangular deep beams and ensures safety, even with the application of high-strength rebar.

Inverted T Beam

For the inverted T 42-inch beam, the single-panel STM method was compared to test value, as listed in Table 3-12. The STM conservatively estimated the shear strength, with experimental values exceeding the predicted STM values by 12-70%.

Table 3-12. Shear strength of inverted T deep beams

Test ID	Shear strength (kip)		Normalized ratio
	Test$^{(1)}$	STM$^{(2)}$	(1)/(2)
IT-L60-W100-0.2-42	480	350	1.37
IT-L60-W100-0.3-42	479	427	1.12
IT-L100-W100-0.2-42	412	361	1.14
IT-L100-W100-0.3-42	532	438	1.21
IT-L60-W100-0.2-75	816	531	1.54
IT-L60-W100-0.3-75	816	610	1.34
IT-L100-W100-0.2-75	743	437	1.70
IT-L100-W100-0.3-75	743	549	1.35

3.2.1.5.4. Rebar strain

The strains in the reinforcing bars were monitored during the tests through strain readings from gauges positioned as shown in Figure 3-66.

Rectangular Beam

The strains in the horizontal ties were consistently smaller than those in the vertical ties across all test cases, with maximum readings of less than 0.002. This indicates that the vertical ties played the primary role in resisting the strains within the concrete strut. Figure 3-72 shows the strains in the vertical ties, which are proportional to the applied load and exceed the yield strain before failure, except in the case of R-L60-W100-75-0.3. R-L60-W100-75-0.3 did not reach the yield strain at failure, likely because the strain gauge was positioned relatively far from the actual cracks. However, the maximum stress in the vertical tie of R-L60-W100-75-0.3 ranged from approximately 100 to 130 ksi, confirming that it effectively served as high-strength reinforcement. In conclusion, the strain data confirms that the web reinforcement functioned as a high-strength material.

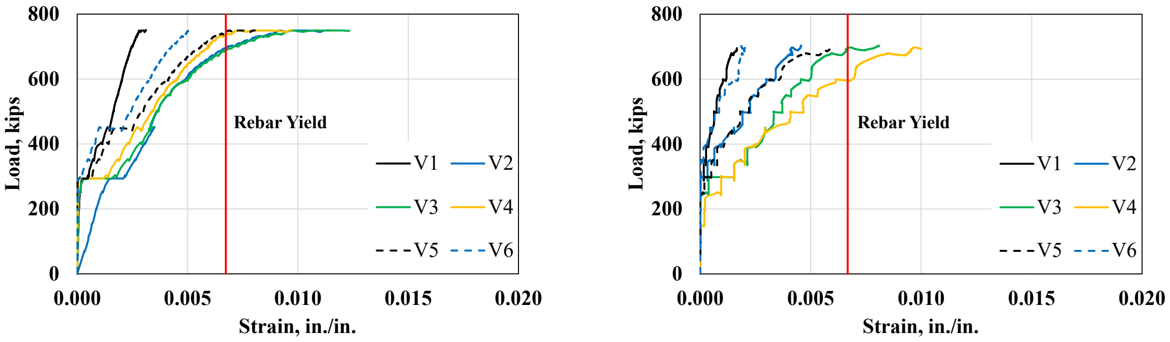

(a) R-L60-W100-42-0.2 (b) R-L60-W100-42-0.3

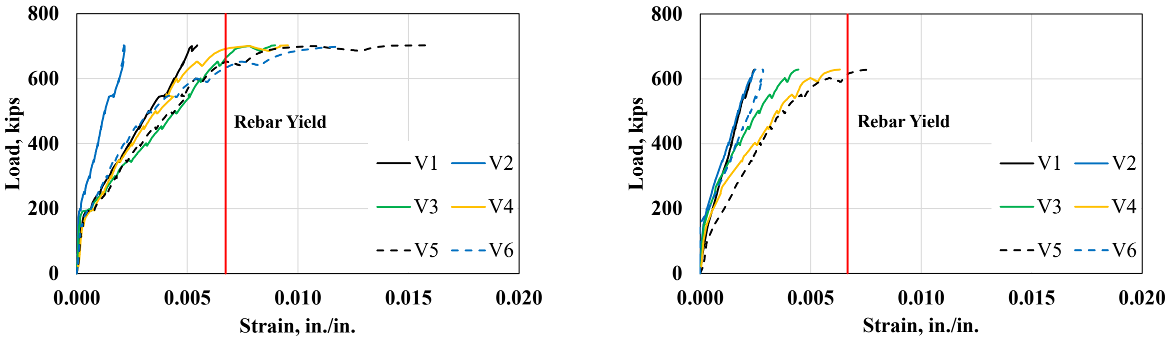

(c) R-L100-W100-42-0.2 (d) R-L100-W100-42-0.3

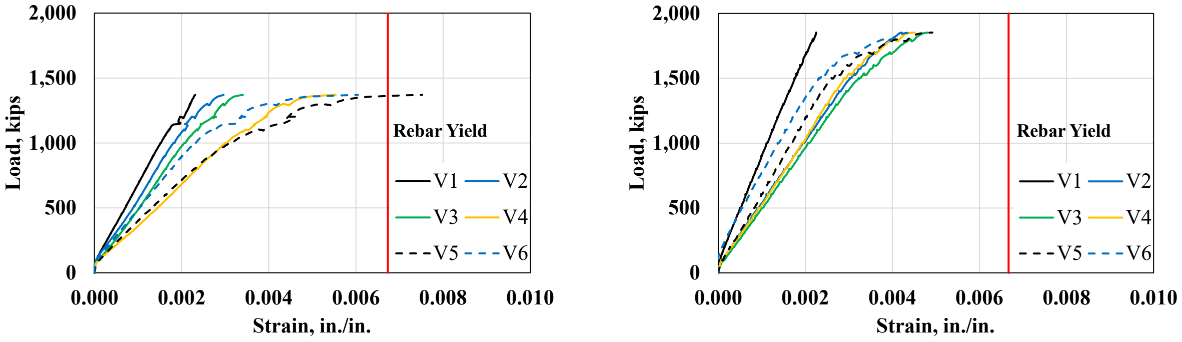

(e) R-L60-W100-75-0.2 (f) R-L60-W100-75-0.3

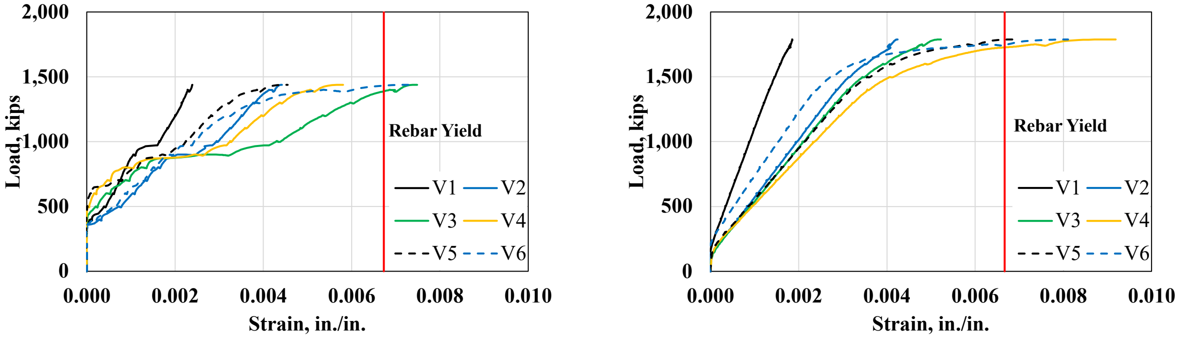

(g) R-L100-W100-75-0.2 (h) R-L100-W100-75-0.3

Figure 3-72. Strain of vertical ties in rectangular deep beams

Figure 3-73 shows the strains in the longitudinal reinforcement along the length of the beam within the shear span. These measurements confirm the validity of two key points: the effectiveness of the strut-and-tie model for estimating the force mechanism in deep beams and the successful application of high-strength steel, allowing for a reduction in the amount of longitudinal reinforcement. To this end, two calculated strain values were compared with the test strain values. One was based on the Bernoulli beam theory, and the other was calculated using the STM. For the 75-inch beams, strains in the two test regions were observed simultaneously since the loading point was located at the center of the beam. Additionally, because the 75-inch beam exhibited a larger strut angle in the crack pattern compared to the 42-inch beam, the strain values calculated using the two-panel STM were also compared with the test strain values.

The strain profiles differed significantly from those calculated using Bernoulli beam theory applied to B-regions. The strain tended to decrease as it approached the supports, though the reduction was not substantial, and the profile resembled that of the single-panel STM for the 42-inch beams. In contrast, for the 75-inch beams, the strain profiles resembled a combination of single-panel and two-panel STM. This supports the observation that the failure mechanism of the 75-inch beams differed from that of the 42-inch beams, as seen in the cracking behavior.

When the same load was applied, stress in the longitudinal bars was obtained using the corresponding measured strain based on rebar tension test results. The transmitted load to the longitudinal bars was then determined. When high-strength steel was used, the observed strain values were higher due to the reduced amount of rebar compared to normal-strength steel. Despite this, the proportion of the load transmitted to the longitudinal bars relative to the applied load was similar, with approximately a 10% difference between high-strength and normal-strength steel. This indicates that the employment of high-strength steel with a reduced quantity for longitudinal reinforcement can achieve a comparable load transfer to that of normal-strength steel.

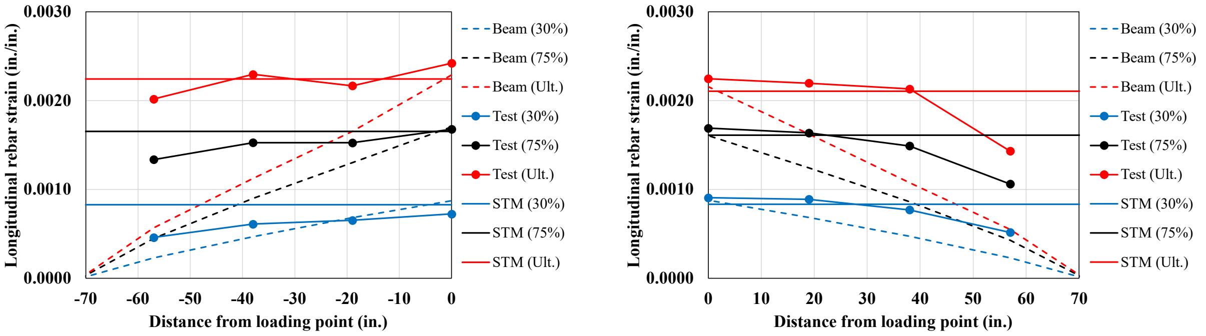

(a) R-L60-W100-42-0.2

(b) R-L60-W100-42-0.3

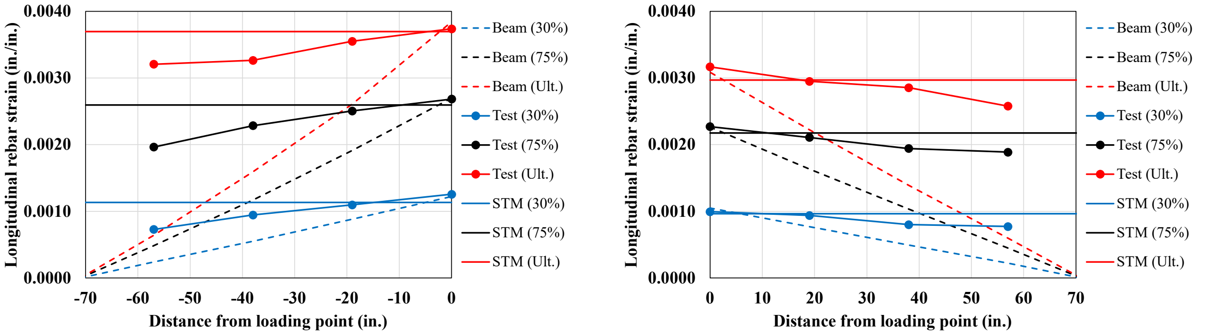

(c) R-L100-W100-42-0.2

(d) R-L100-W100-42-0.3

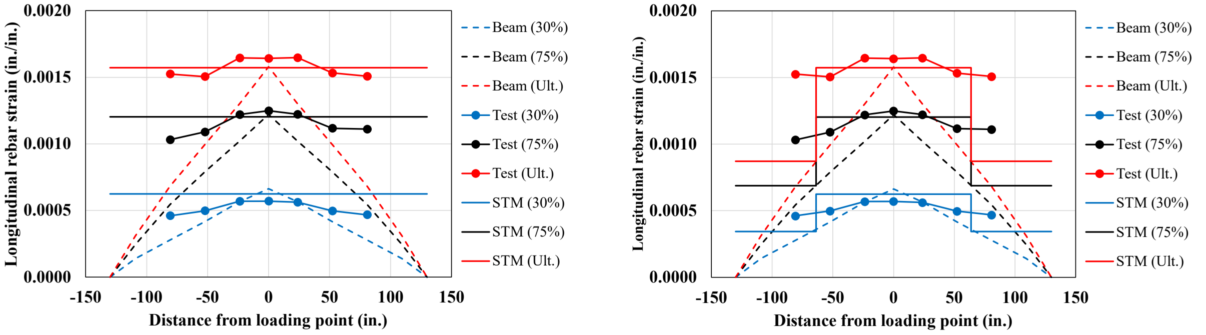

Single panel STM

Two panel STM

(e) R-L60-W100-75

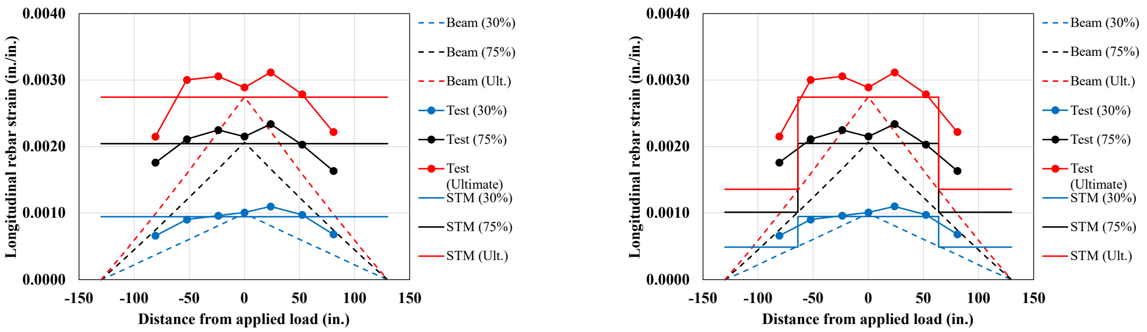

Single panel STM

Two panel STM

(f) R-L100-W100-75

Figure 3-73. Strain of longitudinal bars in rectangular deep beams

Inverted T Beam

Figure 3-74 and Figure 3-75 present the strain data for the reinforcement in the vertical ties, hangers, and ledges of inverted T beams, showing that all strain values are proportional to the applied load. The horizontal ties exhibited significantly lower strains compared to the vertical ties, with maximum readings below 0.003, indicating that the vertical ties played a crucial role in resisting transverse strains within the concrete strut, similar to what was observed in rectangular beams.

The strain behavior of the hanger and ledge reinforcement exhibited trends similar to that of the vertical tie, aligning with the observed crack patterns in the previous chapter. In general, all reinforcements exhibited an increase in strain as the load increased. The web reinforcement within the rectangular section showed higher strain levels in the 0.2% web reinforcement ratio than in the 0.3% ratio. Notably, a sharp strain increase exceeding the yield strain was observed in some vertical web reinforcements toward the end of the experiment. Additionally, in the ledge region, the ledge reinforcements experienced larger strains compared to the hangers due to their smaller diameter. These strains also increased sharply near the end of the experiment, with significant values exceeding the yield strain observed in some ledge reinforcements.

In the inverted T-beam, the load is applied directly to the tension chords, inducing flexural tension at the ledge. To prevent failure of the longitudinal reinforcement during the experimental program, strain gauges were strategically attached to the longitudinal reinforcement at various locations. The maximum strain in the reinforcement was closely monitored throughout the tests until the beam failed. As illustrated in Figure 3-76, high-strength longitudinal reinforcement exhibits larger strain values than normal-strength reinforcement due to the reduced reinforcement quantity. However, this strain increase aligns with the proportional reduction in reinforcement, confirming that high-strength rebar, even in reduced quantities, achieves a load-carrying capacity comparable to normal-strength rebar.

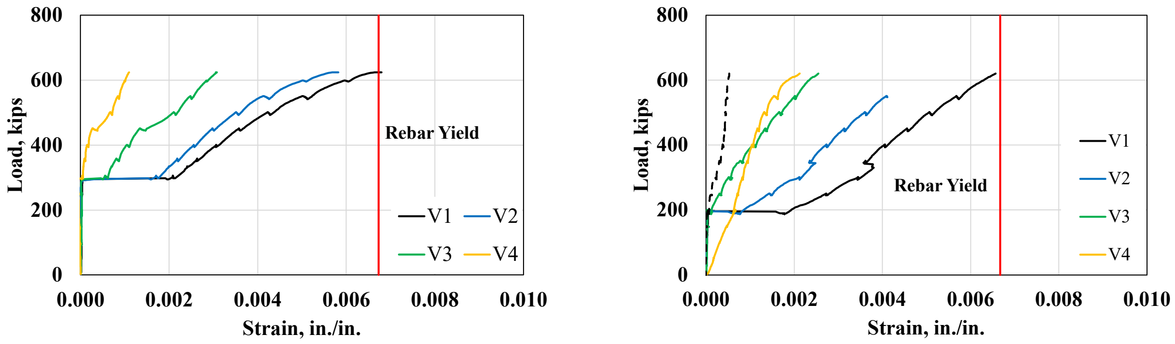

(a) IT-L60-W100-42-0.2

(b) IT-L60-W100-42-0.3

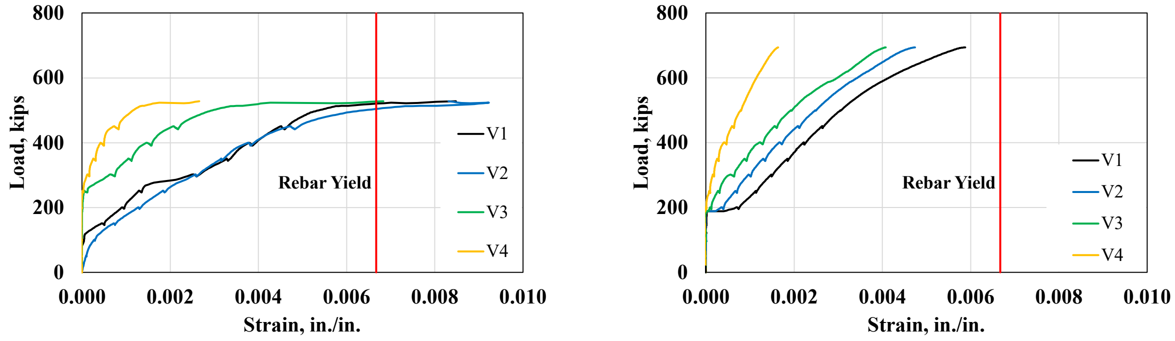

(c) IT-L100-W100-42-0.2

(d) IT-L100-W100-42-0.3

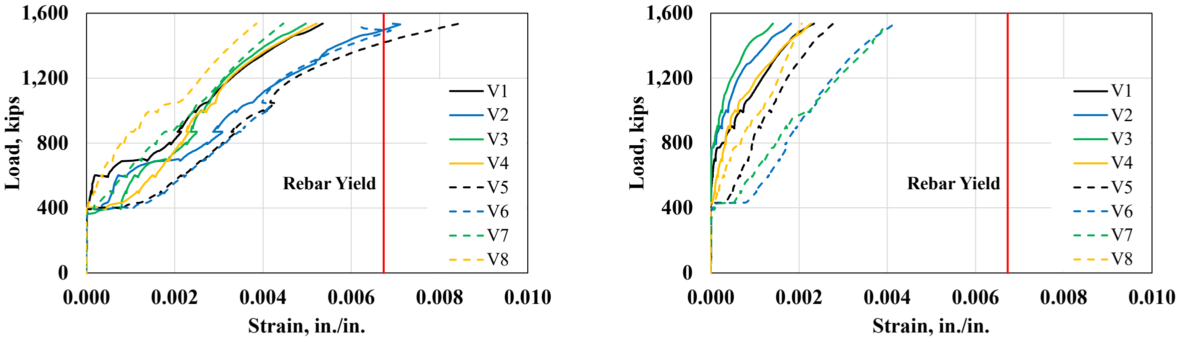

(e) IT-L60-W100-75-0.2

(f) IT-L60-W100-75-0.3

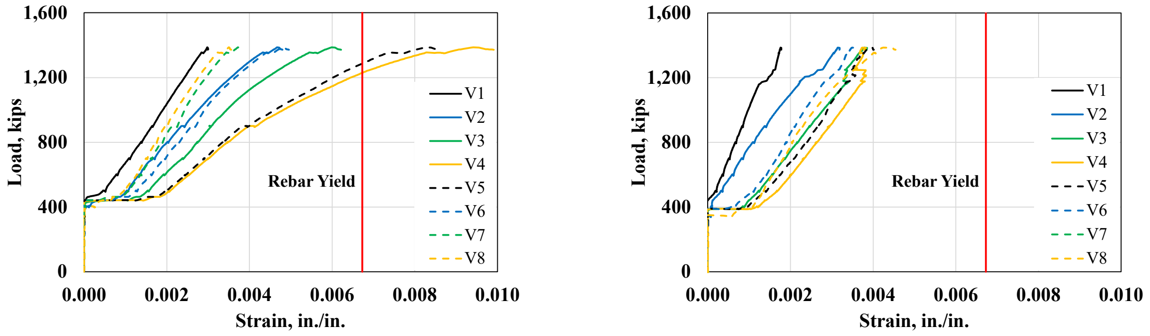

(g) IT-L100-W100-75-0.2

(h) IT-L100-W100-75-0.3

Figure 3-74. Strain of vertical ties in Inverted T beams

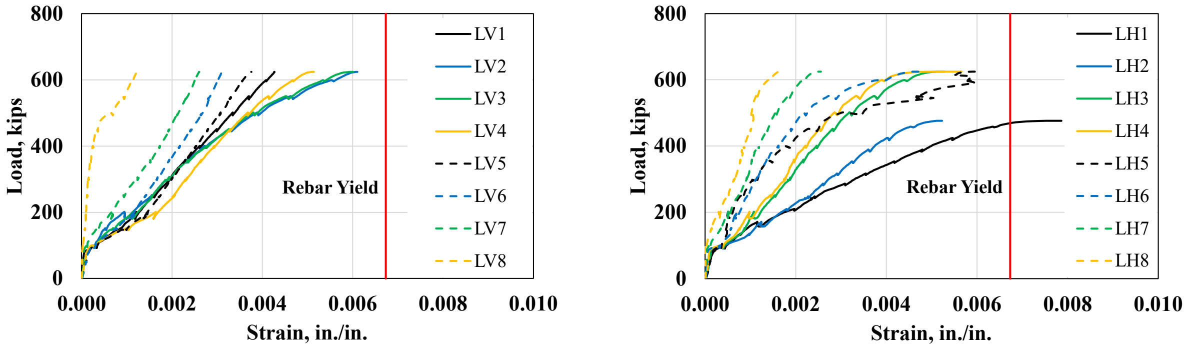

Hanger Ledge

(a) IT-L60-W100-42-0.2

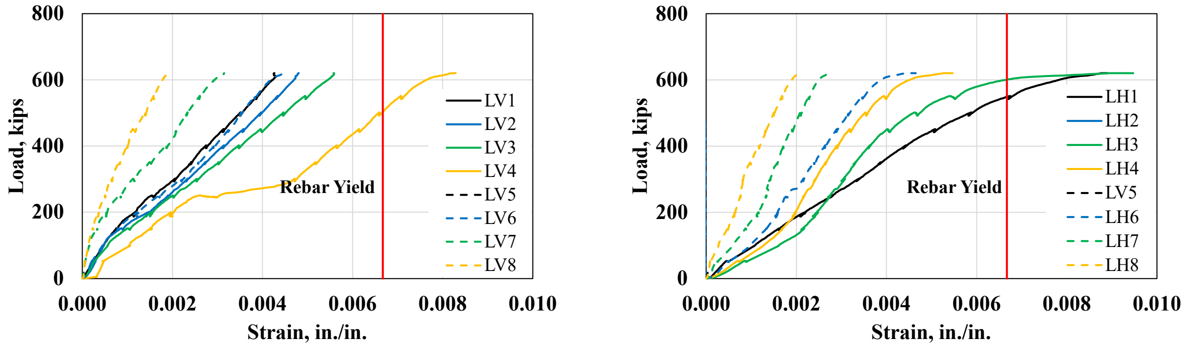

Hanger Ledge

(b) IT-L60-W100-42-0.3

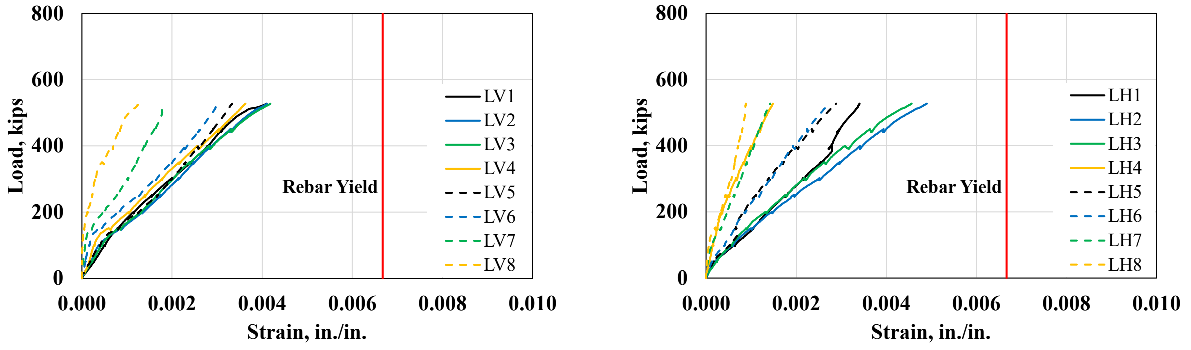

Hanger Ledge

(c) IT-L100-W100-42-0.2

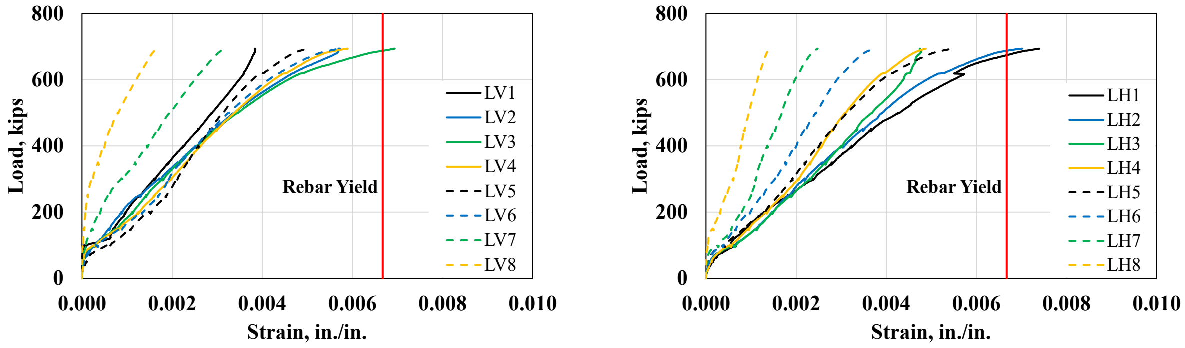

Hanger Ledge

(d) IT-L100-W100-42-0.3

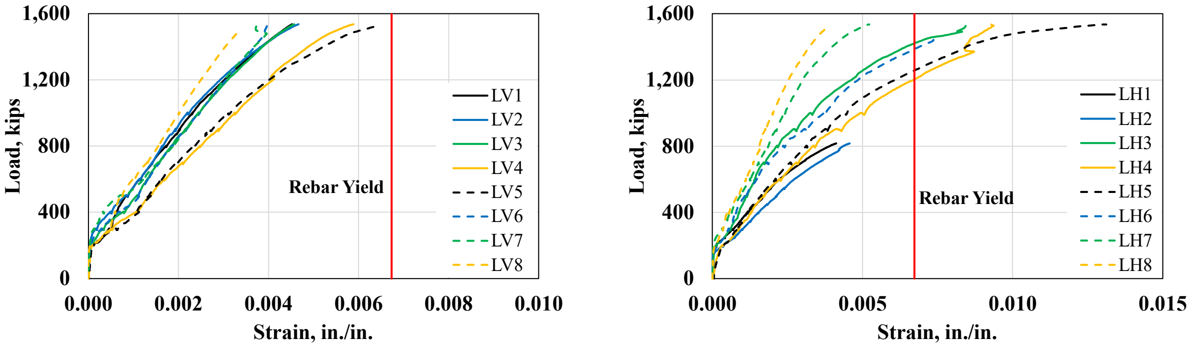

Hanger Ledge

(e) IT-L60-W100-75

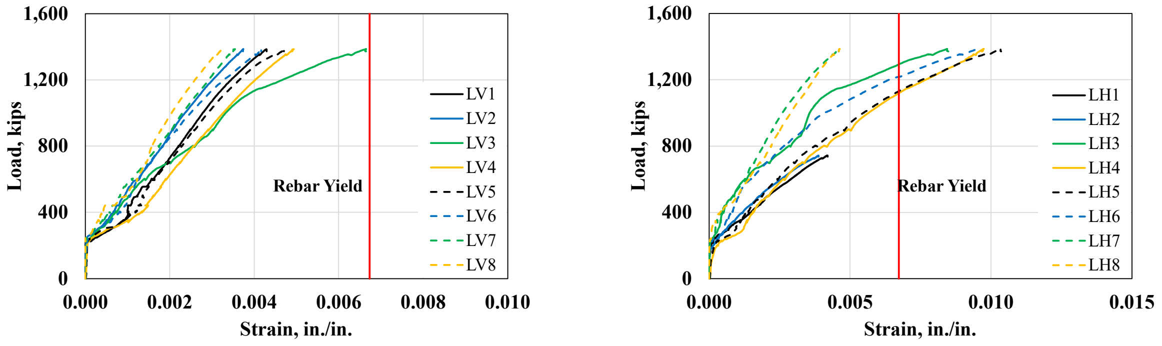

Hanger Ledge

(f) IT-L100-W100-75

Figure 3-75. Strain of rebar in ledge of Inverted T beams

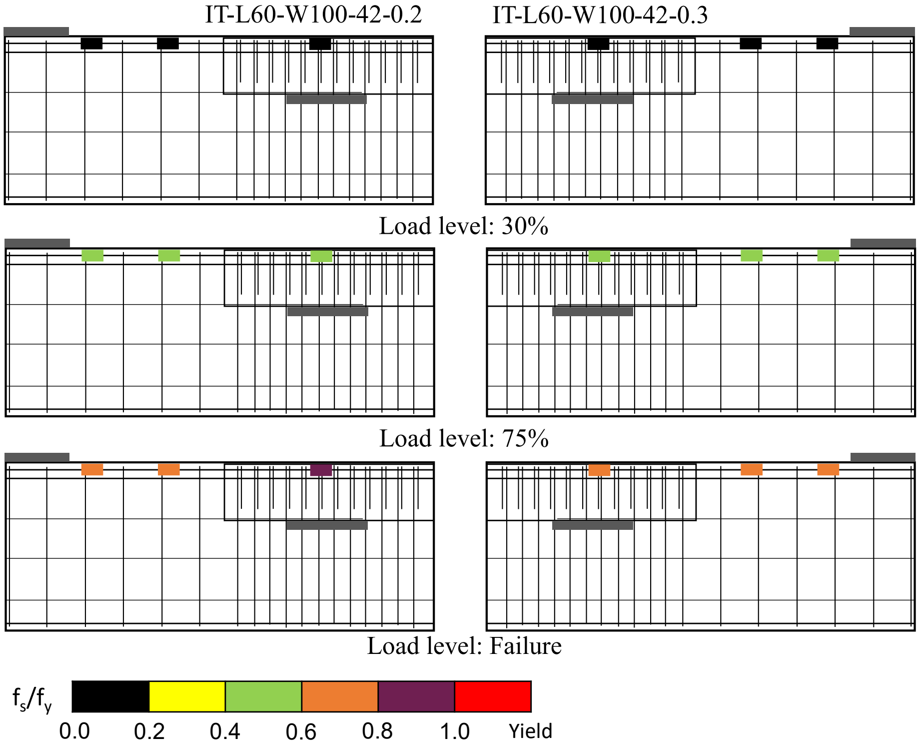

(a) IT-L60-W100-42

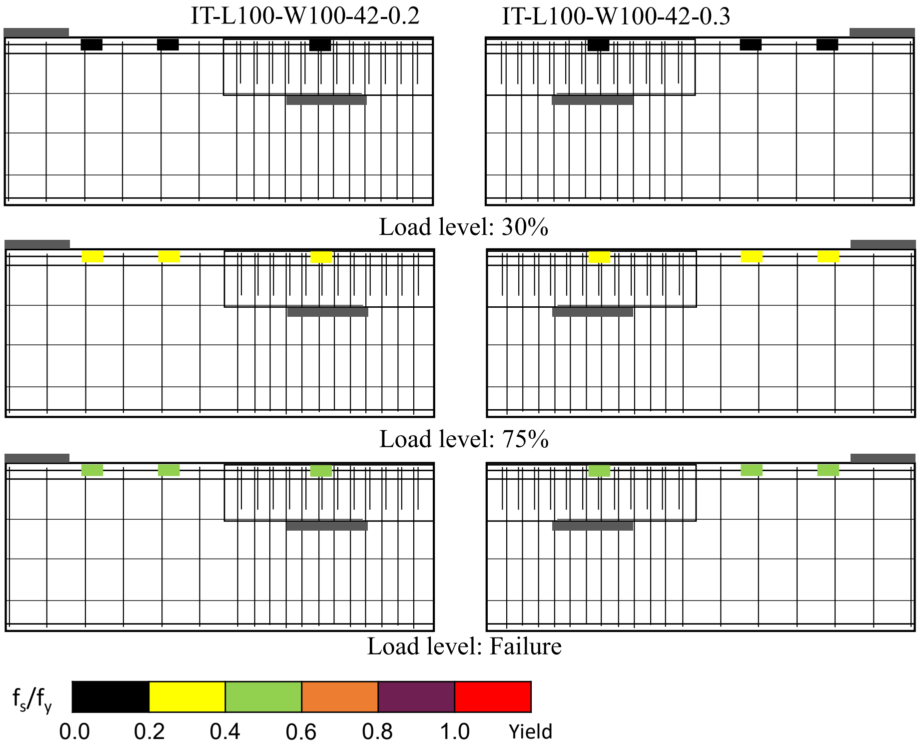

(b) IT-L100-W100-42

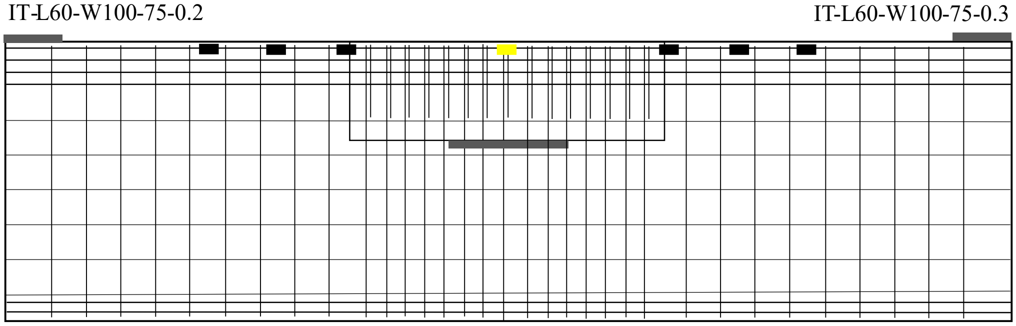

Load level: 30%

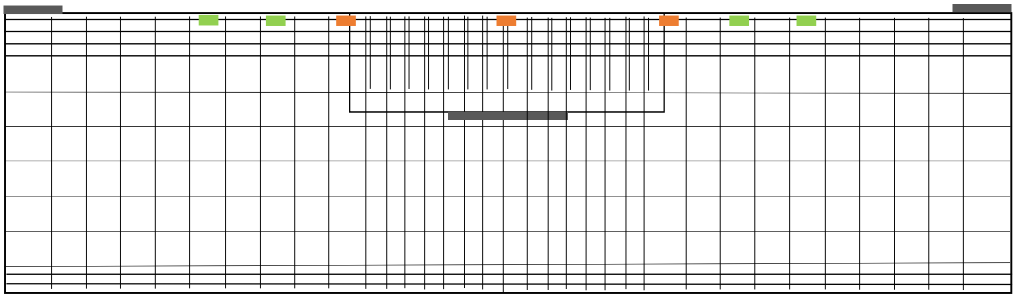

Load level: 75%

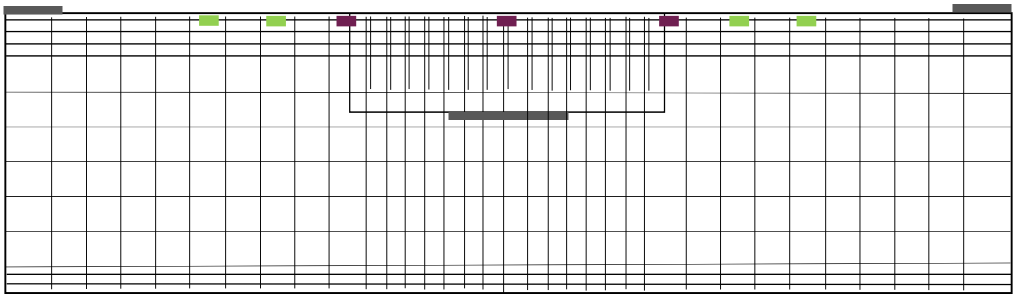

Load level: Failure

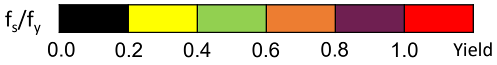

(c) IT-L60-W100-75

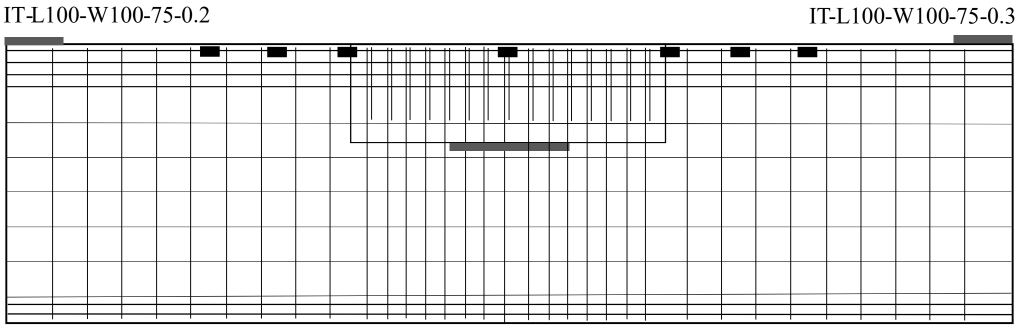

Load level: 30%

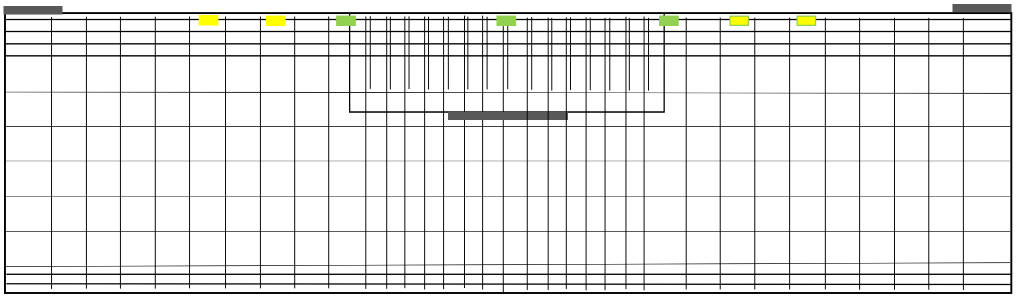

Load level: 75%

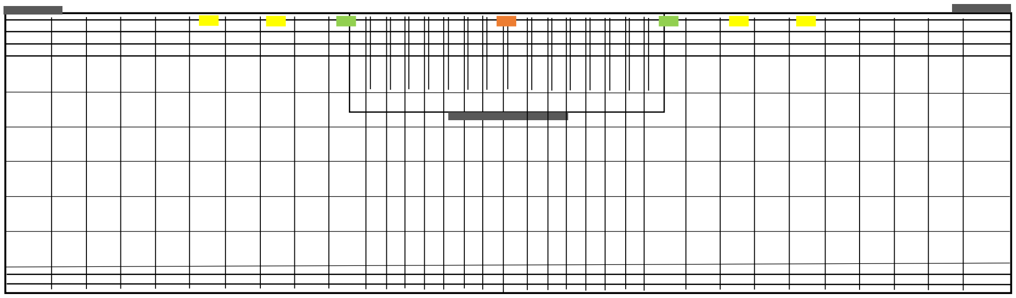

Load level: Failure

(d) IT-L100-W100-75

Figure 3-76. Strain of longitudinal bars in inverted T beams

3.2.1.5.5. Crack widths

Design codes such as ACI 318-19 and AASHTO LRFD (2020) suggest minimum requirements for web reinforcement in STM design to facilitate the redistribution of internal stresses and control crack width by limiting tensile stresses throughout the strut. The minimum requirement proposed by Birrcher et al. (2009), which is the basis the relevant provision of the AASHTO LRFD (2020), specifies that the minimum web reinforcement should be at least 0.003 times the effective area of the strut to ensure diagonal crack width within an acceptable range (less than 0.016 in) at the service level. However, the test data supporting these conclusions were used only normal-strength steel (Grade 60). Since both design codes restrict the strength of reinforcing steel used in STM-designed concrete members, it is important to validate the use of high-strength steel in STM from a serviceability perspective (crack width).

For evaluation of serviceability, the method proposed by previous study (Birrcher et al. 2009) was adopted. The service load was determined as Equation (3-10). The strength reduction factor for compression in strut-and-tie models is 0.70 in AASHTO LRFD (2020). The load factor is a function of the load case in AASHTO LRFD (2020). The Strength I load case was used, with the dead load (self-weight) and the live load (applied load) obtained from the test data. The nominal capacity was calculated using STM based on AASTHO LRFD (2020). Consequently, the service load was calculated to be ranged between 15% and 31% of the maximum applied load. The average service loads were 26%, 19%, and 26%, 17% for the 42-inch rectangular beam, 75-inch rectangular beam, and 42-inch inverted T beam and 75-inch inverted T beam, respectively.

$$\frac{\varphi}{\eta} \approx \frac{\text{Service load}}{\text{Nominal capacity}} \tag{3-10}$$

where,
φ means strength resistance factor; η is the load factor.

As mentioned above section, for 42-inch beams, crack width was obtained using DIC system. This method utilized a camera to monitor a pattern of random speckles on the beam's surface. By tracking the positions of these speckles, the distance between them was calculated through image processing. Subsequently, the crack width was determined by analyzing the changes in distance between speckles positioned on opposite sides of the cracks. For 75-inch beams, the DIC system was not feasible due to the large test area, which made it difficult to ensure high-quality images. Instead, a crack comparator card was used to measure the crack width.

Figure 3-77 shows the crack width corresponding to the applied load. In all cases, it was demonstrated that serviceability was satisfied. Notably, it was confirmed that the web reinforcement ratio of 0.2% or more, used in this study, effectively controlled the maximum crack width below the benchmark crack limit, ensuring serviceability.

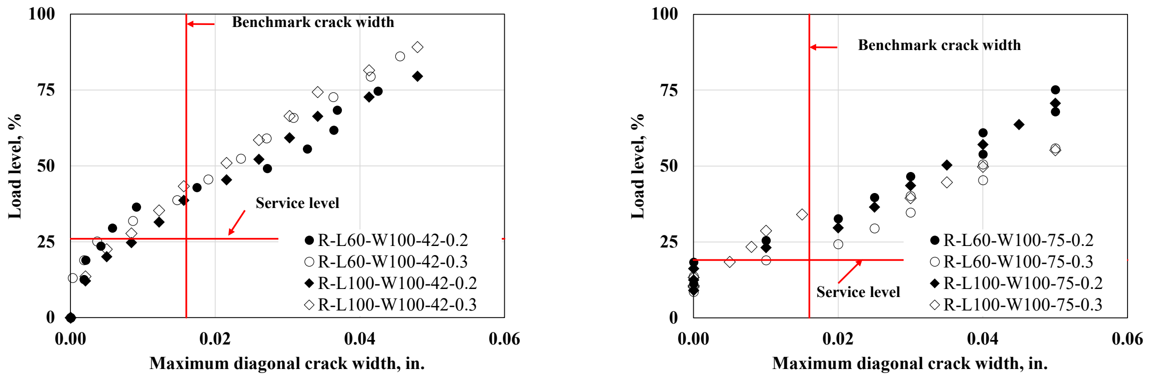

(a) 42-inch rectangular beam

(b) 75-inch rectangular beam

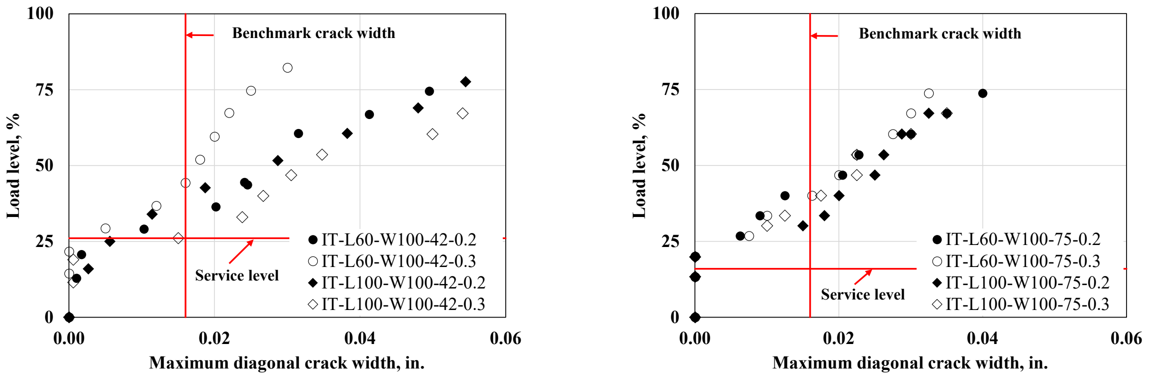

(c) 42-inch Inverted T beam (d) 75-inch Inverted T beam

Figure 3-77. Load-crack width relationship

3.2.1.6. Conclusions

This study conducted a well-organized experimental program involving rectangular and inverted T deep beams to evaluate the applicability of high-strength steel reinforcement. Observations and analyses derived from the test results validated the use of current design codes for high-strength reinforcement. The key conclusions are as follows:

- The strut-and-tie model provided reasonable estimates of the shear capacity for all tested deep beams, including rectangular and inverted T configurations.
- Replacing longitudinal reinforcement with high-strength steel allowed for a reduction in required reinforcement proportional to the strength ratio of high- to normal-strength steel, while maintaining the load-carrying capacity of the longitudinal reinforcement.
- The maximum crack width pattern remained consistent when the web reinforcement ratio exceeded 0.2%, with crack width control meeting benchmark limits at service levels. However, further research is needed to thoroughly assess whether high-strength rebar contributes to further crack width reduction.

3.2.2. Drilled Shaft Footing

3.2.2.1. Specimen Design

To compare the test results with a previously tested specimen (I-2; Yi et al., 2022), the research team designed two footing specimens having the same dimensions but different reinforcement layouts using 100-ksi high-strength reinforcing bars. Unlike specimen I-2, both footing specimens in this project were designed with 100-ksi side face reinforcement. The quantity of 100-ksi side face reinforcement was calculated to be equivalent to the conventional Grade 60 reinforcement used in specimen I-2. This equivalency was determined using an Equation (3-11), which is derived from the minimum shrinkage and temperature reinforcement requirements specified in AASHTO LRFD (2020), Article 10.5.6.

$$\frac{A_s}{s} \geq \rho_s \frac{A_g}{Perimeter} \frac{60}{f_y} \tag{3-11}$$

where,

ρ_s= side face reinforcement ratio in each direction (longitudinal or transverse)

A_g= gross area of the section where the face reinforcement is to be provided perpendicularly (in.^{2})

A_s= area of side face reinforcement in each direction (in.^{2})

$Perimeter$= perimeter of the section where the face reinforcement is to be provided perpendicularly (in.)

s = spacing of side face reinforcement in each direction (in.]

f_y= specified yield strength of reinforcement (ksi]

Shrinkage and temperature reinforcement is generally considered not to affect the load-carrying capacity of structural member. However, large-scale tests and numerical analyses on drilled shaft footings conducted by Yi et al. (2022) revealed that a minimum amount of shrinkage and temperature reinforcement (≥ 0.18%) can redistribute the internal direct strut force to adjacent side surfaces by controlling crack widths formed on the side surfaces of drilled shaft footings. Based on this observation, the minimum shrinkage and temperature reinforcement can be also considered as the minimum crack control reinforcement considered in the design procedure of the strut-and-tie method. Therefore, Yi et al. (2022) recommended providing at least a 0.18% side face reinforcement ratio on all side surfaces of the drilled shaft footing as crack control reinforcement to utilize the maximum nodal efficiency factors when computing nodal strengths.

The amount of side face reinforcement can be reduced by employing 100-ksi high strength reinforcement based on the aforementioned equation. Consequently, the size and spacing of the longitudinal and transverse side face reinforcing bars of the test specimens of this project were determined to have an average side face reinforcement ratio equivalent to that of I-2 (0.33%). The AASHTO LRFD limits the maximum spacing of the shrinkage and temperature reinforcement to 12 inches for footing components thicker than 18 inches (Article 10.5.6). On the other hand, the strut-and-tie method section of AASHTO LRFD limits the maximum crack control reinforcement spacing to the smaller of d/4 or 12 inches (Article 5.8.2.6), which results in approximately 6.65 inches for the effective depth (d = 26.59 inches) of the footing specimens in this project. This discrepancy creates ambiguity about which spacing limit should be followed when designing the skin reinforcement of drilled shaft footings using the strut-and-tie method. To address this issue, the longitudinal side face reinforcement for the project specimens was designed using the less conservative spacing limit of 12 inches. The vertical face reinforcement spacing was kept consistent with specimen I-2, at 6 inches, as determined by its bottom mat reinforcement layout.

For the bottom mat reinforcement of the footing specimens, the grid layout and 90-degree hooked anchorage were employed based on the design recommendations proposed by Yi et al. (2022). Two different reinforcement grades (Grade 60 and 100) of reinforcement were used in the footing specimens of this project to investigate the applicability of 100-ksi high-strength reinforcing bars to the bottom mat reinforcement in drilled shaft footings. The specimen designed with conventional grade bottom mat reinforcement mirrored the bottom mat reinforcement layout of I-2, except that is replaced bundled #8 bars (1.58 in.^{2}/bundle) with a series of single #11 bars (1.56 in.^{2}/bar). The specimen designed with 100-ksi high-strength bottom mat reinforcement had a reduced amount of the bottom mat reinforcement to provide the flexural strength equivalent to the other specimen and I-2.

The reinforcement details of the specimens, along with comparisons to I-2, are summarized in Table 3-13. The design concrete compressive strength is taken to be 3.6 ksi, which is the same as that of I-2. Figure 3-78 depicts the drawing of the reinforcing details of the test specimens.

Table 3-13. Test matrix for drilled shaft footing specimen

Specimen ID	Bottom mat reinforcement		Side face reinforcement		
	Grade	Details	Grade	Details	
				Longitudinal	Transverse
I-2	Gr.60	14-2x#8 at 6.0 in.	Gr.60	#3@3.0 in.	#6@6.0 in.
B60	Gr.60	14-#11 at 6.0 in.	Gr.100	#4@12.0 in.	#4@6.0 in.
B100	Gr.100	9-#11 at 6.0 in.	Gr.100	#4@12.0 in.	#4@6.0 in.

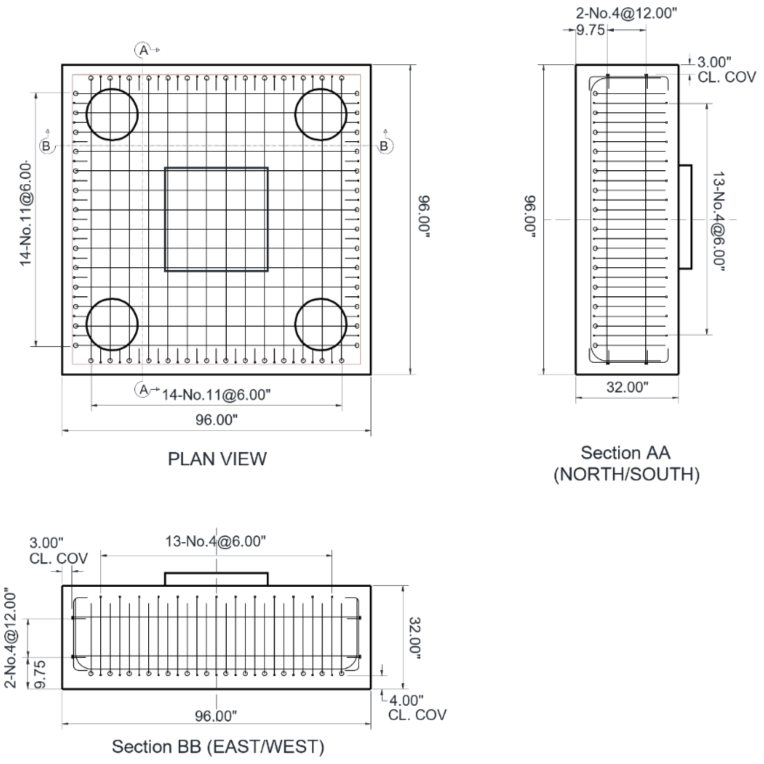

(a) B60

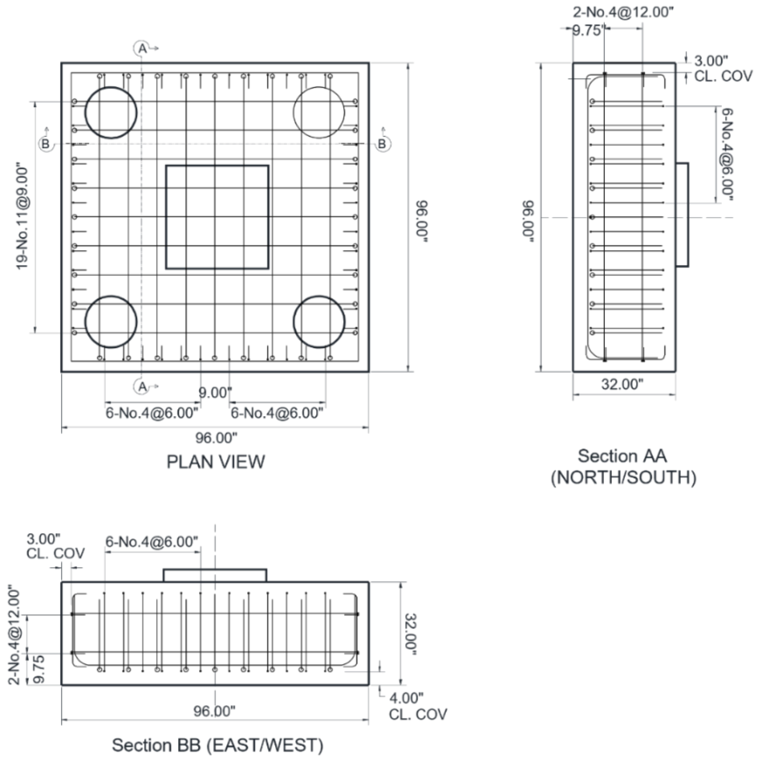

(b) B100

Figure 3-78. Drilled shaft footing specimen's configuration

3.2.2.2. Fabrication

The drilled shaft footing specimens were fabricated according to the sequence illustrated in Figure 3-79. The process began with the assembly of a steel soffit and its supporting frame. Subsequently, a series of strain gauges were installed on the reinforcing bars as planned. The reinforcing bar cages were then assembled on the steel soffit, and the entire steel formwork, which allowed for the simultaneous casting of two drilled shaft footing specimens, was assembled. Concrete was placed in the formwork using external pneumatic and portable vibrators to ensure proper consolidation. After casting, the specimens were cured by covering the formwork with plastic sheeting.

The 4-in. high column stub on the footing specimen was fabricated using high-strength grouting mortar. Before casting the mortar, the casting surface area for the column stub was roughened with an electric hammer drill to prevent any slippage at the interface. A steel jacket made of ¼-inch thick plates was placed at the designated position, and the gap between the surface and the jacket was filled with spray foam. The mortar was then placed inside the jacket and cured along with the footing component until the test day. The mortar was placed in a steel jacket welded to ensure planned dimension of the columns stub.

(a) Steel formwork and supporting frame

(b) Installation of strain gauges

(c) Reinforcing bar cage assembly

(d) Concrete casting

(e) Column stub casting

Figure 3-79. Fabrication of drilled shaft footing specimens

3.2.2.3. Test setup

3.2.2.3.1. Loading Frame

The test setup designed and fabricated by Yi et al. (2022) was also utilized for the footing specimens in this project. The details of the test setup are presented in Figure 3-80.

Figure 3-80. Test setup for drilled shaft footing specimens

Two 2,000-kip hydraulic loading rams were used to apply loading to the specimen, and the specimen was supported by four supporting fixtures simulating drilled shafts. All fixtures had a 16-in. diameter steel plate at its topmost layer, but each was designed with different lateral restraints. One fixture allowed only rotation (pin support), while two adjacent fixtures permitted both rotation and one-way lateral translation (pin-one-way roller support). The fixture located opposite the pin support allowed both rotation and two-way lateral translations. These varied restraints enabled the footing to expand laterally under the given loading condition.

3.2.2.3.2. Instrumentation

The structural behavior of the test specimens was monitored by various types of instrumentations. The instrumentation maps of the footing specimens are illustrated in Figure 3-81.

Three 500-kip load cells were installed at the base of each support fixture to monitor the reaction at each support and overall applied loading during structural testing. Furthermore, a series of linear potentiometers were placed on the bottom surface of the footing to measure the vertical deflection of the test specimens. The vertical deflections were measured at the loading point and at the vicinity of supports. Reinforcing bar strains were measured using strain gauges attached on the selected bottom mat and side face reinforcement.

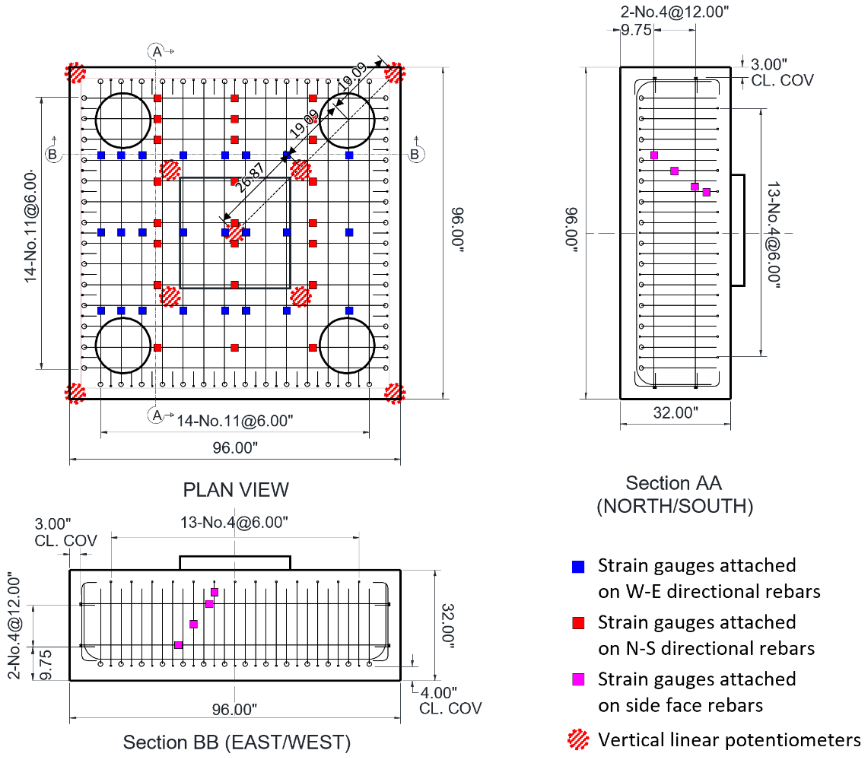

(a) B60

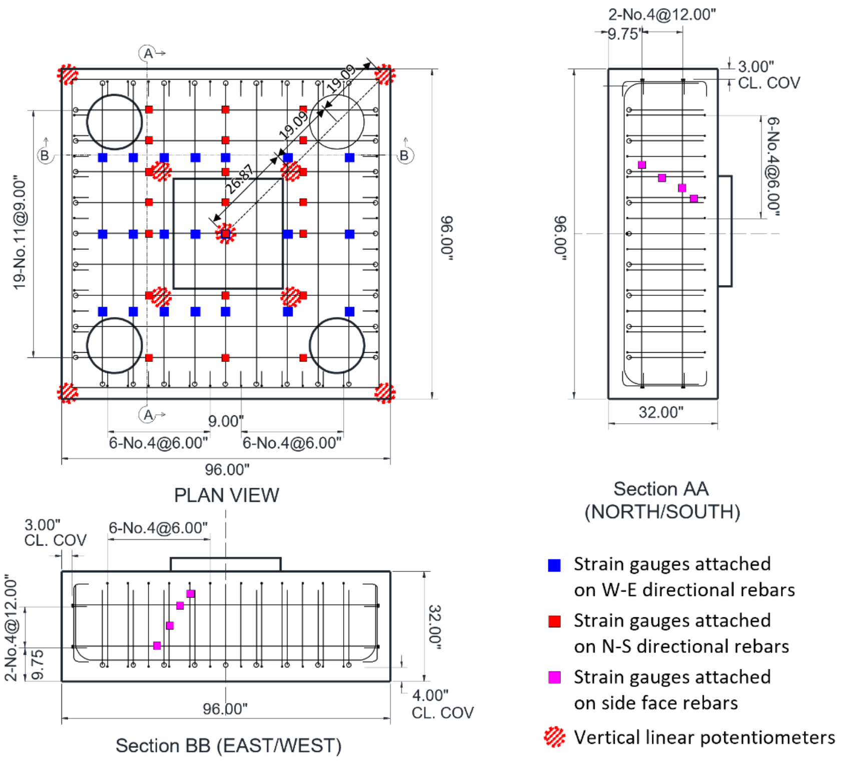

(b) B100

Figure 3-81. Instrumentation maps of drilled shaft footing specimens

3.2.2.3.3. Test Procedure

The loading process was carried out in incremental stages, with each increment representing a load increase significantly less than one-tenth of the estimated nominal capacity determined from preliminary finite element analyses. Specifically, increments of 200 kips were applied, ensuring a monotonically increasing, quasi-static loading at each stage. At predefined load levels, the specimens were visually inspected and their condition was documented through crack mapping and digital photography. This inspection process continued until a significant shear crack, extending down to the support, was identified. After identifying this critical crack, the specimen was continuously loaded until failure.

3.2.2.4. Experimental Results and Discussion

3.2.2.4.1. Overview

This chapter provides a comprehensive analysis of the specimens' behavior during testing, along with the experimental results. Key elements discussed include crack patterns, load-displacement responses, and stress distributions in the bottom mat reinforcing bars. The material properties of the reinforcement and concrete used in drilled shaft footing specimens are summarized in Table 3-14 and Figure 3-82.

Table 3-14. Reinforcing steel and concrete properties (Drilled shaft footing)

Specimen ID	Concrete	Reinforcement		
	Compressive strength (ksi)	Detail	Yield strength (ksi)	Tensile strength (ksi)
B60	6.40	Bottom mat Grade 60 (No.11)	64.9	100.4
		Side surface Grade 100 (No.4)	136.9	173.5
B100	5.76	Bottom mat Grade 100 (No.11)	113.3	125.9
		Side surface Grade 100 (No.4)	136.9	173.5

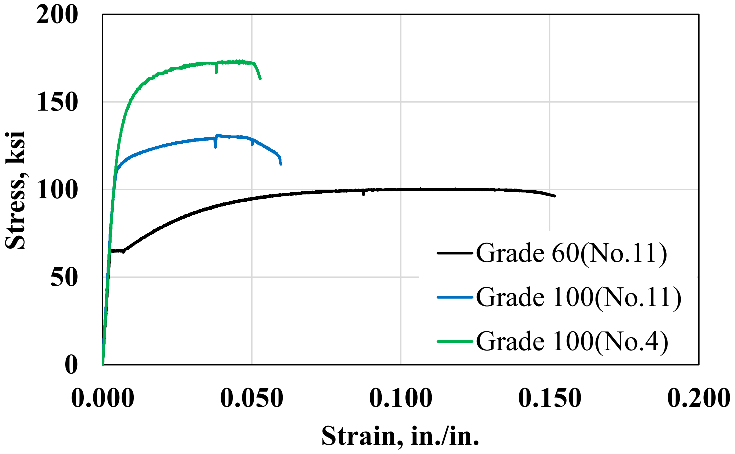

Figure 3-82. Rebar coupon test results (Drilled shaft footing)

3.2.2.4.2. Crack pattern

The crack patterns observed during the tests were comparable each other. Initially, flexural cracks were identified at the lower central region of the side surfaces and propagated approximately halfway up the height of the footing as the applied load increased. Subsequently, a series of arch-shaped cracks formed on the side surfaces between two adjacent supports. As these arch-shaped cracks extended down to the interior face of the supports, their widths gradually increased, ultimately leading to the failure of the test specimens. The post-failure conditions of the test specimens are presented in Figure 3-83.

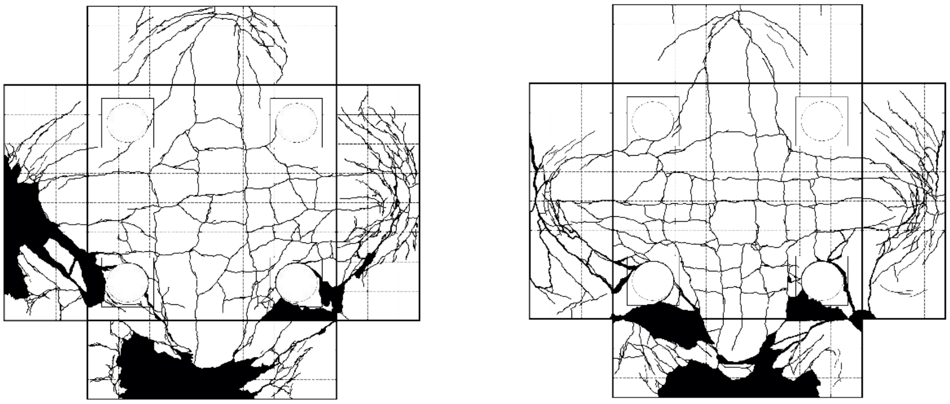

(a) B60 (b) B100

Figure 3-83. Post-failure cracking maps of drilled shaft footing specimens

The specimens failed in a brittle manner, with concrete spalling from the side surfaces along the arch-shaped cracks. Additionally, the widened widths of the arch-shaped cracks could be also identified after the failure. As shown in Figure 3-84, deformed longitudinal side face reinforcement was visible from the exposed surface due to the concrete spalling. It indicates that the amount of the crack control reinforcement amount per spacing (A_s/s) was insufficient to control the cracks formed on the side surfaces, which is necessary to redistribute the strut forces effectively.

(a) B60 (b) B100

Figure 3-84. Deformed side face reinforcement after failure

3.2.2.4.3. Load-Displacement Behavior

The load-deflection responses of the two footing specimens are illustrated in Figure 3-85, where the deflection refers to the adjusted central deflection of the footing, calculated by subtracting the average deflection at the supports from the deflection at the loading point. The load-carrying capacity of specimen B60 was higher than that of B100, which can be attributed to the relatively higher compressive strength of the concrete in B60 compared to B100. Consequently, B60 remained uncracked under relatively higher loads than B100. Despite this, the initial and post-cracking stiffness of the two specimens were comparable.

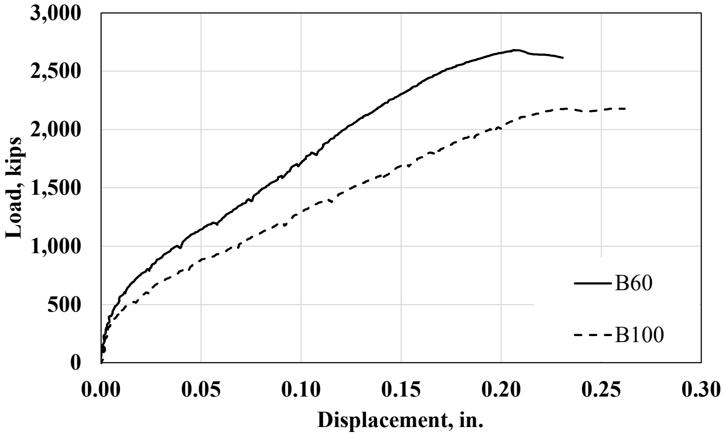

Figure 3-85. Load-deflection curves of drilled shaft footing specimens

3.2.2.4.4. Rebar Strains

The strain gauges installed on the reinforcing bars allowed for the measurement of bar strains during the tests. The research team converted these bar strains into bar stresses using the stress-strain curves of the reinforcement shown in Figure 3-82. To assess the impact of different reinforcement grades in the bottom mat reinforcement, the bar stress distributions of B60 and B100 at the ultimate load level of B100 (2180 kips) were compared, as shown in Figure 3-86.The bar stresses were expressed as percentages of the bar yield strengths.

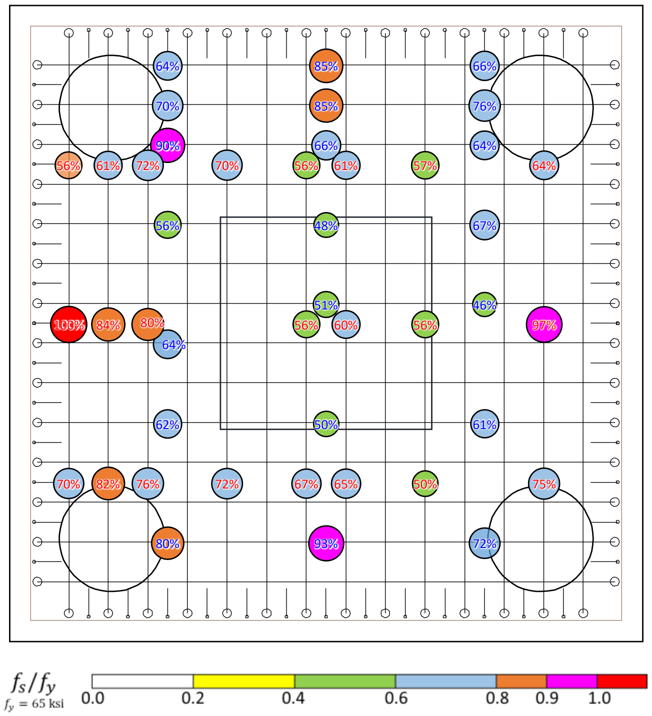

(a) B60

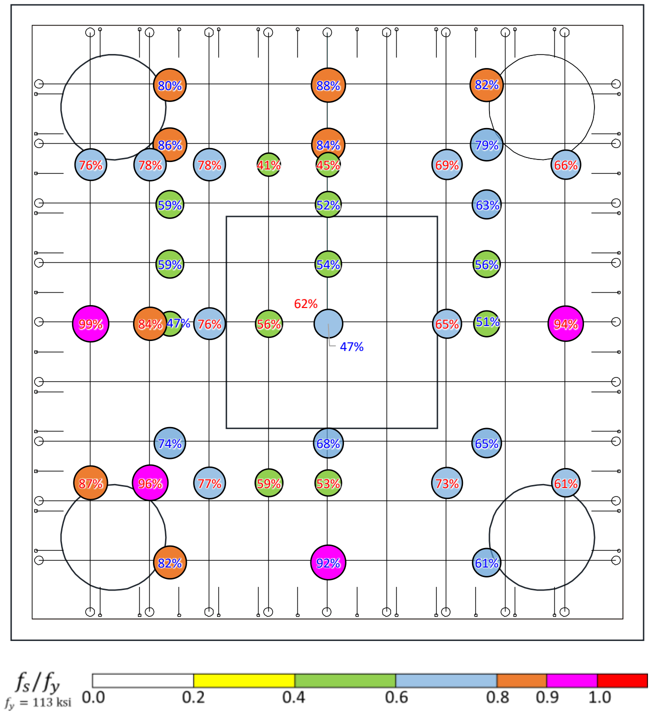

(b) B100

Figure 3-86. Bottom mat reinforcing bar stress distributions of drilled shaft footing specimens at 2179-kip loading

The overall bar stress percentage distributions in B60 and B100 were comparable, regardless of the strain measurement locations. This suggests that the tensile force-resisting mechanism observed in the footing with Grade 60 bars was similarly developed in the footing with Grade 100 bars. The bar stress percentage distributions of the side face reinforcement were also compared, as shown in Figure 3-87. Due to the severe damage observed on the side surfaces of both specimens at failure, the bar stresses at their respective ultimate loads were compared.

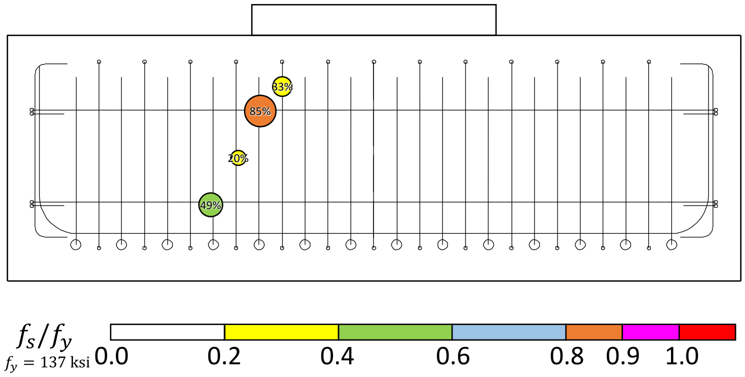

(a) B60

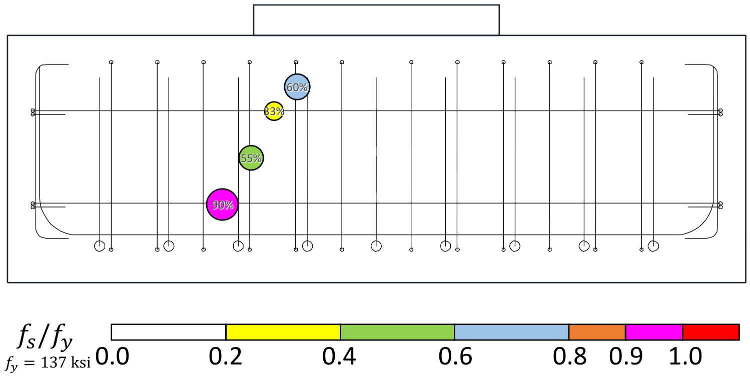

(b) B100

Figure 3-87. Side face reinforcing bar stress distributions of drilled shaft footing specimens at respective ultimate loads

The horizontal side face reinforcing bars experienced high-stress levels in both specimens at ultimate loads, which is consistent with the visual observation of significantly deformed longitudinal side reinforcement post-failure. Additionally, it was observed that the vertical side face reinforcing bars in B100 experienced relatively higher stresses compared to those in B60. It should be noted that the ultimate load of B60 was higher than that of B100 due to its higher concrete compressive strength. Nevertheless, at the ultimate load for both specimens, most of the Grade 60 and Grade 100 bars at the supports had yielded. Given that Grade 100 bars require larger strains to yield compared to Grade 60 bars, it is presumed that the vertical side reinforcing bars in B100 underwent relatively larger strains to satisfy the compatibility condition for the larger strains occurring in the bottom reinforcing bars on the supports.

3.2.2.4.5 Conclusions

This study carried out meticulously designed experiments to assess the applicability of high-strength steel reinforcement in drilled shaft footings. The observations and analyses derived from the test results validate the applicability of current design codes for high-strength reinforcement. The key conclusions are summarized as follows:

- High-strength steel for bottom mat reinforcement in drilled shaft footings maintains similar stress flow and load capacity, even with a reduced quantity. This suggests that the current design code is valid for designing bottom mat reinforcement with high-strength steel.

- The quantity of side surface reinforcement should not be reduced when using high-strength steel. Reducing side surface reinforcement increases strains and poor strain redistribution, resulting in early failure. Therefore, the current minimum reinforcement requirements should be maintained, even with high-strength steel used for side surface reinforcement.

3.3. Supplementary Topics

3.3.1. Tension Lap Splice

3.3.1.1. Specimen Design

Four beam splice tests were conducted to supplement the limitations identified in the previous chapter on tension lap splice with high-strength steel. Addressing the limitations, No.11 large-diameter high-strength reinforcing bar was used, with lap splice presence and rebar grade as test variables. The test matrix is shown in Table 3-15. Specimen ID indicates lap splice presence and rebar grade in sequence. Specimens labeled "LO" include a lap splice, while those labeled "LX" have continuous longitudinal rebars without a lap splice. The number following the ID represents the rebar grade of the longitudinal reinforcement.

Table 3-15. Test matrix of beam splice specimen

Specimen ID	Dimension (in.)	Longitudinal reinforcement		Lap splice presence
		Bar size	Grade	
LX60	21×36	No.11	A615-Grade 60	X
LO60				O
LX100			A615-Grade 100	X
LO100				O

The beam dimensions were selected with reference to the tension lap splice database and the configuration including rebar layout is presented in Figure 3-88 and Figure 3-89. In the lap splice region, transverse reinforcement was placed to optimize confinement in accordance with ACI 318-19 and AASHTO LRFD (2020). All beams were designed to experience flexural failure before splitting failure in the splice region. To ensure the flexural failure mode, transverse reinforcement was placed along the shear spans, located between the loading points and supports, ensuring a shear-to-flexural capacity ratio of at least 2.0. The concrete mix was designed for a target 28-day strength of 5,000 psi. For each test, compressive strength, splitting tensile strength, and modulus of elasticity were measured through cylinder tests according to ASTM C39, C496, and C469 standards, respectively. Reinforcing bar properties were obtained from rebar coupon tests following ASTM A370. All material properties were averaged from three samples (Refer to Figure 3-3).

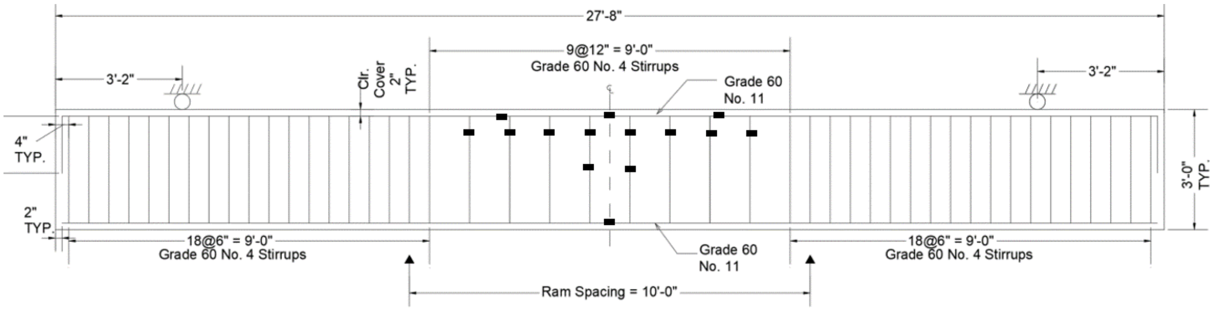

(a) LX60

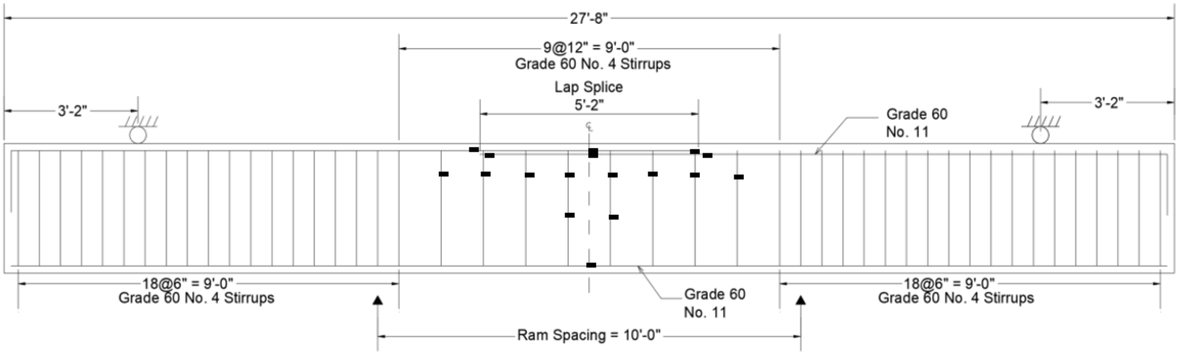

(b) LO60

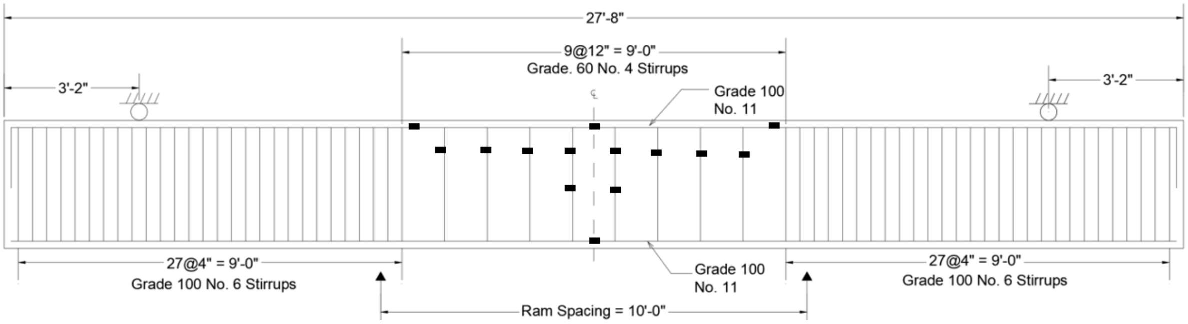

(c) LX100

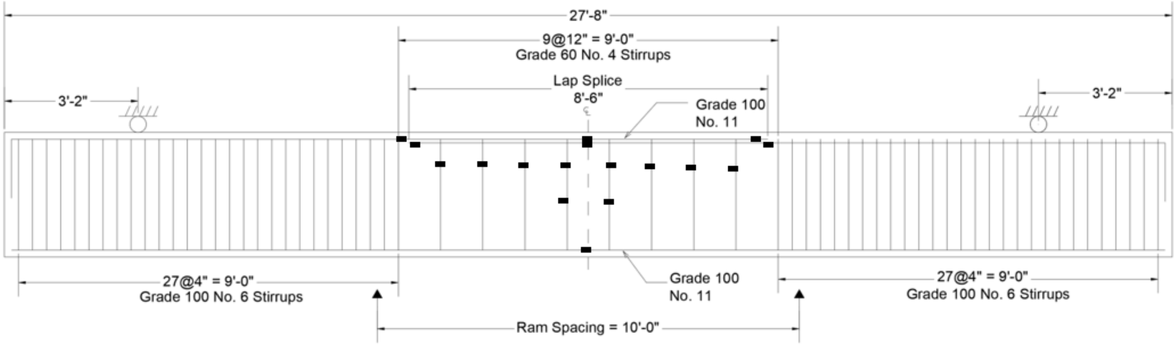

(d) LO100

Figure 3-88. Beam specimen configuration

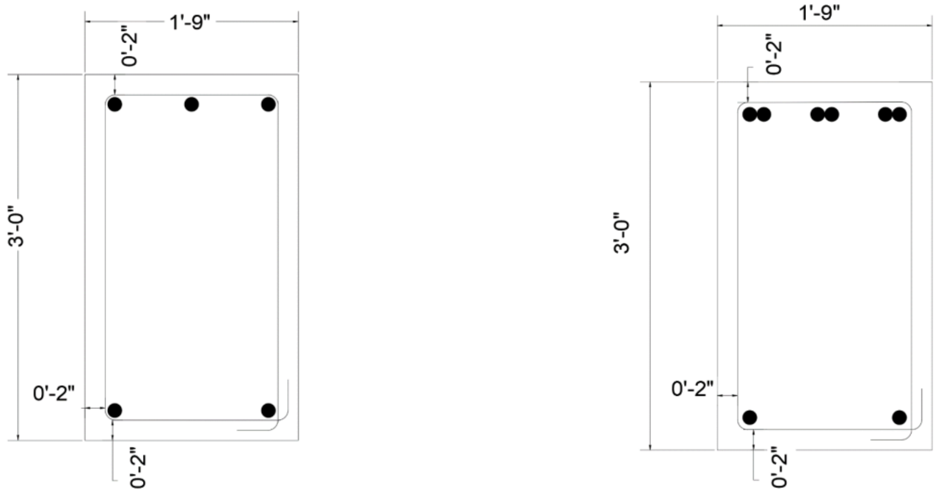

(a) LX60 and LX100 (b) LO60 and LO100

Figure 3-89. Beam cross section at splice region

3.3.1.1.1. Lap Splice Length

The lap splice length was determined based on the calculated lap splice length suggested by ACI 318-19, AASHTO LRFD (2020), ACI 408R-03, and Zaborac and Bayrak (2022). The lap splice length calculations followed the equations provided in these codes and guidelines.

$$l_{st} = 1.3 l_d \tag{3-12}$$

$$l_{d,ACI318} = \frac{3}{40}\frac{f_y}{\lambda\sqrt{f_c'}}\frac{\psi_t\psi_e\psi_s\psi_g}{\left(\frac{c_{b318}+K_{tr318}}{d_b}\right)}d_b \quad \text{Units: psi and in.} \tag{3-13}$$

$$l_{d,AASHTO} = 2.4 d_b \frac{f_y}{\sqrt{f_c'}}\left(\frac{\lambda_{rl}\lambda_{cf}\lambda_{rc}\lambda_{er}}{\lambda}\right) \quad \text{Units: ksi and in.} \tag{3-14}$$

$$l_{d,ACI408} = \frac{\left(\frac{f_y}{f_c'^{1/4}} - 2400\omega\right)\alpha\beta\lambda_{408}}{\varphi 76.3\left(\frac{c\omega+K_{tr408}}{d_b}\right)}d_b \quad \text{Units: psi and in.} \tag{3-15}$$

$$l_{d,Zaborac} = \left(\left(0.17\left(\frac{\lambda_{er}f_y-\frac{F_h}{A_b}}{350\lambda\sqrt[4]{f_c'}}\right)^2\right)\lambda_{rl}\lambda_{cf}\lambda_{rc}\right)d_b \geq 0.25\left(\frac{f_y-\frac{F_h}{A_b}}{18\sqrt{f_c'}}\right)d_b \quad \text{Units: psi and in.} \tag{3-16}$$

where,
l_{st}=tension lap splice length; l_d is the development length in tension
f_y=specified yield strength of reinforcement
f_c'=compressive strength of concrete
$\omega = 0.1\frac{c_{max}}{c_{min}} + 0.9 \leq 1.25$
c_{max}=maximum of c_b
c_s; c_b=bottom concrete clear cover to the bar being developed or spliced

c_s=minimum of c_{so} and $c_{si} + 0.25\ in.$
c_{so}=side concrete clear cover for reinforcing bar
c_{si}=1/2 of the bar clear spacing
c_{min}=minimum of c_{so}, c_b, $c_{si} + \frac{d_b}{2}$
α=reinforcement location factor
β=reinforcement coating factor
λ_{408}=lightweight aggregate concrete factor
φ=capacity reduction factor
c=spacing or cover dimension $\left(c_{min} + \frac{d_b}{2}\right)$
K_{tr408}=transverse reinforcement index $\left(= \frac{0.52 t_r t_d A_{tr}}{s_{tr} n} \sqrt{f_c'}\right)$
s_{tr}=center-to-center spacing of transverse reinforcement
n=number of bars or wires developed along plane of splitting
t_d=term representing the effect of bar size$(= 0.78 d_b + 0.22)$
t_r=term representing the effect of relative rib area$(= 9.6 R_r + 0.28)$
d_b=diameter of reinforcement
R_r=relative rib area of the reinforcement
λ=concrete density modification factor
ψ_t=modification factor for casting position
ψ_e=modification factor for coating of reinforcement
ψ_s=modification factor for size of reinforcement
ψ_g=modification factor for reinforcement grade
c_{b318}=factor that represents the least of the side cover
K_{tr318}=transverse reinforcement index $\left(= \frac{40 A_{tr}}{s_{tr} n}\right)$
λ_{rl}=reinforcement location factor
λ_{cf}=coating factor of reinforcement
λ_{rc}=reinforcement confinement factor
λ_{er}=excess reinforcement factor
F_h=force developed through other measures
A_b=reinforcing bar area

3.3.1.2. Fabrication

The fabrication process, including rebar cage assembly and concrete casting, is illustrated in Figure 3-90.The rebar cage was assembled following the reinforcement details illustrated in Figure 3-88. Strain gauges with a 5 mm gauge length were attached to the reinforcing bars. The installation locations on the bars were ground to make flat surface. After installation, the gauges were protected with waterproof material and epoxy, applied according to manufacturer guidelines to prevent damage from physical impact. Steel formwork, consisting of a bottom piece and four side panels, was used for concrete casting. The bottom form was first positioned on wood cribbing to raise the soffit to the required elevation. The formwork walls were then placed, and the rebar cage was positioned within the form. Front and back side panels were attached, completing the assembly. Plastic spacers were secured to the transverse reinforcement to maintain proper clear cover between the rebar cage and form sides. Concrete casting was subsequently carried out, and each specimen was cured by covering it with a tarp.

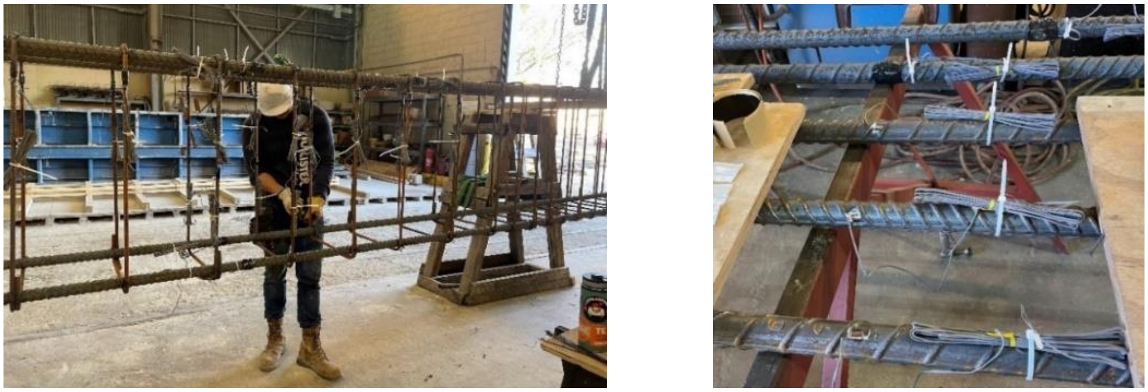

(a) Tying rebar cage (b) Attachment of strain gauge

(c) Wood cribbing, soffit, and formwork (d) Rebar cage in formwork

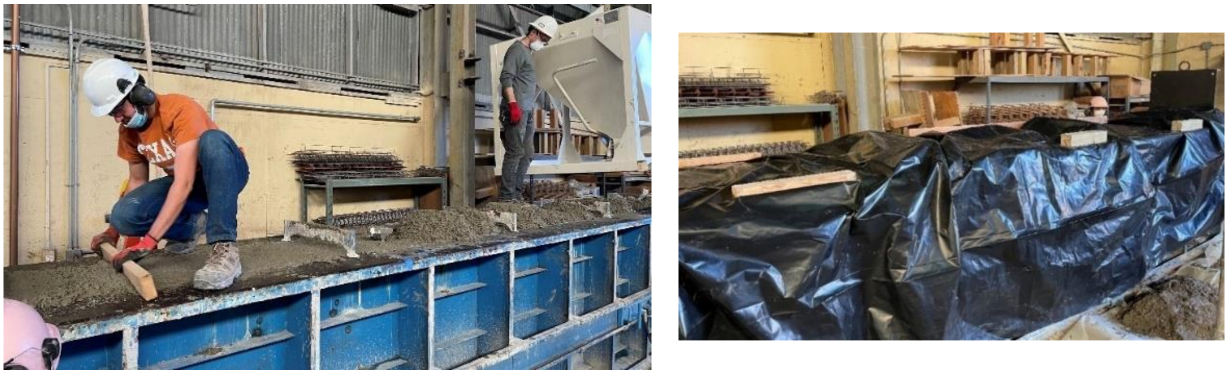

(e) Concrete casting (f) Cure of concrete after casting

Figure 3-90. Fabrication process of beam specimen for splice test

3.3.1.3. Test Setup

3.3.1.3.1. Loading Frame

Figure 3-91 depicts a schematic of test setup and a picture of a beam in the test frame, illustrating the inverted four-point bending test configuration. This setup included two hydraulic rams located beneath the beam. Two crossbeams, two roller supports and 12 threaded rods established the support conditions. Twelve 500-kip load cells were placed above the crossbeams to measure the reaction force during the tests. Each ram was equipped with a tilt saddle and steel plates to accommodate loading eccentricities and ensure even load distribution.

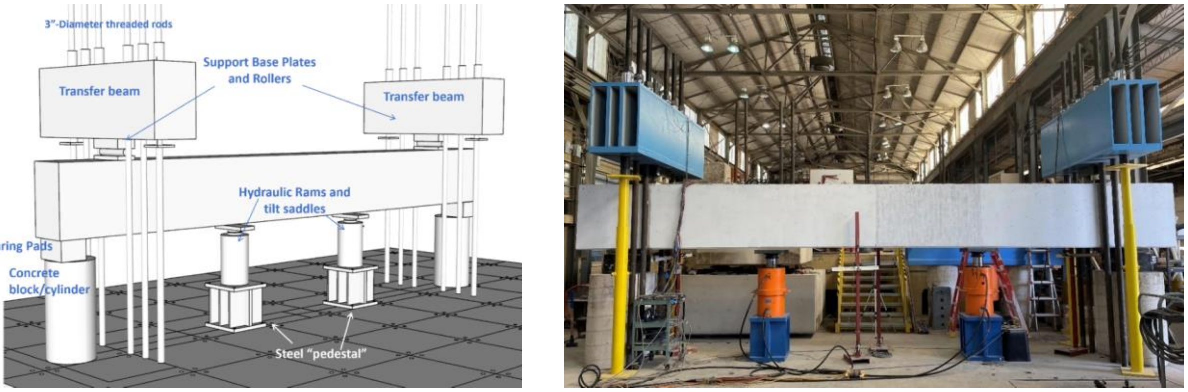

(a) Test setup schematic (b) Beam specimen in test frame

Figure 3-91. Beam splice testing setup

3.3.1.3.2. Instrumentation

Beam specimens were extensively instrumented to measure reactions, displacement of beam, rebar strain and crack widths during the testing.

- Load and displacement measurements

The load for each test was measured using twelve 500-kip capacity load cells, as described in the previous chapter (Refer to Figure 3-91). Linear potentiometers were placed under the beam at the support points and the midpoint, as shown in Figure 3-92. Two potentiometers on either side of the midpoint were measured, and their averaged value was used. The displacement at the support locations were specifically used to eliminate the displacement due to the rigid body motion of the beam from the midpoint displacement measurements, ensuring accurate assessment of beam deflection.

(a) Installation at support position (b) Installation at midpoint

Figure 3-92. Linear potentiometers to measure displacements of beam

- Strain measurements for reinforcing bars

Strain gauges with a 5 mm gauge length were affixed to the reinforcing bars to measure bar strains, which were then converted to stresses using the strain-stress relationship obtained from material testing. In non-spliced beams (LX60 and LX100), strain gauges were installed at the center of the longitudinal bars, aligning with the splice ends of the spliced beams (LO60 and LO100). In the spliced beams, different numbers of strain gauges were attached to each bar to verify the effect of gauge's number on strain measurement as shown in Figure 3-93. Strain readings at the end of splice were cross-checked to confirm that gauge configuration did not interfere with bond between rebar and surrounding concrete.

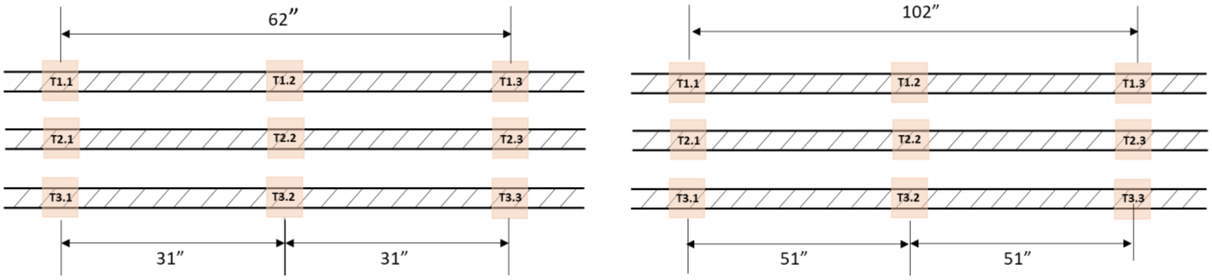

(a) LX60 (b) LX100

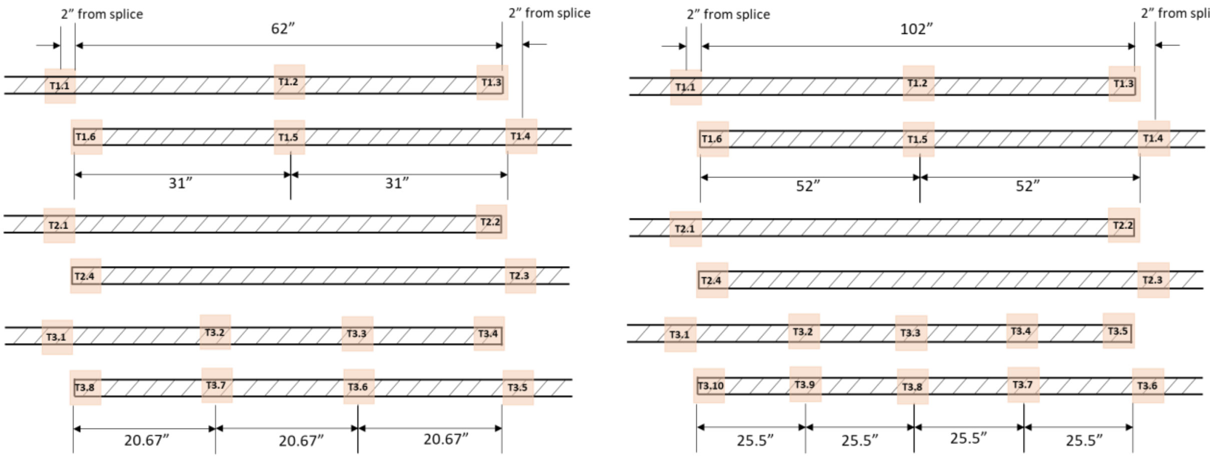

(c) LO60 (d) LO100

Figure 3-93. Strain gauge locations on tension longitudinal rebars

- Crack widths

Cracks were visually inspected and marked to monitor their development. Crack widths were measured using a crack comparator at each load interval. To maintain consistency, all measurements were performed by the same student throughout the test. A Digital Image Correlation (DIC) system monitored the strain field and crack development in the test region. This system used two high-speed cameras to capture the image of speckle pattern applied to the beam surface, covering a rectangle area from the beam center to the midpoint of one loading point, assuming symmetry of the test setup and specimen as shown in Figure 3-94. During testing, surface images were continuously recorded. After the test, a reference image was selected. The DIC system then tracked the relative position of each speckle over time, allowing for the calculation of crack width throughout the test.

Figure 3-94. DIC system setup during testing

3.3.1.3.3. Test Procedure

The beam specimens were lifted until they contacted to support plates, at which point all sensors were tared. Each specimen was loaded in 20-kip increments up to service load level, then in 40-kip increments until failure. At each load level, cracks were marked, and photos were taken of each beam surface to track crack development. LO60 and LO100 specimens were loaded in these increments until failure, while LX60 and LX100 specimens were loaded to peak load, after which they were loaded in 0.5 in. midpoint deflection increment. Testing concluded once the load dropped by approximately 10% from the peak load or concrete crushing occurred.

3.3.1.4. Experimental Results and Discussion

3.3.1.4.1. Overview

This chapter presents a detailed discussion of the observations and measurements of the specimens during testing, along with experimental results. Key aspects include the visual crack patterns, load-displacement behavior, bar strain distribution, and serviceability considerations related to crack width. Table 3-16 presents an overview of material test results. As illustrated in Figure 3-95, the stress-strain curve for Grade 60 rebars shows a typical pattern with an initial elastic region, a distinct yield plateau, and a strain-hardening phase. Conversely, Grade 100 rebars exhibit a parabolic stress-strain curve with an indistinct yield plateau. Therefore, the yield strength of Grade 100 rebar was determined using 0.2% offset method.

Table 3-16. Material properties used in beam splice test

Specimen ID	Concrete			Rebar yield strength (ksi)		
	Compressive strength (psi)	Splitting tensile strength (psi)	Modulus of elasticity (psi)	Longitudinal	Transverse	
					Splice region	Outside
LX60	4623	410	5065	65.4	63.9	63.9
LO60	5292	343	6459			
LX100	5595	362	6663	112.9	64.7	
LO100	5797	341	7033			

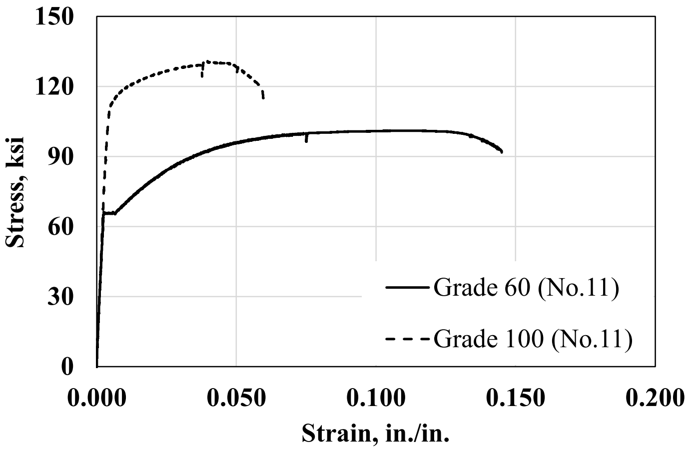

Figure 3-95. Rebar stress-strain curve (Beam splice test)

3.3.1.4.2. Crack pattern

All specimens displayed a similar crack pattern at the early load stages, as shown in Figure 3-96. Flexural cracks appeared on the tension side of each specimen in the test region near the 40-kip load level. As load increased, cracks extended further within the test region and into the shear span region. Throughout the test, cracks propagated from the tension side toward the compression side. Flexural shear cracks began to emerge around 120-kip load level.

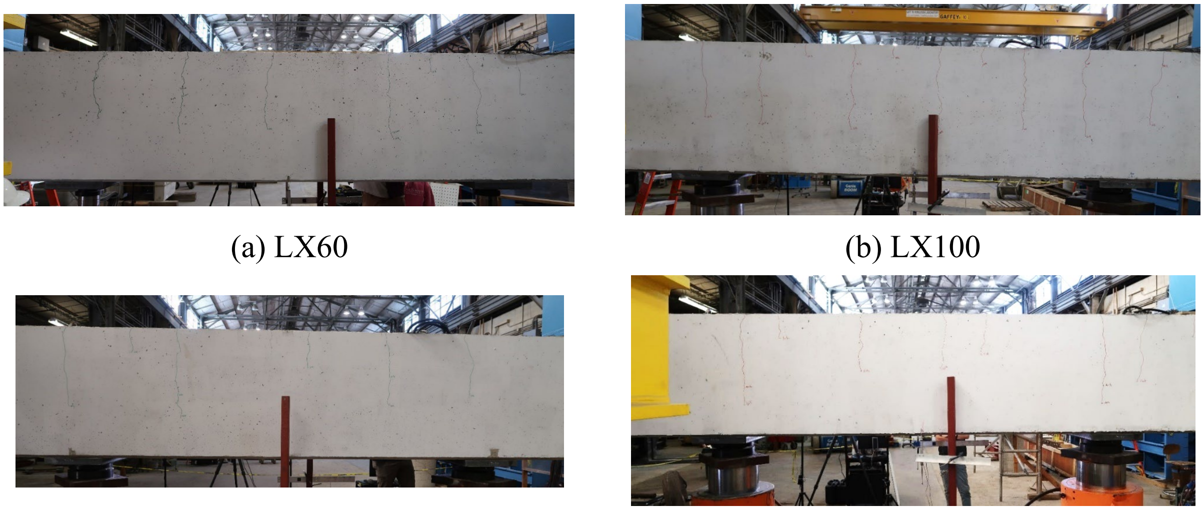

(a) LX60 (b) LX100

(c) LO60 (d) LO100

Figure 3-96. Crack pattern observed at early load stage of 60-kip load level

At failure, different failure modes were observed between the non-spliced and spliced specimens as shown in Figure 3-97. The non-spliced beams (LX60 and LX100) exhibited a typical flexural failure mode, with flexural cracks widening and extending nearly through the full depth of the beam. In contrast, the spliced beams (LO60 and LO100) initiated splitting cracks near the ends of the splice after the tension longitudinal bars reached yield. As the load increased, additional splitting cracks formed, nearly perpendicular to the flexural cracks. These cracks led to a sudden, explosive failure of the splice region at a specific load level. This failure is believed to be caused by slip, as the bond between the rebars and surrounding concrete weakened. This conclusion was supported by the large size of the splitting cracks along the entire lap splice region.

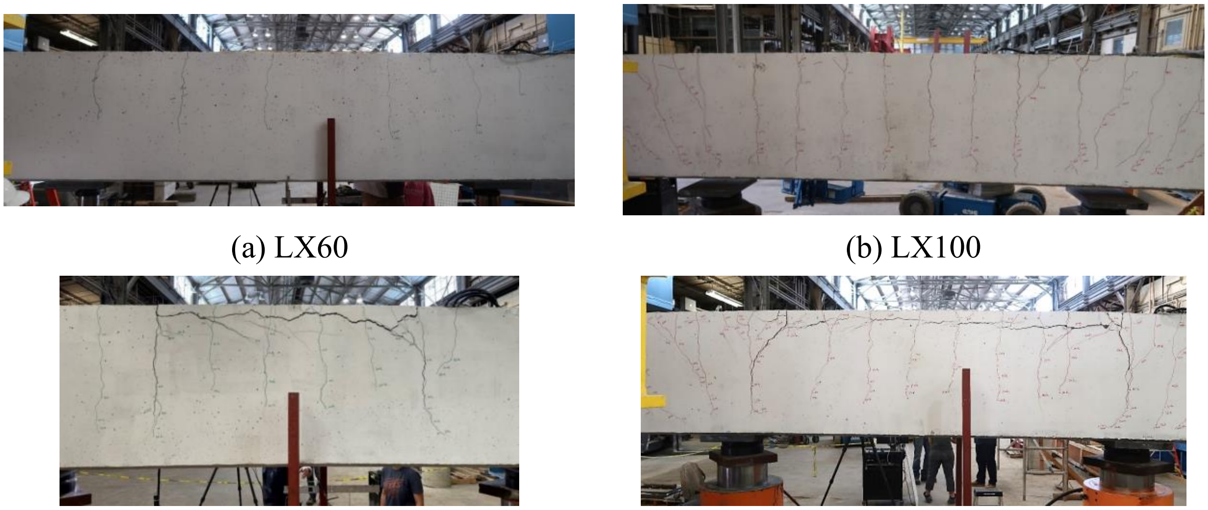

(a) LX60

(b) LX100

(c) LO60

(d) LO100

Figure 3-97. Crack patterns at failure

3.3.1.4.3. Load-Displacement Behavior

Figure 3-98 presents the load-displacement curves for all beams. The load values represent the total applied load, as recorded by the load cells. Displacement values correspond to the averaged midpoint deflection, adjusted to exclude deflection attributed to rigid body motion.

Before cracking, all beams exhibited a similar linear load-displacement response. After cracking, stiffness reduced, however a linear load-displacement relationship continued. In spliced beams (LO60 and LO100), brittle failure occurred, characterized by a sudden drop in load due to concrete splitting along the lap splice region (Refer to Figure 3-97). Up to failure, the load-displacement curves of spliced beams similar to those of non-spliced beams (LX60 and LX100), as spliced beams failed shortly after the tension longitudinal rebars reached yield. In contrast, non-spliced beams showed strain-hardening after rebar yielding, leading to ductile failure mode. The use of high-strength rebars increased the ultimate load capacity. However, the presence of a lap splice reduced load capacity due to brittle failure. Notably, the ultimate load at failure exceeded the design load, defined as the load level at which the tension longitudinal rebar reached yielding.

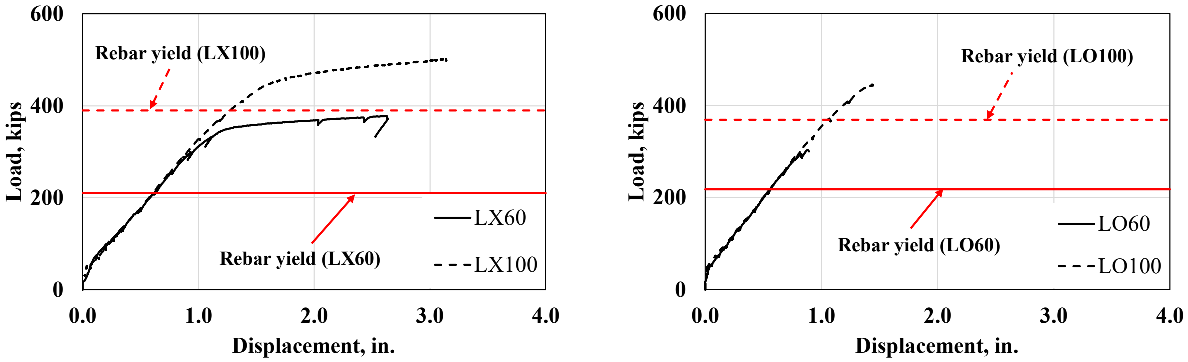

(a) Rebar grade

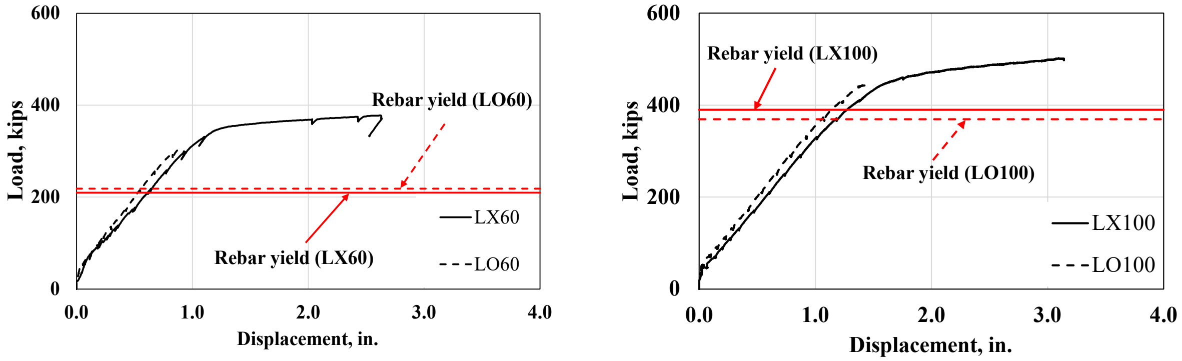

(b) Presence of lap splice

Figure 3-98. Load-displacement curves of beam splice test

3.3.1.4.4. Rebar Strains

The longitudinal bar strains in the test region are shown in Figure 3-99 and Figure 3-100, plotted against the applied loads. In the non-spliced beams (LX60 and LX100), the bar strains consistent within the test regions, and strains among different bars at the same longitudinal position were similar. Conversely, in the spliced beams (LO60 and LO100), strains at the same longitudinal location were still similar across different bars. Therefore, it was confirmed that the placement of the different strain gauges used in this test did not significantly affect the gauge readings. Bar strains in the spliced beams tended to decrease toward the ends of the splice. Although the strains measured at the ends of the splice were nearly zero, the strains at the corresponding locations on the other connected bars were the highest. Additionally, the strains at symmetric locations relative to the bars connected by the lap splice were consistent across all bars, indicating effective stress transfer through the lap splice.

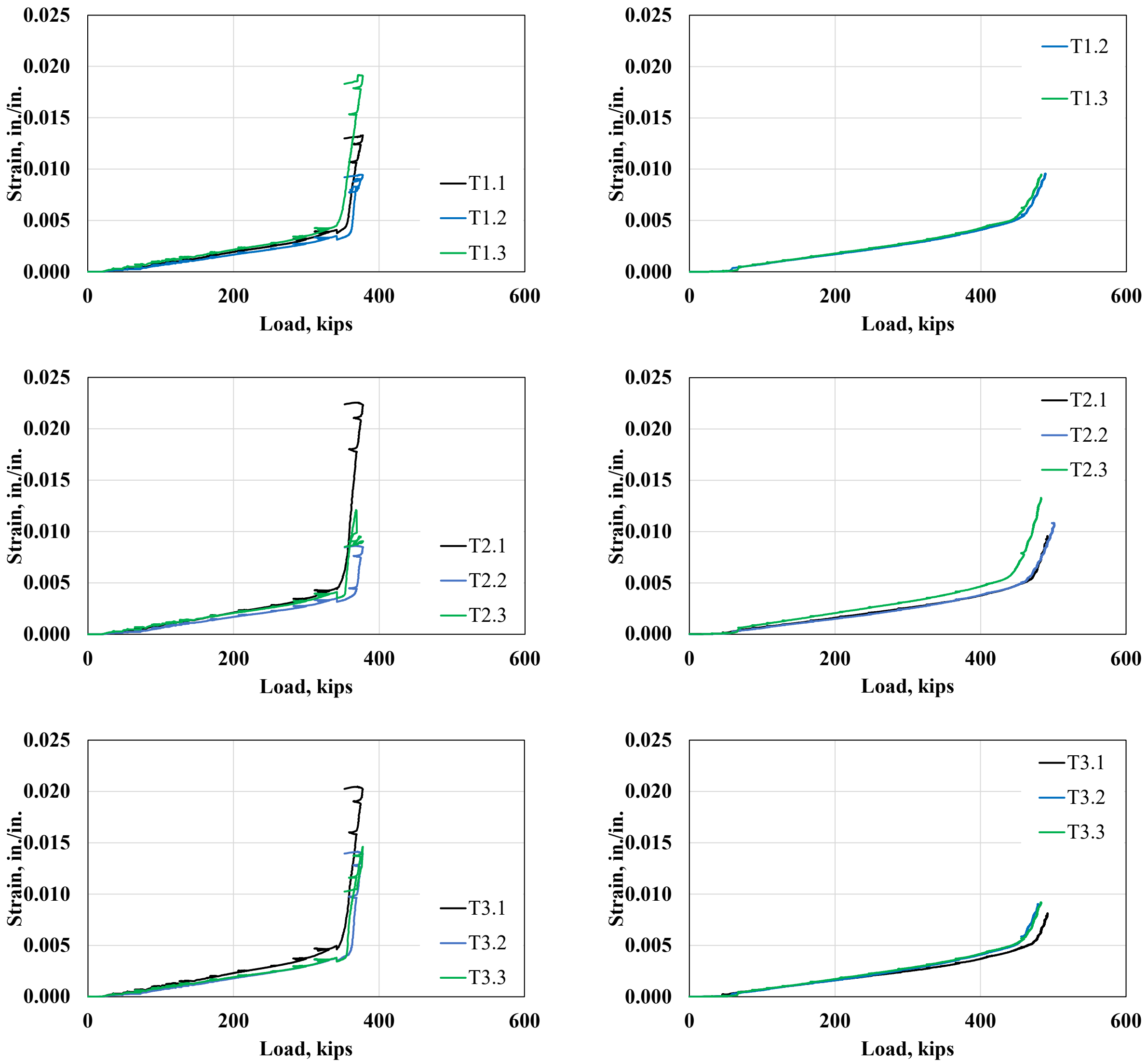

(a) LX60 (b) LX100

Figure 3-99. Bar strains versus applied load for spliced beams

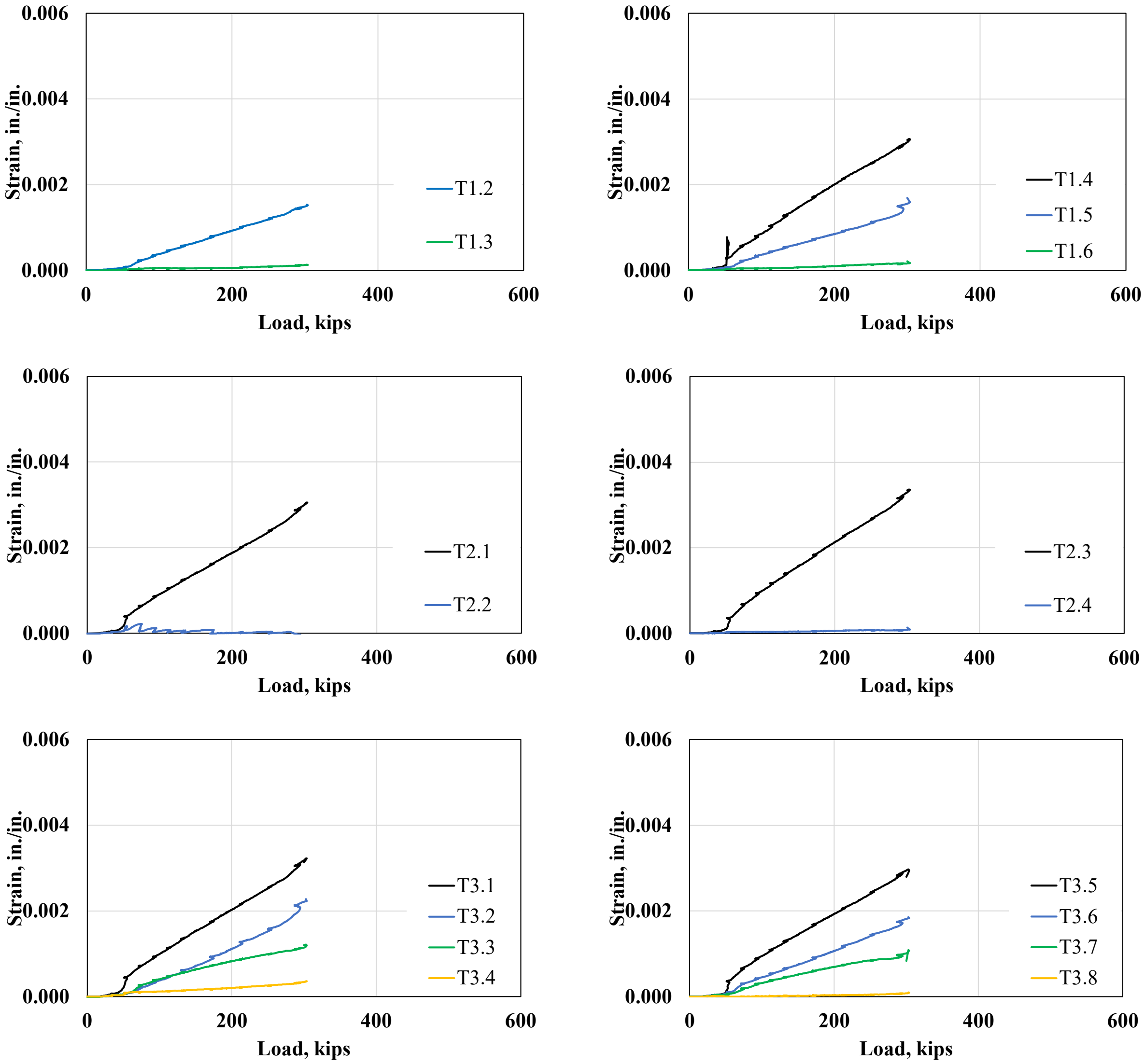
Strain, in./in.
0.006
0.004
0.002
0.000
0
200
400
600
Load, kips
T1.2
T1.3
T1.4
T1.5
T1.6
T2.1
T2.2
T2.3
T2.4
T3.1
T3.2
T3.3
T3.4
T3.5
T3.6
T3.7
T3.8

(a) LO60

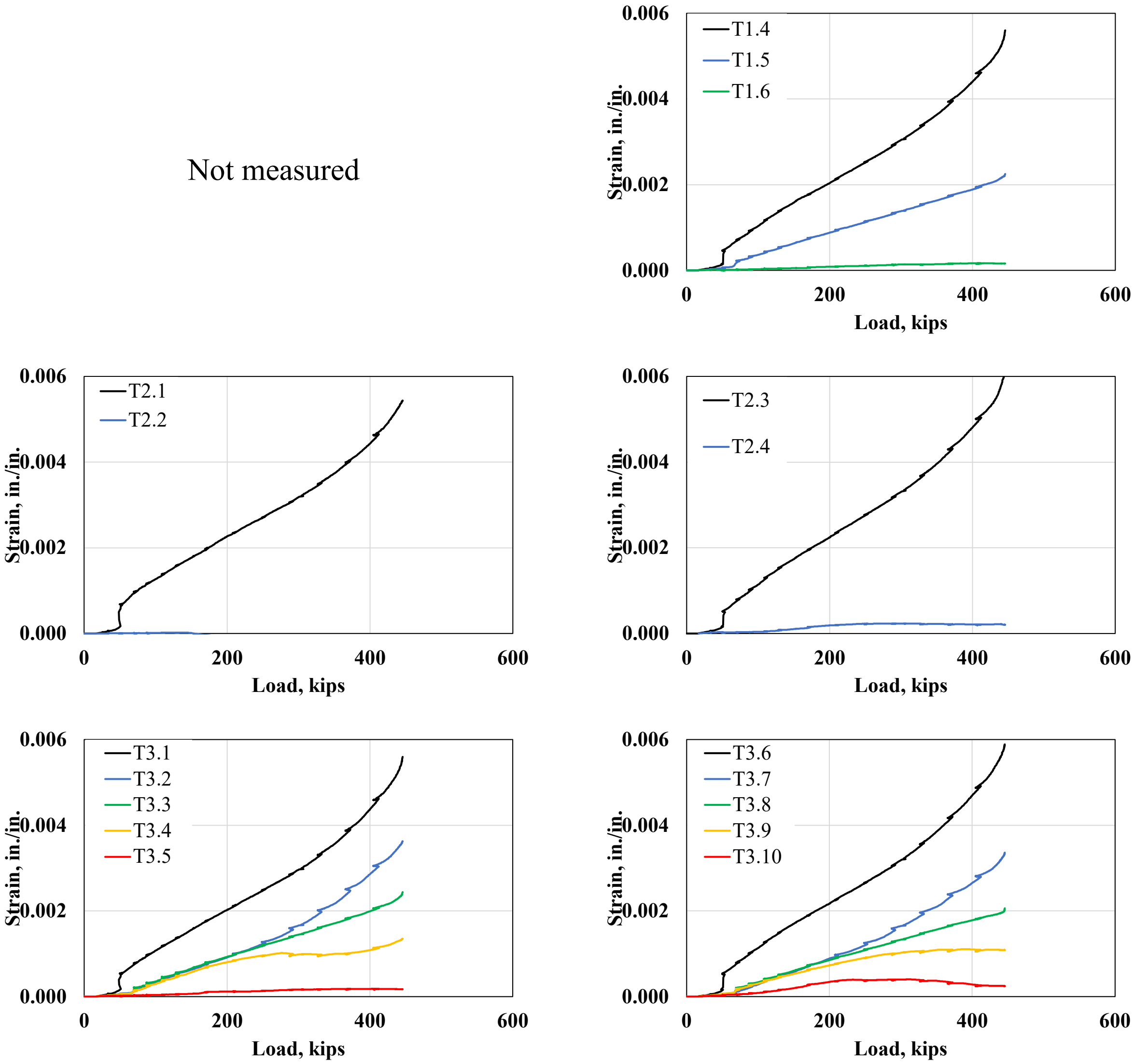

(b) LO100

Figure 3-100. Bar strains versus applied load for spliced beams

3.3.1.4.5. Crack widths

The DIC system was utilized to calculate the crack width, supplementing the visual measurements obtained with the crack comparator card. The DIC system monitored the displacement of the speckles in the concrete surface throughout the test, and crack width was determined based on the variation in displacement. As a result, this vision system provided more accurate crack width readings compared to the visual measurements, which are prone to human error or inconsistencies in interpretation. Crack width was monitored in the test region between the loading points, covering the entire splice region.

Figure 3-101 shows the relationship between the average and maximum crack widths and bar stress for each beam. The service and crack width limits specified by AASHTO and ACI are included to assess the serviceability. The crack width limit recommended by AASHTO LRFD (2020) is 0.017 in., while ACI 224R-01 specifies a limit of 0.016 in. Two different recommended service limits based on rebar stresses were considered: one being two-thirds of the specified yield strength, as outlined in ACI 318-19, and the other being 60% of the specified yield strength, as stated in AASHTO LRFD (2020). The bar stresses were converted from the strains measured throughout the test, using the stress-strain curves derived from material tests.

For the non-spliced beams (LX60 and LX100), the average and maximum crack widths were similar, as cracks were evenly distributed across the pure moment region. In contrast, for the spliced beams (LO60 and LO100), the maximum crack width was larger than the average crack width. This can be attributed to cracks being concentrated locally at both ends of the splice, with relatively narrow cracks within the splice region. This phenomenon was consistent with the observed crack pattern (Refer to Figure 3-97). The specimens with Grade 60 rebars (LX60 and LO60) satisfied the serviceability limit. On the other hand, specimens with Grade 100 rebars (LX100 and LO100) did not satisfy the serviceability limit.

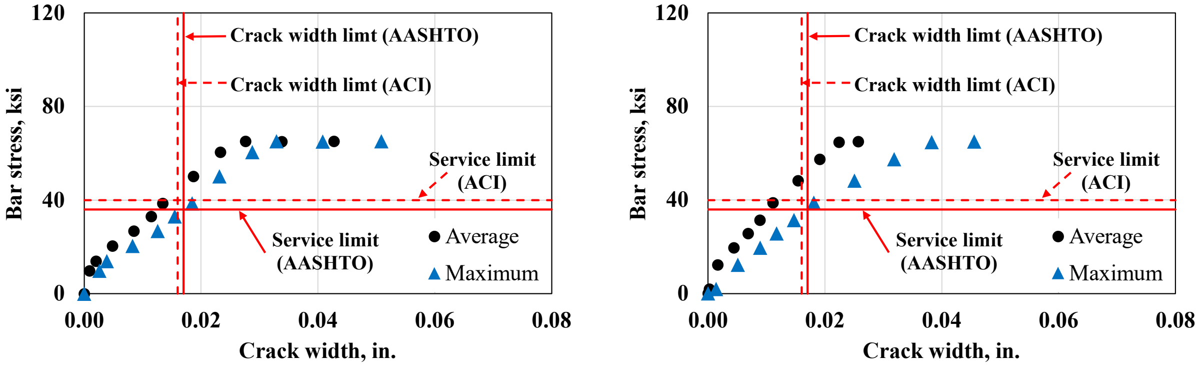

(a) LX60 (b) LO60

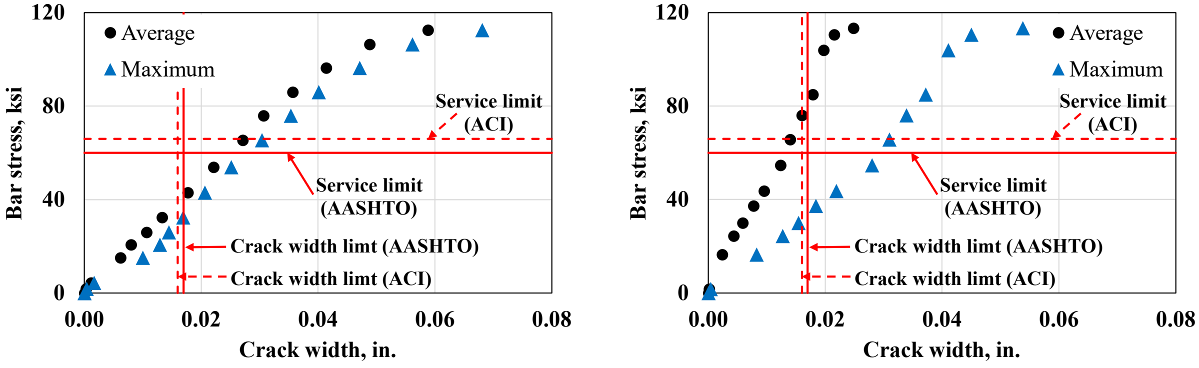

(c) LX100 (d) LO100

Figure 3-101. Crack width versus bar stress in beam splice test

Figure 3-102 compares the maximum crack widths with respect to test variables, including rebar grade and the presence of lap splice. Very similar behavior was observed between maximum crack width and bar stress, regardless of the presence of lap splices (Refer to Figure 3-102(a)). For high-strength rebar, the relationship between maximum crack width and bar stress remained proportional up to failure. In contrast, for normal-strength rebar, the maximum crack width maintained a proportional relationship with bar stress reached the yielding, after which crack width increased without change of bar stress due to the yield plateau (Refer to Figure 3-102(b)). However, similar behaviors were observed up to the yield level of normal-strength rebar. In conclusion, the maximum crack widths were found to be independent of these variables. This suggests that the unsatisfactory serviceability of beams with high-strength bars is not due to different behavior from normal-strength steel but rather to the increased bar stress at the service limit, resulting from the higher yield strength of high-strength rebar.

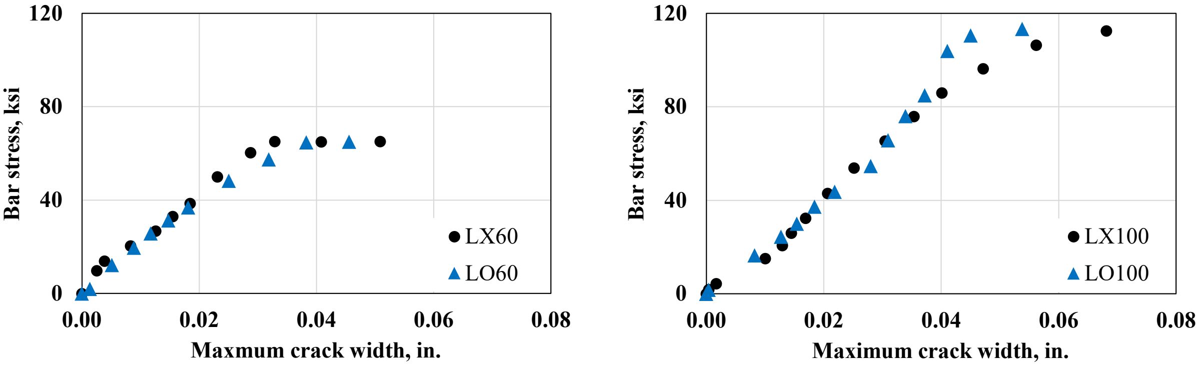

(a) Presence of lap splice

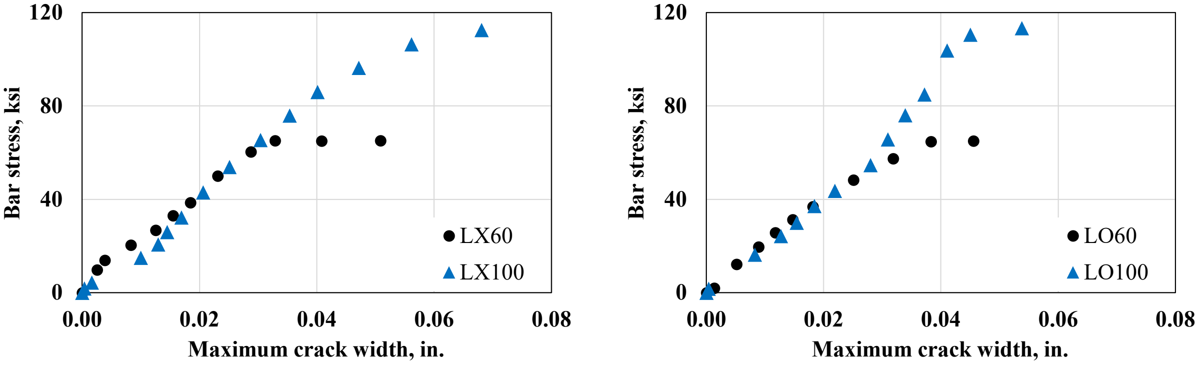

(b) Rebar grade

Figure 3-102. Comparison of maximum crack width according to test variables in beam splice test

ACI 318-19 permits flexural rebar spacing provisions for Grade 100 reinforcement based on studies by Frosch et al. (2014) and Puranmam (2018). Similarly, AASHTO LRFD (2020) references Shahrooz et al. (2011), which indicates that Equation (3-2), can be applied for Grade 100 rebar. However, these studies only considered high-strength rebars with a maximum size of No. 8. Therefore, further analysis is required to determine whether the large-diameter, high-strength rebar can comply with the requirements of current design standards, such as those set by ACI and AASHTO.

Crack widths measured for the beams tested in this study were compared to those predicted using Frosch model, as shown in Figure 3-103. In all cases, the Frosch model showed good agreement with experimental results, supporting that No.11 high-strength reinforcing bars aligned with the current codes. The maximum required rebar spacing calculated using Equations (3-1) and (3-2) for the LX100 and LO100 specimens was 2.8 inches per ACI 318-19 and 3.8 inches per AASHTO LRFD (2020), both of which were significantly smaller than the 7.8 inches used in the test. This explains the unsatisfactory serviceability of beam specimens with high-strength steel. However, these small rebar spacings would require a larger quantity of rebars, resulting in an unjustifiable increase in flexural strength and leading to a conservative and uneconomical design.

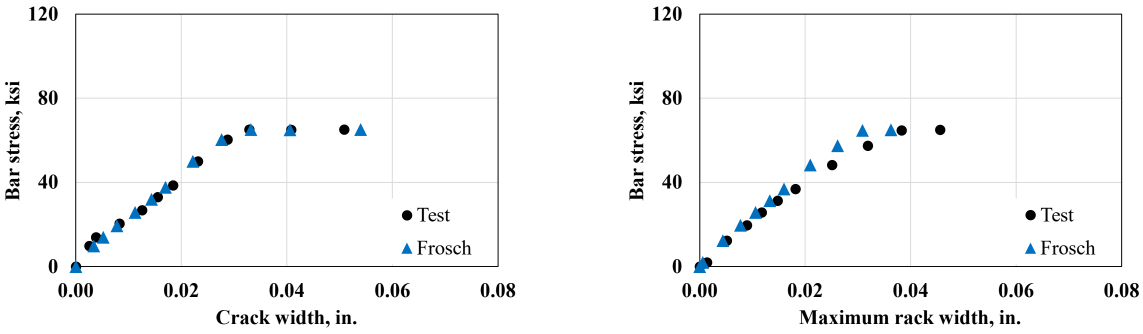

(a) LX60 (b) LO60

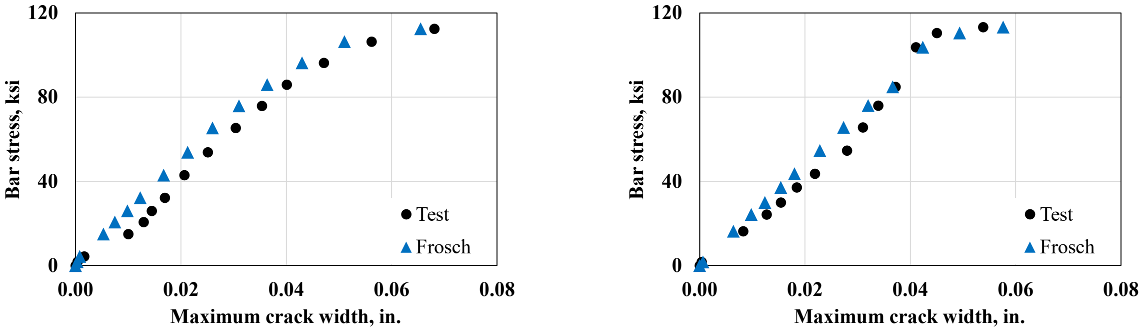

(c) LX100 (d) LO100

Figure 3-103. Measured crack width in beam splice test vs. predicted by Frosch model

3.3.1.4.6. Conclusions

Four large-scale reinforced concrete beams with continuous and spliced No. 11 Grade 60 and Grade 100 rebars were tested in four-point bending configuration. The behavior of large-scale beams reinforced with No.11 bars (with and without lap splices) subjected to tensile stresses was studied. The primary conclusions of this study are as follows:

- Beams with a lap splice exhibited a brittle splitting failure mode due to rebar slip within the splice region, in contrast to beams with continuous reinforcing bar, which demonstrated a typical flexural failure mode. Nevertheless, all beams exceeded their design load capacity, defined as the load at which the flexural reinforcement reaches yielding.

- Rebar stress distribution within lap splice region was analyzed by measuring rebar strains and applying rebar-stress relationship determined from material tests. The results confirmed that the lap splice length used in this study was sufficient to ensure effective stress transfer thorough the lap splice.

- Rebar grade and the presence of a lap splice did not affect cracking behavior. Although beams with normal-strength rebar satisfied serviceability in terms of crack width, those with high-strength rebar did not. Additionally, measured crack widths aligned closely with those predicted by the Frosch model.

- These findings indicate that beams with high-strength rebar exhibit the same cracking mechanism as those with normal-strength rebar. Therefore, No.11 high-strength rebar can be used in tension lap splice applications in compliance with current design codes, though careful consideration is necessary, as it may necessitate an excessive reinforcement to meet the rebar spacing requirement.

3.3.2. Uniaxial Tension

The cracking behavior of reinforced concrete structures caused by tensile stress field is a multifaceted phenomenon influenced by various factors, such as geometries (reinforcement ratio and concrete clear cover length) and material properties (rebar and concrete strength) (Frosch 1999). Given the intricate nature of these interactions, it is essential to conduct experimental validation to thoroughly study how cracking behavior manifests across this diverse array of conditions. The amount of reinforcement can be reduced by employing high-strength bars instead of normal-strength rebars in construction, which is believed to impact the cracking behavior of reinforced concrete. Nevertheless, the understanding of cracking behavior in this regard is still deficient compared to the situations where conventional rebar is employed. The research team conducted a series of uniaxial tension tests to fill this knowledge gap on reinforced concrete prisms.

3.3.2.1. Specimen Design

A total of ten concrete prisms were designed to investigate the effects of various parameters, including reinforcement ratio, concrete clear cover, concrete strength, and rebar strength. Two different sizes of rebar were utilized to evaluate the influence of reinforcement ratio and concrete clear cover on crack performance, and four different specimen widths were considered. Furthermore, two grades of rebar, specifically Grade 60 and Grade 100, were incorporated for comparative analysis. Additionally, concrete design strengths of 5,000 psi and 12,000 psi were selected to assess the impact of concrete strength on crack performance under tensile forces.

In recognition of the potential variability inherent in direct tensile test results, our research team employed a strategy to enhance reliability by fabricating two identical prisms using the same design parameters. This approach facilitates a more robust and reliable assessment of cracking behavior under varying conditions, as Deluce and Vecchio (2013) referenced. Consequently, a total of twenty test specimens are planned. The experimental parameters are detailed in Table 3-17 for reference. The test ID indicates, in order, concrete strength (N for 5,000 psi and H for 12,000 psi), rebar grade, concrete clear cover, and reinforcing steel diameter. The last two numbers, 1 and 2, distinguish identical test specimens.

The total length of the prism has been established at 40 inches, a dimension guided by the insights from previous research (Lee et al. 2019; Moreno et al. 2014; Sturm and Visintin 2023). In order to minimize the risk of premature splitting cracks within the D-region (Moreno et al. 2014; Sturm and Visintin 2023), both ends of the prism are reinforced with confining rebar cages. Consequently, this configuration confines the active test region to a span of 32 inches, as illustrated in Figure 3-104.

Table 3-17. Test matrix of uniaxial tension

Test ID	Rebar ratio (%)	Clear cover (in.)	Design concrete strength (psi)	Rebar grade
N-60-5.5-5-1	1.02	2.438	5,000	60
N-60-3.5-5-1	2.53	1.438		
N-60-7.5-11-1	2.77	3.045		
N-60-6.5-11-1	3.69	2.545		
N-60-5.5-5-2	1.02	2.438		
N-60-3.5-5-2	2.53	1.438		
N-60-7.5-11-2	2.77	3.045		
N-60-6.5-11-2	3.69	2.545		
N-100-5.5-5-1	1.02	2.438		100
N-100-3.5-5-1	2.53	1.438		
N-100-7.5-11-1	2.77	3.045		
N-100-6.5-11-1	3.69	2.545		
N-100-5.5-5-2	1.02	2.438		
N-100-3.5-5-2	2.53	1.438		
N-100-7.5-11-2	2.77	3.045		
N-100-6.5-11-2	3.69	2.545		
H-100-3.5-5-1	2.53	1.438	12,000	
H-100-7.5-11-1	2.77	3.045		
H-100-3.5-5-2	2.53	1.438		
H-100-7.5-11-2	2.77	3.045		

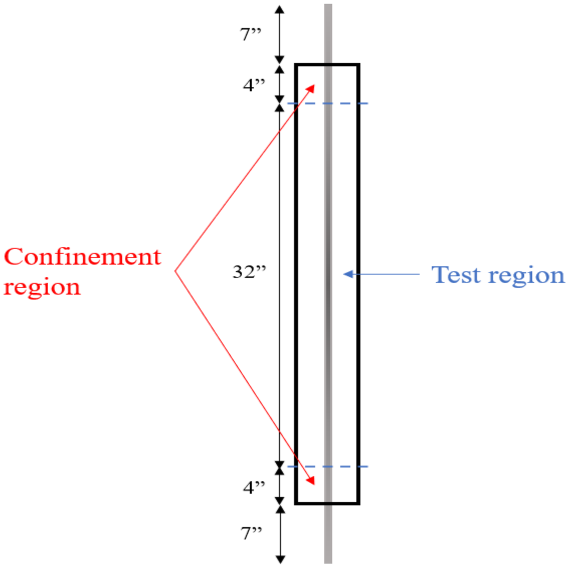

Figure 3-104. Geometry of the specimens

3.3.2.2. Fabrication

The research team fabricates wood forms for the specimens, as depicted in Figure 3-105(a). Furthermore, confining rebar cages are installed with No.2 and No.3 reinforcement to provide confinement at both ends of the prism. It is important to note that shrinkage can substantially influence the load-displacement response of a conventionally reinforced direct tension test, as indicated in previous research (Bischoff 2003). To ensure the precision of the test results, a series of free shrinkage tests following the procedure outlined in ASTM C157 are conducted. A total of five concrete prisms (dimension: 2 in. square with 11.75 in. length) are fabricated with the test specimens from the same batch using specific steel molds, as shown in Figure 3-105(b).

Each type of specimen is fabricated in duplicate. Notably, one of the duplicate specimens is equipped with eight strain gauges positioned with 4-inch spacing along the rebar. This arrangement enabled monitoring the reinforcement's post-yielding behavior (Moreno et al. 2014) and detecting the onset of reinforcement yielding.

(a) Wood form for prism (b) Steel form for shrinkage test

Figure 3-105. Casting preparation for uniaxial tension test

3.3.2.3. Test setup

All specimens are subjected to monotonic tension in a 550-kip universal testing machine under displacement control, and the protruding steel reinforcing bars from both ends of the specimens are gripped. The specimens are tensioned under the loading rate of 0.00354 in/min up to 60% of the yield strength, and it is increased to 0.00954 in/min. After the onset of rebar yielding, the loading rate is increased to 0.0954 in/min. Additionally, the elongation of the central region of each specimen is measured by utilizing two linear potentiometers (LPOTs) on each side (Refer to Figure 3-106). The average displacement recorded by the LPOTs is then divided by the test region's length (32 inches) to calculate the average axial strain of the specimen under tension.

Moreover, a non-contact vision system (Optotrack) plays a pivotal role in capturing the crack patterns and width of the concrete prism until the tension force is exerted on the prisms. This comprehensive approach ensures that testing and data collection processes are as accurate and informative as possible.

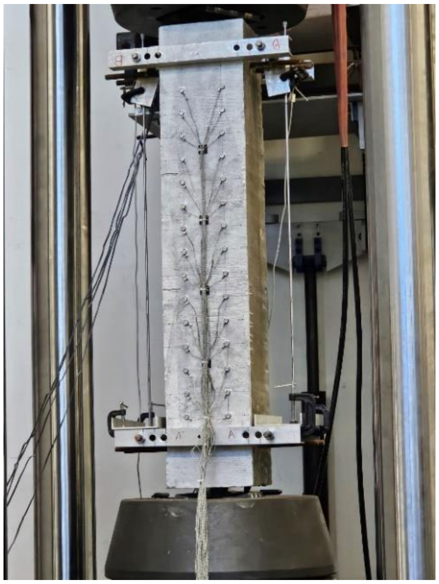

Figure 3-106. Uniaxial tension test setup

Material tests are conducted on six bare steel rebars, representing two distinct grades (Grade 60 and Grade 100), and available in two varying sizes (No. 5 and No. 11). These tests are carried out using a 440-kip capacity universal testing machine, following ASTM A615. The testing procedure involves an initial loading rate of 0.1 in/min until the yield point is reached, at this point, the loading rate is increased to 0.8 in/min until failure occurs. For precise strain measurement on the bared steel bars, an 8-inch extensometer is employed.

3.3.2.4. Experimental Results and Discussion

3.3.2.4.1. Overview

This chapter presents an in-depth discussion of the experimental results and analyses. The material properties used in uniaxial tension tests significantly influence crack behavior, which was a key focus of this study. Consequently, this chapter examines the material test results and the crack behavior observed in the specimens for each variable. A comprehensive discussion on the impact of these variables is also provided.

A summary of concrete properties and the yield and ultimate loads for each reinforced concrete prism specimen is provided in Table 3-18. The yield and ultimate loads for each specimen are determined based on those of the rebar size and grade, as outlined in Table 3-19. To prevent damage to the testing machine resulting from concrete spalling in the event of reinforcement rupture, all specimens are loaded up to approximately 90% of the ultimate capacity of the corresponding bare reinforcing bar. The test limit load is considered to be the ultimate load of the specimen, as it provides a sufficient loading level for examining the post-yielding and post-cracking behaviors of the specimens.

Table 3-18. Concrete properties and yield & ultimate points

Test ID	Shrinkage (%)	Concrete strength (psi)	Yield Load (kip)	Ultimate Load (kip)
N-60-5.5-5-1	0.03	5,051	20	32
N-60-3.5-5-1	0.03	5,324	20	32
N-60-7.5-11-1	0.03	5,324	104	166
N-60-6.5-11-1	0.03	5,051	104	166
N-60-5.5-5-2	0.03	5,051	20	32
N-60-3.5-5-2	0.03	5,051	20	32
N-60-7.5-11-2	0.03	5,324	104	166
N-60-6.5-11-2	0.03	5,324	104	166
N-100-5.5-5-1	0.03	5,051	40	50
N-100-3.5-5-1	0.03	5,324	40	50
N-100-7.5-11-1	0.03	5,324	200	220
N-100-6.5-11-1	0.03	5,051	200	220
N-100-5.5-5-2	0.03	5,051	40	50
N-100-3.5-5-2	0.03	5,051	40	50
N-100-7.5-11-2	0.03	5,324	200	220
N-100-6.5-11-2	0.03	5,324	200	220
H-100-3.5-5-1	0.028	12,208	40	50

H-100-7.5-11-1	0.028	12,787	200	220
H-100-3.5-5-2	0.028	12,208	40	50
H-100-7.5-11-2	0.028	12,787	200	220

The bare reinforcement's yield and ultimate strength values are determined based on the direct tension tests for rebar coupons, as illustrated in Figure 3-107. In the case of conventional steel (Grade 60), the yield strength is identified within the plateau region. However, high-strength steel (Grade 100) does not exhibit a distinct plateau region, necessitating the use of the 0.2% offset line method to determine the yield strength.

Upon thorough analysis, the average yield strength (f_y) and ultimate strength (f_u) for each type of reinforcement are provided in Table 3 1. The average yield strain (ε_y) and ultimate strain (ε_u) for each type of reinforcement are also specified in the same table. As shown in Figure 3-107 and Table 3-19, it can be observed that even if the rebar size changes, rebars of the same grade have similar material properties. Additionally, the elastic modulus before yielding for two different grades of rebar both have values close to 29,000 ksi.

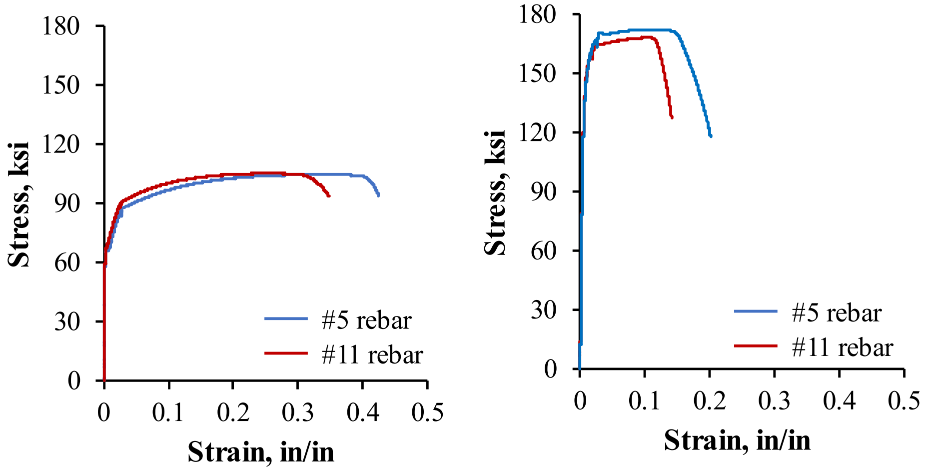

(a) Grade 60 (b) Grade 100

Figure 3-107. Rebar coupon test results

Table 3-19. Yield and ultimate strength for each rebar

Rebar	f_y (ksi)	ε_y	f_u (ksi)	ε_u
Grade 60 (#5)	65.8	66.7	130.1	128.3
Grade 60 (#11)	0.00237	0.00253	0.00687	0.00635
Grade 100 (#5)	104.6	106.2	168.0	159.4
Grade 100 (#11)	0.33276	0.25272	0.13942	0.10929

The shrinkage and concrete cylinder compression tests are conducted concurrently, applying uniaxial loading to the prisms. These material tests aim to ensure the consistent condition of the concrete for all specimens. It was found that the shrinkage and concrete strength remained constant for all specimens when using the same concrete design strength. The detailed shrinkage and concrete cylinder testing results and the reinforced concrete prism testing results are covered in the following section.

3.3.2.4.2. Cracking Behavior

The comparison of cracking behaviors was conducted based on rebar ratio, concrete clear cover length, rebar strength, and concrete strength. The maximum crack width and the number of cracks formed in the test regions were observed for comparison. Data was collected using the optotrack system and a concrete crack width ruler. Additionally, crack behavior was detected on both the front and back surfaces of the specimens, and the average value of the crack behavior in both regions was used for the analysis. The test results of three specimens (N-60-3.5-5-1, N-100-3.5-5-1, and N-100-7.5-11-1) were excluded from the analysis due to errors in the experimental process.

Rebar ratio

To understand the impact of rebar ratio on the concrete cracking behavior under tension force, the results of eight experiments with a concrete clear cover length close to 2.5 were compared (refer to Figure 3-108 and Figure 3-109). Two different rebar ratios, 1.0% and 3.7%, were compared for both Grade 60 and Grade 100 rebar. The maximum crack width at three loading points was compared: 40% of the specimen's capacity, 80% of the capacity, and the yield point. All compared specimens used normal-strength concrete. The results indicate that for both Grade 60 and Grade 100 rebar, an increase in rebar ratio leads to a decrease in maximum crack width.

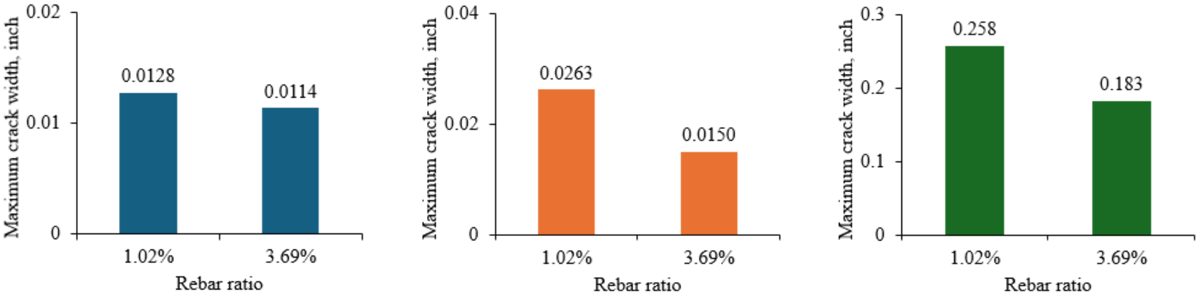

(a) 40 % (b) Yield point (c) 80%

Figure 3-108. Maximum crack width using Grade 60 and normal-strength concrete with 2.5 in. concrete clear cover

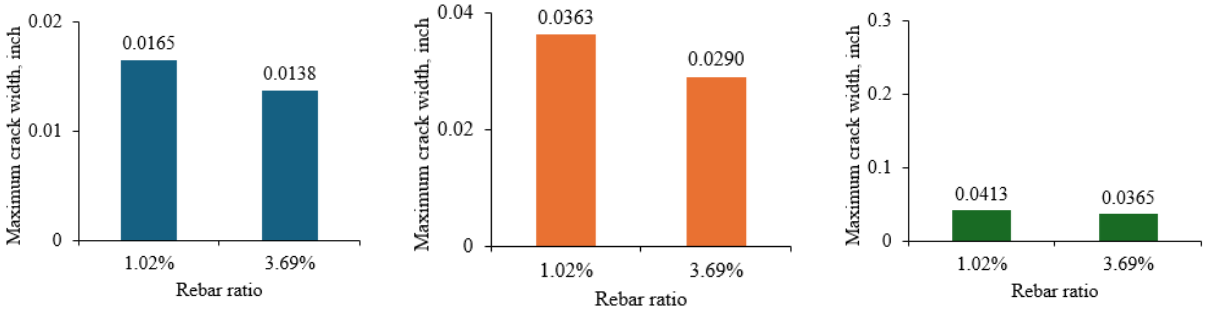

(a) 40 % (b) Yield point (c) 80%

Figure 3-109. Maximum crack width using Grade 100 and normal-strength concrete with 2.5 in. concrete clear cover

Concrete cover length

To assess the influence of concrete cover length on concrete cracking behavior under tension force, nine experiments with a rebar ratio of approximately 2.5% were analyzed (Refer to Figure 3-110 to Figure 3-112). The study compared concrete cover lengths of 1.4 inches and 3.0 inches. Additionally, variations in rebar strength and concrete strength were examined separately. The maximum crack width at the same three loading points was analyzed to compare rebar ratio effects. The findings indicate that, irrespective of rebar strength and concrete strength, an increase in concrete cover length increases maximum crack width. Furthermore, the effect of concrete cover length on maximum crack width becomes more pronounced with higher concrete strength.

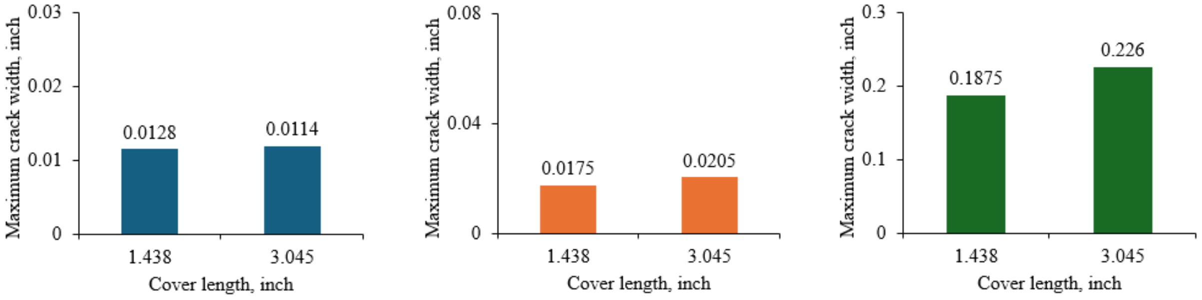

(a) 40 % (b) Yield point (c) 80%

Figure 3-110. Maximum crack width using Grade 60 and normal-strength concrete and with 2.5 rebar ratio

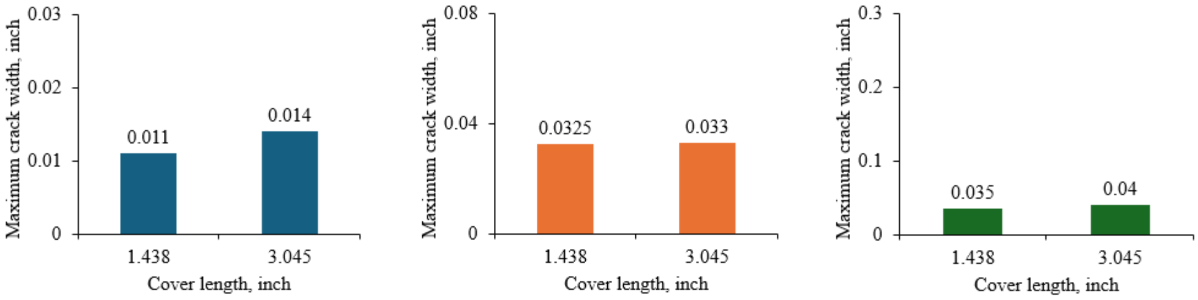

(a) 40 % (b) Yield point (c) 80%

Figure 3-111. Maximum crack width using Grade 100 and normal strength concrete with 2.5 rebar ratio

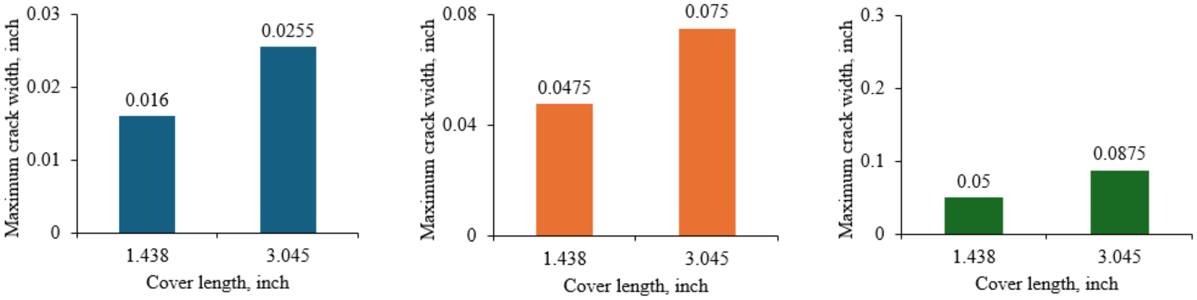

(a) 40 % (b) Yield point (c) 80%

Figure 3-112. Maximum crack width using Grade 100 and high-strength concrete with 2.5 rebar ratio

Rebar strength

Thirteen experimental results were compared to understand rebar strength's effect on concrete cracking behavior under tension force. The material properties of Grade 60 and Grade 100 rebar are explained in Figure 3-107 and Table 3-19. Specimens with the same rebar ratio, concrete cover length, and concrete strength were grouped and compared. The maximum crack width and number of cracks formed in the test region were compared according to rebar strength, and the results are shown in the figure. The x-axis of the figure represents the load ratio, which indicates the applied load relative to the ultimate capacity of the bare reinforcing bar.

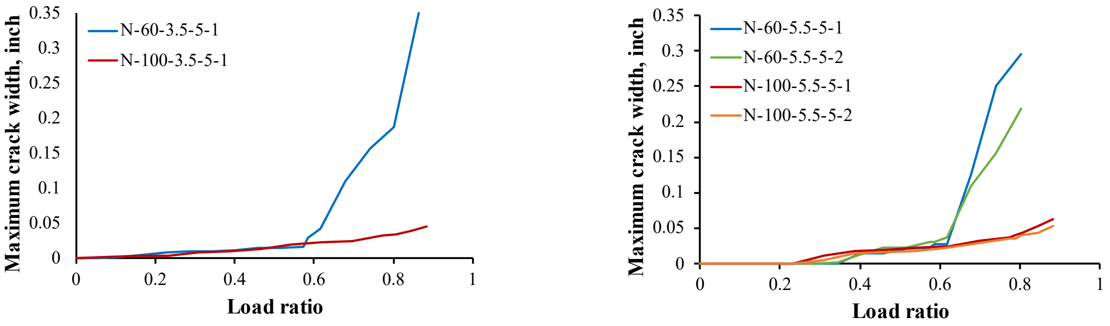

(a) 2.5% rebar ratio & 1.4 in. clear cover (b) 1.0% rebar ratio & 2.4 in. clear cover

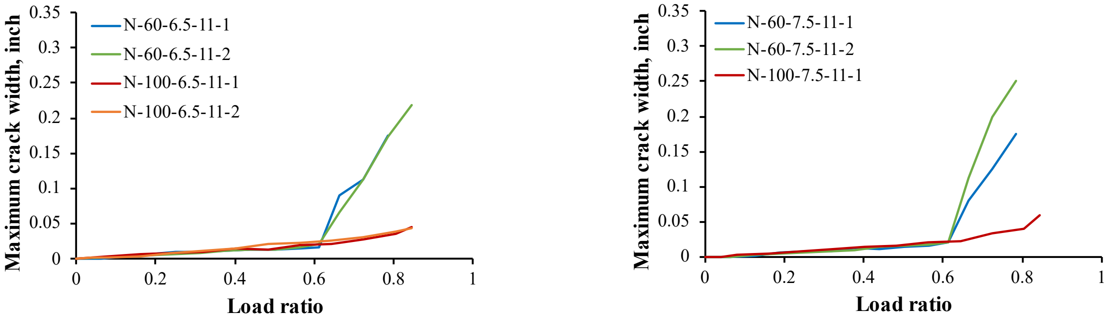

(c) 3.7% rebar ratio & 2.5 in. clear cover (d) 2.7% rebar ratio & 3.0 in. clear cover

Figure 3-113. Number of crack comparisons depending on rebar strength

According to Figure 3-113, it can be observed that up to the point where the rebar yields under load, the maximum crack width based on load ratio remains similar regardless of rebar grade. This indicates that when specimens using Grade 100 rebar achieve an ultimate capacity greater than those using Grade 60, the maximum crack width is smaller with Grade 100 rebar under the same load. Despite similar elastic modulus in both types of rebar, differences in crack width under the same load occur due to variations in crack propagation. Comparing the number of cracks formed based on load ratio reveals that more cracks occur before the yield point when high-strength rebars are used than regular rebars (Refer to Figure 3-114). Therefore, even with the same overall deformation of the specimen under identical load, using high-strength rebars results in more crack formation, thereby reducing the maximum crack width.

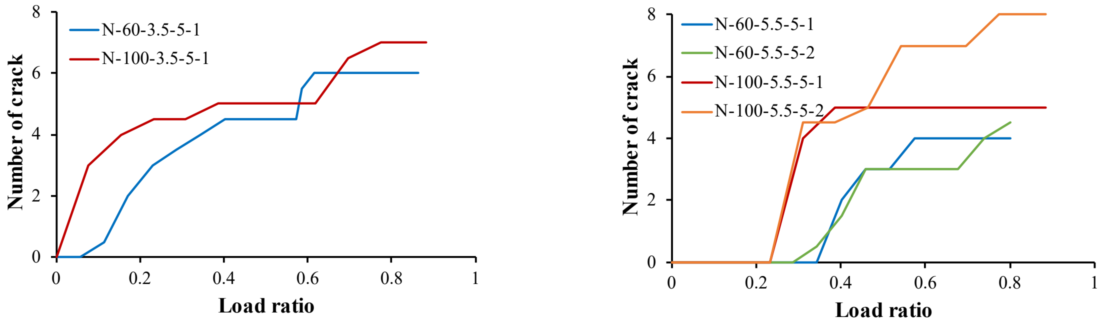

(a) 2.5% rebar ratio & 1.4 in. clear cover (b) 1.0% rebar ratio & 2.4 in. clear cover

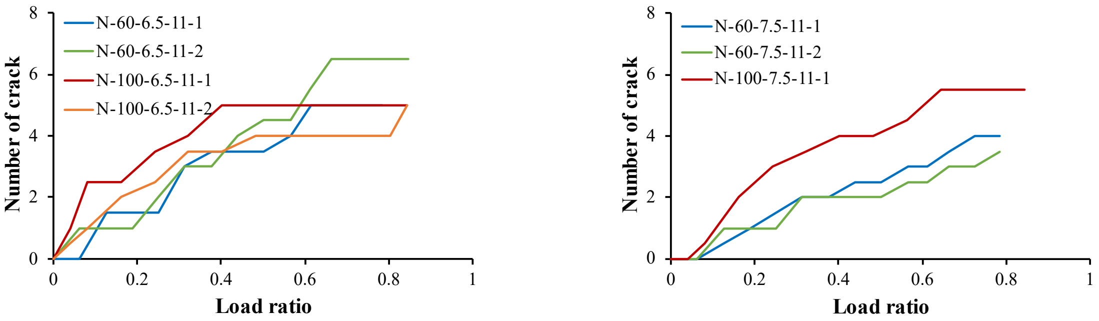

(c) 3.7% rebar ratio & 2.5 in. clear cover (d) 2.7% rebar ratio & 3.0 in. clear cover

Figure 3-114. The number of crack comparisons depends on rebar strength

After surpassing the yield point, specimens with regular rebars demonstrate a more pronounced increase in maximum crack width than those with high-strength rebars. Regular rebar specimens exhibit a stress plateau region post-yielding, where stress remains constant while strain continues to increase. This phenomenon results in an exponential widening of cracks under increasing external loads. Conversely, high-strength rebars lack a distinct plateau region, preventing a sudden increase in crack width beyond the yield point, even with escalating loads. Furthermore, due to their lower ductility compared to regular rebars, high-strength rebars result in narrower cracks from yield to failure. In conclusion, the use of high-strength rebars effectively distributes stress more uniformly than regular rebars, thereby minimizing maximum crack width in overall concrete structures.

Concrete strength

Six experiments were compared to understand the impact of concrete strength on concrete cracking behavior under tension force. Specimens with identical rebar ratio, concrete cover length, and rebar strength were grouped together for comparison (Refer to Figure 3-115 and Figure 3-116). The results indicate that the number of cracks formed in the test regions based on load ratio is not influenced by concrete strength, but there is a trend of increasing maximum crack width when using high-strength concrete. Therefore, it can be noted that the crack control performance decreases when using high-strength concrete of 10 ksi or more. However, these findings could be influenced by differences in concrete mix design, suggesting the need for further detailed research.

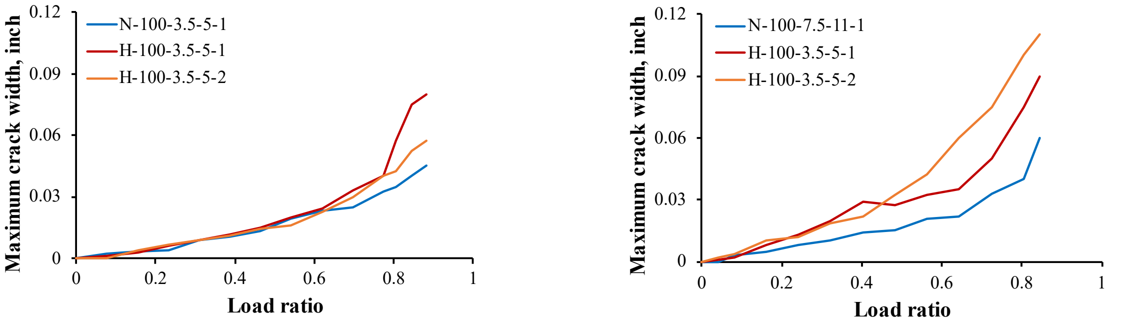

(a) 2.5% rebar ratio & 1.4 in. clear cover (b) 2.8% rebar ratio & 3.0 in. clear cover

Figure 3-115. Maximum crack width comparison depending on concrete strength

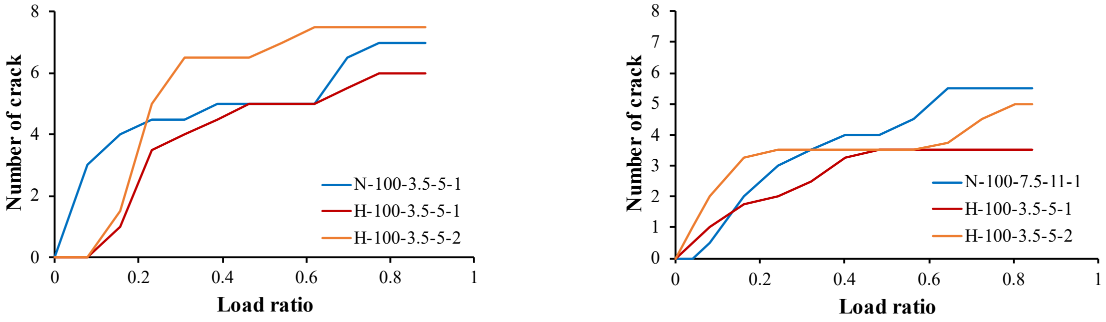

(a) 2.5% rebar ratio & 1.4 in. clear cover (b) 2.8% rebar ratio & 3.0 in. clear cover

Figure 3-116. The number of crack comparisons depends on the concrete strength

3.3.2.4.3. Conclusions

This study investigated the cracking behavior of reinforced concrete structures under uniaxial tension, focusing on the effects of various parameters, including reinforcement ratio, concrete clear cover, rebar strength, and concrete strength. The following conclusions can be drawn from the experimental results:

- Reinforcement ratio: an increase in rebar ratio leads to a decrease in maximum crack width for both Grade 60 and Grade 100 rebar.
- Concrete Cover Length: irrespective of rebar strength and concrete strength, an increase in concrete cover length increases maximum crack width. This effect becomes more pronounced with higher concrete strength.

- Rebar strength: up to the yield point, the maximum crack width based on load ratio remains similar regardless of rebar grade. However, Grade 100 rebar results in smaller maximum crack widths under the same load due to more uniform stress distribution and increased crack formation. After yielding, specimens with Grade 60 rebar show a more pronounced increase in maximum crack width compared to those with Grade 100 rebar.

- Concrete strength: while the number of cracks formed is not significantly influenced by concrete strength, there is a trend of increasing maximum crack width when using high-strength concrete (10 ksi or more). This suggests a decrease in crack control performance with high-strength concrete, though further research is needed to confirm this finding.

3.4. Summary

This chapter presents the experimental findings from the extensive experimental program, accompanied by a detailed discussion. The results and analyses encompass both superstructure and substructure bridge components examined in this project and topics related to the application of high-strength reinforcing bars, such as tension lap splice and uniaxial tension.

The experimental results largely validate the feasibility of using high-strength rebar under current design codes; however, careful consideration is required for serviceability in terms of crack width. A detailed summary of the project's findings, incorporating experimental results, is presented in Chapter 6.

Chapter 4. Finite Element Analysis

4.1. Overview

A series of extensive experiments have been conducted to evaluate the applicability of high-strength steel for various structural components (e.g. beam, girder, deck, footing, bent cap), as outlined in Chapter 3. However, these structural experiments face inherent limitations due to cost, time constraints, and restrictions on the number and scope of measurements for monitoring specimen behavior.

Numerical analysis addresses these limitations by validating experimental results, revealing behaviors that may have gone unnoticed during testing, and enabling parametric studies across variable ranges not covered experimentally. Considering these advantages, this chapter focuses on conducting finite element analysis (FEA) based on previous experimental programs to facilitate a more comprehensive and detailed investigation of high-strength rebar performance.

First, cases requiring numerical analysis were identified, and finite element (FE) models were developed to reflect the experimental configurations for each case. These models were then validated by comparing their results with the corresponding experimental results. Subsequently, the verified FE models were employed to supplement the experimental observations and generate additional insights through further analyses.

The following sections detail the development, validation, and application of the numerical analyses performed in this study.

4.2. Detail of Analysis

4.2.1. CIP-PCP Deck

4.2.1.1. Overview

Experiments on CIP-PCP decks have shown that the cracking behavior near the joints dominates the overall cracking behavior, and the limitations of the measurement due to non-continuous crack propagation and localized rebar strain measurements have been observed. Therefore, in this section, analyses have been performed to overcome these limitations and provide validity for the observation of the characteristic cracking behavior of CIP-PCP decks. In particular, analyses focused on transverse specimens, where the behavior of joints significantly influenced the overall behaviors of deck specimen.

4.2.1.2. FE Model

Figure 4-1 shows the test setup with its corresponding FE model for CIP-PCP deck specimen. The test setup was replicated in the FE model with identical dimensions. Since the deck specimen has a relatively wide width and length compared to its thickness, the mesh size should be controlled based on the thickness. This results in a small element size compared to width and length, leading to a large number of elements, which hinders efficient analysis. To address this, a symmetric half-width numerical model is employed in the FE model, assuming the plane of symmetry.

The element size of the FE models was determined through the mesh sensitivity analysis. The element size of 2-inch was concluded for appropriate analysis considering both predictive accuracy of load-carrying capacity and efficiency such as computation time. In the FE model, the deck specimen was represented using hexahedral elements. Other components, such as the load and support plates, were modeled using tetrahedral elements due to their complex geometry. Reinforcement bars and strands were applied as linear truss elements with two nodes. Material properties of concrete and reinforcing bar obtained from laboratory tests were utilized with the material model provided by ATENA 3D.

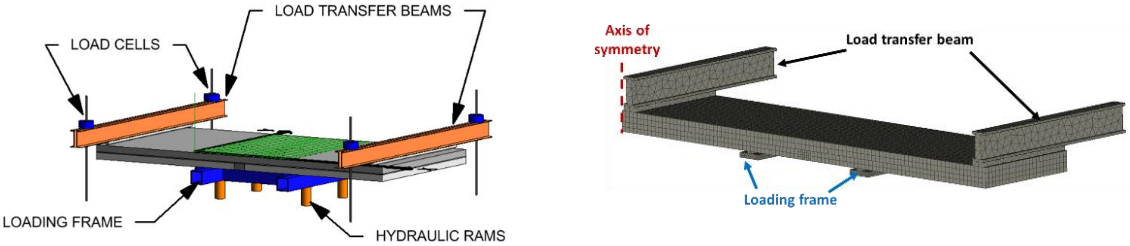

(a) Test setup (b) FE model

Figure 4-1. Test setup and FE model configuration of CIP-PCP deck

Two cases were considered to verify the influence of interface conditions between CIP and PCP: the first case assumed a perfect bond condition at the interface, while the second case used the interface material model provided by the ATENA 3D program. This interface material model simulates the interface behavior using a penalty method that accounts for parameters such as interface stiffness and tensile strength, cohesion and friction coefficient. For more information, please refer to the ATENA theory manual.

4.2.1.3. FEA Results and Discussion

When assuming perfect bond conditions at the interface between CIP and PCP, FEA exhibited a significantly higher load capacity compared to the test results for all three transverse direction specimens, as shown in Figure 4-2.

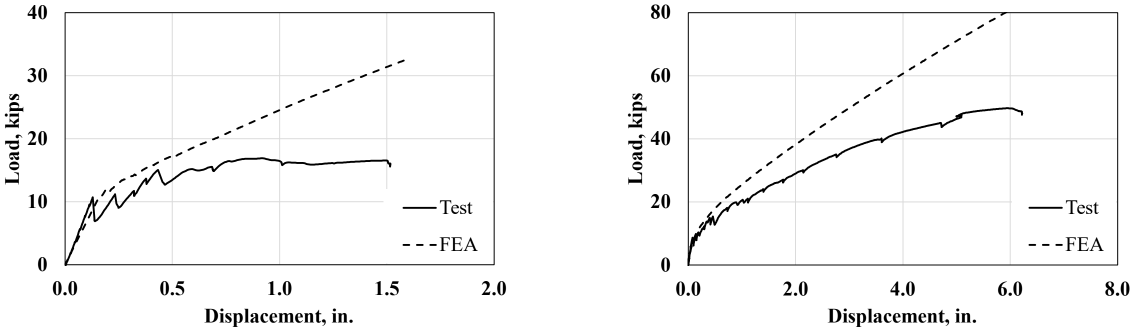

(a) TN specimen (b) TH1 specimen

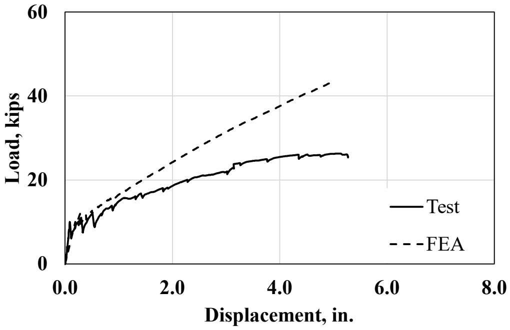

(c) TH2 specimen

Figure 4-2. Load-deflection curve comparison on transverse deck specimen with perfect bond condition (Ultimate stage)

Additionally, the crack pattern behaved similarly to a CIP deck due to the assumption of a perfect bond between CIP and PCP layer. Specifically, major cracks were observed at the center of the deck, rather than at the joint, as illustrated in Figure 4-3, and the cracks were uniformly distributed, unlike the experimental investigation. This indicates that accurate simulation of the CIP-PCP deck requires proper modeling of the interface between the CIP and PCP.

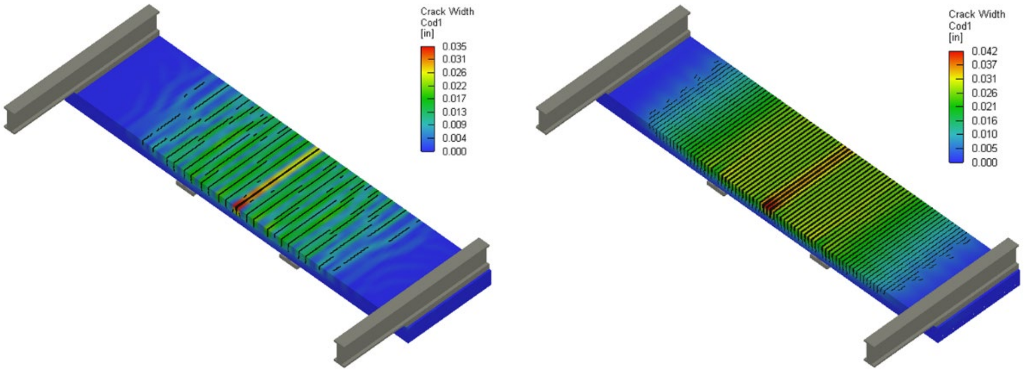

(a) TN specimen (b) TH1 specimen

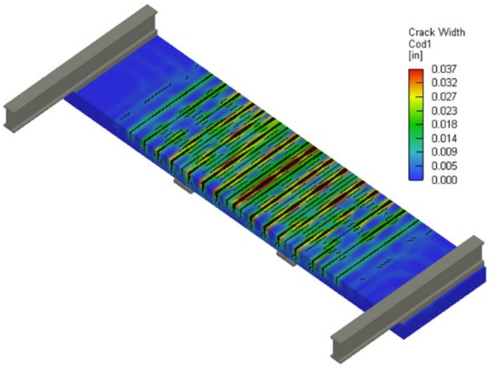

(c) TH2 specimen

Figure 4-3. Crack patterns comparison of transverse direction specimens with perfect bond condition (Ultimate stage)

Therefore, the interface material model was applied to the FE model, and the analysis was performed. For application of the interface properties, the contact condition with default values from the ATENA manual were employed in the FE model.

Considering the characteristics of the interface, the load-deflection curves from the analysis were confirmed to capture the experimental results well, as shown in Figure 4-4. In addition, the crack pattern results captured the occurrence of primary cracks at the joint, which is consistent with the actual behavior observed in the experiments, as depicted in Figure 4-5.

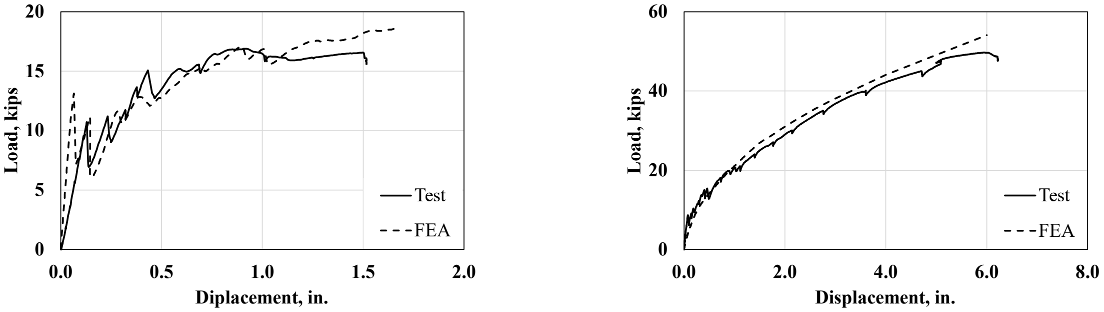

(a) TN specimen

(b) TH1 specimen

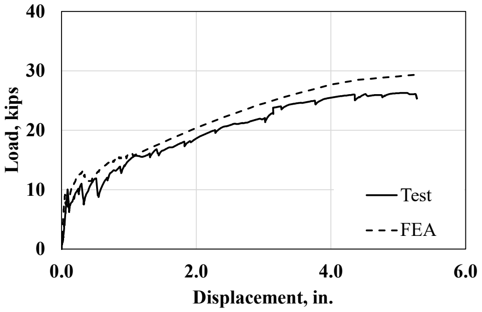

(c) TH2 specimen

Figure 4-4. Load-deflection curve comparison of transverse specimen with interface model

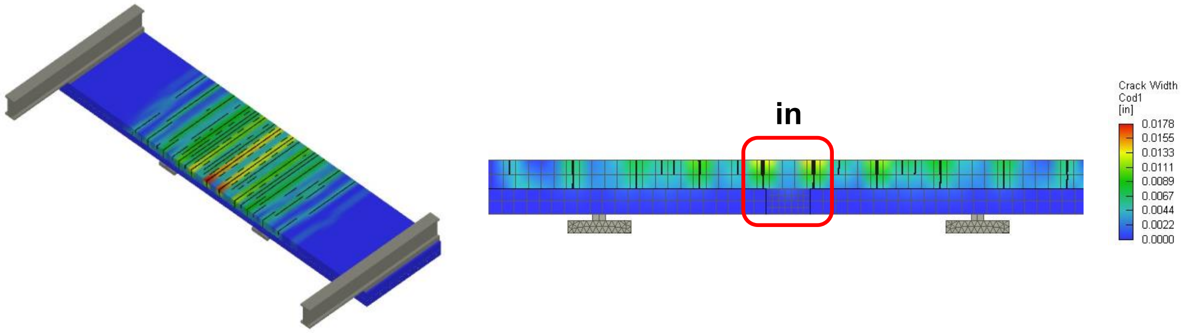

(a) TN specimen

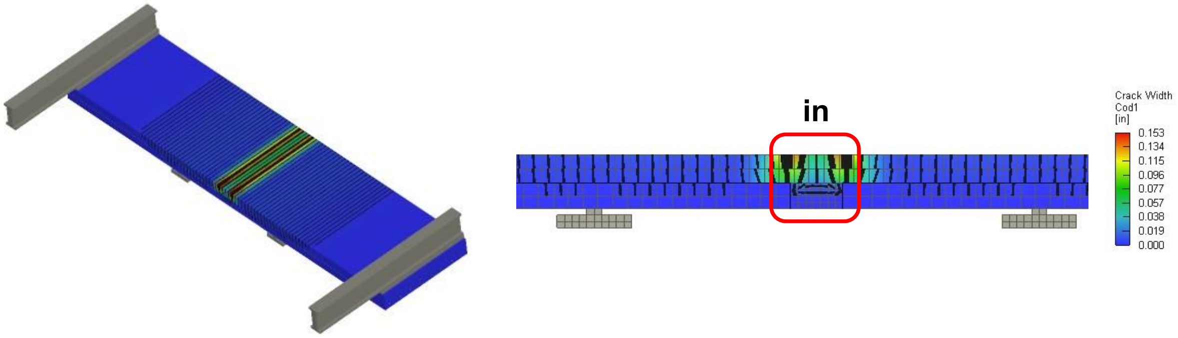

(b) TH1 specimen

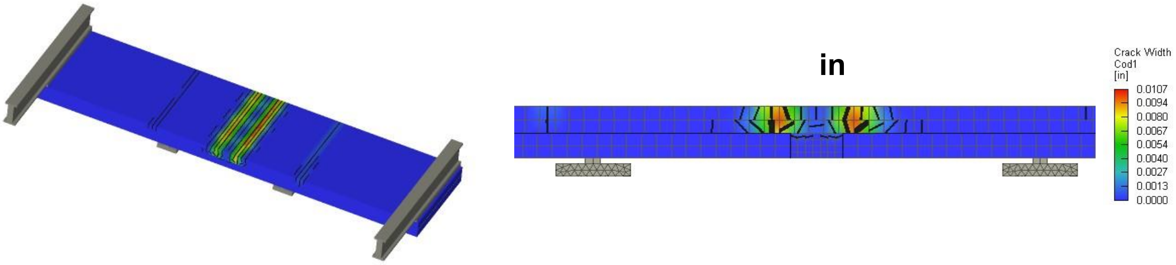

(c) TH2 specimen

Figure 4-5 Crack patterns comparison of transverse direction specimens with interface model (Ultimate stage)

4.2.1.4. Conclusions

Nonlinear finite element analysis highlighted the importance of accurately modeling the interface between CIP and PCP for predicting the behavior of CIP-PCP decks. Specifically, assuming a perfect bond at the interface resulted in overestimating the load capacity and misrepresenting crack patterns. Notably, the Atena 3D Interface model, calibrated using concrete strength properties obtained from material tests, provided reasonable and accurate predictions.

4.2.2. Prestressed Girder

4.2.2.1. Overview

Unlike the Tx-girder, the box beam includes an end block, and the reinforcement placed in the end block is designed to prevent cracks caused by temperature differences of the end block and void region that occur when the concrete cures. Additionally, these reinforcements prevent bursting, lateral, and splitting cracks that can occur in the end region during the initial prestress stage when the strands are released. This study aims to analyze whether the reinforcement placed in the end block affects the shear capacity of the box beam. For this purpose, two reinforcements of different strengths were placed in the end block with the same design.

The experimental study revealed that the strength of the reinforcement used in the end block did not affect the shear capacity of the box beam. However, while the experiments allowed for a comparison of the strength values, they were limited in analyzing the internal stress mechanisms and understanding why using high-strength reinforcement did not impact the shear strength of the prestressed box beam. Therefore, to analyze the internal stress mechanisms according to the type of rebar used in the end block and to understand why the grade of rebar in the end block does not affect the overall shear capacity of the structure, the ATENA program was used for FEA of pretensioned girders. The FEA is complemented by a full-scale experimental program conducted in Task 8, presenting the validated procedure for modeling the prestressed box beam girder under shear loading. To compare the internal stress mechanisms when the load carried by the end block is maximized, experimental specimens with relatively short loading points (when the shear span-to-depth ratio a/d is less than 2.0) were analyzed using numerical methods.

4.2.2.2. FE Model

The development methodology of the model adheres to the approach suggested by Jang (2024). This subsection briefly summarizes the modeling approach, including mesh descriptions, loading and boundary conditions, and constitutive models for the prestressed box beam girders. Material models and theories not introduced in this chapter follow the built-in functions of the ATENA 3D program (Cervenka et al., 2021). To minimize the analysis time in this study, the specimens are modeled with full girder lengths but only half of the cross-section width. To employ the symmetric half-width numerical model, the plane of symmetry is translationally restrained in its normal direction. The total process to develop the models is divided into two main stages based on the construction process: (1) the prestress transfer stage and (2) the testing stage.

The mesh geometry and element size of the FE model remain consistent throughout. Based on mesh sensitivity analysis to interpret the stress mechanism of thin webs with large bottom flange prestressed girders, previous researchers deem an element size of 2.0 inches appropriate (Alirezaei Abyaneh et al., 2019). Therefore, a typical element size of 2.0 inches is applied to model all regions of the specimen.

All 3D solid elements are developed using linear interpolation functions. Primarily, first-order hexahedral (brick) elements are adopted for concrete elements, while tapered geometries near the flanges are modeled using tetrahedral elements. Additionally, tetrahedral elements are used to model loading plates, bearing plates, and steel supports where brick elements are not suitable. For all rebar, including strands and shear reinforcement, 2D truss bar elements are employed. Figure 4-6 illustrates the finite element mesh created for the tested specimen.

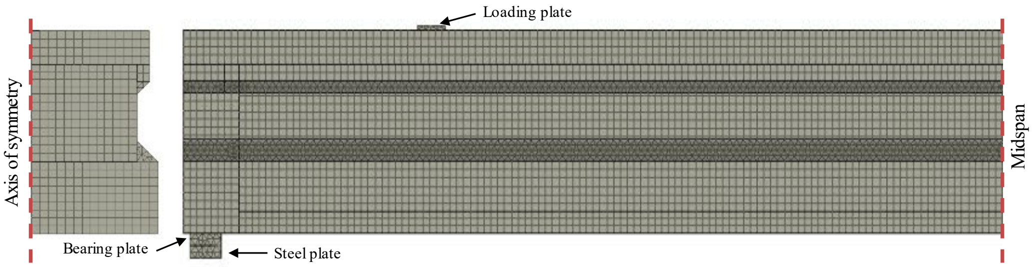

Figure 4-6. FE model for pretensioned box beam girder

To model the prestressed girder, a total of five loading conditions and two support conditions are considered. The five loading conditions consist of girder self-weight, pretensioning, concrete volumetric strain, deck self-weight, and shear force (as detailed in Table 4-1). Girder self-weight is applied as the body load, taking into account the material unit weight, and deck self-weight is applied as a uniform load on top of the girder. The pretensioning force is assumed to be the jacking force applied to the strands during the fabrication of the specimens, with a force of 44 kips applied to each strand. Additionally, the volumetric strain is intended to capture the prestress loss induced by relaxation, shrinkage, and creep that developed prior to the time of testing, taken as -0.35×10-3, as recommended by previous research (Alirezaei Abyaneh et al., 2019). Finally, the loads induced during shear testing are applied in the form of prescribed displacement using 0.01-inch increments.

Table 4-1. Loading condition for FE model of box beam girder

Load case	Loading condition	Type
1	Girder self-weight	Body load
2	Pretensioning	Pre-stressing
3	Concrete volumetric strain	Shrinkage
4	Deck self-weight	Uniform load
5	Shear force	Prescribed deformation

Two sets of support conditions are considered to detect the initial deformation (camber) caused by prestress force and the deformation due to external shear force. Until the external load is applied, the live end and dead-end portions of the girder are designated with roller and pin supports to detect the deformation of the prestressed beam caused by prestressing force and volumetric strain. To detect the deformation caused by the deck's weight and shear force, the centerline of the steel supports installed at both ends of the girder is designated with pin supports. The relationship between loading conditions and boundary conditions is illustrated in Figure 4-7.

Loading condition **Boundary condition**

- Girder self-weight
- Pretensioning
- Volumetric strain

- Deck self-weight
- Shear force

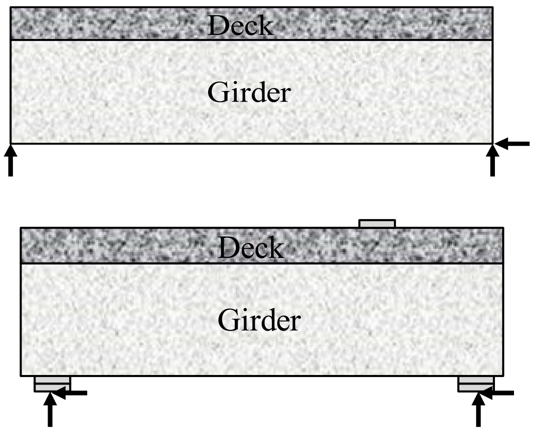

Figure 4-7. Loading and boundary condition for each stage of FE model

Six material models are defined to model the box beam: covering girder concrete, deck concrete, prestressing strand, steel reinforcement, steel plate, and bearing plate. Material properties obtained from material experiments are applied, while default material properties from ATENA 3D are used for other variables (Cervenka et al., 2021). An appropriate tension stiffening factor is also assumed for the relative limiting value of tensile strength in the tension softening diagram to enhance numerical stability at the analysis's ultimate stage. A tension stiffening factor of 0.2 is assumed for all specimens' models, consistent with other studies on prestressed girders (Okumus et al., 2012; Van Meirvenne et al., 2018), to comply with the stress-crack opening relation proposed by the CEB-FIP Model Code 2020 (2023).

The bond properties between the prestressing strand and concrete, crucial for considering the prestress transfer at the beam's end region, are also defined as material models in ATENA 3D. The bond model from Bigaj (1999) is adopted to effectively capture prestressing stress transfer length and prestress transfer stage concrete damage. The slip and bond strength relation is automatically calculated based on concrete compressive strength, strand diameter, and qualitative measurement of the bond in this model.

4.2.2.3. FEA Results and Discussion

Before analyzing the stress mechanism of the prestressed box beam using FEA models, the predictive capabilities of the developed model are assessed using a series of experimental results. The load-deflection responses and crack patterns at the ultimate stages (failure mechanisms) are key aspects in validating the FEA model for shear testing (Alirezaei Abyaneh et al., 2019).

Therefore, this study compares the load-deflection curves of the four box beams from the experimental and FEA results for failure mechanisms under shear loading.

The load-deflection responses from the finite element models for the four box beam specimens are compared with the experimental results. As depicted in Figure 4-8, the FE models successfully predict the behavior of the box beams in terms of initial stiffness, load capacity, and ultimate deflection. This outcome indicates that the FE model accurately captures the shear behavior of the prestressed box beam under loading conditions. The ultimate capacities of the girders are predicted to be within approximately 6% of the measured capacities, as shown in Table 4-2, which is within the suitable accuracy range for prestressed girders (Alirezaei Abyaneh et al., 2019).

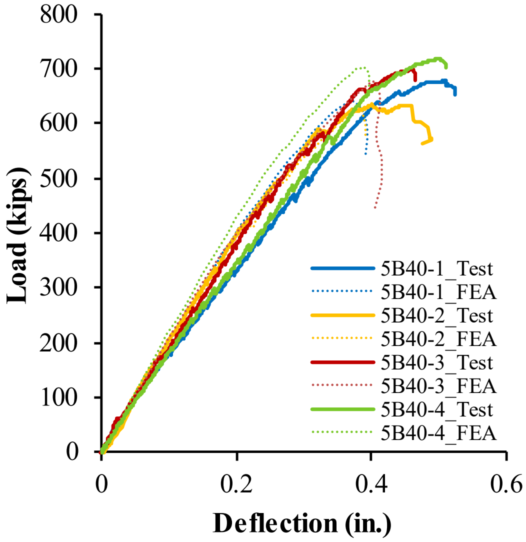

Figure 4-8. Load-deflection curve comparison of box girder

Table 4-2. Ultimate capacity comparison of box girder

Test ID	$V_{u,test}^{(a)}$ (kip)	$V_{u,FEA}^{(b)}$ (kip)	Ratio (a)/(b)
5B40-1	678	641	1.06
5B40-2	635	628	1.01
5B40-3	698	677	1.03
5B40-4	718	703	1.02

The failure mechanism results of FEA and experiments for box beams are compared based on the crack patterns at the ultimate conditions, as illustrated in Figure 4-9 to Figure 4-12. The findings suggest that crack propagation is nearly identical in both the experimental and FEA results. Furthermore, the FEA results indicate that when using only one support, diagonal cracks in the longitudinal direction occur more prominently toward the back of the support, closer to the girder's edge, compared to when two supports are used. Additionally, the differences in crack distribution in the girder's cross-section based on the support condition align with the experimental results.

Thus, it can be argued that the developed FEA model effectively detects the failure mechanism of the specimens.

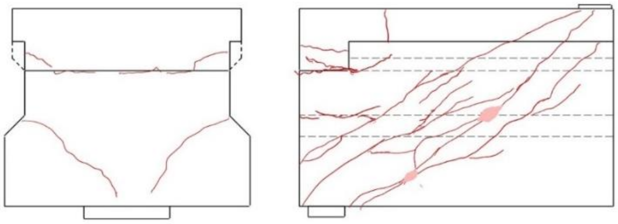

(a) Test

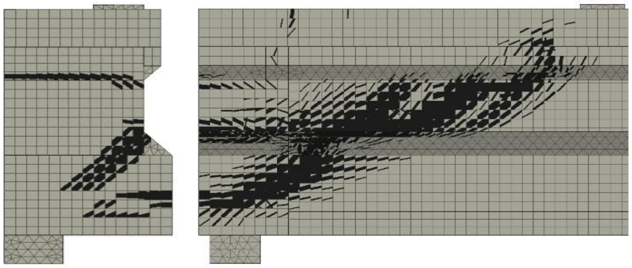

(b) FEA

Figure 4-9. Crack pattern comparison for 5B40-1

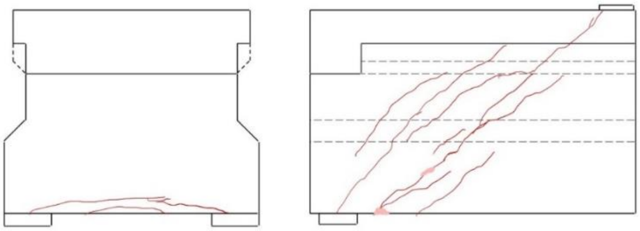

(a) Test

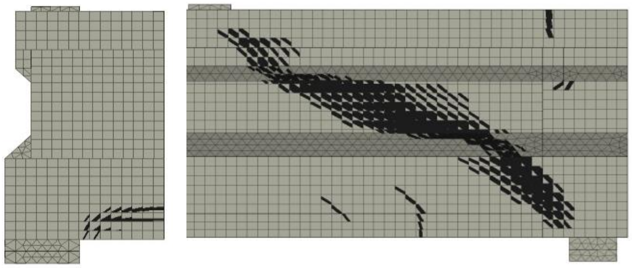

(b) FEA

Figure 4-10. Crack pattern comparison for 5B40-2

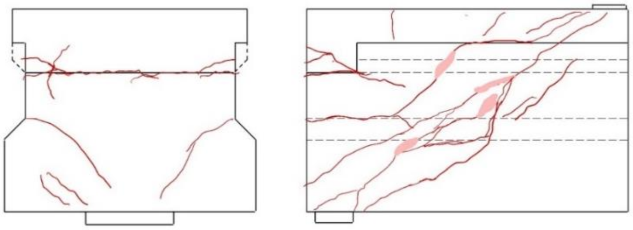

(a) Test

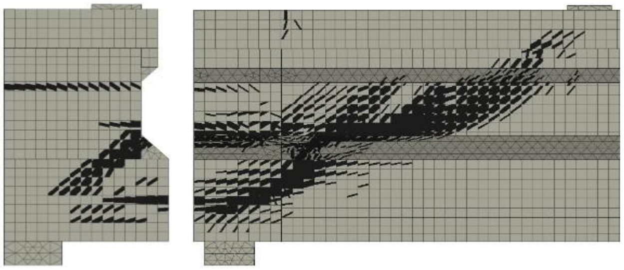

(b) FEA

Figure 4-11. Crack pattern comparison for 5B40-3

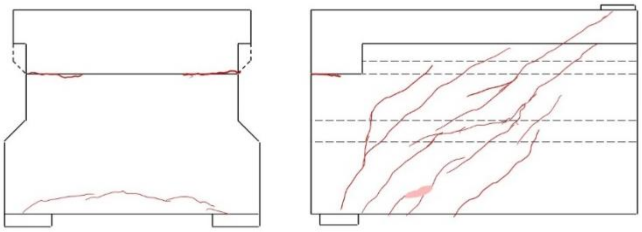

(a) Test

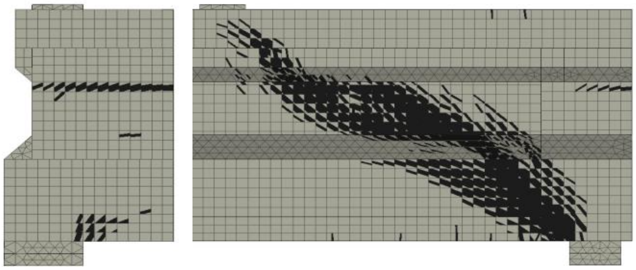

(b) FEA

Figure 4-12. Crack pattern comparison for 5B40-4

Utilizing the developed FE model, the analysis focuses on the stress mechanism within the end block. The distribution of principal stresses in the end region reinforcement (end block and shear reinforcement) is employed to analyze the stress mechanism of the specimen. The stress distribution of reinforcement for each specimen is depicted in Figure 4-13.

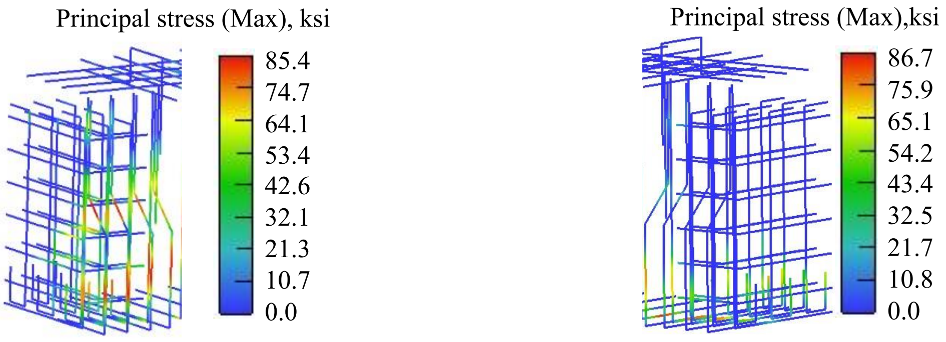

5B40-1 (One support) 5B40-2 (Two supports)

(a) Grade 60

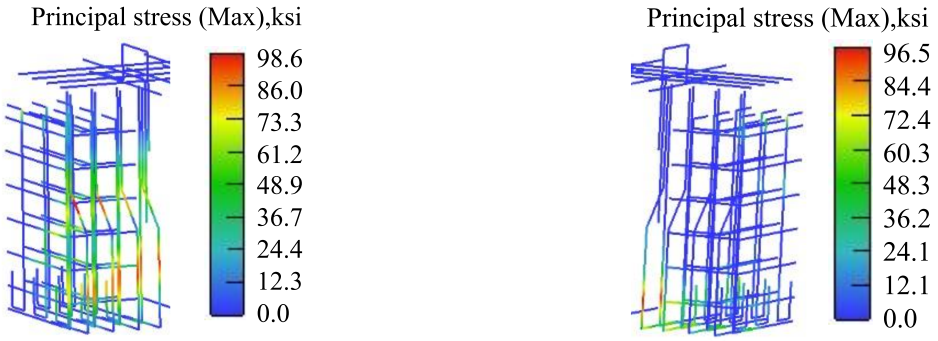

5B40-3 (One support) 5B40-4 (Two supports)

(b) Grade 100

Figure 4-13. Stress mechanism at the end block with respect to rebar grade

The stress mechanisms were compared when Grade 60 and Grade 100 rebars were used as end block reinforcement and shear reinforcement in box beams under different support conditions. The results showed that when two supports were used, the stress flowed directly from the loading point to the supports, causing the rebars in the end block to experience minimal stress due to shear forces. Therefore, when two supports are used in a prestressed box beam, the reinforcement in the end block does not influence the resistance to shear forces, and there is no correlation between the strength of the reinforcement in the end block and the overall shear capacity of the girder.

In contrast, when a single support was used, the reinforcement in the end block experienced stress due to shear forces, unlike the case with two supports. However, the stress flow formed in the reinforcement of the end block was similar, and the maximum principal stress observed at the ultimate shear capacity was also nearly identical. Thus, even with a single support, the strength of the rebar in the end block does not affect the overall shear performance of the prestressed box beam.

Consequently, the analysis of the stress mechanisms of the end block reinforcement under shear forces using FEA explained why the strength of the reinforcement in the end block is unrelated to the shear capacity of the prestressed box beam.

4.2.2.4. Conclusions

The comprehensive study presented in this technical memorandum aimed to investigate the impact of end block reinforcement on the shear capacity of prestressed box beams. The developed FEA models were validated against experimental results, showing accurate predictions of load-deflection responses and failure mechanisms. The ultimate capacities of the girders predicted by the FEA models were within approximately 6% of the measured capacities, demonstrating the reliability of the numerical approach.

The FEA successfully demonstrated that the strength of the end block reinforcement does not influence the shear capacity of prestressed box beams. This finding was consistently observed in both experimental and numerical analyses. The stress mechanisms revealed by FEA provided a robust explanation for the observed experimental results, highlighting the independence of end block reinforcement strength from the overall shear performance. The validated FEA models serve as a reliable tool for predicting the shear behavior of prestressed box beams, offering valuable insights for future design and analysis efforts.

4.2.3. Deep Beams

4.2.3.1. Overview

Deep beams have complex reinforcement details, including large-sized longitudinal reinforcement and transverse reinforcement, which consist of vertical and horizontal ties for crack control. However, members in the D-region designed using the strut-and-tie method still face rebar strength limitations due to a lack of test data.

The experimental work presented in the previous chapter evaluated the application of high-strength rebar in deep beams in accordance with the provisions of current design regulations. However, limitations remained in the cross-validation data available for comparing and verifying the experimental findings. To address this, this chapter incorporates a process of validating the experimental results using FEA.

4.2.3.2. FE Model

Figure 4-14 shows the test setup of deep beams and its associated FE model. The model accurately replicates all test conditions, including the geometry, boundary conditions, and loading conditions, with matching dimensions. The deep beams were loaded through displacement control method. Reaction forces were obtained at the same locations as the load cells in the experiments.

The element size was determined as 2 inches through preliminary analysis. Concrete beams were modeled with 3D hexahedral (brick) elements. For steel plates, as well as load transfer beams, tetrahedral elements were used due to geometric constraints. The reinforcing bars were represented using 2D truss bar elements.

After accounting for the self-weight of the concrete beam and load transfer beam, displacement increments of 0.003 inches were gradually applied at the hydraulic ram location. The concrete material model from the ATENA program was employed, using the strength values obtained from cylinder tests. For the rebars, the stress-strain curve from the coupon experiments was directly applied.

Notably, each beam was subjected to two tests. After the first test, the damaged part was reinforced using a pre-tensioned clamp, and then the second test was carried out. For the 42-inch beam, it was found that the first test did not significantly affect the second test region due to the reinforcement by the pre-tensioned clamp. Therefore, the FEA for the second test of the 42-inch beam did not consider pre-existing damage. For the 75-inch beam, although the loading point was in the middle of the beam, the load-deflection curve of the second test showed a similar shape to the first test, except for the ultimate capacity. This similarity may be attributed to the strengthening of the damaged region. Therefore, the FEA for the second test of the 75-inch beam also did not consider pre-existing damage.

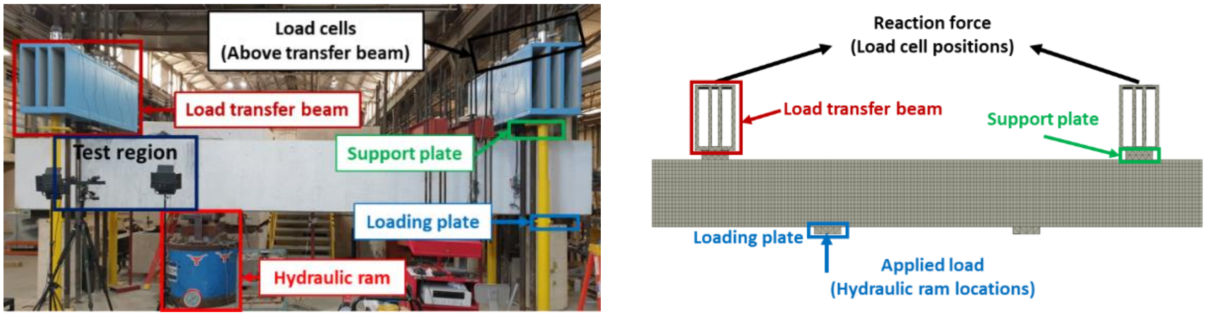

Figure 4-14. Test setup and FE model configuration for deep beams

4.2.3.3. FEA Results and Discussion

Although the rectangular deep beam tests differed in dimensions and load locations depending on the variables, the same test setup and loading conditions were used. Considering this, the analysis results of the 42-inch rectangular deep beam were compared with the experimental results to develop the FE model. The developed FE model was then used in the analysis, considering variables such as the grade of longitudinal reinforcing bar, crack control reinforcement ratio, and beam dimensions. The FEA results were compared and analyzed against the experimental data. Moreover, the main objective of the deep beam shear test is to confirm the applicability of the strut-and-tie model to deep beams with high-strength steel. Therefore, the ultimate capacity and failure mode, including the crack pattern observed in the FEA, were compared with the test results.

Table 4-3 summarizes the ultimate shear capacity from each test and the corresponding FEA results. FEA successfully predicted the ultimate shear capacity of the deep beams within the range of 10% in all cases, except for the case of L100-W100-0.3-42. This discrepancy is may be due to the relatively lower ultimate shear capacity was measured for the L100-W100-0.3-42 beam compared to other 42-inch height beams.

Table 4-3. Ultimate capacity comparison for test and FEA of deep beams

Test ID	$V_{u,test}^{(a)}$ (kip)	$V_{u,FEA}^{(b)}$ (kip)	Ratio (b)/(a)
L60-W100-0.2-42	567	581	1.02
L60-W100-0.3-42	536	562	1.05
L100-W100-0.2-42	537	552	1.03
L100-W100-0.3-42	479	562	1.17
L60-W100-0.2-75	711	716	1.01
L60-W100-0.3-75	938	889	0.95
L100-W100-0.2-75	743	756	1.02
L100-W100-0.3-75	915	895	0.98
IT-L60-W100-0.2-42	480	492	1.03

Figure 4-15 to Figure 4-23 compare the crack patterns at various load steps observed in both the experiment and FEA.

For rectangular beams, at the initial loading stage, some flexural cracks appeared on the tension side in the shear span. As the load increased, diagonal cracks from the tip of the flexural cracks propagated toward the loading point. Cracks continued to propagate and widen with increasing load, and strut-to-node interface failure occurred at ultimate applied loads. In particular, failure occurred at the node (CCC node) in the loading plate. FEA successfully predicts these cracking patterns and can particularly identify failure modes where direct strut failure occurs at the strut-to-node interface. Moreover, FEA can capture cracks developing in the concrete above the loading plate as it approaches failure.

In the case of the inverted T-beam, unlike the rectangular beam, the test revealed a ledge failure mode accompanied by the yielding of the ledge reinforcement. Similarly, in the FEA, the maximum principal strain was observed at the edge of the ledge, which was consistent with the experimental results, and the yielding of the ledge reinforcement was also confirmed.

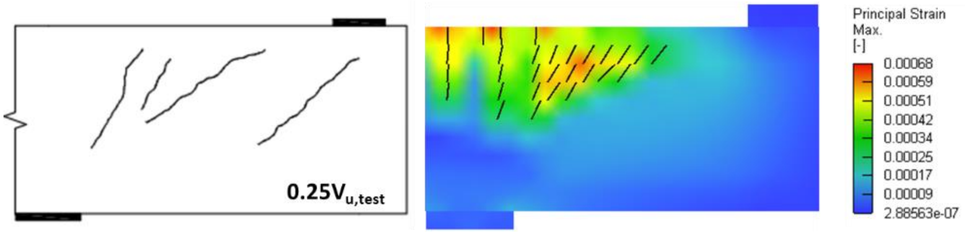

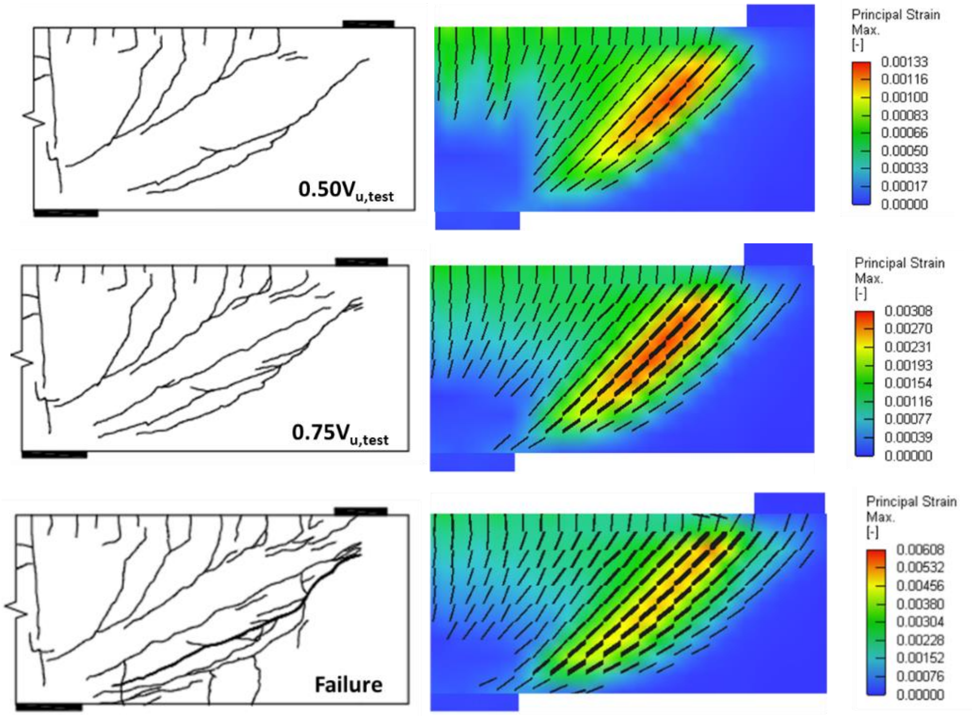

Figure 4-15. Crack patterns comparison of R-L60-W100-42-0.2 specimen

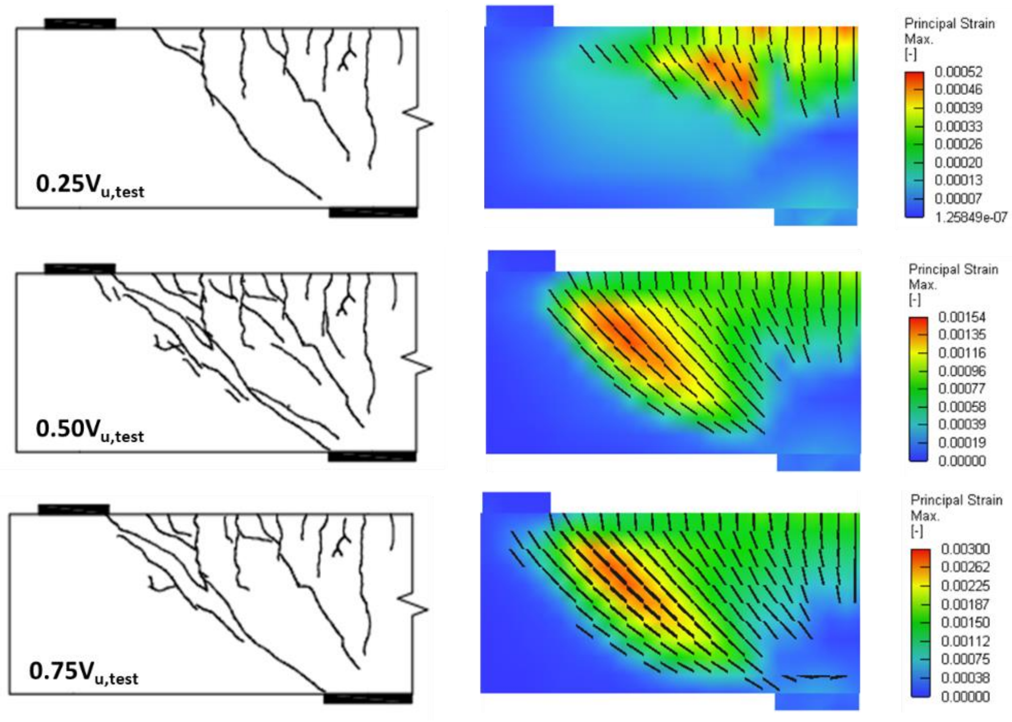

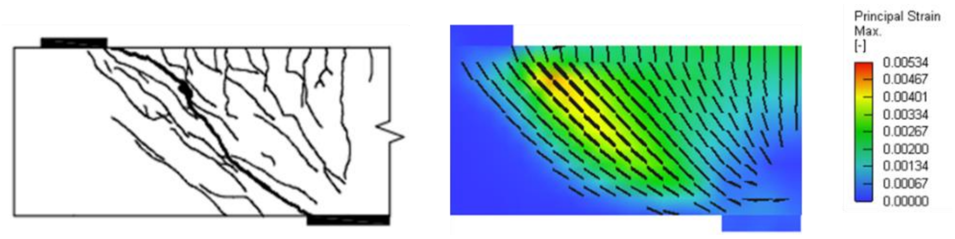

Figure 4-16. Crack patterns comparison of R-L60-W100-42-0.3 specimen

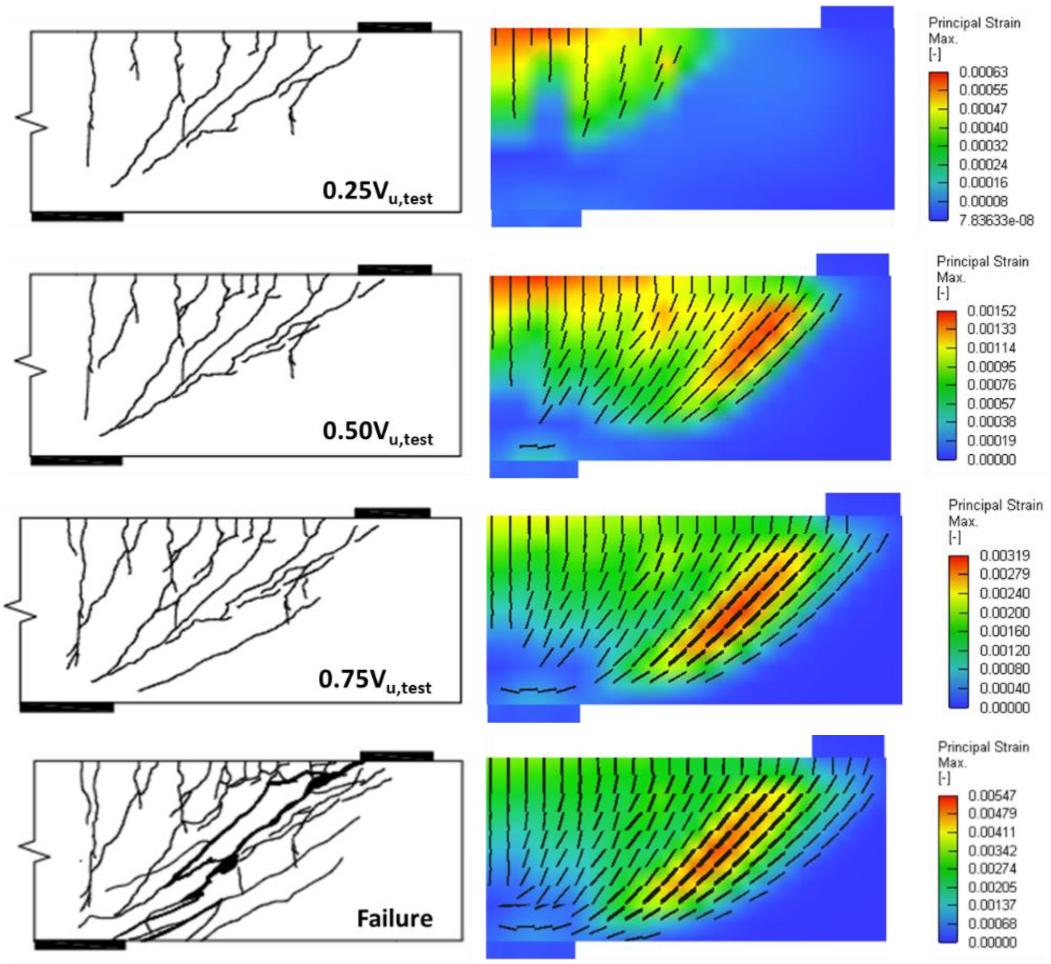

Figure 4-17. Crack patterns comparison of R-L100-W100-42-0.2 specimen

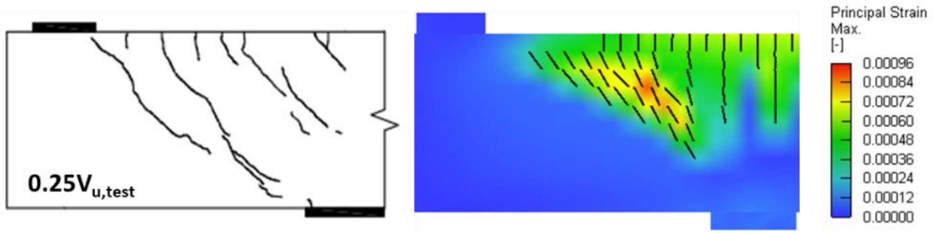

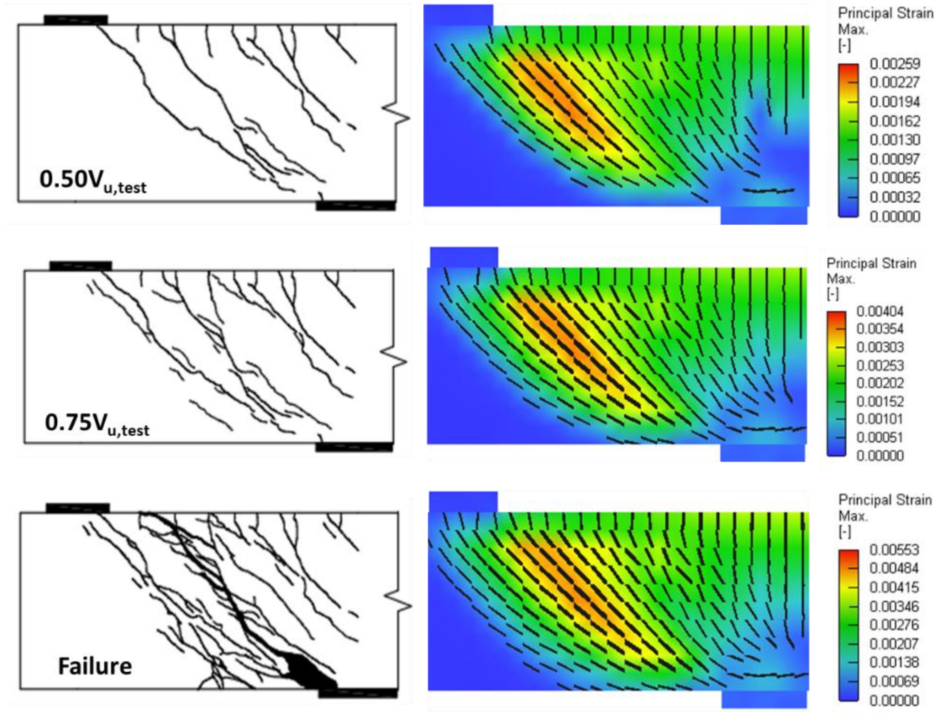

Figure 4-18. Crack patterns comparison of R-L100-W100-42-0.3 specimen

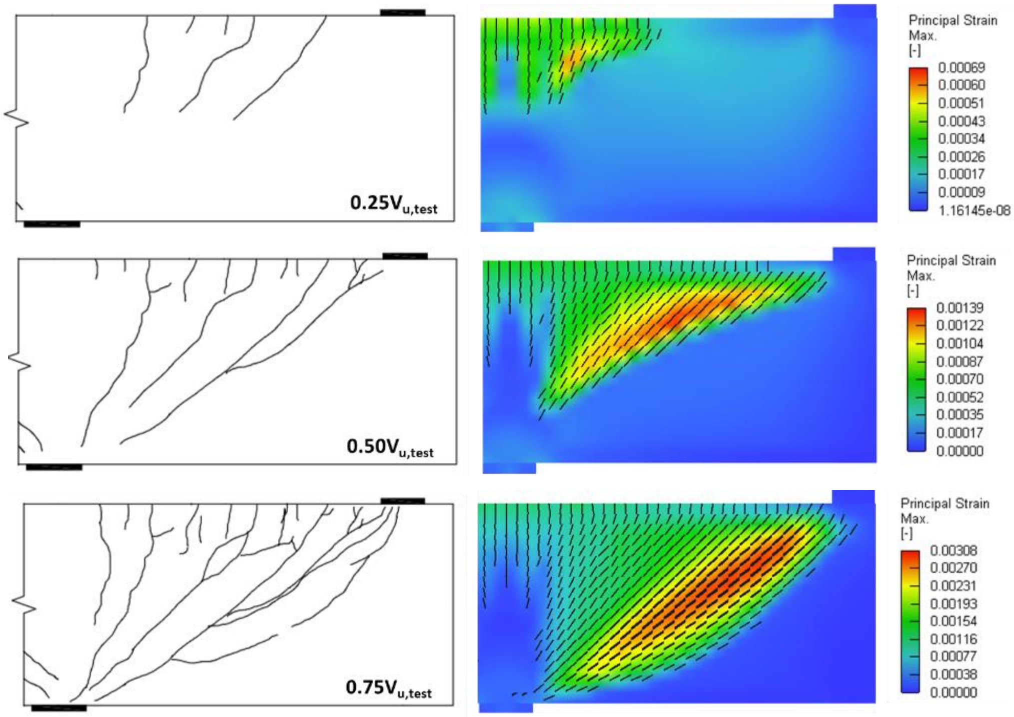

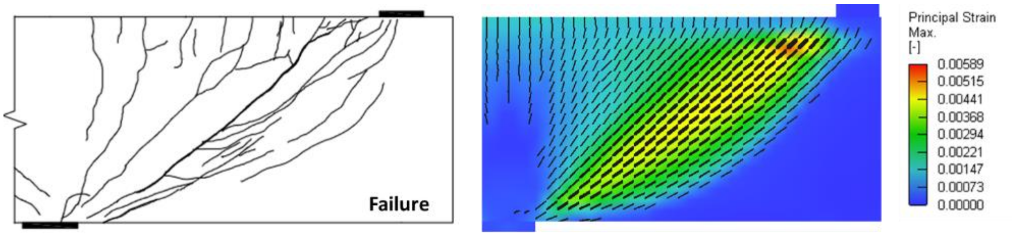

Figure 4-19. Crack patterns comparison of R-L60-W100-75-0.2 specimen

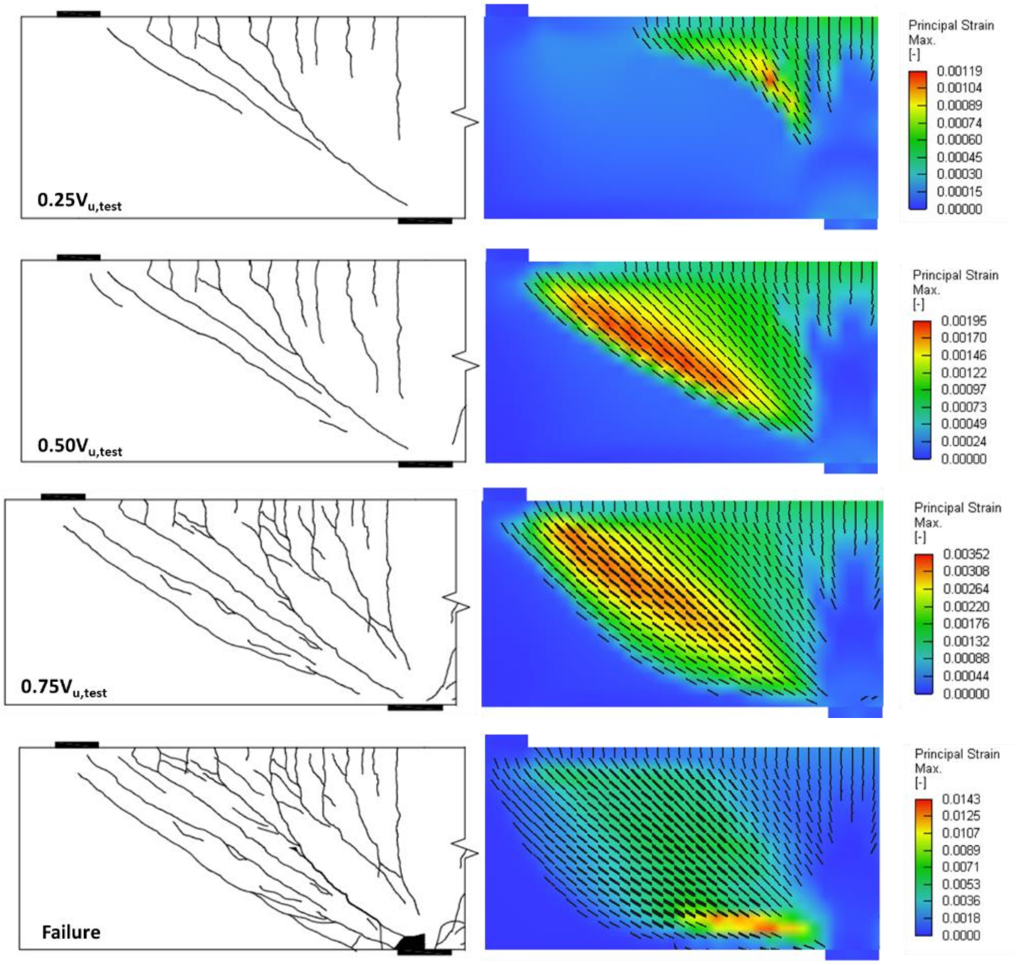

Figure 4-20. Crack patterns comparison of R-L60-W100-75-0.3 specimen

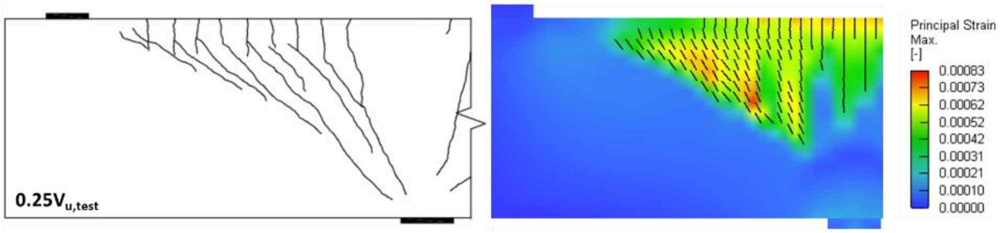

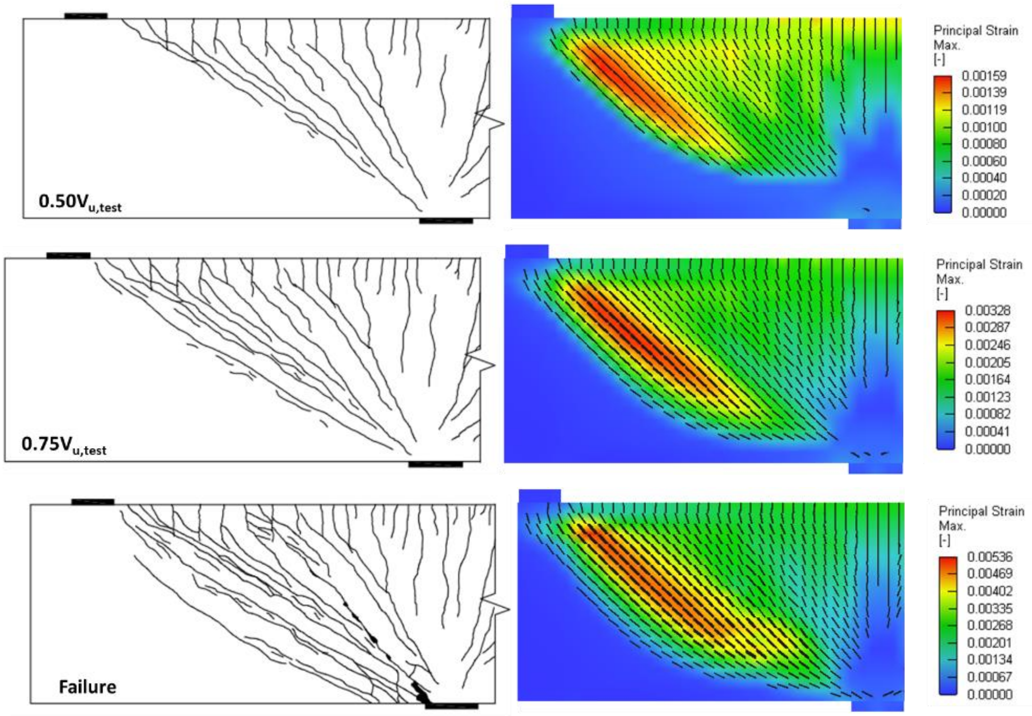

Figure 4-21. Crack patterns comparison of R-L100-W100-75-0.2 specimen

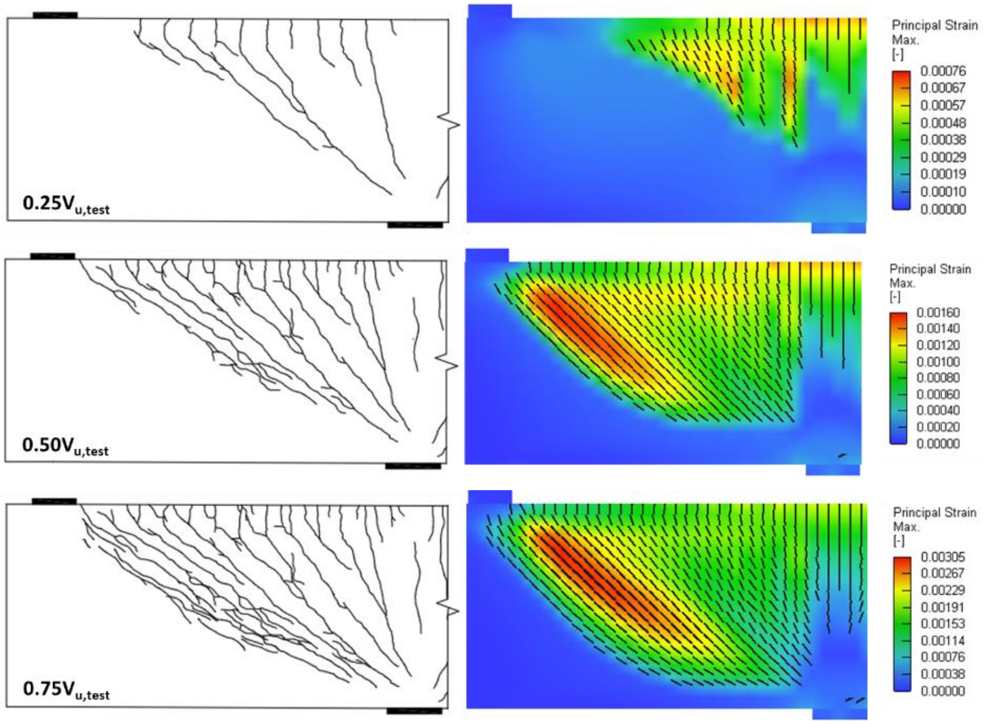

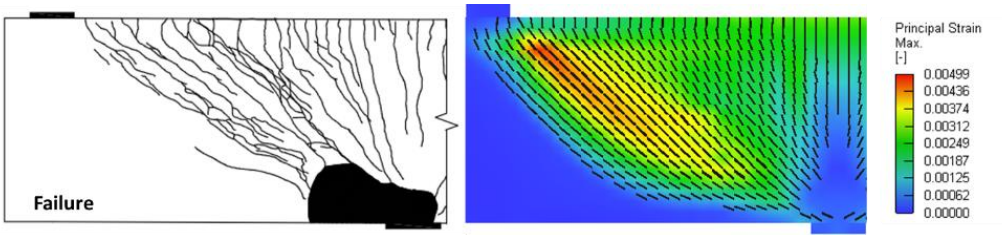

Figure 4-22. Crack patterns comparison of R-L100-W100-75-0.3 specimen

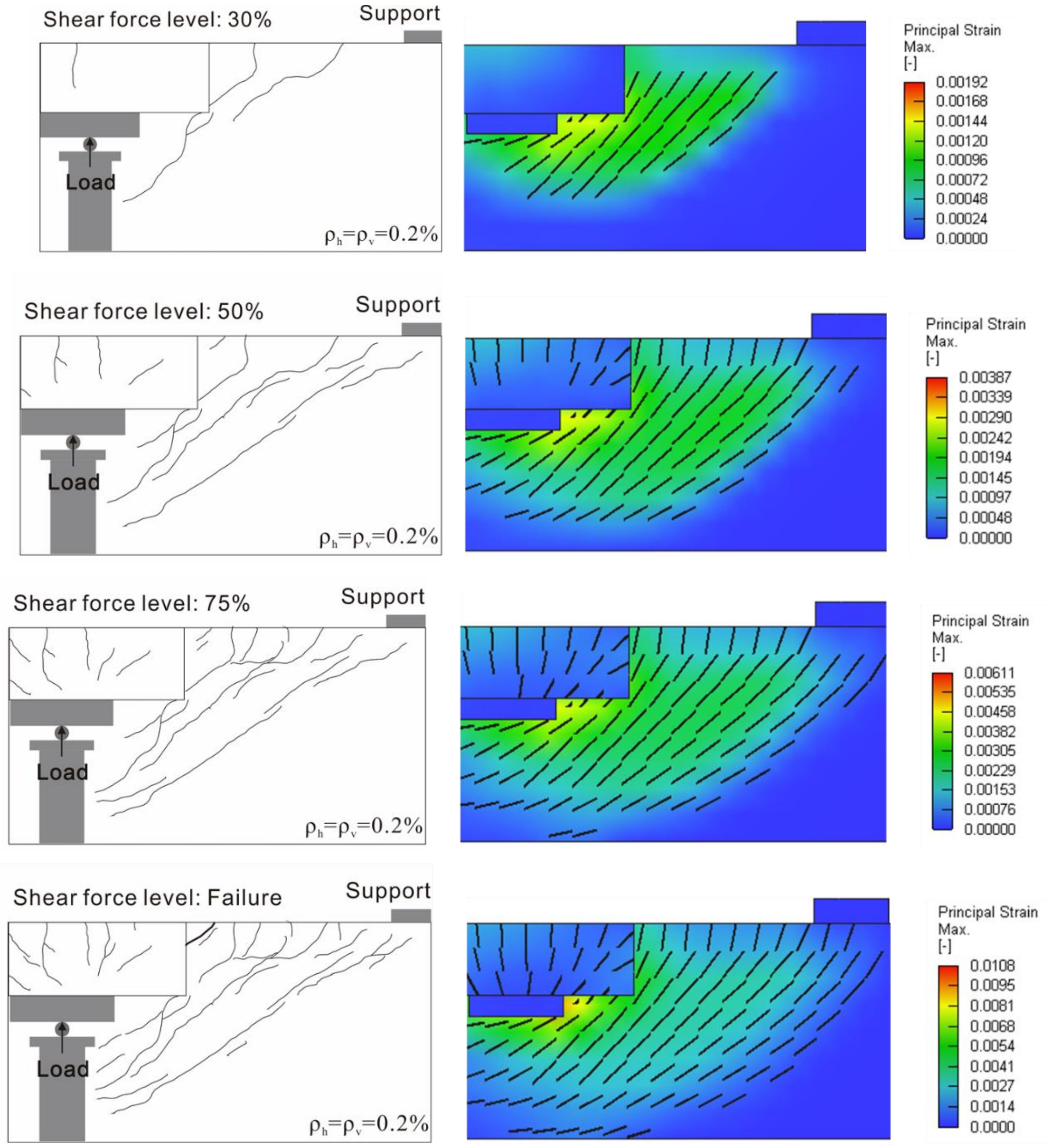

Figure 4-23. Crack patterns comparison of IT-L60-W100-42-0.2 specimen

Additionally, the maximum stress in the longitudinal reinforcement and the force transmitted through it were analyzed. The results were compared between the use of high-strength rebar with reduced quantity and normal-strength rebar, as summarized in Table 4-4. The comparable transmitted forces indicate that the reduced quantity of high-strength longitudinal reinforcement can effectively carry the loads.

Based on these results, it was confirmed that the FEA can effectively predict deep beam experimental results. Specifically, the shear behavior was effectively predicted when high-strength rebar was applied for reinforcement.

Table 4-4. Stress and force of longitudinal rebar of rectangular deep beams

Test ID	$0.25V_{u,test}$		$0.50V_{u,test}$		$0.75V_{u,test}$		$V_{u,test}$	
	Avg. stress (ksi)	Total force (kip)	Avg. stress (ksi)	Total force (kip)	Avg. stress (ksi)	Total force (kip)	Avg. stress (ksi)	Total force (kip)
L60-W100-0.2-42	11.5	209	26.1	473	40.6	735	55.3	1,001
L100-W100-0.2-42	18.0	190	41.3	437	64.4	680	87.2	922
L60-W100-0.3-42	11.9	216	25.5	462	39.7	719	54.1	980
L100-W100-0.3-42	19.2	203	44.9	475	68.6	726	92.3	975
L60-W100-0.2-75	13.7	455	18.8	623	29.2	971	39.7	1,318
L100-W100-0.2-75	22.1	501	35.8	702	47.8	1,079	75.2	1,476
L60-W100-0.3-75	12.5	414	21.3	706	35.4	1,176	47.2	1,567
L100-W100-0.3-75	23.5	462	38.4	754	57.7	1,132	87.7	1,721

4.2.3.4. Conclusions

FEA was conducted on deep beams to validate the experimental test results. Using ATENA 3D software, the research team developed an FE model incorporating variables such as reinforcement arrangement, beam height, and cross-sectional shape. The analysis confirmed that the model effectively predicted the experimental outcomes, reinforcing the validity of the experimental conclusions and providing a foundation for future parametric studies.

4.2.4. Drilled Shaft Footing

4.2.4.1 Overview

Drilled shaft footings are structural members designed to transfer loads from a bridge pier to drilled shafts embedded in soft soil. As such, they typically feature complex reinforcement details to ensure the full development of reinforcement bars extending from the columns and drilled shafts. This results in highly congested reinforcement cages, significantly increasing fabrication time and cost. The experimental work described in the previous chapter supports reducing the amount of mat reinforcement in drilled shaft footings by replacing normal-strength steel reinforcement with high-strength steel reinforcement. Specifically, studies demonstrated that using high-strength steel for bottom mat reinforcement maintained similar stress flow and load capacity, even with reduced reinforcement. However, a sudden side failure was observed when the amount of side surface reinforcement was decreased. Notably, the experiment focused solely on cases with reduced side reinforcement, and stress flow was assessed using a limited number of gauges. To address these limitations, comprehensive verification was conducted through the FEA.

4.2.4.2. FE Model

The drilled shaft footing specimens are subjected to concentric axial loading; therefore, one-quarter drilled shaft footing finite element mesh was developed by taking advantage of the symmetric loading condition.

The element size of the FE models of this study was determined based on the mesh sensitivity analysis conducted for drilled shaft footing conducted in a previous study (Yi et al. Forthcoming. The mesh analysis concluded that a typical element size of 2.0-inches is appropriate for drilled shaft footing models considering both capacity estimation accuracy and computational efficacy (e.g., CPU time.

The FE model comprises two macro elements: footing and auxiliary components (loading and supporting plates. Except for the round-shaped supporting plate, which was modeled with tetrahedral elements, the model was developed using first-order hexahedral (brick solid elements. The reinforcing bars in the test specimen were modeled in the finite element model using three-dimensional linear truss elements with two nodes. Figure 4-24 illustrates developed finite element meshes for the analysis.

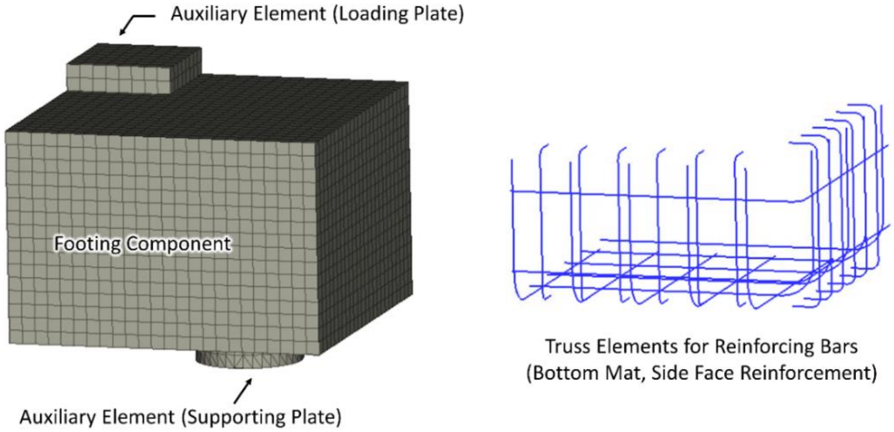

Figure 4-24. FE model developed for one-quarter drilled shaft footing (left) and truss elements developed for reinforcement (right)

Two internal faces of the quarter-footing FE model were laterally restrained for the symmetric conditions. A vertical restraint was provided at the center of the supporting plate component to simulate the actual supporting condition, allowing rotation and lateral translation. Prescribed vertical displacements are imposed at the whole surface of the loading plate with increments of 0.01 inches. The self-weight of the footing was also considered by the way of body force, 150 lb/ft^3. The analysis was continued until a significant drop in computed load was identified. Figure 4-25 illustrates the loading and boundary conditions imposed to the FE model.

The material properties of the concrete in each footing FE model were determined by as-measured concrete compressive strength on respective test day. All other parameters related to the concrete were estimated by the program automatically. The stress-strain curves obtained from tensile reinforcing bar tests were directly imported to the program for the material properties of the truss elements developed in the FE model. Further, perfect bond between concrete and reinforcement was assumed for the analyses.

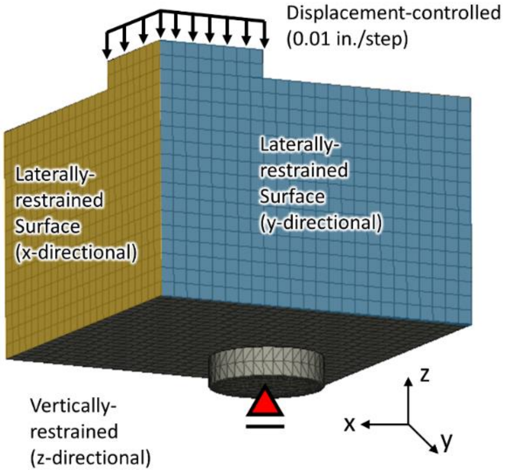

Figure 4-25. Loading and boundary conditions in FE models for drilled shaft footings

4.2.4.3. FEA Results and Discussion

The developed FE models for drilled shaft footings can be validated by comparing the analysis results with those attained from large-scale tests. Therefore, the load-deflection responses and crack patterns measured from the tests were compared with those computed from the FEA. The stress distribution of the bottom mat reinforcement was investigated using the verified FE models to clarify the impact of applying high-strength steel on the bottom mat reinforcement of drilled shaft footings.

Figure 4-26 compares the measured and computed load-deflection responses of the tested drilled shaft footing specimens. Even though the analysis result overestimated the first cracking load of the specimen with high-strength bottom mat reinforcement, the developed models could predict overall responses accurately, as measured in the tests. Table 4-5 compares the ultimate load-carrying capacities computed from the analyses and those measured from the tests. The ultimate capacity ratios of experimental and numerical obtained from both specimens are close to 1.00 and comparable, which indicates that the developed model can predict the ultimate capacity with a reasonable accuracy level.

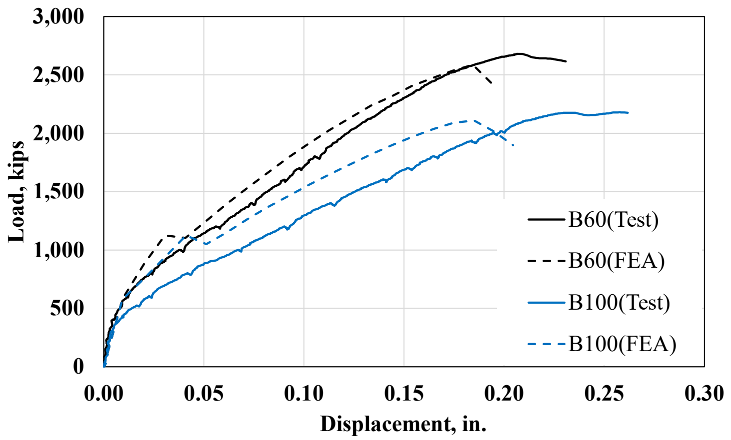

Figure 4-26. Load-deflection comparison of drilled shaft footings

Table 4-5. Ultimate capacity comparison of drilled shaft footings

Test ID	$V_{u,test}^{(a)}$ (kip)	$V_{u,FEA}^{(b)}$ (kip)	Ratio (b)/(a)
B60	2,680	2,587	1.04
B100	2,170	2,108	1.03

The computed crack patterns in the finite element models were compared with those observed in the experimental program. Because some exterior surfaces of the test specimen were severely damaged due to impact during failure and the covering concrete spalled off, the least damaged exterior side of the test specimen after the test was selected as the experimental crack pattern at the ultimate load. Further, the test specimens were dissected in half using a diamond chain saw to inspect the interior crack pattern. Both exterior and interior crack patterns obtained from the analyses and tests are compared in Figure 4-27.

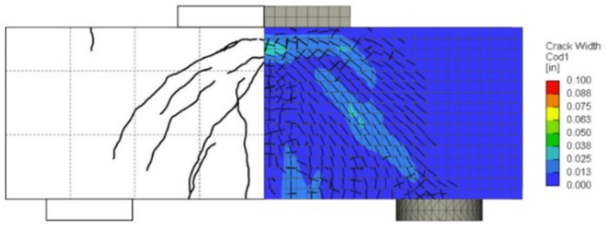

(a) B60 specimen

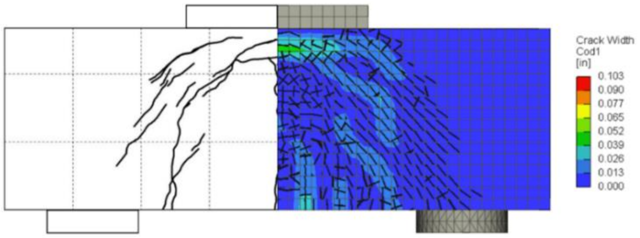

(b) B100 specimen

Figure 4-27. Crack pattern comparison at respective ultimate loads of drilled shaft footings

Overall, the measured and computed crack patterns are comparable. The analyzed crack patterns of both specimens showed a series of arch-shaped cracks and a large crack opening at the elevation of the 90-degree hook ends of the bottom mat reinforcement on the exterior faces, consistent with the crack pattern observed in the tested specimens. The computed interior crack pattern was also almost identical to that observed from dissected test specimens. Therefore, the developed FE models could accurately capture the failure mechanisms of the footing specimens. The validated FE models were used to investigate the effect of applying high-strength steel to the bottom mat reinforcing bars of drilled shaft footings. Figure 4-28 shows the stress distributions of the truss elements in the finite element models at respective ultimate loads.

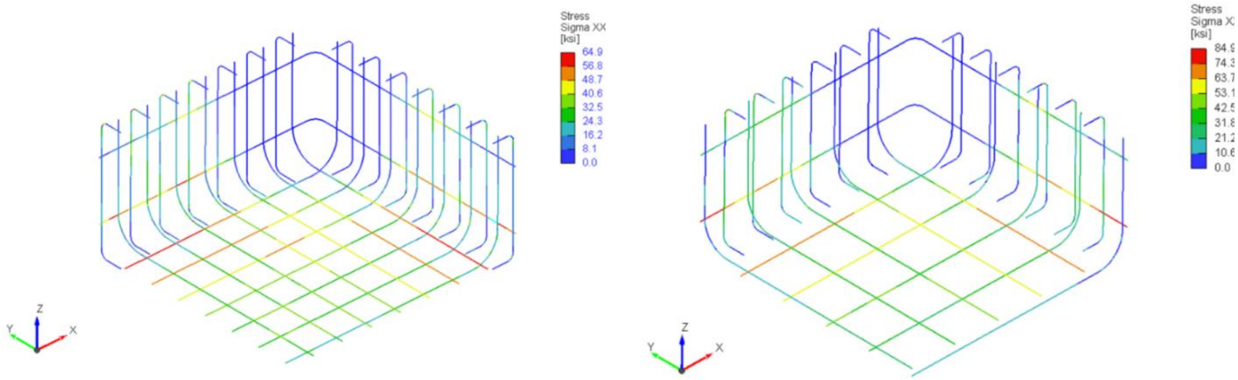

(a) B60 specimen

(b) B100 specimen

Figure 4-28. Stress distributions at ultimate loads in FEA of drilled shaft footings

Regardless of the grades of bottom mat reinforcing bars, the reinforcing bars placed within the diameter of the support plate experienced a relatively higher stresses than those placed between the supports. This trend is consistent with the conclusions carried out from other previous studies (Clarke 1973; Kim et al. 2023; Suzuki et al. 1998; Yi et al. 2022, Forthcoming.). To clarify the influence of the grade of steel of the bottom mat reinforcement on the reinforcing bar stress development in drilled shaft footings, the research team compared the analysis results of two finite element models, focusing on the maximum bar stresses developed in four reinforcing bar groups: vertical face, horizontal face, bottom mat reinforcement placed within the support plate diameter, and that placed between the supports. Since the test specimens failed at different loads, the maximum stresses in the bar groups were compared at several load levels from 500 kip to 2,000 kip with an interval of 500 kip. The comparison result is summarized in Table 4-6.

Table 4-6. Maximum bar stress in FEA of drilled shaft footings

Load (kip)	Maximum stress (ksi)							
	B60				B100			
	Bot. mat bars placed within shafts	Bot mat bars placed between shafts	Horizontal side face bars	Vertical side face bars	Bot mat bars placed within shafts	Bot mat bars placed between shafts	Horizontal side face bars	Vertical side face bars
500	1.3	1.3	0.6	0.2	1.4	1.4	0.6	0.2
1,000	11.2	7.9	21.6	1.1	24.1	14.4	48.3	2.8
1,500	23.2	13.7	36.3	19.0	41.3	26.9	62.2	24.5
2,000	36.0	20.5	43.1	25.7	58.3	36.4	79.4	29.7

The analysis result indicates that the bottom mat stress developments before the first cracking (500 kips) are comparable regardless of the reinforcement grades. Considering the nominal strength ratio of 1.67 (100 ksi/60 ksi), the bottom mat reinforcement groups in B100 were subjected to relatively higher stress levels than those in B60 at 1,000-kip loading. However, the arch-shaped cracks at side surfaces redistributed the bottom mat reinforcement stresses, which induces stresses in the side face reinforcement as load increases. At 2,000 kip, the bottom mat stress level ratios computed in both groups (within/outside of the diameter of support) become comparable and close to the nominal strength ratio of 1.67. This indicates that a small amount of high-strength steel can effectively substitute for a large amount of conventional strength reinforcement to carry a similar load level. On the other hand, it should be noted that the bottom mat reinforcement did not fully yield until the specimens reached their ultimate states. Further, the side face reinforcement placed with the high-strength bottom mat reinforcement experienced a relatively higher stress level than the conventional bottom mat reinforcement to redistribute the higher strains that occurred in the high-strength bottom mat reinforcement.

4.2.4.4. Conclusions

This study's nonlinear finite element analyses performed for drilled shaft footings were intended to supplement test data and attain insights for investigating the effects of substituting the conventional strength steel (Grade 60) bottom mat reinforcement of drilled shaft footings to the high-strength steel (Grade 100).

The research team developed finite element models for the drilled shaft footing specimens of the experimental program of this study with the ATENA 3D software. The analysis showed that the developed models successfully predict the load-deflection responses and crack patterns observed in the experimental program. Using the validated model, stress developments in different grades of the bottom mat reinforcement were investigated and compared. The stress distributions proved that Grade 100 steel reinforcement successfully substituted conventional steel in the bottom mat reinforcement of drilled shaft footings by developing higher stress levels to carry a similar load level. However, the substitution also caused relatively higher stresses in the side face reinforcement to redistribute the high strains developed in Grade 100 bottom mat reinforcing bars.

As described, the numerical finite element analyses carried out for drilled shaft footings provided valuable data and insights into understanding the influence of the implication of Grade 100 steel reinforcement in the bottom mat reinforcement of drilled shaft footings. The findings from the analyses indicate that the use of high-strength rebar can significantly contribute to reducing the design and fabrication costs required for drilled shaft footing design by reducing vast amounts of reinforcement. Combined with test results, the FEA of this project will be utilized to propose a set of design recommendations that can contribute to the application of Grade 100 reinforcing bars in designing drilled shaft footings.

4.2.5. Tension Lap Splice

4.2.5.1. Overview

Experiments revealed that specimens with lap splices exhibited similar behavior to those with continuous reinforcing bars until the longitudinal bars reached their yield strength. Beyond yielding, specimens with lap splices experienced a sudden load drop accompanied by splitting cracks in the splice region, leading to failure. In contrast, specimens with continuous bars displayed distributed cracks throughout the constant moment region, whereas cracks in specimens with lap splices were concentrated at the splice ends.

For numerical analysis, perfect bond conditions between reinforcing bars and surrounding concrete are typically assumed. However, the experimental findings highlighted the necessity of applying bond models to simulate the behavior of beams with spliced reinforcement accurately. These models better capture the interaction between reinforcing bars and the surrounding concrete, particularly in the presence of lap splices.

This chapter focuses on deriving an appropriate bond model to predict the flexural behavior of lap-spliced reinforced concrete (RC) beams using regular and high-strength reinforcement. The ATENA 3D software was employed for the analysis, utilizing two bond models available within the program: one based on the CEB-FIP 1990 Model Code and the other from Bigaj (1999). The finite element analysis (FEA) results were then compared with experimental outcomes to identify the bond model most suitable for predicting the flexural behavior of lap-spliced RC beams.

4.2.5.2. FE Model

Figure 4-29 depicts the test setup alongside its corresponding FE model. The setup conditions, including concrete beams, support and loading plates, and the load transfer beams, were replicated in the model with identical dimensions. The FE model was configured to apply loads to the beam specimens through displacement control at the hydraulic ram location. Reaction forces were monitored from locations matching the load cells installed in the test.

To ensure efficient analysis time and converged results, the mesh geometry and element size were determined through preliminary analysis. An element size of 3 inches was selected to model the beam specimens. Concrete elements were modeled using 3D hexahedral (brick) elements, while support and loading plates, and load transfer beams—where brick elements were unsuitable due to geometry—were modeled with tetrahedral elements. Rebars were modeled using 2D truss bar elements.

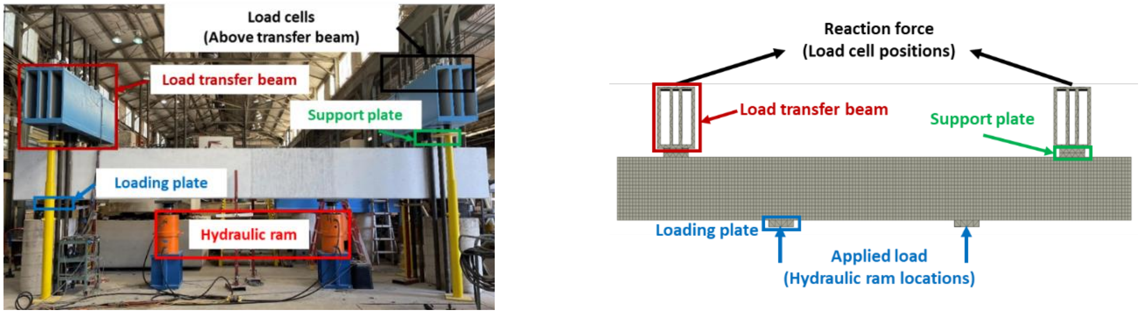

(a) Test setup (b) FE model

Figure 4-29. Test setup and FE model configuration of beam splice test

The load was applied in two steps: (1) The self-weight of the concrete beam and load transfer beam was simulated using body forces. (2) Load was applied incrementally in 0.003-inch increments at the hydraulic ram location.

Material models were developed using data from tests on concrete cylinders and rebar coupons. For concrete, the ATENA program offers a fracture-plastic constitutive model based on classical orthotropic smeared crack formulation and crack band model. This model incorporates a Rankine failure criterion, exponential softening, and can operate either as a rotated or fixed crack model. The hardening/softening plasticity model is derived from the Menétrey-Willam failure surface.

As mentioned above, two bond models (CEB-FIP 1990 Model Code and Bigaj) were utilized simulating bond behaviors between longitudinal bars and surrounding concrete. The property of these two models is the bond-slip relationship, and this relationship are generated key factors such as compressive strength of concrete, diameter and type of reinforcing bars (ribbed or smooth bars). Particularly, the bond model from CEB-FIP 1990 Model Code was defined also considering confinement conditions and the quality of concrete casting.

Deriving all necessary parameters through experiments is challenging; therefore, ATENA automatically generates them based on uniaxial compressive strength of concrete. For a comprehensive theoretical understanding of this model, ATENA Theory Manual can be referred. The stress-strain curves obtained from rebar coupon tests were directly utilized as input data for material model of reinforcing bar. Unlike the bilinear or trilinear models commonly used for simplicity, these are unsuitable for high-strength steels due to the lack of a clear yield plateau.

4.2.5.3. FEA Results and Discussion

To validate the developed FE model, the FEA results were compared with the test results of the LX60 specimen. To determine the differences in ductility and ultimate capacity with and without lap splices, as well as stress transfer in the splice region, the load-strain curves, crack patterns, and rebar strain profiles from the FEA were compared with those from the experiment. The comparisons included the load-deflection curve, cracking pattern, and rebar strain profile.

Figure 4-30 shows the load-deflection curves of both FEA and test of LX60 specimen. As shown in the Figure, the FE models properly predict the entire curves shape of the LX60 specimen. In particular, the maximum load capacity is estimated within approximately 1% of the measured capacity, which is within the suitable accuracy range.

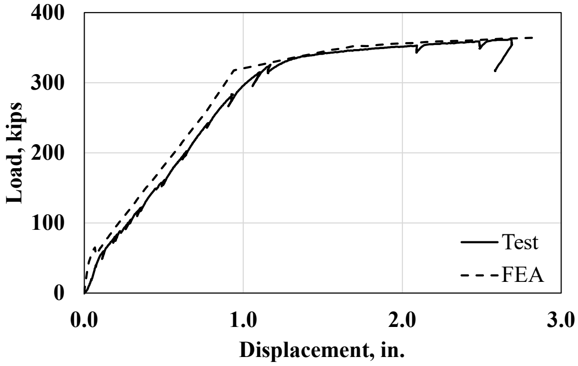

Figure 4-30. Load-deflection curve comparison of LX60 specimen

Figure 4-31 illustrates the crack patterns at various load steps observed in both the experiment and FEA. At the initial loading stage, flexural cracks appeared on the tension side in the test region, defined as the region between the loading points. As the load increased, these cracks propagated toward the compression side, and diagonal cracks developed from the tip of flexural cracks outside the test region. Cracks continued to propagate and widen with increasing load. As shown in the figure, the FEA accurately predicted the crack pattern.

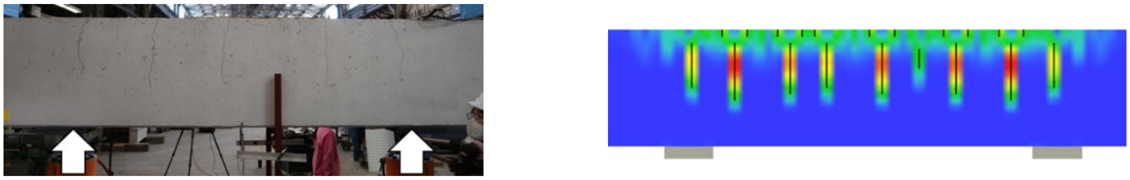

(a) 60 kip

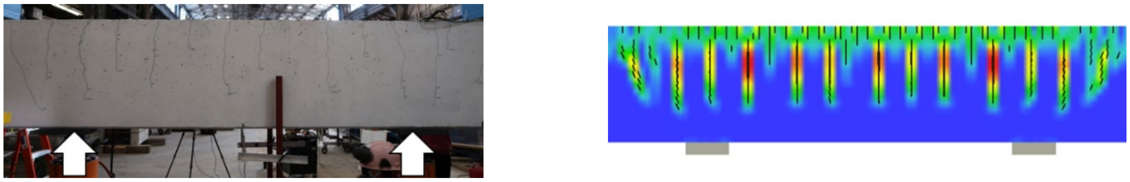

(b) 100 kip

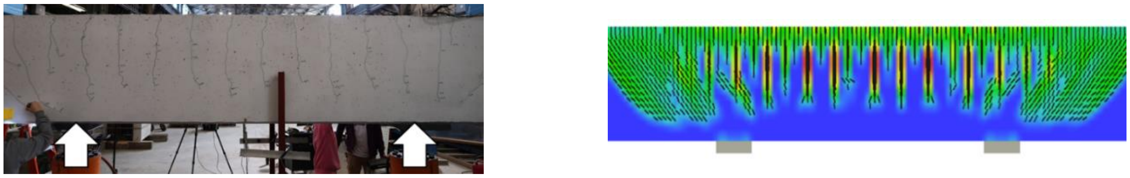

(c) 200 kip

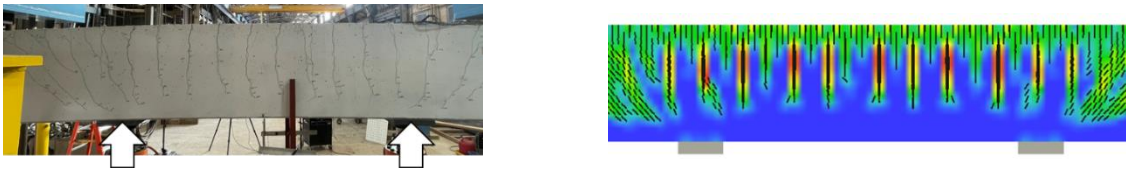

(d) 280 kip

Figure 4-31. Crack patterns comparison of LX60 specimen at each load step

Rebar strain was monitored in the FEA at the same locations as the attached strain gauges in the test. Figure 4-32 shows the gauge positions, and Figure 4-33 compares the rebar strain results between test and FEA. All three flexural rebars exhibited similar gauge readings at the same longitudinal positions. As the load increased, the rebar strain increased linearly. The strain also tended to increase rapidly at the point where hardening appeared in the load-deflection curve. It was demonstrated that the FEA effectively predicted rebar strains under applied loads.

By comparing test results with FEA results, including load-deflection curves, crack patterns, and rebar strains, the FE model was verified to accurately predict the behaviors of the LX 60 specimen. The other three beam specimens (LX100, LO60, and LO100) were analyzed utilizing this FE model.

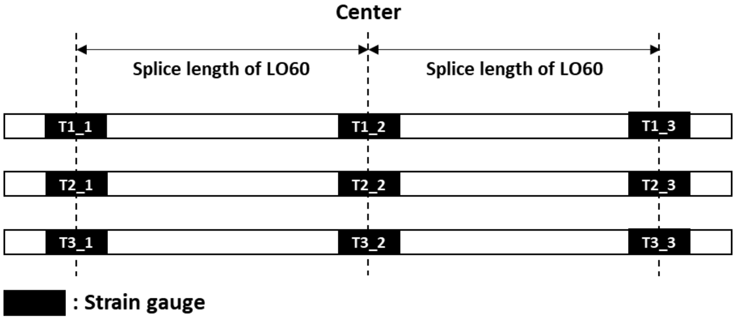

Figure 4-32. Rebar strain gauge locations of LX60 specimen

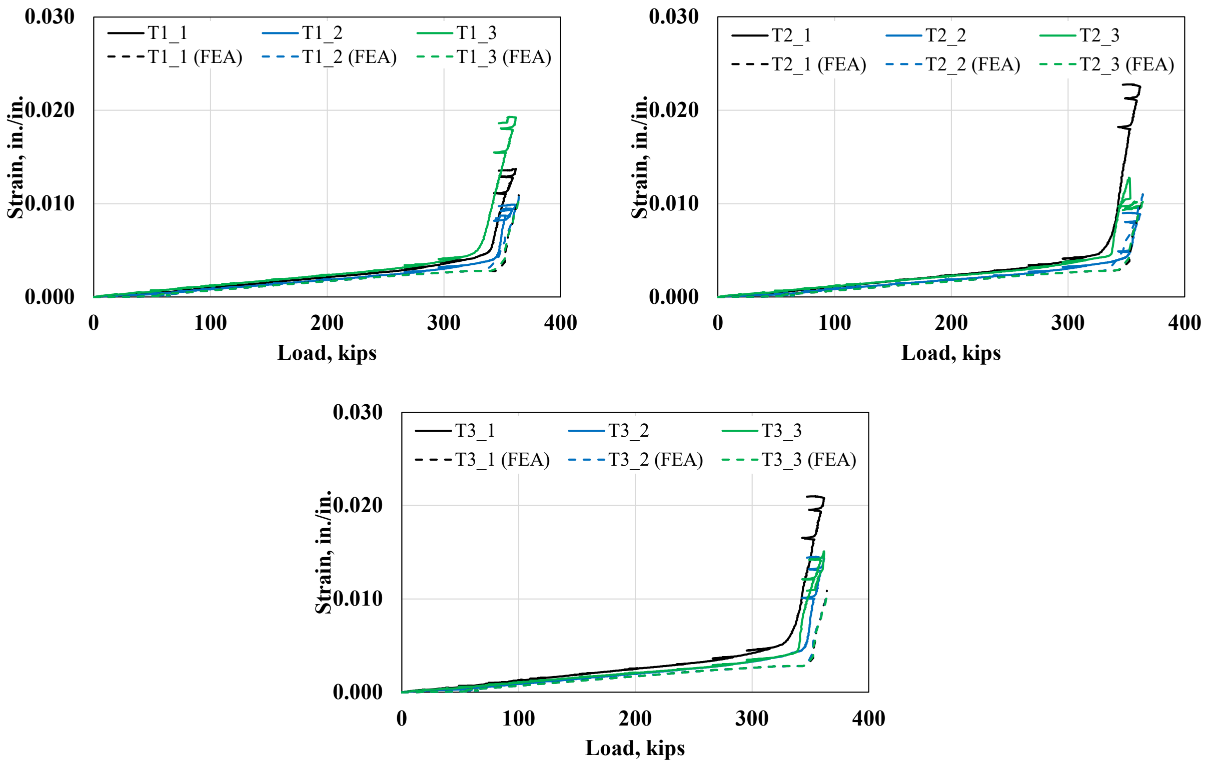

Figure 4-33. Rebar strains comparison of LX60 specimen

For analysis of LO60 specimen, two bond models from the CEB-FIB Model Code 1999 and Bigaj (1999) were utilized. The CEB-FIB Model Code 1999 requires concrete compressive strength, reinforcement type, concrete confinement, bar diameter and bond quality. On the other hand, the Bigaj (1999) model requires concrete compressive strength, bar diameter and bond quality. Based on the actual test conditions, bond quality was assumed to be good, and confinement condition was selected for analysis.

The LO60 specimen, which used a lap splice, experienced brittle failure with a rapid drop in load due to splitting cracks in the splice region. The shape of the load-deflection curve was well predicted by the FEA, as shown in Figure 4-34.

At the initial loading stage, the cracking pattern of the LO60 specimen was similar to that of the LX60 specimen. Flexural cracks appeared on the tension side within the test region and propagated towards the compression side, accompanied by the development of diagonal cracks outside the test region. However, in contrast to the LX60 specimen, the major cracks in the LO60 specimen were located at the end of the splice, with these being the widest cracks. Additionally, a relatively small number of cracks were observed within the test region compared to LX60 specimen. As shown in the Figure 4-35, the FEA accurately predicted the crack pattern of LO60.

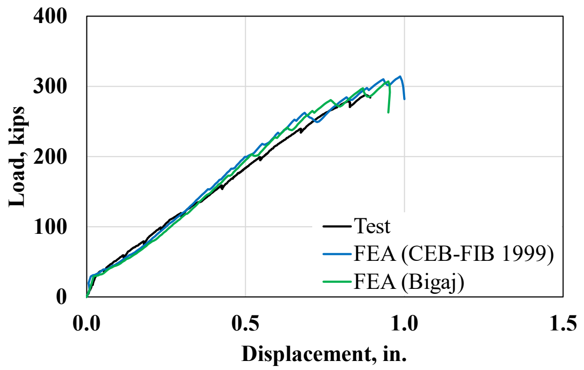

Figure 4-34. Load-deflection curve comparison of LO60 specimen

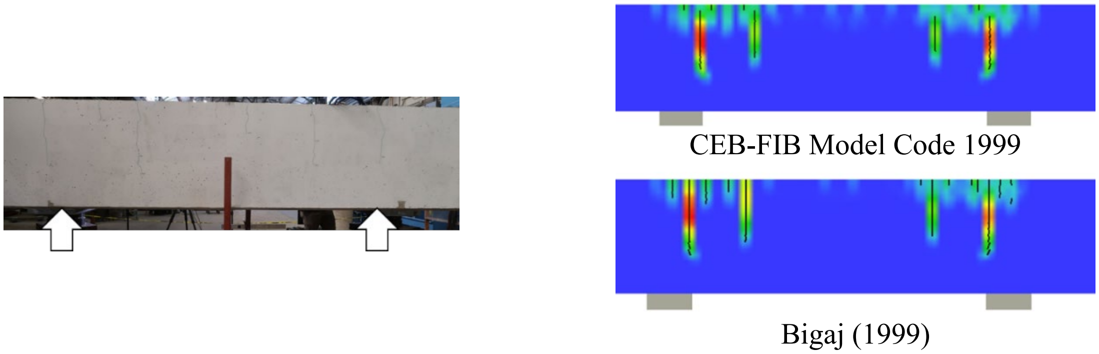

(a) 60 kips

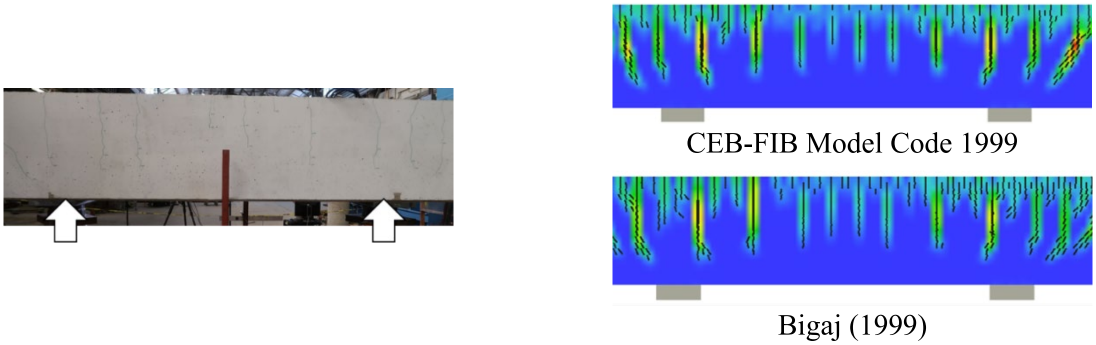

(b) 100 kips

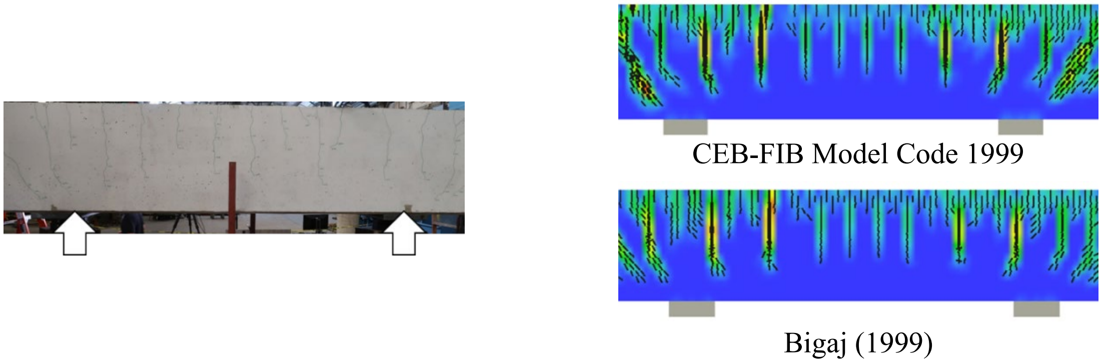

(c) 200 kips

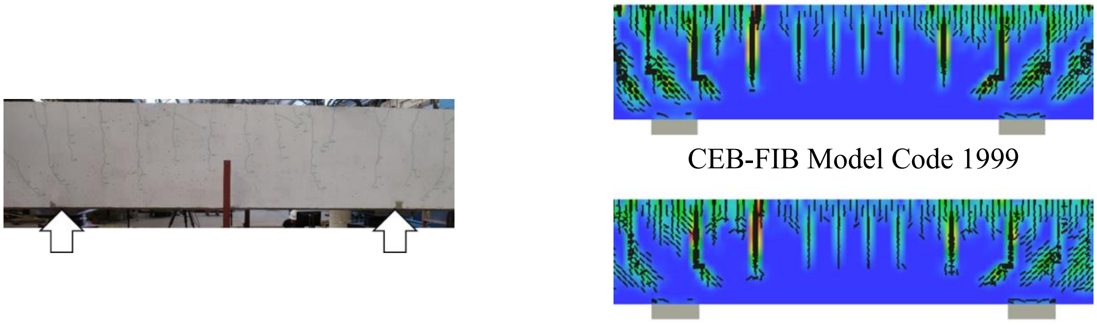

CEB-FIB Model Code 1999

Bigaj (1999)

(d) 280 kips

Figure 4-35. Crack patterns comparison of LO60 specimen at each load step

The rebar strains of the LO60 specimen obtained from FEA were compared with those measured in the test. The gauge locations attached to the LO60 specimen are shown in Figure 4-36. Gauges were installed within the splice region, with two to four gauges on each of the three splice regions to observe the effect of the number of gauges on the reading values.

The rebar strain showed a maximum value at one splice end, decreased along the length direction, and showed a minimal value close to 0 at the splice end on the opposite side of the rebar. This confirmed that the splice effectively transferred the reinforcement stress. This trend provides a rational basis for explaining the observed crack pattern, where the widest crack occurs at the end of the splice and relatively narrower crack widths are observed within the splice region. The rebar strains were effectively captured in the FEA, as illustrated in Figure 4-37.

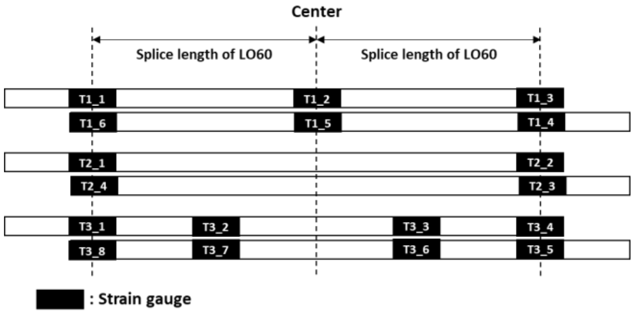

Figure 4-36. Rebar strain gauge locations of LO60 specimen

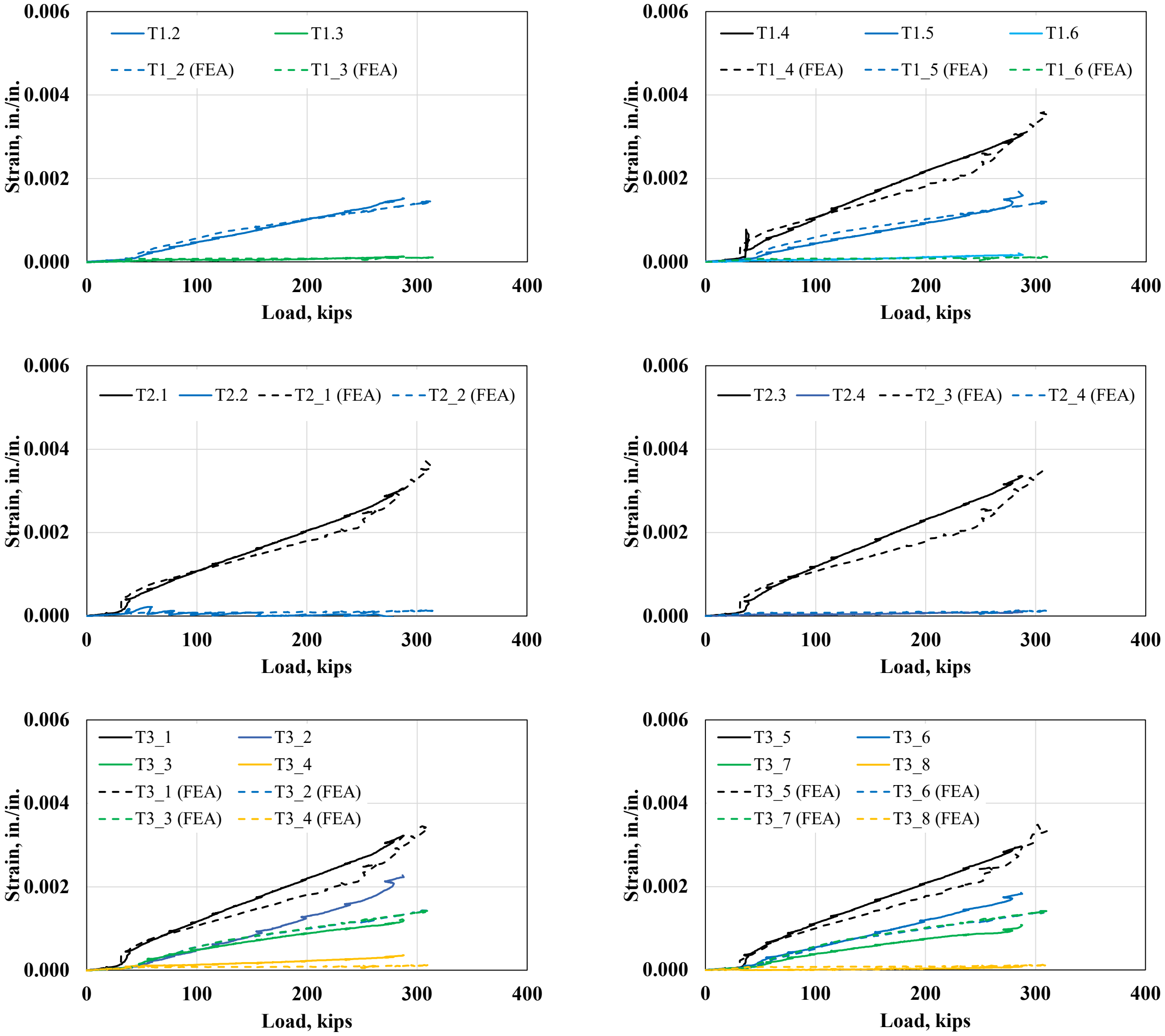

(a) CEB-FIB Model Code 1999

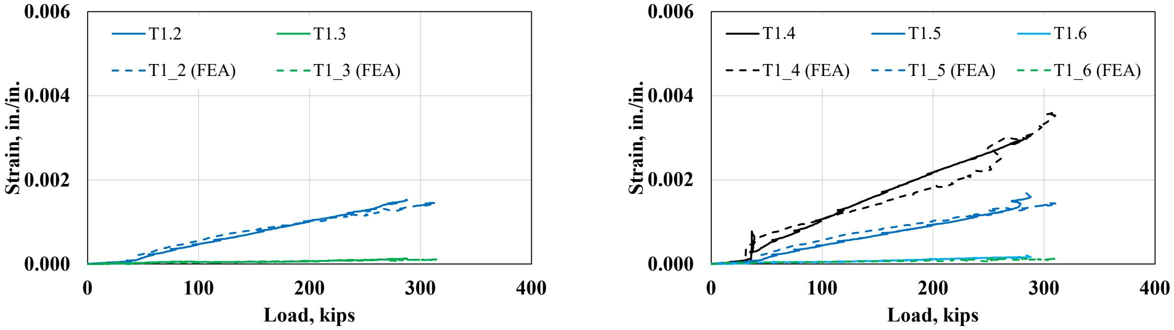

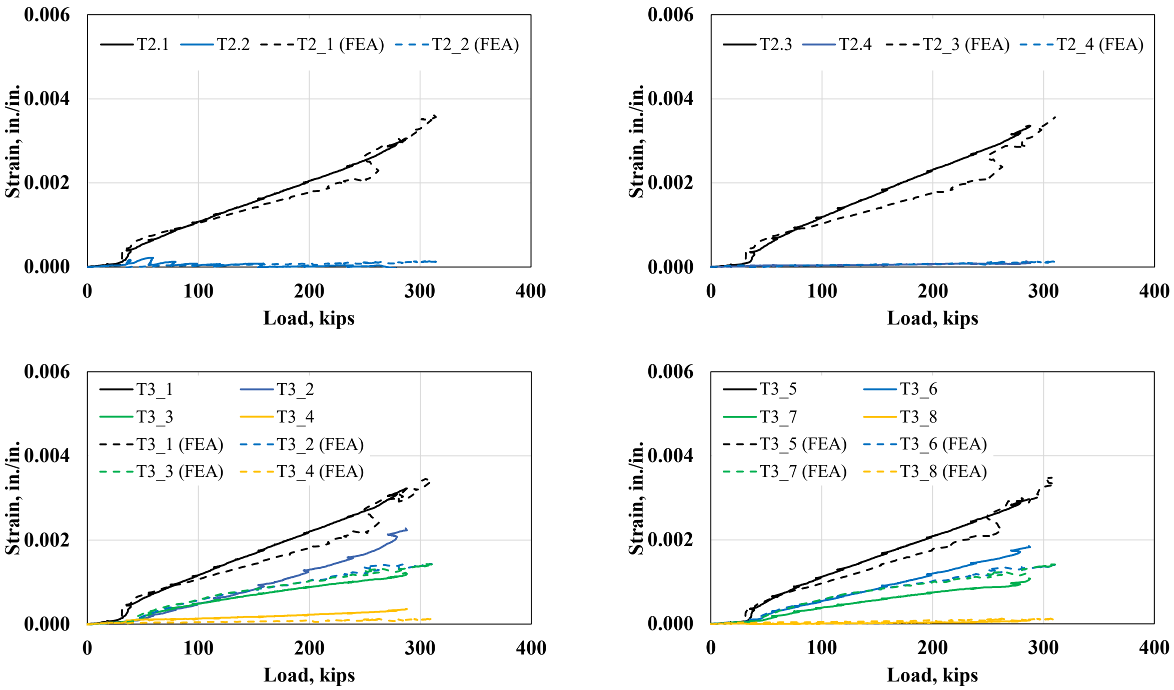

(b) Bigaj (1999)

Figure 4-37. Rebar strains comparison of LO60 specimen with interface model

The FEA of the LX100 and LO100 specimens was performed using the same FE model as for the LX60 and LO100 specimens. The only modifications were to the concrete strength and the rebar stress-strain curves, which are specific to each test specimen. The load-deflection curves, crack patterns, and rebar strains obtained from the FEA were compared with the test results, as illustrated in Figure 4-38 and Figure 4-41. It was confirmed that the FEA also accurately predicted the behavior of RC beams, both with and without lap splices, when high-strength rebar was used.

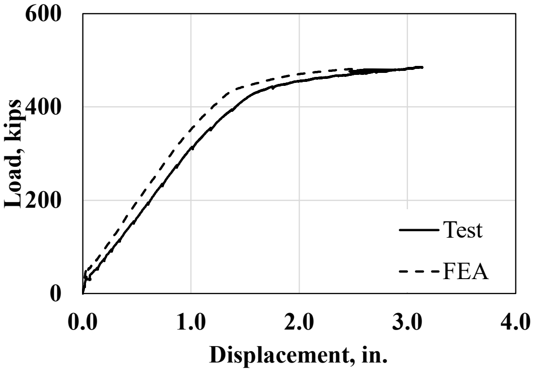

Figure 4-38. Load-deflection curve comparison of LX 100 specimen

(a) 60 kip

(b) 100 kip

(c) 200 kip

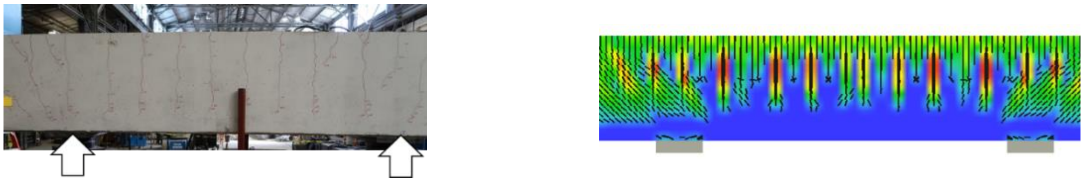

(d) 280 kip

Figure 4-39. Crack patterns comparison of LX100 specimen at each load step

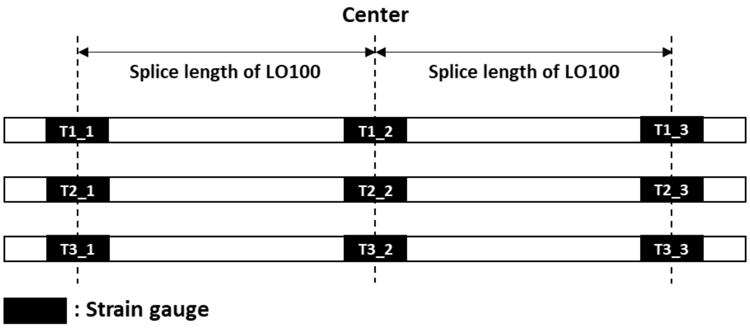

Figure 4-40. Rebar strain gauge locations of LX100 specimen

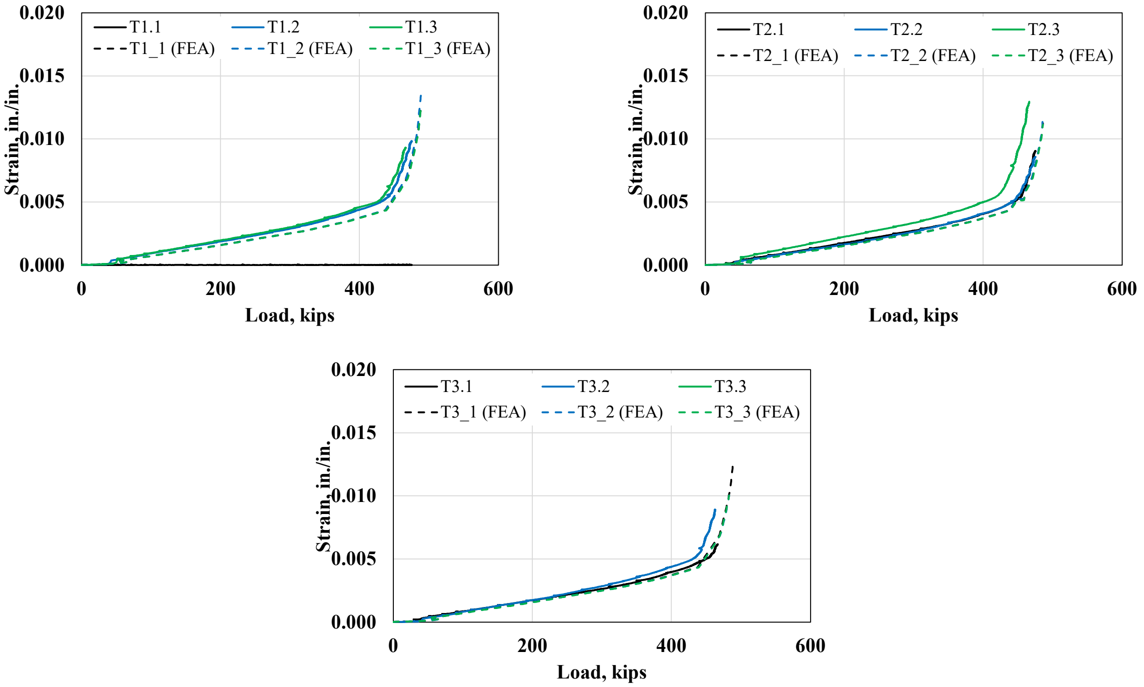

Figure 4-41. Rebar strains of LX100 specimen

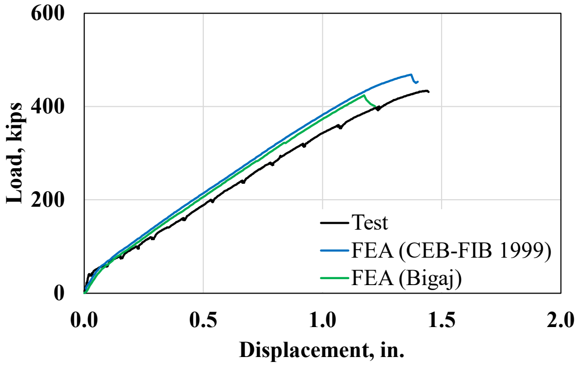

Figure 4-42. Load-deflection curve comparison of LO100 specimen

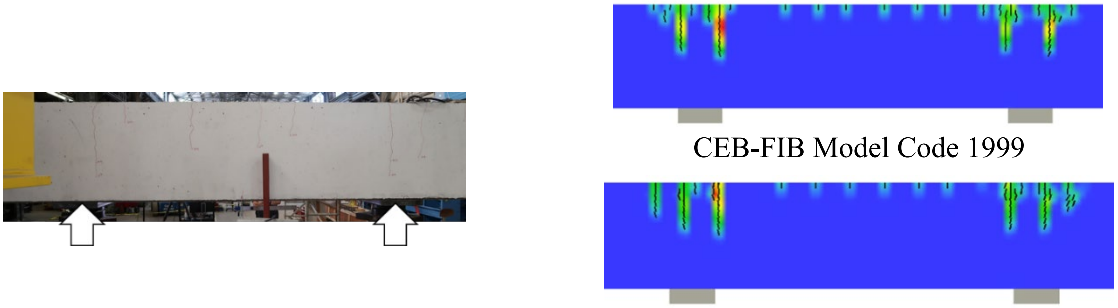

CEB-FIB Model Code 1999

Bigaj (1999)

(a) 60 kips

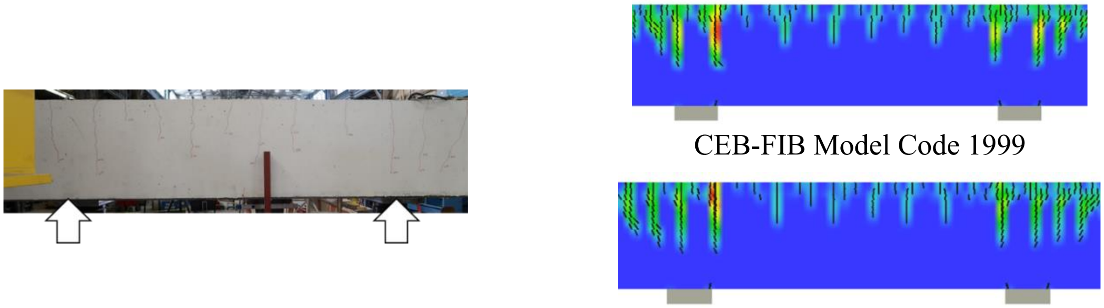

CEB-FIB Model Code 1999

Bigaj (1999)

(b)100 kips

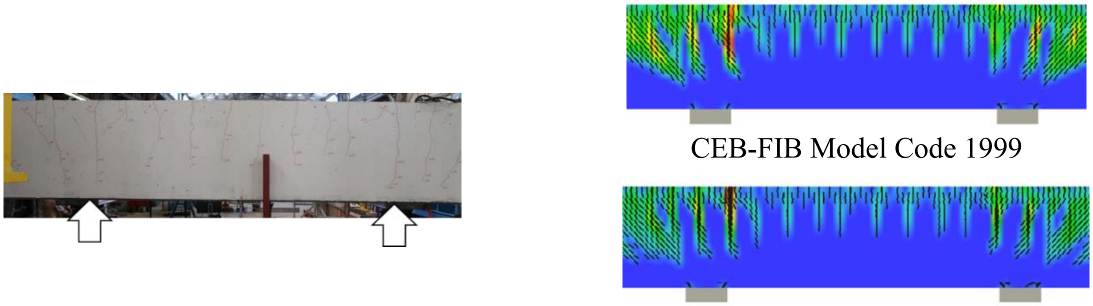

CEB-FIB Model Code 1999

Bigaj (1999)

(c) 200 kips

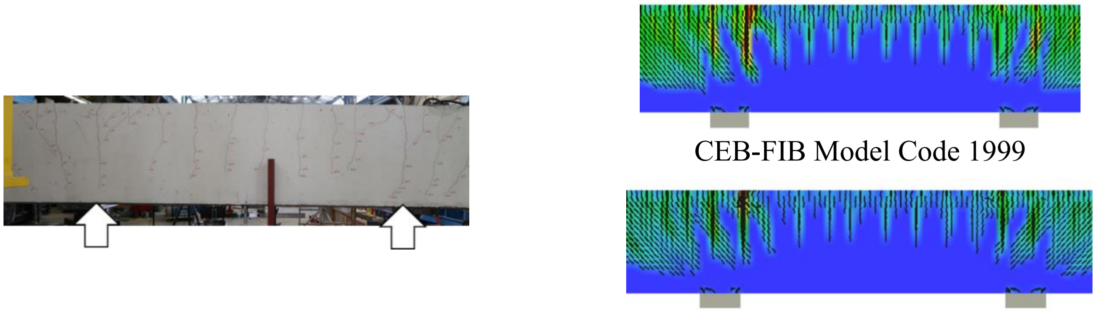

CEB-FIB Model Code 1999

Bigaj (1999)

(d) 280 kips

Figure 4-43. Crack patterns comparison of LO100 specimen

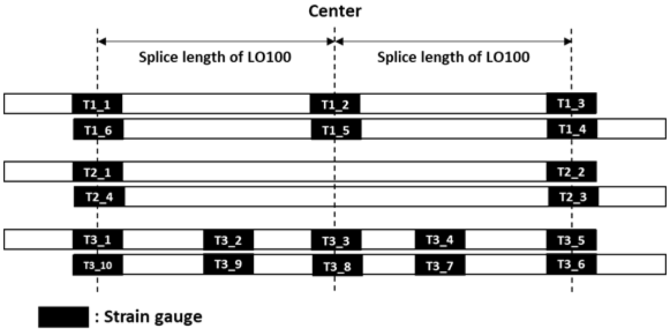

Figure 4-44. Rebar strain gauge locations of LO100 specimen

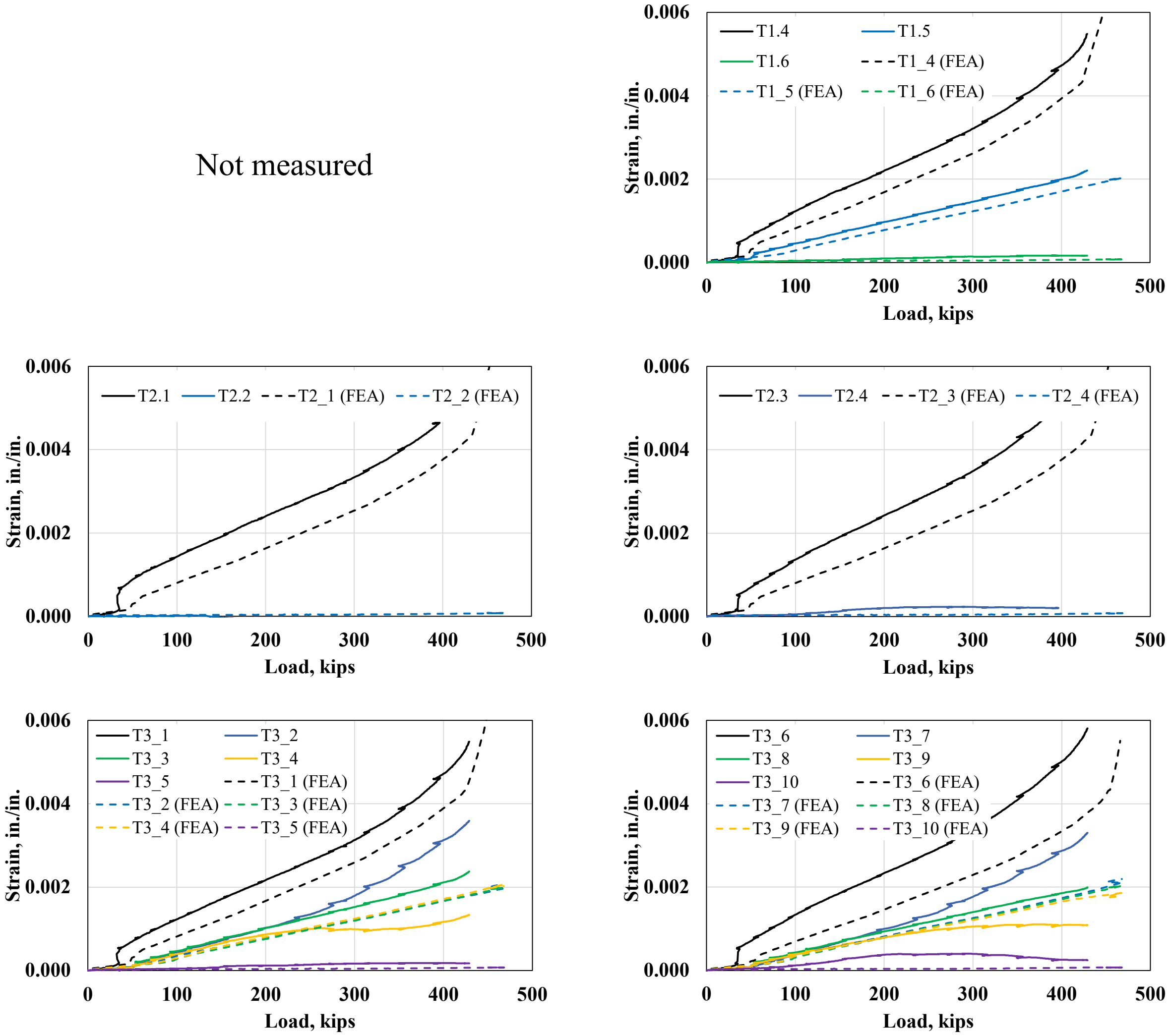

(a) CEB-FIB Model Code 1999

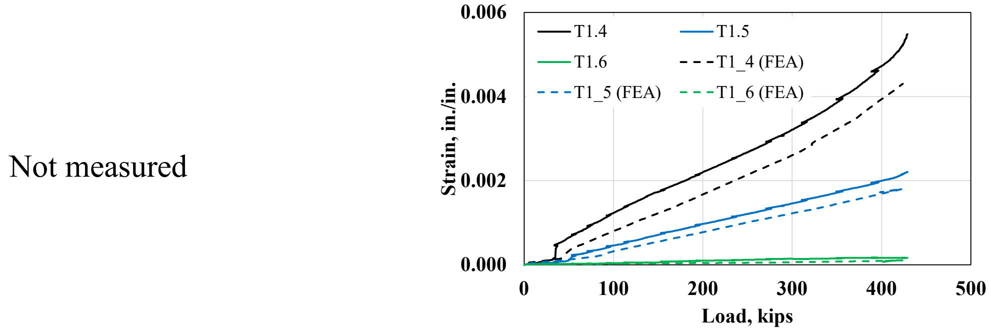

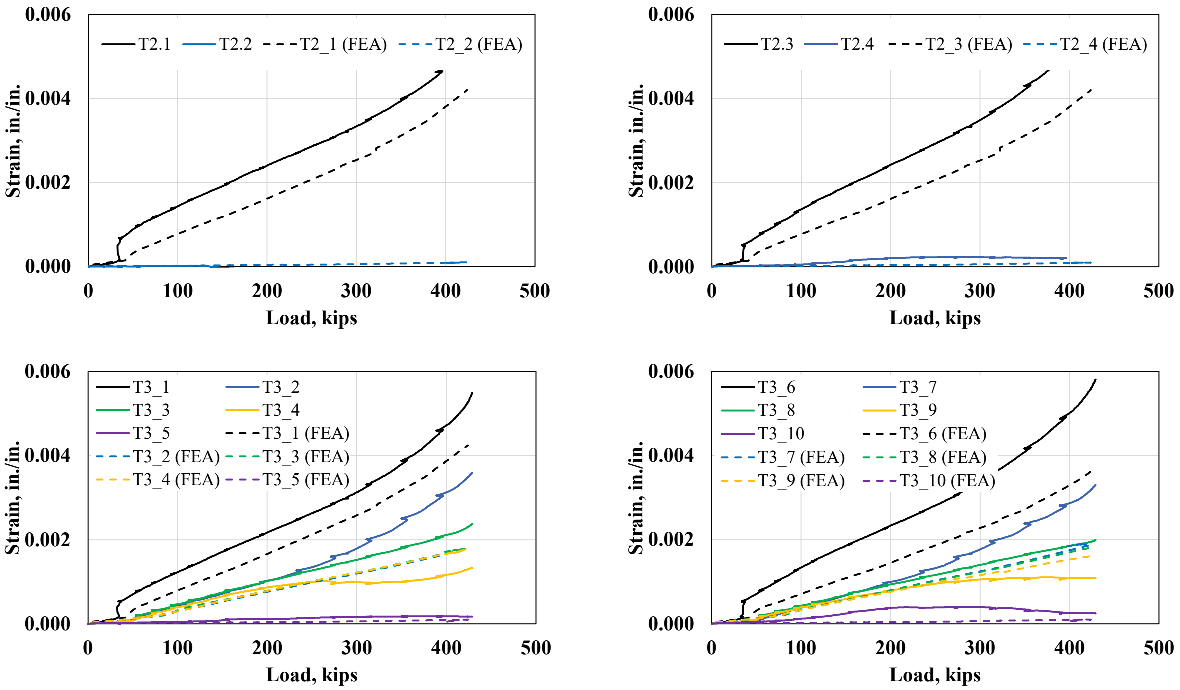

Bigaj (1999)

Figure 4-45. Rebar strains comparison of LO100 specimen

4.2.5.4. Conclusions

Through FEA, it was demonstrated that the developed FE model accurately predicts the behavior of concrete beams with both tension lap splices and continuous longitudinal bars. By directly incorporating the stress-strain relationships of the reinforcing bars into the FE model, it effectively predicted the behavior of RC beams with both normal-strength and high-strength rebar. Specifically, the FEA successfully estimated load-deflection curves, crack patterns, and rebar strain distributions. The developed FE model is anticipated to be highly beneficial for the design and analysis of spliced concrete beams, whether they have lap splices or not, and regardless of whether normal-strength or high-strength rebars are used.

4.3. Summary

This chapter presents a comprehensive nonlinear finite element analysis study that offers an in-depth understanding of the structural behavior of various bridge components with high-strength reinforcement based on experimental work conducted in this project.

The FE model was developed and validated by comparing it with representative structural components tested in each experimental task, such as load capacity and crack patterns. The model successfully predicted the behavior of these components. This validated FE model confirmed that the overall behavior of bridge structural components with high-strength reinforcement was accurately predicted, yielding effective and reliable results.

The findings from this study are expected to provide a broader understanding, including insights into behavioral aspects that cannot be physically observed in experiments. They also offer valuable guidance for future design and analysis through parametric studies, contributing to more efficient and effective practices in structural engineering.

Furthermore, all FE models requiring updates, including those based on ongoing experimental work, will be incorporated into future research reports to ensure the continued high quality of the analysis results.

Chapter 5. Practical Applications

5.1. Overview

Previous experimental and finite element analysis studies have extensively explored the applicability of high-strength reinforcement to reinforced concrete (RC) members. Generally, it has been observed that the use of high-strength reinforcement reduces the amount of reinforcement needed while maintaining comparable load performance and remains compatible with current design codes.

In this chapter, a series of example calculations are conducted using standard sections or drawings of existing bridge elements in Texas, rather than the specific members tested in the experiments. This approach aims to suggest practical applications of high-strength reinforcement for Texas bridges.

5.2. Superstructures

5.2.1. Bridge Deck

The research team chose two TxDOT bridge decks: identified as 5XB28 and Tx-62. Load combinations from a previous study were referred to in the flexural strength calculations (ChromX Optimization Report, 2020). The procedure is as follows. First, a load calculation was performed. Dead loads (deck self-weight, wearing surface, and barrier weight) and live loads (lane load and truck load) were considered and analyzed using ATENA 2D. Then, the load-carrying capacity and rebar spacing for control of crack width was verified based on the load calculation results. Lastly, conventional Grade 60 reinforcing bars were replaced with Grade 80 and Grade 100 reinforcing bars to maintain load-carrying capacity, and the serviceability was verified using the rebar layout of high-strength reinforcing bars. For transverse reinforcement, Equation (3-2) in accordance with AASHTO LRFD (2020) were used to determine the minimum rebar spacing.

For longitudinal reinforcement, the required spacing of the bottom rebar was calculated using Equation (5-1) in accordance with AASHTO LRFD (2020). The top rebar spacing was determined using the following Equation (5-2).

$$220/\sqrt{S} \leq 67\text{percent} \tag{5-1}$$

$$A_s \geq \frac{1.30bh}{2(b+h)f_y} \tag{5-2}$$

where,

S=effective span length

A_s=area of reinforcement in each direction and each face (in.^{2}/ft)

b= least width of component section (in.)

h= least thickness of component section (in.)

f_y specified minimum yield strength of reinforcement ≤75.0 ksi

5.2.1.1. 5XB28

5.2.1.1.1. Load Calculation

The 5XB28 deck details are shown in Figure 5-1. Dead loads (deck self-weight, wearing surface, and barrier weight) and live loads (lane load and truck load) were considered and analyzed using ATENA 2D, as shown in Figure 5-2. The results are listed in Table 5.5-1.

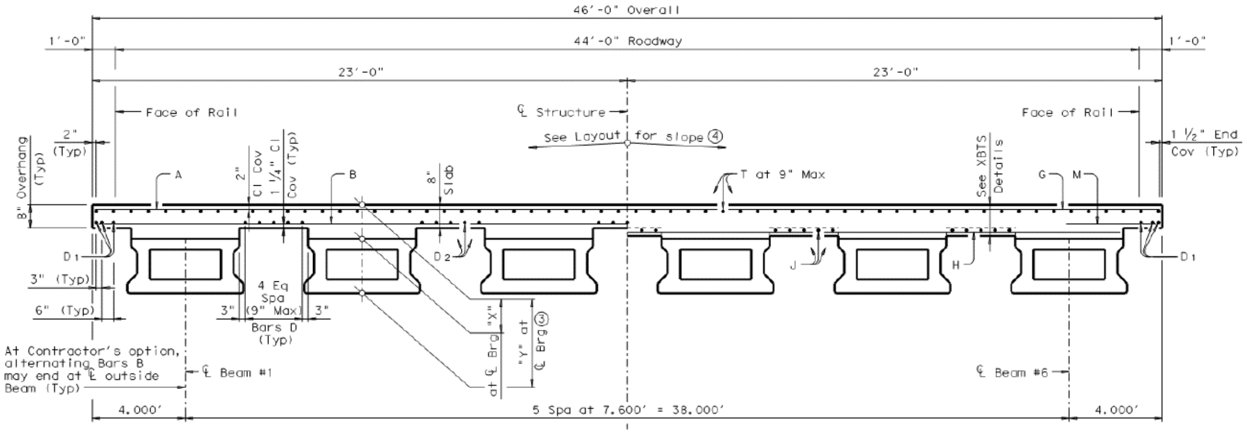

Figure 5-1. 5XB28 details

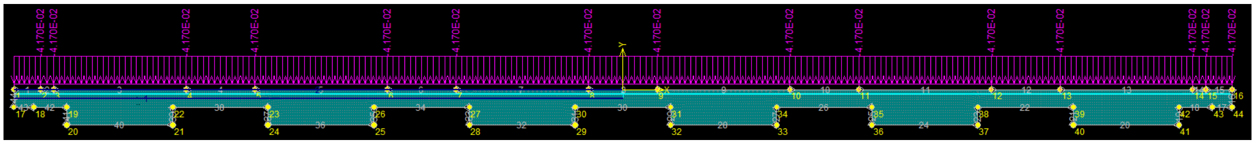

Figure 5-2. ATENA 2D Model for 5XB28

Table 5.5-1 Load calculation result (5XB28)

Section	Dead load (kip-ft)			Live load (kip-ft)	Service moment (kip-ft)	Factored moment (kip-ft)
	Self-weight	Wearing surface	Barrier	Lane & Truck		
Positive	0.05	0.03	-0.24	3.45	3.29	5.84
Negative	-0.14	-0.03	0.01	-1.97	-2.12	-3.64

5.2.1.1.2. Reinforcement layout

The sectional flexural strength at the positive and negative sections was calculated using the strain compatibility method, assuming that strain is proportional to the distance from the neutral axis. For conservative evaluation, the effect of tension stiffening of concrete was not considered. Then, the calculated flexural resistance was compared to the factored moment in Table 5.5-1. It was found that the use of the current TxDOT transverse layout satisfied the required strength. The rebar layout using a high-strength reinforcing bar was designed to maintain the flexural strength of the current rebar layout. Additionally, rebar spacing was checked in accordance with the current version of AASHTO LRFD (2020).

Transverse Reinforcement

The current transverse rebar layout of 5XB28 was used in accordance with the TxDOT bridge design manual (2021). The current layout used #5 at 6 in. spacing using Grade 60 reinforcing bars. If Grade 80 reinforcing bars are used for transverse reinforcement, the spacing can be increased from 6 in. to 8 in. When using Grade 100 rebars as transverse reinforcement, the spacing increases from 6 in. to 10 in. For both Grade 80 and Grade 100 reinforcing bars, the same rebar size as Grade 60, was used. For all cases, the details of the calculation procedure are shown in Appendix C.

Longitudinal Reinforcement

The current longitudinal rebar layout used 5-#5 at 9 in. spacing between girders at the bottom, and #4 at 9 in. spacing was used at the top using Grade 60 rebars. In the case of Grade 80 rebars used for longitudinal reinforcement, which uses the same size rebar as Grade 60, the bottom rebar spacing increased from 9 in. to 12 in., and the top rebar spacing increased from 9 in. to 12 in. When using Grade 100 rebars as longitudinal reinforcement, the bottom rebar layout was changed to #4 with a spacing of 10 in., and the top rebar layout changed to #3 with a spacing of 9 in. The details of the calculation procedure are shown in Appendix C.

Table 5.5-2 Reinforcement layout with respect to rebar grade (5XB28)

Grade	Bottom transverse reinforcement				Top transverse reinforcement			
	Layout	Flexural strength (kip-ft)	Weight (lb/ft)	Remark	Layout	Flexural strength (kip-ft)	Weight (lb/ft)	Remark
60	#5@6"	18.87	95.96	-	#5@6"	16.54	95.96	-
80	#5@8"	18.67	71.97	↓25	#5@8"	16.55	71.97	↓25
100	#5@10"	18.51	57.57	↓40	#5@10"	16.55	57.57	↓40
Grade	**Bottom longitudinal reinforcement**				**Top longitudinal reinforcement**			
	Layout		**Weight (lb/ft)**	**Remark**	**Layout**		**Weight (lb/ft)**	**Remark**
60	5-#5 btw. girders		26.08	-	#4@9"		40.97	-
80	4-#5 btw. girders		20.86	↓20	#4@12"		30.73	↓25
100	4-#4 btw. girders		13.36	↓49	#3@9"		23.06	↓44
				Total				
Grade	**Weight (lb/ft)**				**Remark**			
60	258.96				-			
80	195.52				↓24			
100	151.57				↓41			

5.2.1.2. Tx62

5.2.1.2.1. Load Calculation

The Tx62 deck details are shown in Figure 5-3. Dead loads (deck self-weight, wearing surface, and barrier weight) and live loads (lane load and truck load) were considered and analyzed using ATENA 2D, as shown in Figure 5-4. The results are listed in Table 5.5-3.

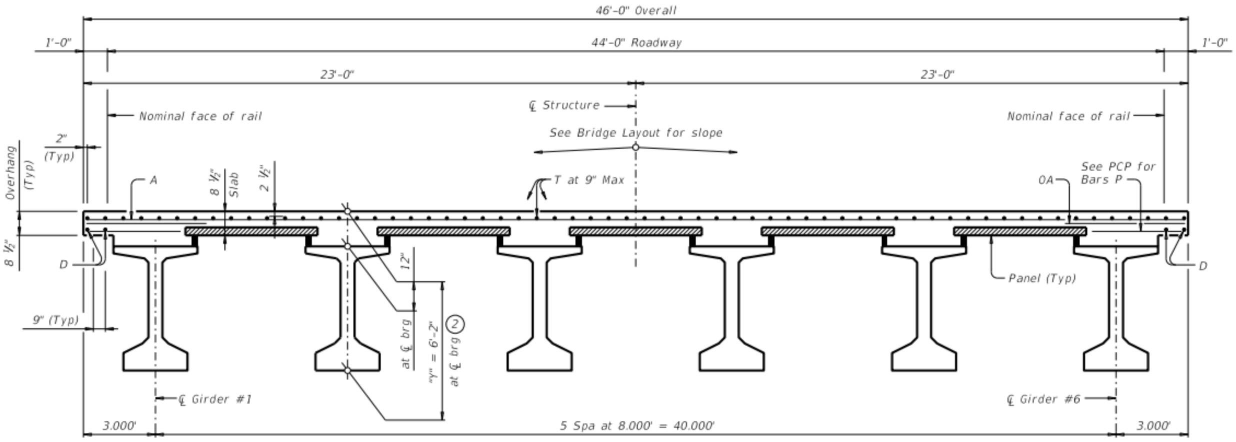

Figure 5-3. Tx62 details

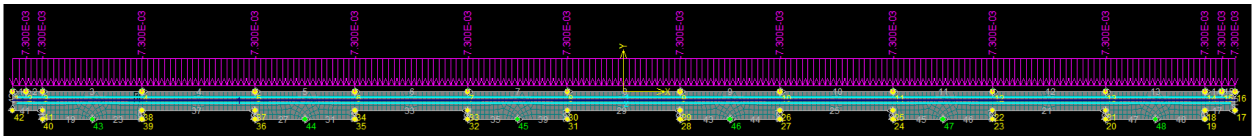

Figure 5-4. ATENA 2D Model for Tx62

Table 5.5-3 Load calculation result (Tx62)

Section	Dead load (kip-ft)			Live load (kip-ft)	Service moment (kip-ft)	Factored moment (kip-ft)
	Self-weight	Wearing surface	Barrier	Lane & Truck		
Positive	0.25	0.04	-0.21	2.81	2.89	5.01
Negative	-0.60	-0.10	0.19	-2.01	-2.52	-4.16

5.2.1.2.2. Reinforcement layout

Transverse Reinforcement

The current rebar layout of Tx62 was used in accordance with the TxDOT bridge design manual (2021). The bottom of the decks used prestressed concrete panels (PCP). Therefore, only the top transverse reinforcement layout was considered for the calculation. The current top layout used #4 at 9 in. spacing using Grade 60 reinforcing bars. For both Grade 80 and Grade 100 reinforcing bars, the rebar layout changed to #3 with a spacing of 6.5 in. to satisfy the spacing for crack control. The details of the calculation procedure are shown in **Appendix D**.

Longitudinal Reinforcement

The current longitudinal rebar layout used #4 at 9 in. spacing at the top using Grade 60 rebars. In the case of Grade 80 rebars used for longitudinal reinforcement, the bottom rebar spacing, which are the same size as Grade 60 rebars, increased from 6 in. to 8 in., and the top rebar spacing was increased from 9 in. to 12 in. When using Grade 100 rebars as longitudinal reinforcement, the bottom rebar spacing increased to 9.5 in., and the top rebar lay changed to #3 with a spacing of 9 in. The details of the calculation procedure are shown in Appendix C.

Table 2.4 Reinforcement layout with respect to rebar grade (Tx62)

Grade	**Top transverse reinforcement**		
	Layout	**Weight [lb/ft]**	**Remark**
60	#4@9"	40.97	-
80	#3@6.5"	31.93	↓22
100	#3@6.5"	31.93	↓22
Grade	**Top longitudinal reinforcement**		
	Layout	**Weight [lb/ft]**	**Remark**
60	#4@9"	40.97	-
80	#4@12"	30.73	↓25
100	#3@9"	23.06	↓44
	Total		
Grade	**Weight [lb/ft]**		**Remark**
60	81.94		-
80	62.66		↓24
100	54.99		↓33

5.2.1.3. Conclusion

Two types of TxDOT decks were used for example calculations. A new rebar layout using high-strength steel (Grade 80 and 100) was proposed to maintain the load-carrying capacity of the previous rebar layout using a conventional reinforcing bar (Grade 60). It was confirmed that the quantity of reinforcement can be reduced as much as the strength ratio between conventional steel and high-strength steel. Furthermore, the size and spacing of rebars should be considered together to satisfy the rebar spacing limit for crack control in AASHTO LRFD (2020).

5.2.2. Prestressed Girders

The research team intends to compare the reinforcement layouts of a pretensioned beam using Grade 60 reinforcement and high-strength reinforcement (Grade 80 and Grade 100). For comparison, the Tx-girder and box beam, which follow the TxDOT standard designs, were used for calculation based on the sectional design method proposed by AASHTO LRFD (2020).

The reinforcement in the end region of the pretensioned beam should resist the splitting force due to the prestressing strand. The factored splitting resistance provided by reinforcement in the ends of pretensioned beams shall be taken as the following equation.

$$P_r = f_s A_s \tag{5-3}$$

where,
P_r = factored splitting resistance of pretensioned anchorage zoned provided by reinforcement at the end of pretensioned beams (kip)
A_s= total area of reinforcement located within the end of the beam (in.^{2})

From the above equation, the stress in the steel (f_s) cannot exceed 20 ksi for crack control at the ends of the beam. Therefore, the amount of rebar at the end region cannot be reduced due to the stress limit, even if the high-strength rebar is used. As a result, the research team decided to keep the reinforcement design at the end of the pretensioned girder and determined that shear reinforcement was the main concern in the calculation.

5.2.2.1. Tx-girder

Tx-62 was chosen for the example calculation.

5.2.2.1.1. Current reinforcement layout

The geometry and rebar layout of the Tx-62 suggested in the TxDOT bridge design manual (2021) were considered in the calculation. The cross-section and rebar layout are shown in Figure 5-5. The spacing of the shear reinforcement for the main shear region in Tx-62 is 8 in., and 31 rebars are deployed in the main shear region. In addition, the shear strength was calculated as 297 kips using Grade 60 shear reinforcement. The calculation for shear strength and shear reinforcement spacing for the current TxDOT layout is shown in Appendix D.

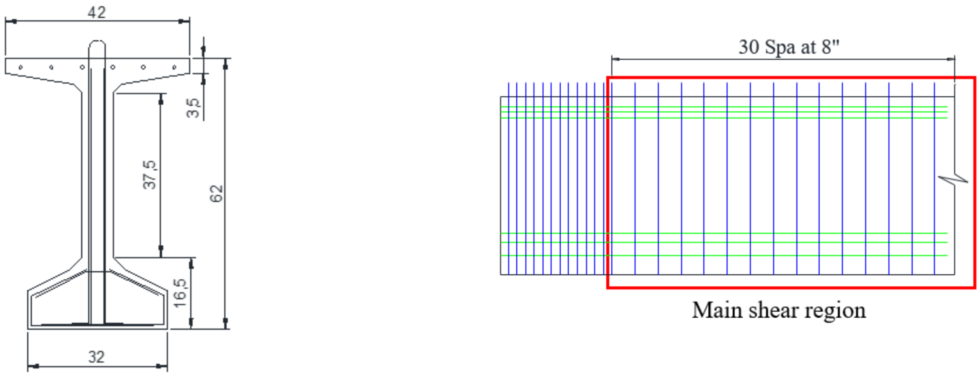

(a) Cross-section (b) Rebar layout

Figure 5-5. Details of Tx-62

5.2.2.1.2. Shear reinforcement layout using high-strength rebar

The spacing of the high-strength shear reinforcement is calculated to achieve a similar shear strength as the beam using Grade 60. The sectional design method also concerns the updated rebar spacing. The minimum transverse reinforcement and maximum spacing of transverse reinforcement, as determined by Equations (5-4) and (5-5), were also taken into account.

$$A_v \geq 0.0316\lambda\sqrt{f_c'}\frac{b_v s}{f_y} \tag{5-4}$$

$$\begin{aligned} s_{max} &= 0.8d_v \leq 24\ in.\ if\ v_u < 0.125f_c' \\ s_{max} &= 0.4d_v \leq 12\ in.\ if\ v_u \geq 0.125f_c' \end{aligned} \tag{5-5}$$

where,

A_v= area of a transverse reinforcement within distance s (in^2.)

λ= concrete density modification factor

b_v= effective web width is taken as the minimum web width (in.)

s = spacing of transverse reinforcement (in.)

s_{max}= maximum permitted spacing of transverse reinforcement (in.)

d_v= effective shear depth taken as the distance (in.)

v_u= shear stress (ksi)

When Grade 80 is selected as the shear reinforcement, the spacing for the shear rebar can be increased to 10.65 in. for 297 kip shear strength. The calculated spacing for Grade 100 shear reinforcement was 13 in. for the same shear strength. However, the spacing was reduced from 13 in. to 12 in. to satisfy the limitation in Equation (5-5), as shown in Figure 5-6. The results are summarized in Table 5-4, and the details of calculations for shear strength and shear reinforcement spacing are shown in Appendix B.

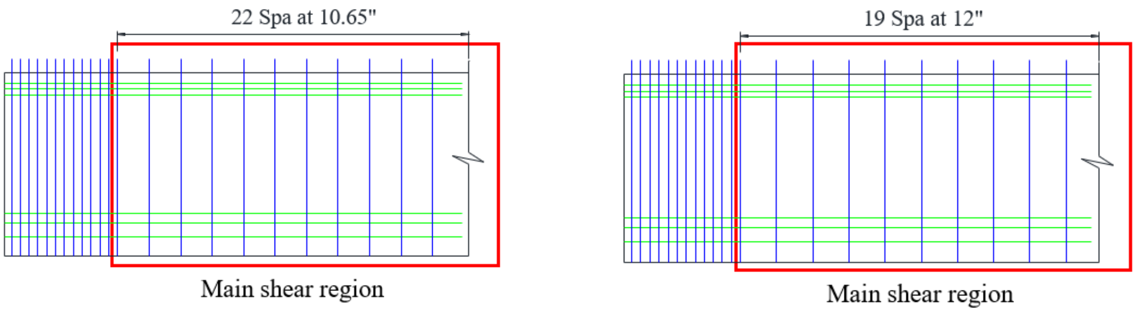

(a) Grade 80 (b) Grade 100

Figure 5-6. Rebar layout of Tx-62

Table 5-4. Summary of rebar quantity for Tx-62 girder

Type		Grade	No. of rebar	Weight (lb)	Compare
Vertical	**R bar**	60	62	508	-
		80	54	443	↓13
		100	51	418	↓18
	S bar	60, 80, 100	26	190	Same
Confinement	**C bar**	60, 80, 100	32	86	Same
	CH bar	60, 80, 100	16	27	Same
Top longitudinal	**U bar**	60, 80, 100	2	17	Same
	T bar	60, 80, 100	6	180	Same
Top confinement	**A bar**	60, 80, 100	45	55	Same
Total		60	-	1,063	-
		80	-	998	↓6
		100	-	973	↓8

5.2.2.2. Box beam

5B40 was chosen for the example calculation.

5.2.2.2.1. Current reinforcement layout

The geometry and rebar layout of the 5B40 proposed in the TxDOT bridge design manual (2021) were applied for the calculation. The cross-section and rebar layout are shown in Figure 5-7. The spacing of the shear reinforcement for the main shear region in 5B40 is 6 in., and 39 rebars are deployed in the main shear region. In addition, the shear strength of example 5B40 using Grade 60 shear reinforcement is 298 kips based on the sectional design method. The calculation for shear strength and shear reinforcement spacing for the current TxDOT layout is shown in Appendix B.

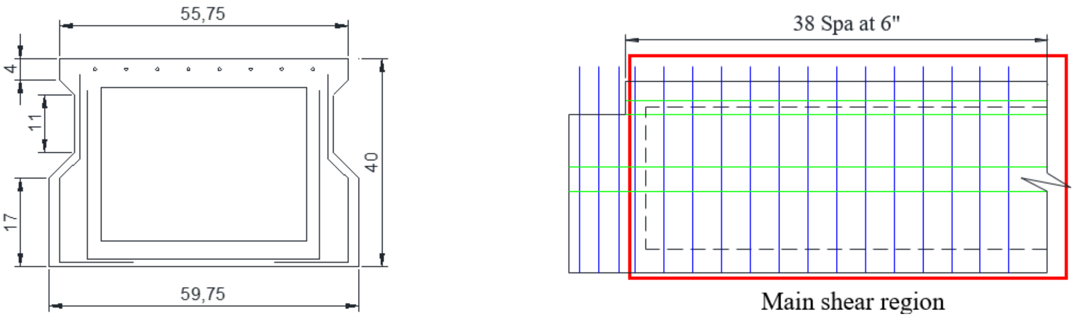

(a) Cross-section (b) Rebar layout

Figure 5-7. Details of 5B40

5.2.2.2.2. Reinforcement layout using high-strength rebar

When Grade 80 is selected as the shear reinforcement, the spacing for the shear rebar can be increased to 8 in. for 298 kip shear strength. The calculated spacing for Grade 100 shear reinforcement was 10 in. for the same shear strength. All cases with Grade 80 and Grade 100 satisfied the spacing limit in Equations (5-4) and (5-5), as shown in Figure 5-8. The results are summarized in Table 5-5, and the details of calculations for shear strength and shear reinforcement spacing are shown in Appendix B.

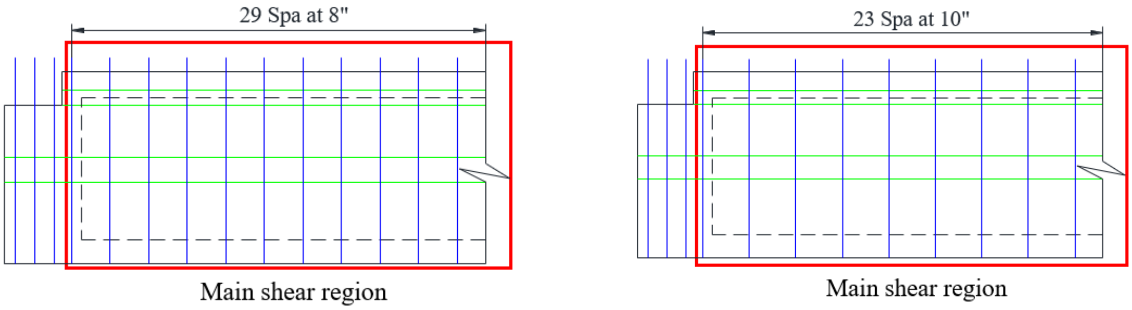

(a) Grade 80 (b) Grade 100

Figure 5-8. Rebar layout of 5B40

Table 5-5. Summary of rebar quantity for 5B40 box beam

Type		Grade	No. of rebar	Weight (lb)	Compare
Vertical	**C bar**	60	64	423	-
		80	55	364	↓14%
		100	49	324	↓23%
	A bar	60	81	409	-
		80	72	364	↓11%
		100	66	333	↓19%
End block	**M bar**	60, 80, 100	6	19	Same
	N bar	60, 80, 100	6	15	Same
Confinement	**U bar**	60, 80, 100	88	251	Same
Top longitudinal	**D bar**	60, 80, 100	8	350	Same
Top confinement	**B bar**	60, 80, 100	81	234	Same
Total		60	-	1,292	-
		80	-	1,233	↓5%
		100	-	1,193	↓8%

5.2.2.3. **Conclusion**

Example calculations were performed using two types of TxDOT prestressed girders. The calculations considered only the replacement of vertical (shear) reinforcement for the prestressed girders. Vertical reinforcement was reduced considering the minimum and maximum transverse rebar spacing proposed by AASHTO LRFD (2020), and it could be reduced by about 20% by less than the rebar strength ratio. Since the vertical rebar amount is not as large as the longitudinal reinforcement, the total rebar quantity could be reduced by approximately up to 8%.

5.2.3. Bent Cap

The research team used an example inverted T bent cap from a previous research study (FHWA/TX-12/5-5253-01-1: Strut-and-Tie Model Design Examples for Bridges) and also one design example from an existing bridge project. Calculations were performed to consider two benefits: (1) Enhancement of load-carrying capacity; (2) Reduction of rebar quantity. First, the same rebar layout was used, but the conventional rebars were replaced with high-strength rebars to improve the load-carrying capacity, and the net tensile strain was compared. Second, the rebar quantity was reduced as much as the rebar strength ratio between the conventional rebar and high-strength rebar to maintain load-carrying capacity. The longitudinal reinforcement, vertical ties, and ledge were considered. The reinforcement at the end face and longitudinal bars at the flange in the red circle in Figure 2.9 were ignored because these rebars are not the target for the use of high-strength steel, and the quantity of these rebars is very small compared to the entire quantity of rebar. The rebar spacing was controlled by following the serviceability limit proposed by AASHTO LRFD (2020).

5.2.3.1. Inverted T bent (FHWA/TX-12/5-5253-01-1)

The geometry of the bent cap of the previous study (FHWA/TX-12/5-5253-01-1: Strut-and-Tie Model Design Examples for Bridges) is presented in Figure 5-9. This bent cap was treated in two ways based on the assumed boundary condition at the column. First, the substructure was designed to behave as a moment frame. Second, the bent cap was designed as the columns are simply supported. In this study, these two cases are considered.

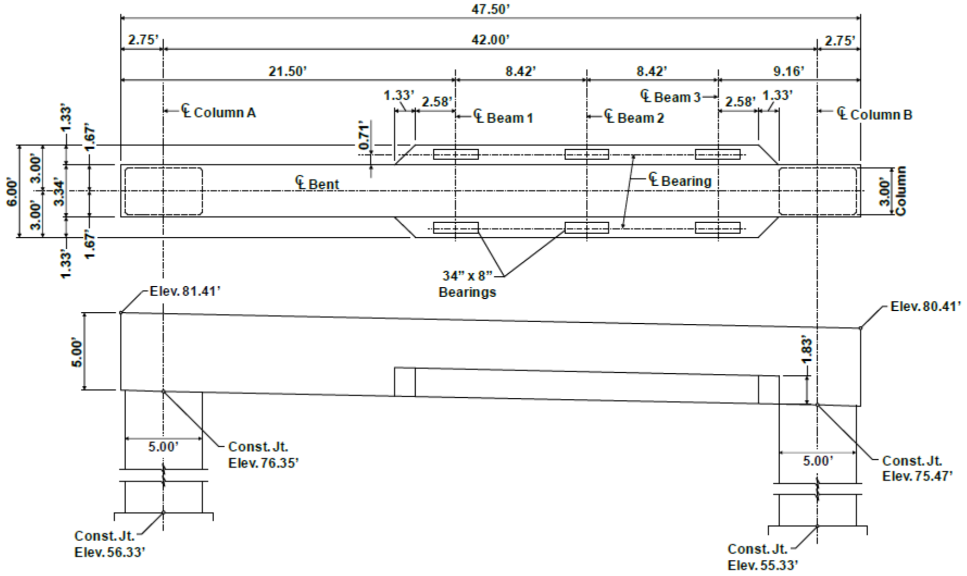

Figure 5-9. Plan and elevation views of inverted T bent cap (FHWA/TX-12/5-5253-01-1)

5.2.3.1.1. Enhancement load-carrying capacity

Moment frame

One-to-one replacement of high-strength reinforcing bars with conventional rebars was assumed to maximize the enhancement of load-carrying capacity. The moment-curvature relations were obtained based on the conditions of equilibrium and strain capability, as shown in Figure 5-10 It was confirmed that the load-carrying capacity increased by using the high-strength rebar, but the ductility decreases.

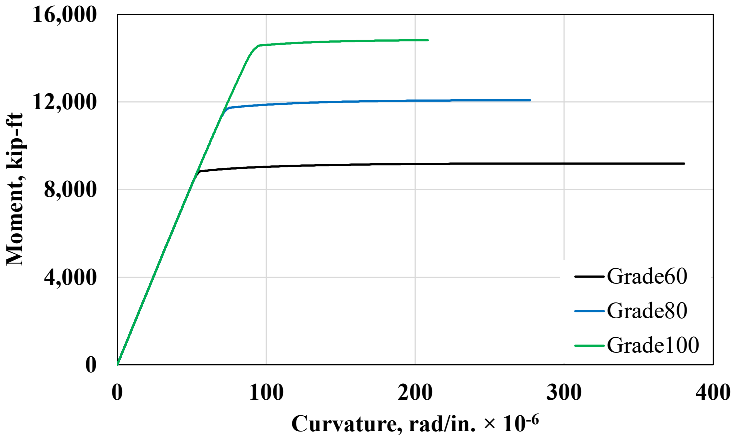

Figure 5-10. Moment-curvature relation according to rebar grade (Moment frame case)

The net tensile strain (ε_t) was obtained depending on the rebar grade and compared with the strain limit proposed by AASHTO LRFD (2020). As shown in Figure 5-11, the use of high-strength rebar causes the reduction of net tensile strain. In particular, the tension-controlled limit (ε_{tl}) is not satisfied when suing Grade 100 rebar. The net tensile strain can be increased by using high-strength concrete in combination with high-strength rebar as shown in Figure 5-11. When Grade 80 rebar was used together with high-strength concrete of 10 ksi, and Grade 100 rebar with high-strength concrete of 15 ksi, the net tensile strain could be increased to the level of the case of using conventional rebar of Grade 60.

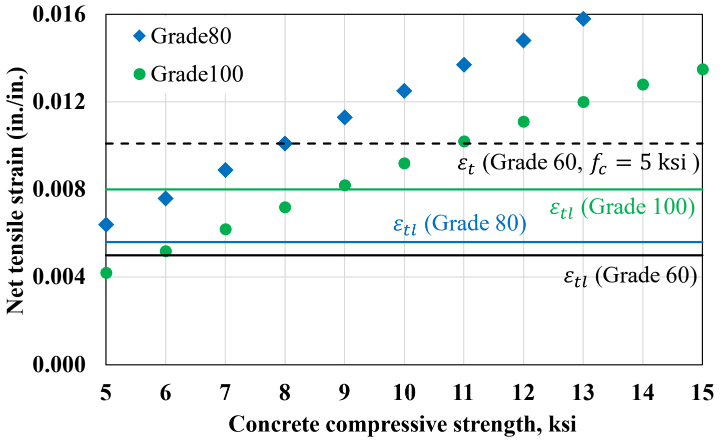

Figure 5-11. Net tensile strain with high-strength rebar according to concrete strength (Moment frame case)

Simply supported

The moment-curvature relations and net tensile strain in the case of designed as simply supported were obtained as shown in Figure 5-12 and Figure 5-13, following the same process as in the above section. Similar trends to those observed earlier were identified: as the rebar strength increased, the section's ductility decreased. The tension-controlled limit was not satisfied when using Grade 100 rebar, but the net tensile strain could be increased by incorporating high-strength concrete. Specifically, when Grade 80 rebar was used with high-strength concrete of 8 ksi, or Grade 100 rebar with high-strength concrete of 11 ksi, a net tensile strain comparable to that achieved with conventional Grade 60 rebar was observed.

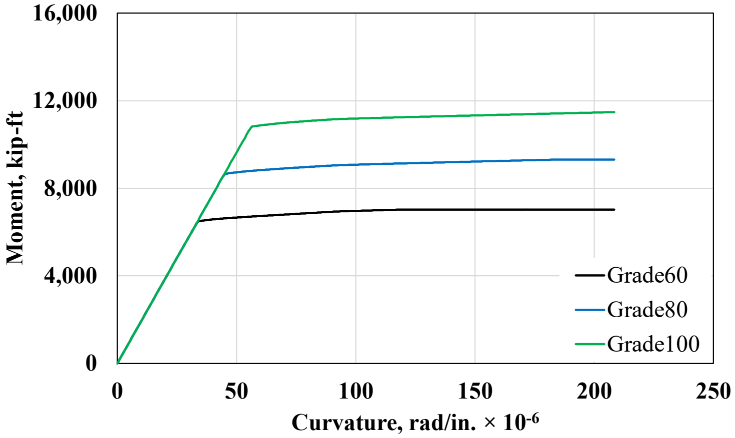

Figure 5-12. Moment-curvature relation according to rebar grade (Simply supported case)

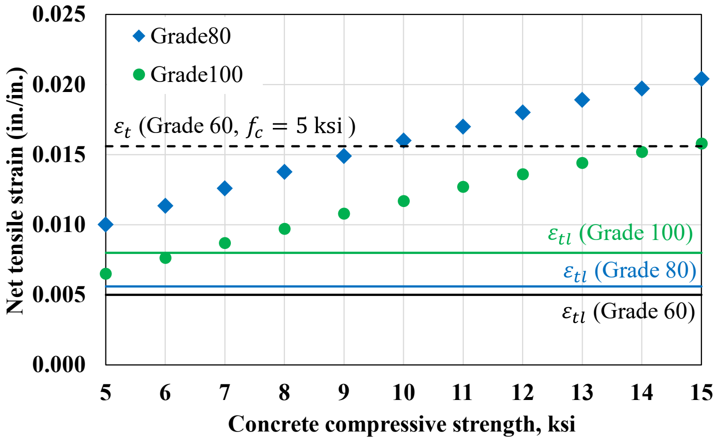

Figure 5-13. Net tensile strain with high-strength rebar according to concrete strength (Simply supported case)

5.2.3.1.2. Reduction of rebar quantity

Moment frame

The moment frame case used a strut and tie model (STM) as shown in Figure 5-14.

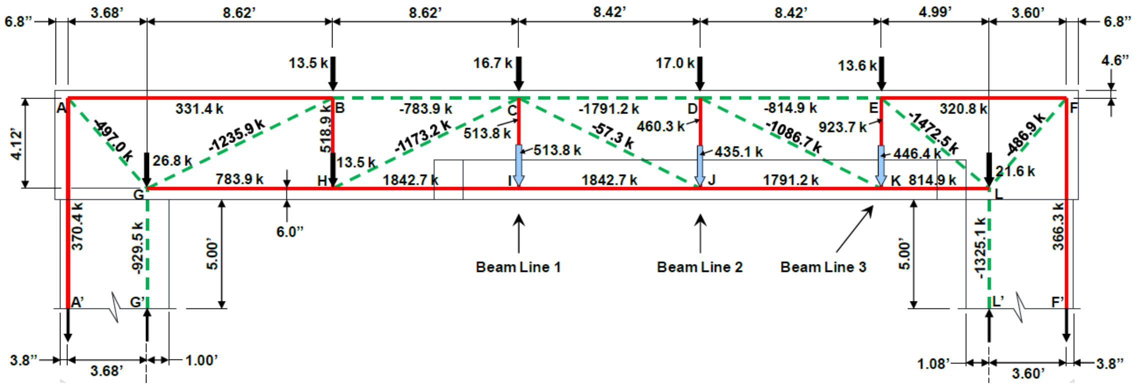

Figure 5-14. STM designed moment frame in previous research (FHWA/TX-12/5-5253-01-1)

Longitudinal Ties

The longitudinal reinforcement along top and bottom chords was designed considering the force in Ties AB, HI, and IJ, respectively (Refer to Figure 5-14). The required number of longitudinal ties was calculated to satisfy the required load capacity. When using Grade 80 rebars, the top chord can be reduced from 15 to 11, and the bottom chord can be reduced from 22 to 17. If Grade 100 rebars are used for longitudinal ties, the top chord can be reduced from 15 to 9, and the bottom chord can be reduced from 22 to 14. The details of the calculation procedure are shown in Appendix A.

Vertical Ties

The vertical ties were designed in the same method as longitudinal ties based on the calculated force in Ties EK, CI, and BH. The number of vertical ties was calculated to satisfy the required load capacity. The details of the calculation procedure are shown in Appendix A. The calculation results were summarized in Table 5-6. The required spacing increased as much as the strength ratio between Grade 60 and high-strength rebars.

Ledge Reinforcement

The local STM was developed at each section where the ledge supports a beam load due to the complex flow of forces within the inverted-T cross-section, and the ledge reinforcement was determined to carry the force in Tie C_sF_s in Figure 5-15. Local strut-and-tie model for moment frame design (FHWA/TX-12/5-5253-01-1). Each of the stirrups within the ledge will be paired with the stirrups of the stem to simplify construction. The details of the calculation procedure are shown in Appendix A.

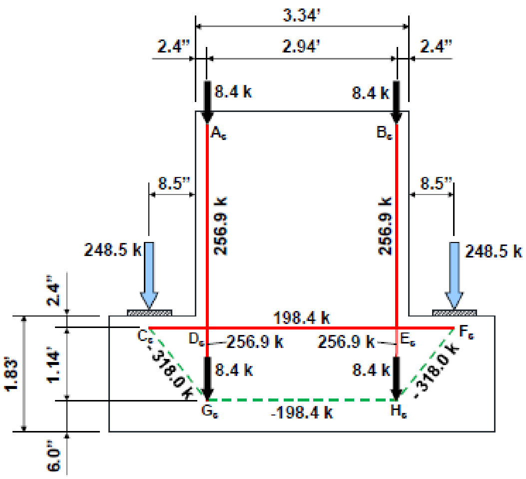

Figure 5-15. Local strut-and-tie model for moment frame design (FHWA/TX-12/5-5253-01-1)

Crack control reinforcement

AASTHO LRFD (2020) suggested a minimum crack control reinforcement of 0.3% in each direction. For example, if 2 legs of #6 stirrups were used, the required spacing of the vertical tie is calculated as Equation (5-6). Additionally, the skin reinforcement of #6 bars parallel to longitudinal ties was determined following this limit in Equation (5-7).

$$A_v = 0.003 b_w s_v, s_v = \frac{A_v}{0.003 b_w} = \frac{2 \times 0.44}{0.003 \times 40} = 7.3\ in \tag{5-6}$$

$$A_h = 0.003 b_w s_h, s_h = \frac{A_h}{0.003 b_w} = \frac{2 \times 0.44}{0.003 \times 40} = 7.3\ in \tag{5-7}$$

where,

A_v= total area of vertical crack control reinforcement within spacing in s_v (in.^{2})

b_w= width of member's web (in.)

s_v, s_h= spacing of vertical and horizontal crack control reinforcement, respectively (in.)

A_h= total area of horizontal crack control reinforcement within spacing in s_h (in.^{2})

Considering this, the calculated required spacing for vertical ties and ledge reinforcement and the limitation for crack control are shown in Table 5-6. As can be seen in the Table, the limited spacing for crack control is larger than the calculated required spacing in some cases. In this case, it should be designed using limited spacing.

Table 5-6. Required spacing for vertical ties and ledge reinforcement (FHWA/TX-12/5-5253-01-1)

Location	Calculated required spacing (in.)			Max. spacing for crack control (in.)		
	Gr. 60	Gr. 80	Gr. 100	Gr. 60	Gr. 80	Gr. 100
Tie EK	6.4	8.5	10.6	14.7		
Tie CI	5.7	7.6	9.6	7.3		
Tie BH	9.5	12.6	15.8	7.3		
Tie C_sF_s	7.4	9.9	12.4	-		

Reinforcement layout

The reinforcement details considering all of the above are shown in Figure 5-16 and Figure 5-17. Additionally, the quantity of all rebars was calculated and listed in Table 5-7. The reinforcement of corbel was used as the same as the current layout. It was found that the longitudinal reinforcement can be reduced as much as the rebar strength ratio. On the other hand, for vertical reinforcement, the reduction depended on the crack control reinforcement requirement. Therefore, vertical reinforcement had a smaller reduction than longitudinal rebar.

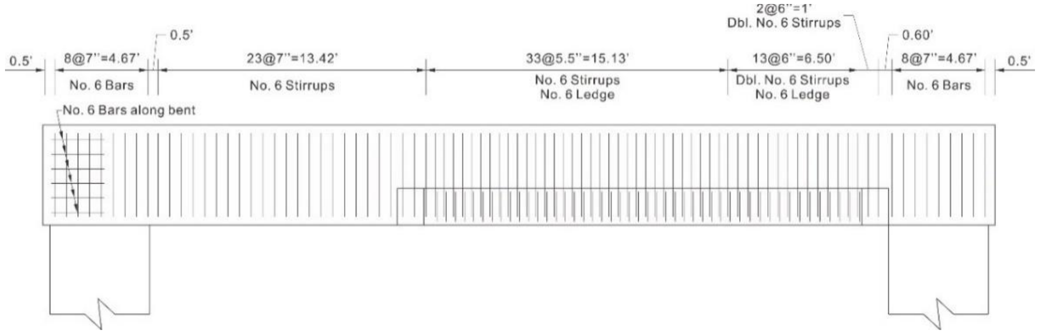

(a) Grade 60

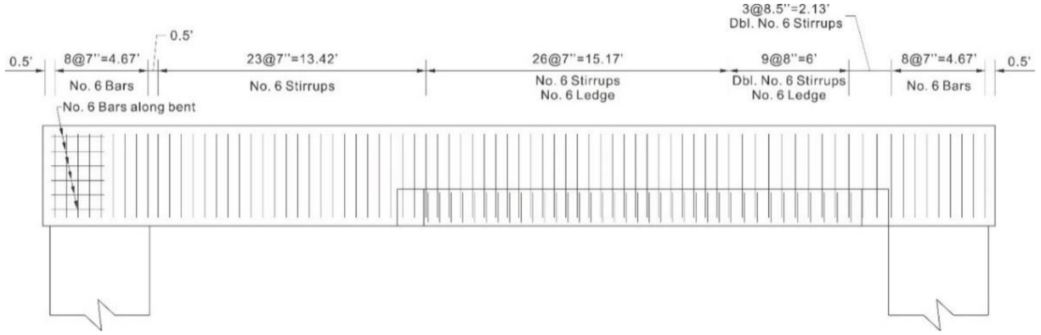

(b) Grade 80

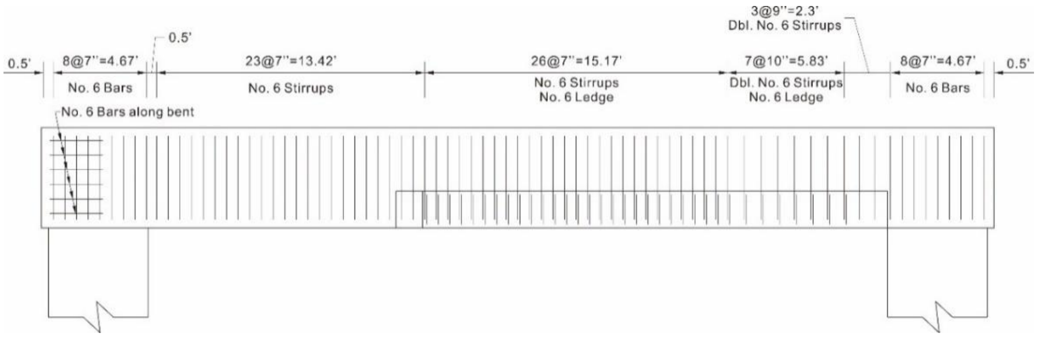

(c) Grade 100

Figure 5-16. Rebar details of moment frame case

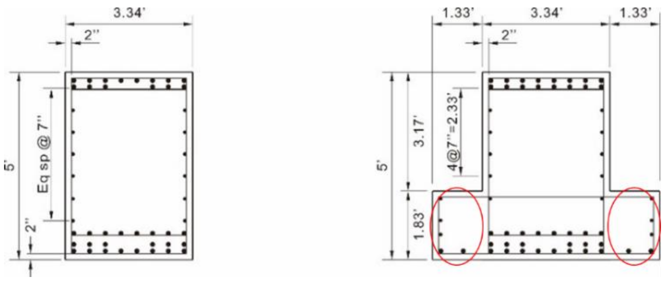

(a) Grade 60

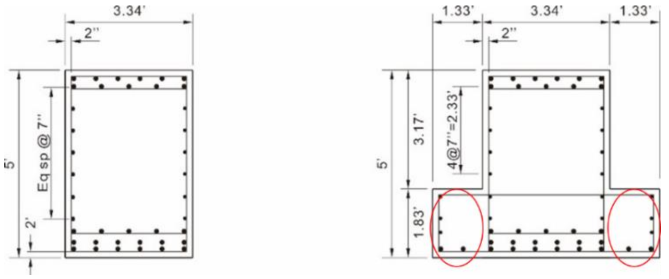

(b) Grade 80

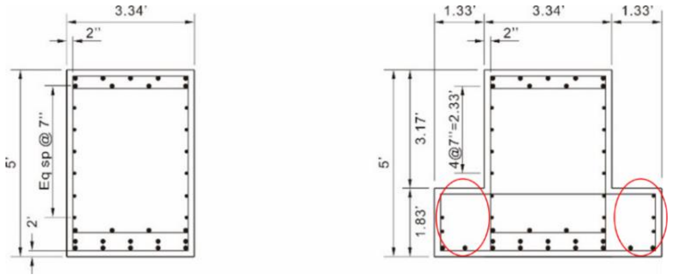

(c) Grade 100

Figure 5-17. Cross-section details of moment frame case

Table 5-7. Summary of rebar quantity for moment frame case

Type	Size	Grade	No. of rebar	Weight (lb)	Compare
Longitudinal	#11	60	37	9,115	-
		80	28	6,898	↓24
		100	23	5,666	↓38
Skin	#6	60, 80, 100	12	836	Same
Vertical	#6	60	75	1,727	-
		80	68	1,566	↓9
		100	68	1,566	↓9
	Dbl. #6	60	15	961	-
		80	12	769	↓20
		100	10	641	↓33
Ledge	#6	60	47	1,012	-
		80	36	775	↓23
		100	34	732	↓28
Corbel	#6	60, 80, 100	6	222	Same
	#11	60, 80, 100	4	524	Same
Total		60	-	14,397	-
		80	-	11,590	↓19
		100	-	10,187	↓29

Simply supported

STM for simply supported assumption is shown in Figure 5-18 and Figure 5-19. The reinforcement was designed in the same process as the moment frame, and the details of the calculation procedure are shown in Appendix A. The results are shown in Figure 5-20 and Figure 5-21, and the rebar quantity was calculated and listed in Table 5-8. For simply supported design, the required quantity of reinforcing bars was slightly larger than that of the moment frame design because of the reduced truss depth. A similar trend was confirmed when using high-strength steel. The longitudinal reinforcement can be reduced by the strength ratio of rebars. However, vertical reinforcement can be reduced by a lower amount than longitudinal rebar due to the spacing limit for crack control.

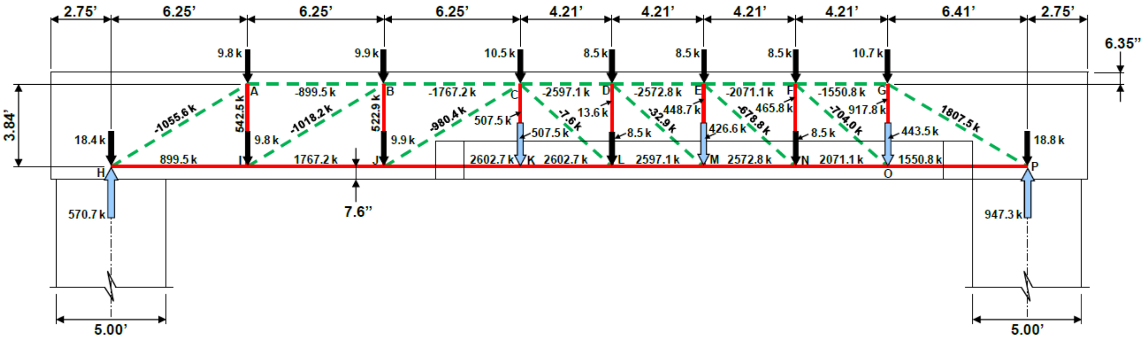

Figure 5-18. STM designed simply supported in previous research (FHWA/TX-12/5-5253-01-1)

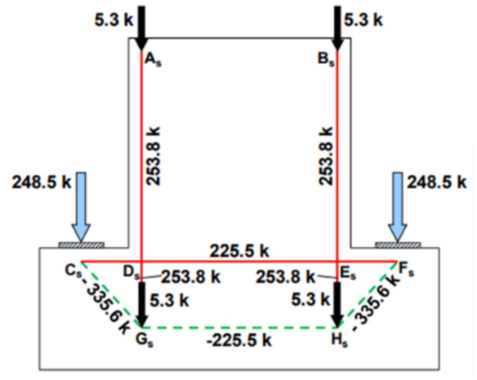

Figure 5-19. Local strut-and-tie model for simply supported design (FHWA/TX-12/5-5253-01-1)

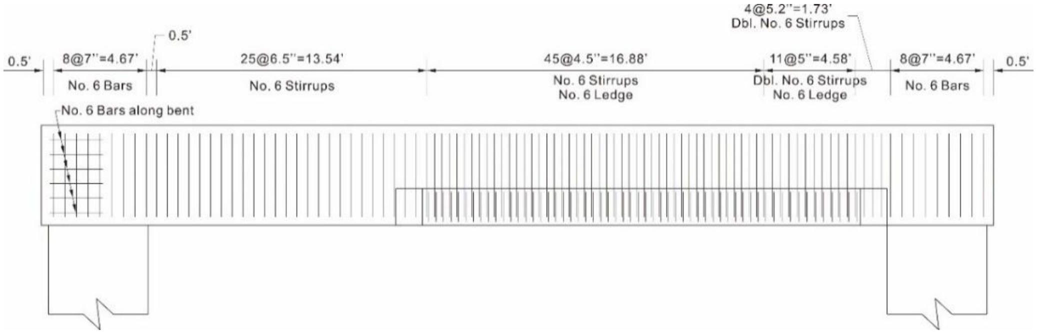

(a) Grade 60

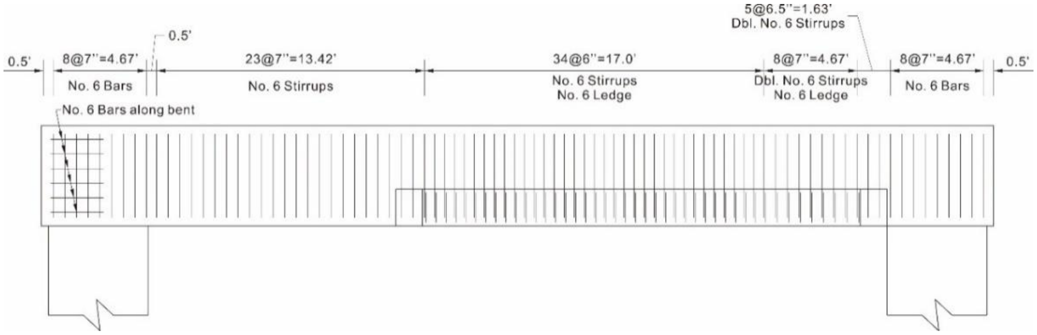

(b) Grade 80

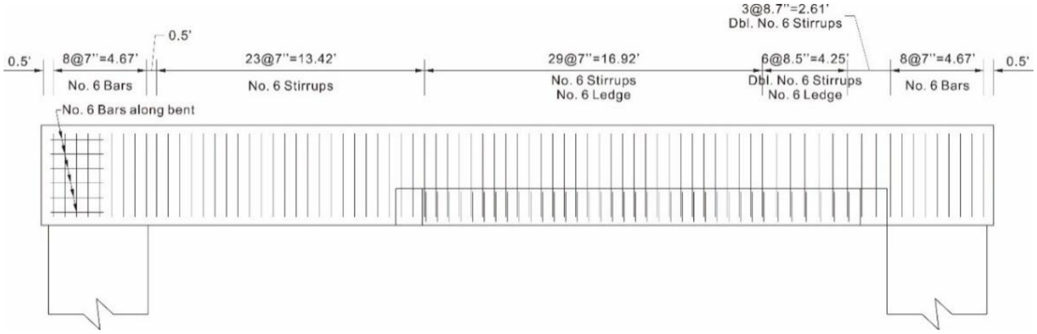

(c) Grade 100

Figure 5-20. Rebar details of simply support case

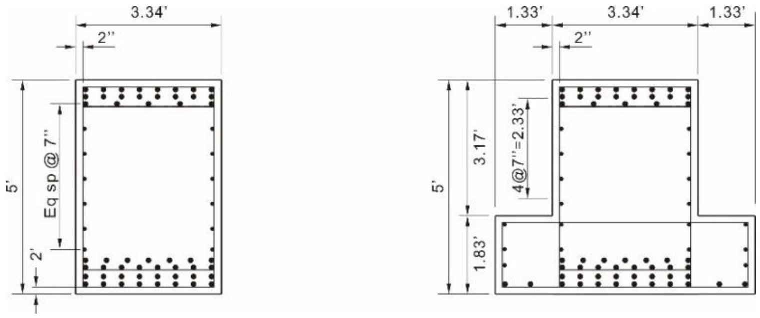

(a) Grade 60

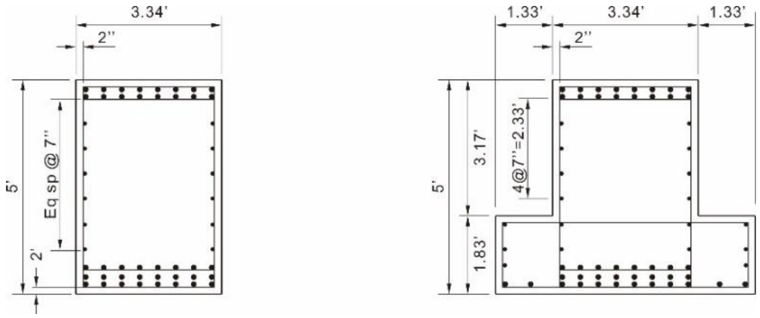

(b) Grade 80

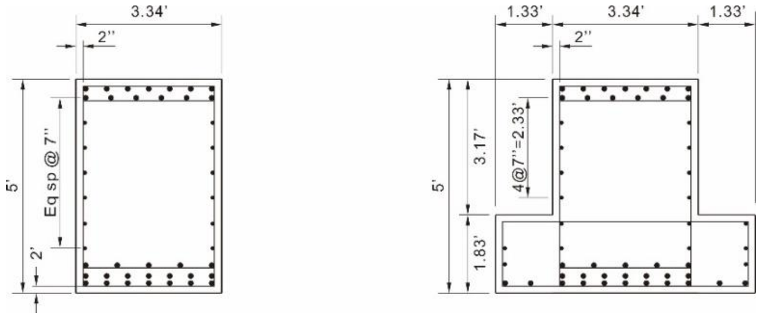

(c) Grade 100

Figure 5-21. Cross-section details of simply support case

Table 5-8. Summary of rebar quantity for simply support case

Type	Size	Grade	No. of rebar	Weight (lb)	Compare
Longitudinal	#11	60	52	12,810	-
		80	40	9,854	↓23
		100	32	7,883	↓38
Skin	#6	60, 80, 100	12	836	Same
Vertical	#6	60	89	2,050	-
		80	76	1,750	↓15
		100	71	1,635	↓20
	Dbl. #6	60	15	961	-
		80	13	833	↓13
		100	9	577	↓40
Ledge	#6	60	57	1,227	-
		80	43	926	↓25
		100	36	775	↓37
Corbel	#6	60, 80, 100	6	222	Same
	#11	60, 80, 100	4	524	Same
Total		60	-	18,630	-
		80	-	14,945	↓20
		100	-	12,452	↓33

5.2.3.2. IH-610 Buslane (TxDOT)

The research team used the rebar layout and cross-section of the IH-610 bus lane provide by TxDOT as a second bent cap example case. The two types of inverted T cross-section bents of the IH-610 bus lane (Bent 5 and 11) were used.

5.2.3.2.1. Enhancement load-carrying capacity

Bent 5

The moment-curvature relations of bent 5 is shown in Figure 5-22, and the net tensile strain is obtained as shown in Figure 5-23. The load-carrying capacity increased with the use of high-strength reinforcing bars, but the ductility decreased.

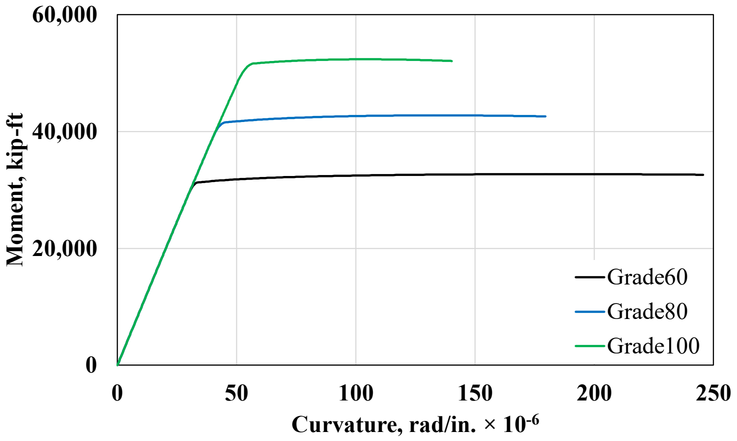

Figure 5-22. Moment-curvature relation according to rebar grade of bent 5

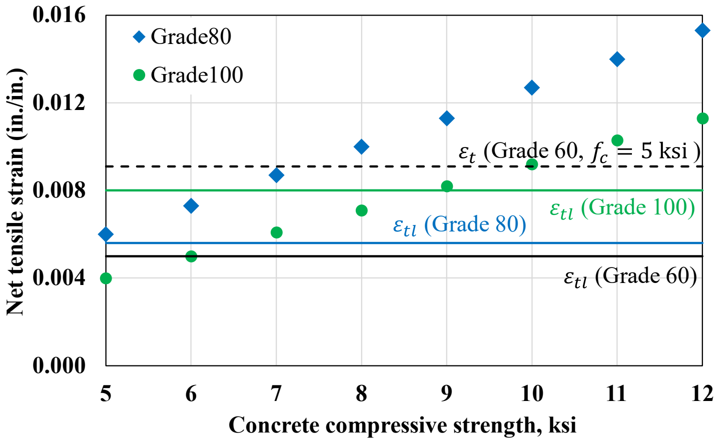

Figure 5-23. Net tensile strain using high-strength rebar according to concrete strength of bent 5

Bent 11

The moment-curvature relations and the net tensile strain are shown in Figure 5-24 and Figure 5-25. The load-carrying capacity increased with the use of high-strength reinforcing bars, but the ductility decreased.

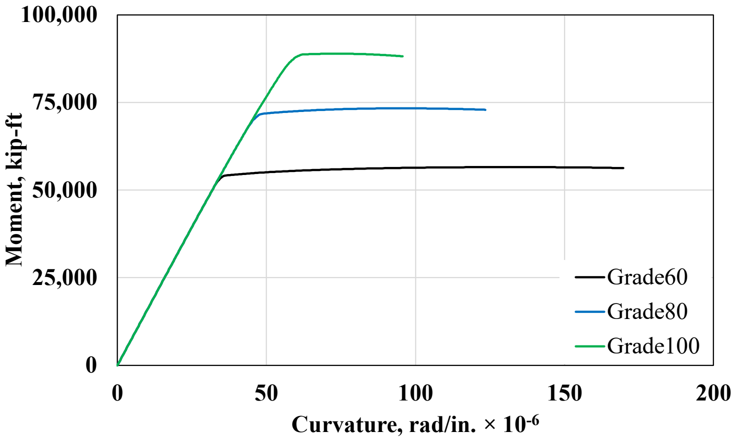

Figure 5-24. Moment-curvature relation according to rebar grade of bent 11

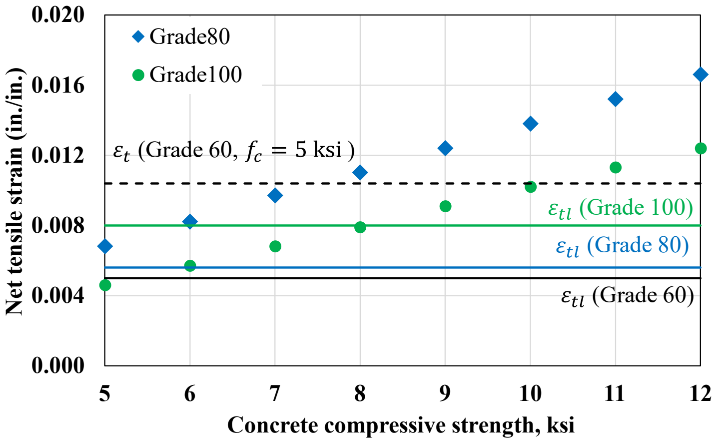

Figure 5-25. Net tensile strain using high-strength rebar according to concrete strength of bent 11

5.2.3.2.2. Reduction of rebar quantity

Bent 5

The load capacity of longitudinal reinforcement, vertical ties, and ledge were calculated using the current rebar layout in Figure 5-26. The high-strength rebar was applied under the assumption that the current load capacity was maintained. Since bent 5 is regarded as D-region, STM was used for calculation. The details of the calculation are shown in Appendix A. The results are shown in Figure 5-27 and Figure 5-28, and the rebar quantity was calculated and listed in Table 5-9.

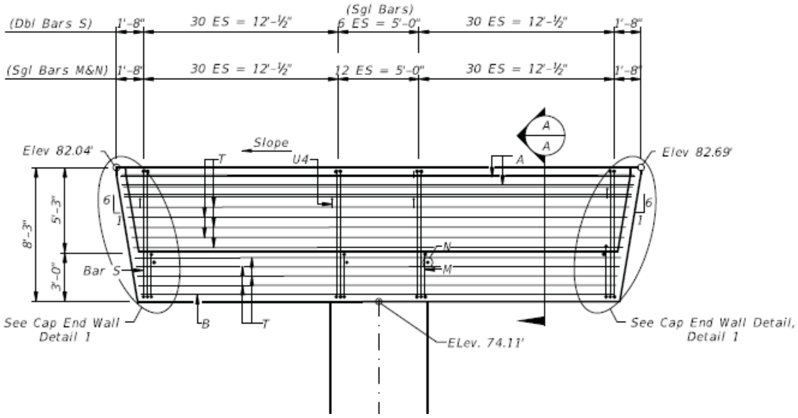

(a) Elevation

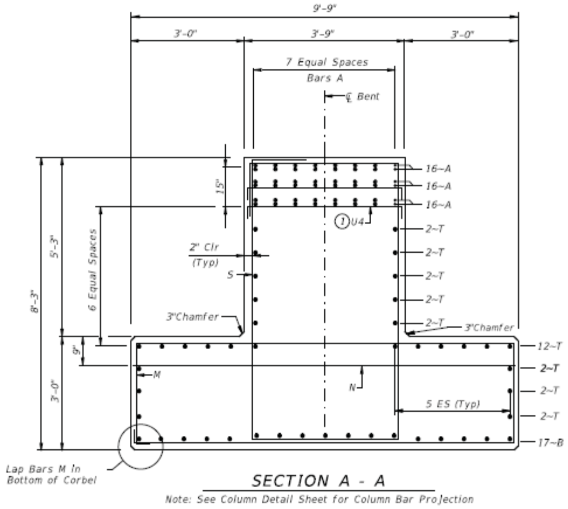

(b) Cross-section

Figure 5-26. Details of bent 5

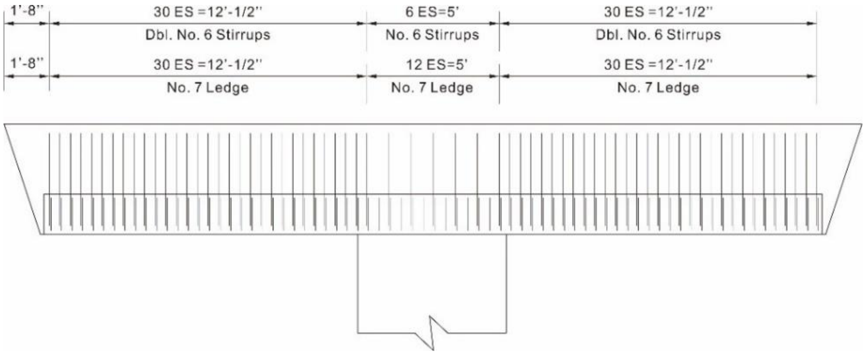

(a) Grade 60

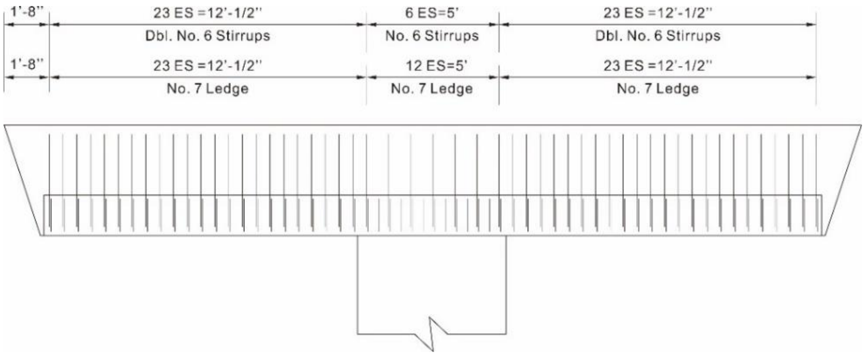

(b) Grade 80

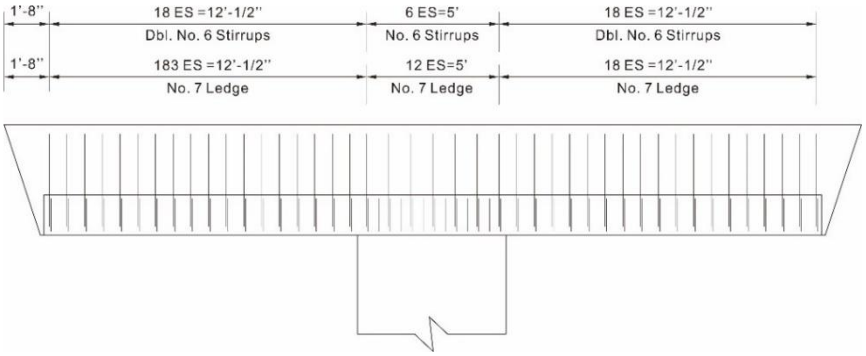

(c) Grade 100

Figure 5-27. Rebar details of bent 5

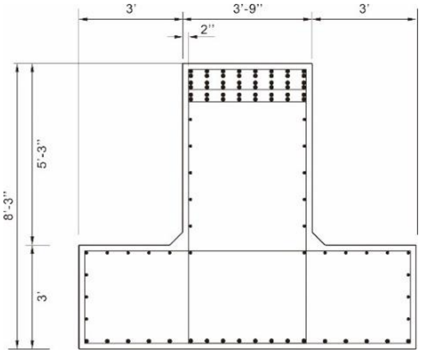

(a) Grade 60

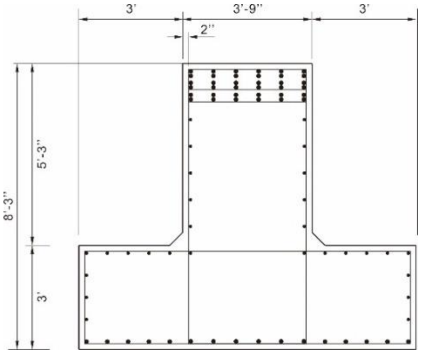

(b) Grade 80

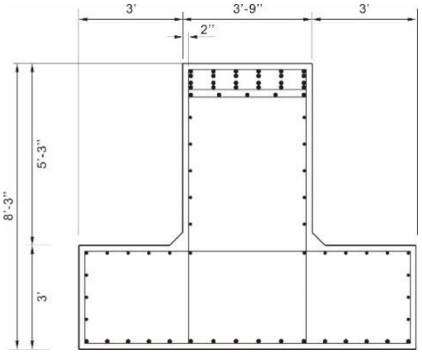

(c) Grade 100

Figure 5-28. Cross-section details of bent 5

Table 5-9. Summary of rebar quantity for bent 5

Type	Size	Grade	No. of rebar	Weight (lb)	Compare
Longitudinal	#11	60	55	9,273	-
		80	42	7,072	↓24
		100	34	5,723	↓38
Skin	#7	60, 80, 100	12	719	Same
Vertical	#6	60	129	4,779	-
		80	101	3,742	↓22
		100	81	3,001	↓37
Ledge	#7	60	73	3,954	-
		80	59	3,196	↓19
		100	49	2,654	↓33
Corbel	#7	60, 80, 100	16	1,006	Same
	#11	60, 80, 100	10	1,558	Same
Total		60	-	21,325	-
		80	-	17,293	↓19
		100	-	14,661	↓31

Bent 11

Another bent of IH 610 bus lane was used for calculation. The current rebar layout is shown in Figure 5-29. The same calculation procedure in previous chapter was performed. However, the rectangular section can be regarded as B-region. Thus, the shear resistance provided by shear reinforcement was calculated by Equations (5-8) to (5-10) in accordance with AASTHO LRFD (2020) for B-region. The details of the calculation are shown in Appendix A.

$$V_s = \frac{A_v f_y d_v (cot\theta + cot\alpha) sin\alpha}{s} \tag{5-8}$$

$$\theta = 29 + 3500\varepsilon_s \tag{5-9}$$

$$\varepsilon_s = \frac{\left(\frac{|M_u|}{d_v} + V_u\right)}{E_s A_s} \tag{5-10}$$

where,

A_v= total area of transverse reinforcement within spacing in s (in.^{2})
s= spacing of transverse reinforcement (in.)
d_v= effective shear depth (in.)
θ= angle of inclination of diagonal compressive stresses (degrees)
α= angle of inclination of transverse reinforcement to longitudinal axis (degrees)
ε_s= net longitudinal tensile strain at the centroid of the tension reinforcement
M_u= factored moment at the section (kip-in.)
V_u= factored shear force (kip)
E_s= modulus of elasticity of steel reinforcement (ksi)
A_s= area of non-prestressed steel on the flexural tension side of the member (in.^{2})

Generally, the sectional design method was verified as more conservative compared to STM (FHWA/TX-09/0-5253-1: Strength and Serviceability Design of Reinforced Concrete Deep Beams). However, the calculation assumed to maintain current shear resistance by shear reinforcement. As a result, the both design methods: sectional method and STM showed a similar required spacing of transverse reinforcement. The results are shown in Figure 5-30 and Figure 5-31, and the rebar quantity was calculated and listed in Table 5-10.

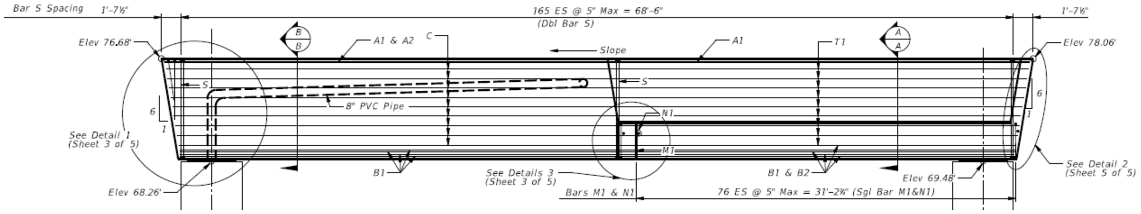

(a) Elevation

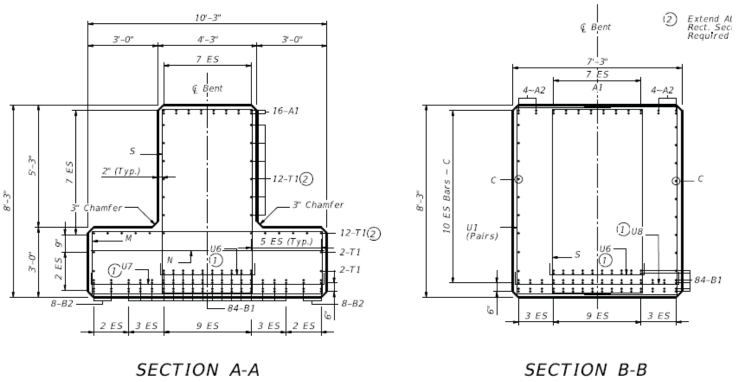

(b) Cross-section

Figure 5-29. Details of bent 11

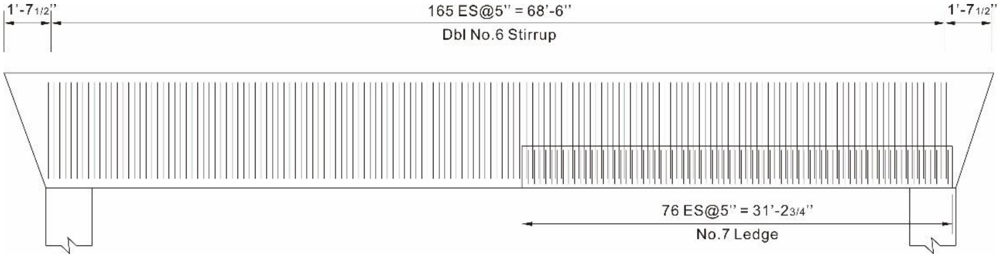

(a) Grade 60

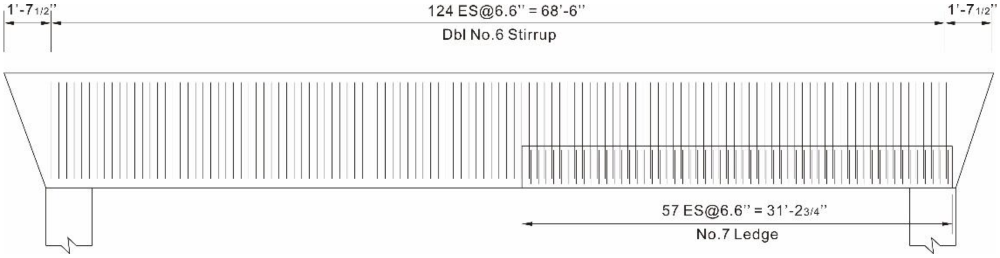

(b) Grade 80

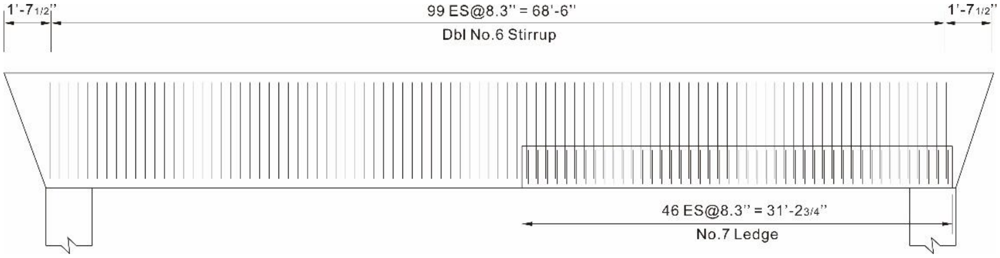

(c) Grade 100

Figure 5-30. Rebar details of bent 11

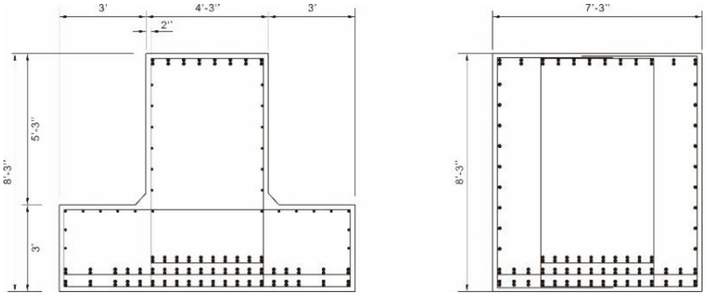

(a) Grade 60

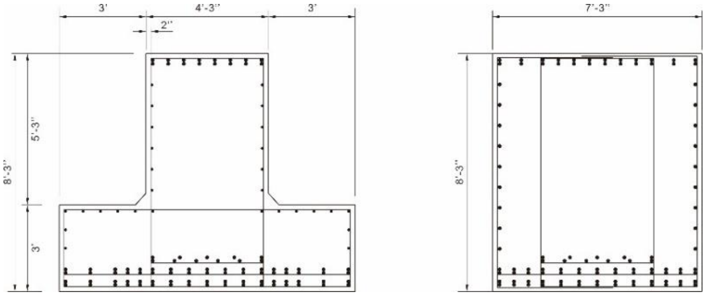

(b) Grade 80

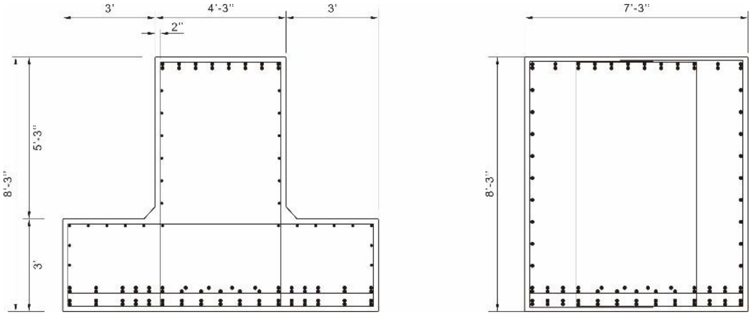

(c) Grade 100

Figure 5-31. Cross-section of bent 11

Table 5-10. Summary of rebar quantity for bent 11

Type	Size	Grade	No. of rebar	Weight (lb)	Compare
Longitudinal	#11	60	100	37,710	-
		80	75	28,282	↓25
		100	61	23,000	↓39
Skin	#7, #11	60, 80, 100	-	5,901	Same
Vertical	#6	60	332	12,799	-
		80	250	9,638	↓25
		100	200	7,710	↓40
Ledge	#7	60	77	4,328	-
		80	58	3,260	↓25
		100	46	2,586	↓40
Corbel	#7	60, 80, 100	14	2,044	Same
	#11	60, 80, 100	24	4,527	Same
Total		60	-	67,308	-
		80	-	53,652	↓20
		100	-	45,767	↓32

5.2.3.3. Conclusion

The inverted T bent caps in the previous example study and TxDOT drawing were used for an example calculation. The bent cap in the previous example was considered in two ways depending on the design method: moment frame and simply supported. Through the detailed calculation process, it was confirmed that the load-carrying capacity can be increased by applying high-strength rebar, while the tension-controlled section cannot be certain because the ductility decreases. Additionally, it was observed that when high-strength concrete was used together, it was possible to increase the ductility to satisfy the tension control limit and to secure a level of ductility similar to that in the case of using the conventional rebar. On the other hand, the amount of rebar can be reduced by the rebar strength ratio between the conventional rebar and high-strength rebar while maintaining the load-carrying capacity. However, vertical ties were reduced by a smaller amount to satisfy the minimum reinforcement ratio of 0.3% for crack controlling proposed by AASHTO LRFD (2020). Example calculations with two TxDOT bent caps in IH 610 bus lane also confirmed similar results as above.

However, the currently proposed minimum amount of reinforcement for crack control was verified only when using the conventional rebar of Grade 60. Therefore, it is necessary to examine whether the minimum crack control reinforcement is effective even when high-strength rebar is used through experimental verification.

5.2.4. Drilled Shaft Footing

The research team considered the drilled shaft supported footing in the previous study (FHWA/TX-21/0-6953-R1: 3D Strut-and-Tie Modeling for Design of Drilled Shaft Footings). Series I-2 and II-7 specimens were chosen for example calculations.

5.2.4.1. Series I-2

The details of I-2 specimen of drilled shaft footing are shown in Figure 5-32. STM for the drilled shaft footing suggested in the previous study is shown in Figure 5-33.

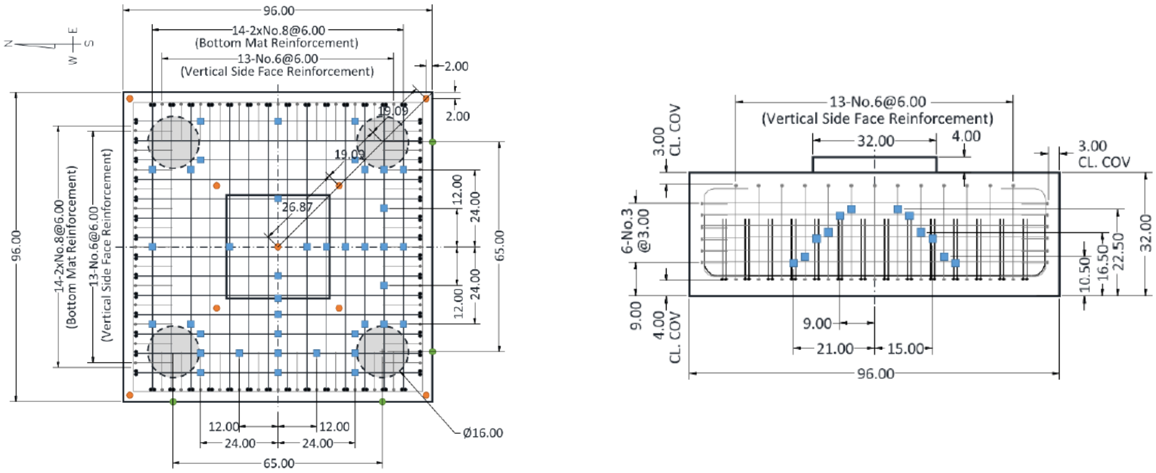

(a) Plan view (b) Side view

Figure 5-32. Details of I-2 footing specimen (FHWA/TX-21/0-6953-R1)

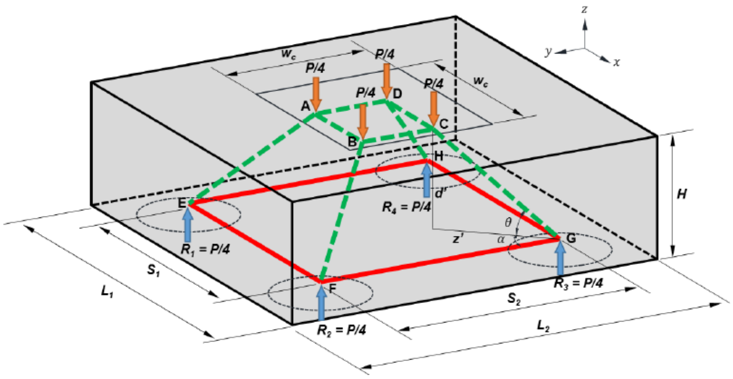

Figure 5-33. STM of drilled shaft footing (FHWA/TX-21/0-6953-R1)

5.2.4.1.1 *Bottom Mat*

The required quantity of the bottom mat was calculated considering the force in Ties EF, GH, FG, and EH, respectively (Refer to Figure 5-33). The required number of longitudinal ties was calculated to maintain the load capacity of the current layout using Grade 60. Additionally, the sectional method was used for calculation, and the rebar quantity using high-strength rebar was controlled to maintain the flexural strength at the section. It was found that the rebar quantity can be reduced as much as the rebar strength ratio using both methods. The results are shown in Figure 5-34 and Table 5-11, and the details of the calculation procedure are shown in Appendix C.

5.2.4.1.2. *Side Surface Reinforcement*

AASHTO LRFD (2020), Article 5.10.6 suggests shrinkage and temperature reinforcement on each face in each direction of the reinforced concrete member as shown in Equation (5-2). This equation is written to show that the required reinforcement ratio of 0.18% is distributed uniformly around the perimeter of the component. Based on this, Equation (3-11) is suggested to compare the quantity of face reinforcement provided to each footing with the required equivalent 0.18% ratio. Although the current code limits the yield strength up to 75 ksi, calculations were performed using 80 and 100 ksi for comparison in this study. The results are shown in Figure 5-34 and Table 5-11, and the details of the calculation procedure are shown in Appendix D.

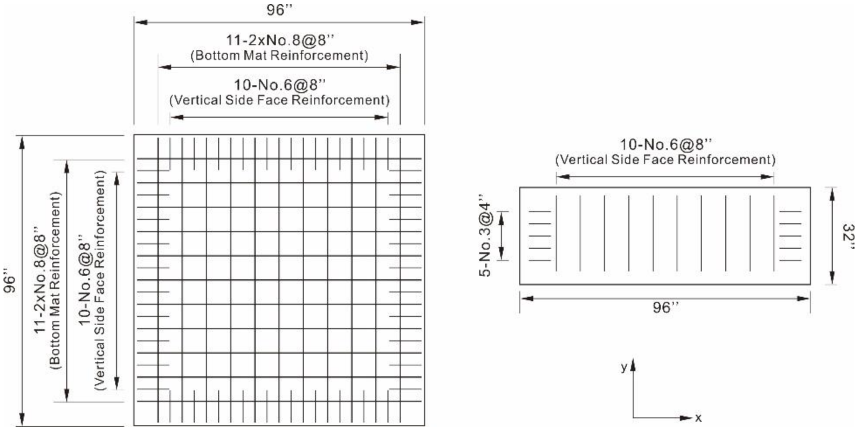

(a) Grade 80

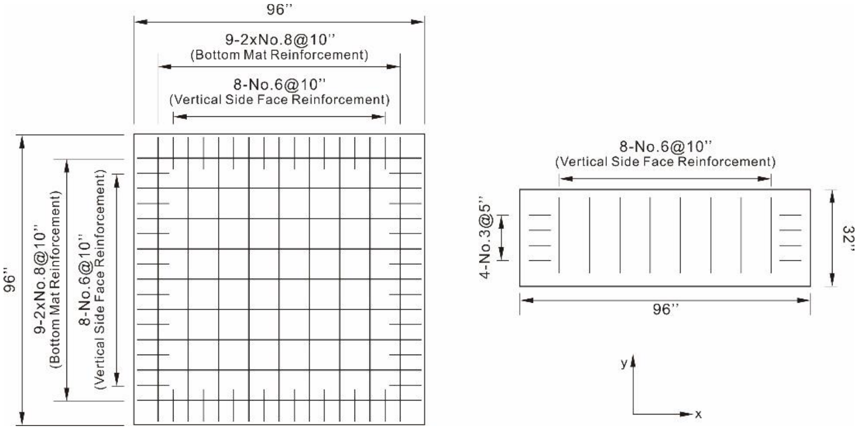

(b) Grade 100

Figure 5-34. Rebar layout of I-2 footing specimen

Table 5-11. Summary of rebar quantity for I-2 footing specimen

Type	Size	Grade	No. of rebar	Weight (lb)	Compare
Bottom mat (STM)	#8	60	56	1,146	-
		80	44	901	↓21
		100	36	819	↓36
Bottom mat (Sectional method)	#8	60	56	761	-
		80	44	441	↓21
		100	36	360	↓36
Side surface reinforcement (STM)	(Hor.) #3	60	12	34	-
		80	10	28	↓17
		100	8	23	↓33
	(Ver.) #6	60	26	81	-
		80	20	63	↓23
		100	16	50	↓38
Side surface reinforcement (Sectional method)	(Hor.) #3	60	12	34	-
		80	8	23	↓33
		100	6	17	↓50
	(Ver.) #6	60	26	81	-
		80	14	44	↓46
		100	12	38	↓54
Total (STM)		60	-	1,262	-
		80	-	991	↓21
		100	-	810	↓36
Total (Sectional method)		60	-	1,262	-
		80	-	967	↓23
		100	-	791	↓37

5.2.4.2. Series II-7

The details of II-7 specimen of drilled shaft footing are shown in Figure 5-35. The required quantity of the bottom mat and side surface reinforcement were calculated through the same calculation procedure as the previous section. The results are listed in Figure 5-36 and Table 5-12, and the details of the calculation procedure are shown in Appendix C.

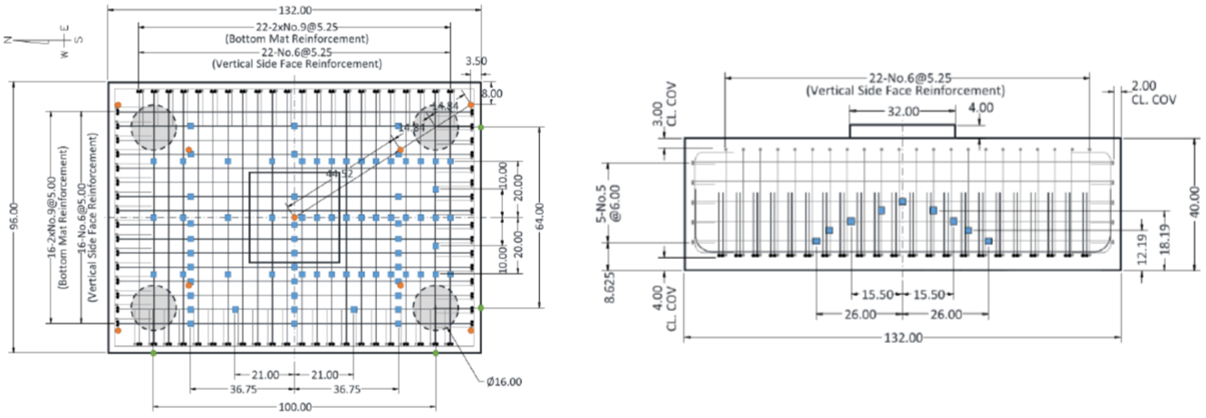

(a) Plan view (b) Side view

Figure 5-35. Details of II-7 footing specimen (FHWA/TX-21/0-6953-R1)

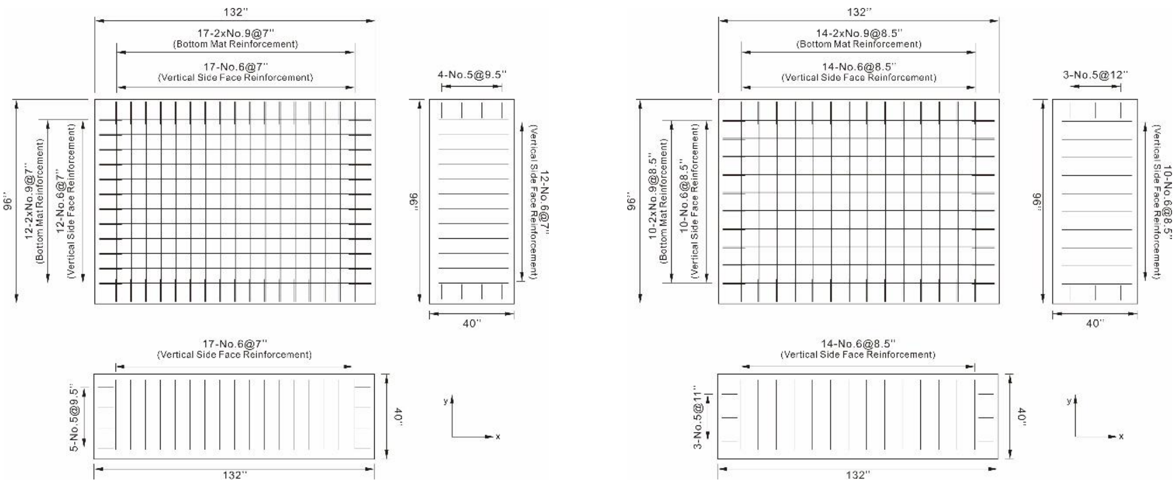

(a) STM, Grade 80 (b) STM, Grade 100

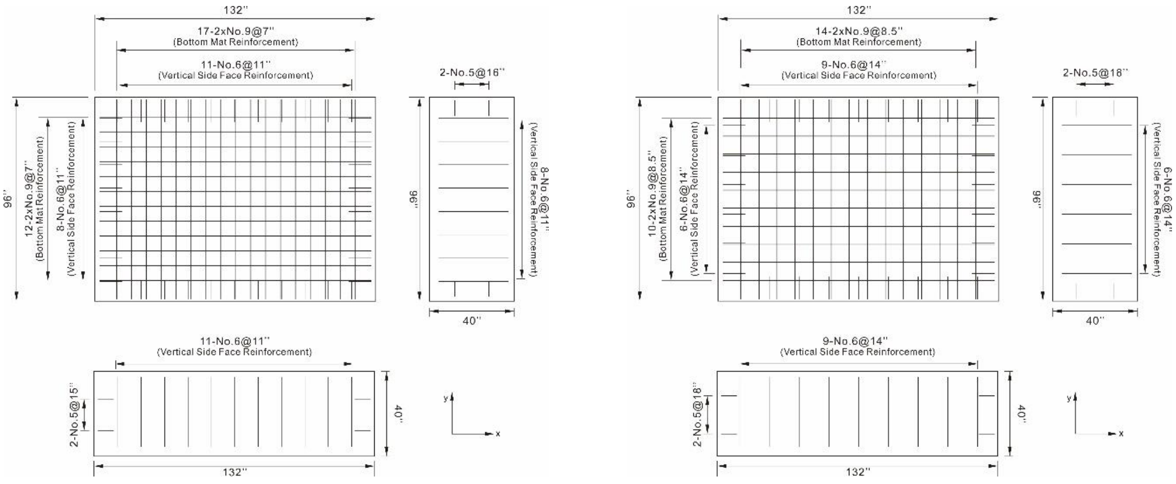

(c) Sectional method, Grade 80 (d) Sectional method, Grade 100

Figure 5-36. Rebar layout of II-7 footing specimen

Table 5-12. Summary of rebar quantity for II-7 footing specimen

Type	Size	Grade	No. of rebar	Weight (lb)	Compare
Bottom mat (STM)	#8	60	76	1,938	-
		80	60	1,479	↓24
		100	48	1,224	↓37
Bottom mat (Sectional method)	#8	60	76	1,938	-
		80	58	1,479	↓24
		100	48	1,224	↓37
Side surface reinforcement (STM)	(Hor.) #5	60	20	191	-
		80	16	153	↓20
		100	12	115	↓24
	(Ver.) #6	60	76	314	-
		80	58	240	↓40
		100	48	198	↓37
Side surface reinforcement (Sectional method)	(Hor.) #5	60	20	191	-
		80	8	76	↓60
		100	8	76	↓60
	(Ver.) #6	60	76	314	-
		80	38	157	↓46
		100	30	124	↓54
Total (STM)		60	-	2,443	
		80	-	1,872	↓23
		100	-	1,537	↓37
Total (Sectional method)		60	-	2,443	-
		80	-	1,712	↓30
		100	-	1,424	↓42

5.2.4.3. Conclusion

Example calculations were performed using two types of drilled shaft footing specimens utilized in a previous study. STM and sectional method were both used for calculation. Bottom mat reinforcement was calculated by modifying the rebar quantity so that tie load capacity was maintained for STM, and the flexural strength was maintained for the sectional method. The side surface reinforcement was calculated to satisfy the minimum reinforcement ratio of 0.3% and 0.18% for the STM and sectional methods, respectively. Regarding side surface reinforcement, the yield strength of rebar is currently limited to 75 ksi, but Grade 80 and Grade 100 were applied in the calculations for comparison. As a result of the calculation, it was possible to reduce the rebar quantity by the rebar strength ratio.

5.2.5. Summary

The practical applicability and benefits of high-strength reinforcing bars were validated through example calculations based on actual bridge components considered in the experiments. A detailed summary of these findings is provided in Chapter 6.

Chapter 6. Conclusions

This project, initiated by the Texas Department of Transportation (TxDOT) under Project 0-7090, aimed to evaluate the feasibility of using high-strength rebar in Texas bridges. To achieve this objective, the research team addressed knowledge gaps identified by reviewing prior studies and current design codes. An extensive experimental program was undertaken across various bridge components, supplemented by nonlinear finite element analysis to enhance the experimental findings. Additionally, example calculations were performed using actual bridge elements. The outcomes of this comprehensive work were integrated to assess the applicability of high-strength rebar. A summary of the key results from each chapter is provided below:

Chapter 2: The research team reviewed previous research and current design codes, including ACI 318-19 and AASHTO LRFD (2020), to examine the use of high-strength steel in various bridge elements. This review identified the limitations and challenges of employing high-strength steel in bridge applications.

Chapter 3: An extensive experimental program was undertaken, comprising 44 large-scale structural tests on various bridge components and 20 concrete prism tests to investigate cracking behavior in detail. The conclusions drawn from each major experiment are as follows:

- CIP-PCP Deck: A high-strength rebar arranged the same as a normal-strength rebar demonstrated enhanced load capacity. Additionally, high-strength rebar with reduced quantities—achieved by increasing rebar spacing—exhibited comparable load capacity to normal-strength rebar. Crack width control was primarily influenced by rebar spacing, regardless of the rebar grade, with wider cracks observed as spacing increased. The crack width limits outlined in ACI 224R-01 and AASHTO LRFD (2020) were satisfied at the service moment levels specified by AASHTO LRFD (2020). Therefore, while adherence to current design codes is recommended when using high-strength rebar, in practical applications, serviceability should be evaluated. If serviceability criteria are met, rebar spacing can be increased to optimize design efficiency.

- Prestressed Girder: The shear strength of prestressed girders with high-strength shear reinforcement can be conservatively predicted using the design method outlined in AASHTO LRFD (2020). High-strength steel specimens with increased spacing exhibit comparable shear capacity to normal-strength steel specimens. Additionally, variations in strand layouts, such as the use of harped strands, and differences in support conditions were found to have no significant effect on strength and serviceability. When high-strength reinforcement is used with increased shear reinforcement spacing, more cracks develop compared to normal-strength reinforcement, resulting in a wider region of crack formation and increased crack widths. Nevertheless, under service conditions, the crack widths for all specimens remain within the limits specified by AASHTO LRFD (2020).

- Deep Beam: Even with the application of high-strength reinforcement in deep beams, the strut-and-tie method recommended by AASHTO LRFD (2020) provided reasonable shear strength estimates. When longitudinal reinforcement was replaced with high-strength steel, the required reinforcement could be reduced in proportion to the strength ratio compared to normal-strength steel. Furthermore, cracking was controlled within the AASHTO LRFD (2020) benchmark width limit of 0.017 in. at service loads when the web reinforcement ratio was 0.2% or higher. However, the influence of high-strength rebar on crack width control performance at a web reinforcement ratio of 0.2%, which is below the current AASHTO standard of 0.3%, requires detailed investigation in future research.

- Drilled Shaft Footing: A reduced amount of high-strength steel, based on the strength ratio between high- and normal-strength steel, in the bottom mat reinforcement in drilled shaft footings results in comparable stress distribution and load capacity to footings reinforced with normal-strength steel. This indicates that the current design code remains valid for designing bottom mat reinforcement with high-strength steel. However, the quantity of side surface reinforcement should not be reduced when using high-strength steel. Reducing side surface reinforcement leads to increased strains and poor strain redistribution, which can result in premature failure. Therefore, the current minimum reinforcement requirements should be maintained, even with high-strength steel used for side surface reinforcement.

- Tension Lap Splice: Beams with a lap splice exhibited a brittle, splitting failure mode due to rebar slip within the splice region, in contrast to beams with continuous reinforcing bars, which demonstrated typical flexural failure. Nonetheless, all beams exceeded their design load capacity, defined as the load at which the flexural reinforcement reaches yielding. Rebar stress distribution within the lap splice region demonstrated that the lap splice length followed by AASHTO LRFD (2020) was sufficient for effective stress transfer. The maximum crack width in spliced beams closely aligned with those predicted by the Frosch model. These findings indicate that beams with high-strength rebar exhibit similar cracking mechanisms to those with normal-strength rebar. Therefore, No. 11 high-strength rebar can be used in tension lap splice applications in accordance with current design codes, although careful consideration is necessary, as it may require excessive reinforcement to meet rebar spacing requirements.

- Uniaxial Tension: An increase in the reinforcement ratio reduces the maximum crack width, regardless of the reinforcement grade. Conversely, an increase in the concrete cover length results in a wider maximum crack width, independent of the rebar strength or concrete strength, with the effect being more pronounced at higher concrete strengths. The maximum crack width is similar across specimens up to the rebar yielding point. However, high-strength rebar specimens exhibit a more uniform stress distribution and a greater number of cracks, leading to a smaller maximum crack width compared to normal-strength reinforcement specimens. Notably, normal reinforcement specimens show a more substantial increase in maximum crack width after yielding than high-strength reinforcement specimens. Concrete strength has a negligible impact on the number of cracks, but the maximum crack width tends to increase when high-strength concrete (10 ksi or more) is used.

Chapter 4: A finite element analysis of various bridge components using high-strength reinforcement is performed based on experimental work. FE models are developed to accurately simulate the joint behavior of the CIP-PCP deck, the shear behavior of prestressed girders, deep beams, and drilled shaft footings, and the behavior of beams with tension lap splices with varying parameters. These models are validated by comparing them with experimental results. The validated FE models confirm the validity of the experimental results in this project. They serve as reliable tools for predicting structural behavior and offer valuable insights for future design and analysis work.

Chapter 5: Practical application with example calculations using various bridge components such as bridge deck, bent cap, prestressed girder, and drilled shaft footing were performed to evaluate the benefits of replacing conventional reinforcing bars with high-strength reinforcing bars. When the current rebar layout was maintained, the load capacity enhancement was clearly confirmed, but there was a limit to the decrease of ductility. The net tensile strain, according to the rebar grade used, was calculated and compared with the tension control limit proposed in AASHTO LRFD (2020) to check the ductility. In particular, when using Grade 100 rebar, the tensile control limit was not satisfied in some cases. However, it was verified through calculations that this limitation can be overcome by using it together with high-strength concrete. To reduce rebar quantity, the rebar layout was designed to maintain the load-carrying capacity of existing bridge components with conventional rebar. All calculation procedures to examine the strength capacity followed AASHTO LRFD (2020). In particular, rebar spacing was determined according to the serviceability limits proposed by AASHTO LRFD. As a result, in most cases, it was possible to reduce the rebar by the rebar strength ratio between conventional rebar and high-strength rebar. Therefore, it is expected that high-strength rebars can solve congestion issues and improve workability. However, as mentioned earlier, usability limitations may lead to inefficient rebar layouts when using high-strength rebar due to required spacing. In some cases, even when high-strength rebar is used, the amount of rebar cannot be reduced because the current spacing requirements must be maintained. These challenges vary across different bridge elements and require further experimental evidence through additional testing to be fully addressed.

In conclusion, this research project justifies the application of high-strength reinforcing bars by integrating experimental results, analytical models, and practical applications with example calculations. It demonstrates the feasibility of using high-strength reinforcing bars in various bridge elements, offering benefits such as increased load capacity and reduced rebar quantities. This project provides the experimental foundation for a new standard addressing high-strength rebar employment's limitations. However, additional experimental evidence is recommended to extend beyond current spacing limitations related to serviceability.

Chapter 7. Value of Research

7.1. Introduction

TxDOT Project #0-7090 explored the implementation of high-strength reinforcing bars in Texas bridge components, marking a notable advancement in bridge engineering. The research introduced innovative design concepts and construction techniques aimed at transforming bridge construction in Texas by overcoming the challenges associated with data gaps and validation that hinder the widespread use of high-strength rebar. By employing a comprehensive approach that integrated experimental investigations with advanced analytical methods, the project provided valuable insights and practical guidelines for evaluating and validating the structural performance and serviceability of bridge elements incorporating high-strength rebar in both superstructures and substructures. The following sections explore the diverse value of this research as listed in

Table 7-1. Selected Benefit Area

Benefit Area	Qual	Econ	Both
Level of Knowledge	X		
Management and Policy	X		
Quality of Life	X		
Customer Satisfaction	X		
Environmental Sustainability	X		
System Reliability		X	
Increased Service Life		X	
Improved Productivity and Work Efficiency		X	
Expedited Project Delivery		X	
Reduced Administrative Costs		X	
Traffic and Congestion Reduction		X	
Reduced User Cost		X	
Reduced Construction, Operations, and Maintenance Cost		X	
Materials and Pavements		X	
Infrastructure Condition		X	
Freight movement and Economic Vitality		X	
Intelligent Transportation Systems		X	
Engineering Design Improvement			X
Safety			X

7.2. Level of Knowledge

This research enhances the understanding of incorporating high-strength rebar into bridge construction. By integrating experimental investigations and numerical analyses, it evaluates the applicability of high-strength rebar in bridge components in alignment with current design standards. The study provides valuable experimental data derived from large-scale structural tests, demonstrating the increased load capacity achievable with high-strength rebar and a comparable load capacity when the rebar quantity is reduced based on the strength ratio between conventional and high-strength rebar. Although increased rebar spacing may challenge crack width control, it remains within the serviceability requirements specified by design standards. Therefore, the findings affirm that high-strength rebar can effectively replace conventional rebar under current design codes. This research not only advances theoretical understanding but also offers practical guidelines for future studies and applications in bridge engineering.

7.3. Management and Policy

It establishes a robust evidence base that can guide updates to design standards to reflect the use of high-strength steel, ensuring the bridge component’s superior performance and efficiency. This enables policymakers to promote resource optimization by endorsing the use of high-strength steel, which could potentially reduce material quantities and associated costs without compromising structural integrity. Lastly, it informs sustainable construction policies by highlighting the environmental benefits, such as reduced resource consumption and a longer service life, thus aligning bridge construction practices with broader environmental and economic goals.

7.4. Quality of Life and Customer Satisfaction

The utilization of high-strength steel in bridge construction considerably enhances quality of life and customer satisfaction by providing infrastructure that is safer, more durable, and cost-effective. Bridges constructed with high-strength steel exhibit superior structural performance, leading to extended service life and diminished maintenance requirements, thereby minimizing disruptions and enhancing reliability for daily commuters. urthermore, the material’s capacity to support greater loads and endure extreme conditions ensures heightened user safety, cultivating public confidence in the infrastructure. From the customer satisfaction perspective, high-strength steel's effectiveness facilitates streamlined construction processes, thereby reducing construction time and related inconveniences, such as traffic delays. Furthermore, the economic advantages associated with diminished material usage and lowered maintenance expenses can result in more budget-friendly public projects, ultimately benefiting taxpayers. In conclusion, the integration of high-strength steel significantly contributes to the establishment of resilient infrastructure that aligns with public needs while enhancing convenience, safety, and overall satisfaction.

7.5. System Reliability and Increased Service Life

The implementation of high-strength steel in bridge constructions significantly enhances system reliability while extending the service life of infrastructure. High-strength steel is characterized by its superior mechanical properties, including improved load-carrying capacity. This contributes to the reliable performance of bridges under heavy traffic and extreme conditions, thereby mitigating the risk of structural failures and ensuring consistent functionality over extended periods. Moreover, the prolonged service lifespan of bridges built using high-strength steel significantly decreases the incidence of substantial repairs or replacements, thereby lowering long-term expenses and minimizing operational interruptions. The superior durability of this material results in a reduced need for maintenance activities, which guarantees consistent service delivery and availability for users. By improving system reliability and extending service longevity, high-strength steel facilitates the development of infrastructure that effectively accommodates the increasing demands of contemporary transportation networks, thereby offering enduring value and contributing to sustainable development.

7.6. Improved Productivity and Work Efficiency

The incorporation of high-strength steel in bridge construction significantly enhances productivity and workability by facilitating streamlined design and construction processes. This material's superior strength enables the utilization of smaller quantities of material to achieve equivalent or superior structural capacity, thereby reducing handling and installation time. Such efficiency results in expedited project completion, minimizing labor requirements and accelerating overall timelines. Furthermore, the diminished weight and enhanced spacing of high-strength steel rebar facilitate on-site assembly, thereby improving workflow and mitigating the likelihood of errors during construction. The material's compatibility with advanced construction methodologies, including prefabrication and modular assembly, further maximizes efficiency by allowing for more precise and standardized processes. By promoting expedited and more efficient construction, high-strength steel effectively contributes to cost savings, improved project scheduling, and an overall enhancement in productivity within the field of bridge engineering.

7.7. Expedited Project Delivery

One significant advantage of this research is the potential for expedited project delivery. The utilization of high-strength steel in bridge construction ensures a comparable load capacity while requiring fewer materials, thereby decreasing the time needed for material handling, fabrication, and installation. This development results in reduced construction timelines without compromising structural integrity or safety. High-strength steel is particularly suitable for advanced construction methods, such as prefabrication and modular assembly, which allow for manufacturing large components off-site and their subsequent rapid assembly on-site. This approach minimizes the duration of construction activities, lessens disruption to traffic and local communities, and accelerates project completion.

7.8. Reduced User Cost

The adoption of the hybrid precast column system results in reduced user costs in several ways. Firstly, the expedited construction process minimizes the duration of traffic disruptions, reducing fuel consumption and time lost due to delays. Secondly, the increased durability and service life of the precast column system mean fewer repairs and maintenance activities, which often lead to costly detours and extended travel times for users. Lastly, the improved reliability of the transportation infrastructure reduces the likelihood of unexpected closures and the associated costs for alternative routes. These factors collectively lower the overall expenses for daily commuters and commercial vehicles.

7.9. Reduced Construction, Operations, and Maintenance Cost

The research demonstrates significant potential for reducing construction, operations, and maintenance costs through the use of the hybrid precast column system. The efficient construction process, characterized by the use of precast elements, decreases labor and material costs associated with on-site formwork and prolonged curing times. Additionally, the durability and robustness of the precast columns lead to lower maintenance costs over the structure’s lifespan. The enhanced structural performance reduces the frequency and extent of repairs, further lowering long-term expenses. These cost savings make the hybrid precast column system an economically viable option for bridge construction and maintenance.

7.10. Materials and Pavements

Incorporating high-strength steel in bridge construction offers significant advantages for materials and pavements by enhancing resource efficiency and bolstering resilient infrastructure. The high-strength steel's exceptional strength and its reduced usage in structural components minimize overall material consumption and result in lighter bridge designs. This decrease in weight can subsequently lessen the pressures on foundation systems and pavements, which enhances long-term performance and lowers maintenance needs. These efficiencies improve the lifespan and reliability of materials and pavements, contributing to cost savings and sustainable infrastructure development.

7.11. Infrastructure Condition

Implementing high-strength steel in bridge construction positively impacts infrastructure conditions by enhancing strength performance. This leads to bridges maintaining their structural integrity for extended periods, thereby improving the overall infrastructure condition.

High-strength steel contributes to a more stable and well-maintained infrastructure network by reducing the need for frequent repairs and replacements. Additionally, its increased load-bearing capacity allows bridges to withstand better the stresses imposed by heavy traffic and environmental factors, further prolonging their lifespan and reducing the strain on maintenance resources. As a result, the incorporation of high-strength steel leads to improved infrastructure conditions, providing long-term value and ensuring safe and reliable transportation networks.

7.12. Freight movement and Economic Vitality

Given its exceptional strength-to-weight ratio, high-strength steel facilitates the transportation of a reduced quantity of materials while achieving equivalent or enhanced structural performance. This characteristic makes transporting steel components over extended distances more efficient and economically viable. Consequently, this efficiency in freight movement reduces transportation expenses, as fewer shipments are required for the same volume of materials. The reduced weight and improved load-carrying capacity using high-strength steel contribute to a more efficient use of freight infrastructure, reducing wear and tear on transportation routes and logistics systems. High-strength steel bolsters economic vitality, allowing for longer-lasting and more efficient bridge construction and ensuring uninterrupted freight movement over bridges. This reduces downtime due to repairs or maintenance, thereby boosting productivity. In the long term, using high-strength steel leads to cost savings in transportation and infrastructure maintenance, contributing to overall economic growth by optimizing logistics and trade activities.

7.13. Intelligent Transportation Systems

Incorporating high-strength steel in bridge construction can significantly enhance the performance and integration of Intelligent Transportation Systems (ITS). Bridges constructed with high-strength steel, owing to their durability and extended lifespan, provide a stable and long-term foundation for ITS technologies—including sensors, cameras, and communication systems. The robustness of high-strength steel ensures that these systems can operate optimally without being compromised by structural degradation over time, thereby reducing the necessity for frequent maintenance and system downtimes. Furthermore, high-strength steel's capability to support more extensive and advanced infrastructure systems facilitates the integration of innovative technologies such as real-time traffic monitoring, vehicle tracking, and automated toll collection directly into the bridge structure. These systems rely on stable, reliable infrastructure to function effectively, and high-strength steel affords the requisite strength and durability to accommodate these technologies.

7.14. Engineering Design Improvement

Incorporating high-strength steel in bridge construction yields considerable advancements in engineering design by augmenting structural performance, material efficiency, and design adaptability. The exceptional strength-to-weight ratio of high-strength steel facilitates a more judicious utilization of materials, permitting designers to decrease the quantity of steel needed while sustaining or even enhancing load-bearing capacity. This increased efficiency culminates in cost reductions and fosters the development of lighter and more streamlined bridge configurations, which can be especially beneficial in regions constrained by spatial or weight limitations. By incorporating high-strength steel, engineers can push the boundaries of bridge design, improving structures' safety, efficiency, and longevity while supporting the development of more sustainable and economically viable infrastructure.

7.15. Safety

The utilization of high-strength steel in the domain of bridge construction significantly enhances safety by augmenting structural integrity, durability, and resilience. Its superior strength enables bridges to support elevated loads, thereby mitigating the risk of failure and ensuring safety during peak traffic periods as well as under extreme environmental conditions. This leads to the development of more stable structures capable of withstanding adverse circumstances. Furthermore, the prolonged service life and diminished necessity for maintenance and repairs contribute to the creation of safer transportation networks by reducing potential hazards associated with construction zones. Ultimately, high-strength steel fulfills a pivotal role in guaranteeing the safety and longevity of bridge infrastructure.

References

AASHTO LRFD Bridge Design Specifications, 9th edition, American Association of State Highway and Transportation Officials, Washington, D.C, 2020.

ACI Committee 224. 2002. "Control of Cracking in Concrete Structures (ACI 224R01)," American Concrete Institute, Farmington Hills, MI: ACI.

ACI Committee 318, ACI 318-19/ACI 318R-19 Building Code Requirements for Reinforced Concrete and Commentary, American Concrete Institute, Farmington Hills, MI, 2019.

ACI Committee 408, "Bond and Development of Straight Reinforcing Bars in Tension," American Concrete Institute, Farmington Hills, MI, 2012.

ASTM A370-21. 2021. "Standard Test Methods and Definitions for Mechanical Testing of Steel Products," West Conshohocket, PA: ASTM International.

ASTM C39/C39M-21. 2021 "Standard Test Method for Compressive Strength of Cylindrical Concrete Specimens," West Conshohocket, PA: ASTM International.

ASTM C496/C496M-17. 2017. "Standard Test Method for Splitting Tensile Strength of Cylindrical Concrete Specimens,". West Conshohocken, PA: ASTM International.

ASTM C469/C469M-22. 2022. "Standard Test Method for Static Modulus of Elasticity and Poisson's Ratio of Concrete in Compression,". West Conshohocken, PA: ASTM International.

Avendano, A., C. Hovell, A. Moore, D. Dunkman, E. Nakamura, O. Bayrak, and J. Jirsa. 2013. Pretensioned Box Beams: Prestress Transfer and Shear Behavior. 278. Austin, TX: The University of Texas at Austin.

Azimov, U. 2012. "Controlling Cracking in Precast Prestressed Concrete Panels," Master Thesis, The University of Texas at Austin.

Bayrak, O., Chao, S.H., Jirsa, J.O., Klingner, R.E., Azimov, U., Foreman, J., Foster, S., Karki, N., Kwon, K.Y. and Woods, A. 2013. "Bridge Deck Reinforcement and PCP Cracking," No. FHWA/TX-12/0-6348-2.

Birrcher, D., Tuchscherer, R., Huizinga, M., Bayrak, O., Wood, S., and Jirsa, J. 2009. "Strength and Serviceability Design of Reinforced Concrete Deep Beams," Report No. FHWA/TX-09/0-5253-1, Center for Transportation Research, University of Texas at Austin, Austin, Texas.

Chamberlain, C. 1997. "Evaluation of Longitudinal Cracking in End Regions of Pretensioned Box Beams." Masters Thesis. Austin, TX: The University of Texas at Austin.

Clarke, J. L. 1973. Behavior and design of pile caps with four piles. 19. Technical Report 24.489. London, England: Cement and Concrete Association.

Code, CEB-FIP Model. 1990. "Model code for concrete structures," Comité Euro-International du Béton, Secretariat Permanent, Case Postale 88.

Desalegne, A.S. and Lubell, A.S., 2010. “Shear Behavior of Concrete Slabs Longitudinally Reinforced with High-Performance Steel.” ACI Struct. J., 107(2). 228.

Desalegne, A.S. and Lubell, A.S., 2015. Shear in Concrete Beams Reinforced with High-Performance Steel. ACI Struct. J., 112(6). 783.

de Dios Garay-Moran, J. and Lubell, A.S., 2016. Behavior of Deep Beams Containing High-Strength Longitudinal Reinforcement. ACI Struct. J., 113(1), 17.

E.construct, Project: Optimizing Deck Slab Reinforcement Utilizing ChromX 2100 for TxDOT, 2019.

Folliard, K., Smith, C., Sellers, G., Brown, M. and Breen, J.E. 2003. “Evaluation of alternative materials to control drying-shrinkage cracking in concrete bridge decks,” No. FHWA/TX-04/0-4098-4.

Foreman, J. M. 2010. “Controlling Cracking in Prestressed Concrete Panels,” Master Thesis, The University of Texas at Austin.

Foster, S. W. 2010. “Reducing Top Mat Reinforcement in Bridge Decks,” Master Thesis, The University of Texas at Austin.

Frosch, Robert J.; Fleet, Eric T.; and Glucksman, Rebecca. 2020. “Development and Splice Lengths for High-Strength Reinforcement, Volume I: General Bar Development,” Bowen Laboratory Research Reports.

Frosch, R. J. 1999. “Another Look at Cracking and Crack Control in Reinforced Concrete,” ACI Structural Journal, V.96, No. 3, pp. 437-442.

Frosch, R. J. 2001. “Flexural Crack Control in Reinforced Concrete. Design and Construction Practices to Mitigate Cracking,” SP-204. American Concrete Institute, Farmington Hills, MI, pp. 135–154.

Hassan, T.K., Seliem, H.M., Dwairi, H., Rizkalla, S.H. and Zia, P., 2008. “Shear behavior of large concrete beams reinforced with high-strength steel.” ACI Struct. J., 105(2), 173.

Kareem, R.S., Jones, C., Dang, C.N., Prinz, G.S. and Hale, W.M. 2020. “Structural performance of concrete bridge decks reinforced with Grade-830 steel bars,” Structures. Vol. 27, 1396-1404.

Kim, H., R. A. Boehm, Y. Yi, S. Mühlberg, Z. D. Webb, J. Choi, J. Murcia-Delso, T. D. Hrynyk, and O. Bayrak. 2023. “Effects of reinforcement details on behavior of drilled shaft footings.” ACI Structural Journal, 120 (1): 285–301. https://doi.org/10.14359/51737145.

Kwon, K. Y. 2012. “Design Recommendations for CIP-PCP Bridge Decks,” Ph.D. dissertation, University of Texas at Austin.

Lee, J.Y., Choi, I.J. and Kim, S.W., 2011. “Shear Behavior of Reinforced Concrete Beams with High-Strength Stirrups.” ACI Struct. J., 108(5), 620-629.

Lee, J.Y., Lee, J.H., Lee, D.H., Hong, S.J. and Kim, H.Y., 2018. “Practicability of Large-Scale Reinforced Concrete Beams Using Grade 80 Stirrups.” ACI Struct. J., 115(1), 269-280.

Merrill, B.D. 2002. “Texas’ use of precast concrete stay-in-place forms for bridge decks,” Concrete Bridge Conference.

Munikrishna, A., Hosny, A., Rizkalla, S. and Zia, P., 2011. "Behavior of concrete beams reinforced with ASTM A 1035 grade 100 stirrups under shear." ACI Struct. J., 108(1), 34-41.

Nakamura, E., A. R. Avendaño, and O. Bayrak. 2013. "Shear Database for Prestressed Concrete Members." ACI Structural Journal, 110 (6): 26.

O'Callaghan, M. R. 2007. "Tensile stresses in the end regions of pretensioned I-beams at release." Master's Thesis. Austin, TX: The University of Texas at Austin.

Ou, Y.C. and Bui, C.T., 2024. "Shear Strength and Crack Width Control of Concrete Beams with High-Strength Shear Reinforcement." J. Struct. Eng., 150(3), 04024013.

Ross, B., H. Hamilton, and G. Consolazio. 2013. "Design Model for Confinement Reinforcement in Pretensioned Concrete I-Girders." Journal of the Transportation Research Board, 2331 (1): 59–67.

Rulon, R., Lequesne, R. D., Lepage, A., and Darwin, D. 2022. "Lap Splicing of Large High-Strength Steel Reinforcing Bars," SM Report No. 148, The University of Kansas Center for Research, Inc., Lawrence, KS.

Salomon, A.L. and Moen, C.D. 2014. "Structural design guidelines for concrete bridge decks reinforced with corrosion-resistant reinforcing bars," No. FHWA/VCTIR 15-R10, Virginia Dept. of Transportation.

Salomon, A.L. and Moen, C.D. 2017. "Design, installation, and condition assessment of a concrete bridge deck constructed with ASTM A1035 CS no. 4 bars," No. VTRC 17-R16, Virginia Transportation Research Council.

Schnittker, B., and O. Bayrak. 2008. "Allowable Compressive Stress at Prestress Transfer," Technical Report. Austin, TX: The University of Texas at Austin.

Seliem, H. M., Lucier, G., Rizkalla, S. H., and Zia, P. 2008. "Behavior of Concrete Bridge Decks Reinforced with High-Performance Steel," ACI Struct. J., 105(1): 78-86, 2008.

Shahrooz, B.M., 2011. "Design of concrete structures using high-strength steel reinforcement," (Vol. 679). Transportation Research Board.

Shahrooz, B. M., R. A. Miller, K. A. Harries, Q. Yu, and H. G. Russell. 2017. "Strand Debonding for Pretensioned Girders," Washington, DC: Transportation Research Board.

Shin, D., Haroon, M., Kim, C., Lee, B.S. and Lee, J.Y., 2019. "Shear Strength Reduction of Large-Scale Reinforced Concrete Beams with High-Strength Stirrups." ACI Struct. J., 116(5), 161-172.

Sim, C. and Frosch, R.J. 2020. "Cracking Behavior of Slabs with Corrosion-Resistant and High-Strength Reinforcing Bars," ACI Struct. J., 117(5).

Sumpter, M.S., Sami H. Rizkalla, and Paul Zia., 2009. "Behavior of High-Performance Steel as Shear Reinforcement for Concrete Beams." ACI Struct. J., 106(2), 171.

Suzuki, K., K. Otsuki, and T. Tsubata. 1998. "Influence of bar arrangement on ultimate strength of four-pile caps." Transactions of the Japan Concrete Institute, 20: 195–202.

TxDOT. 2023. "Bridge Design Guide," Texas Department of Transportation.

TxDOT. 2024. “Bridge Design Manual – LRFD,” Texas Department of Transportation.

Williams C., Deschenes D., and Bayrak O. 2011. “Strut-and-tie Model Design Examples for Bridges of Reinforced Concrete Deep Beams,” Report No. FHWA/TX-12/5-5253-01-1, Texas Department of Transportation, TX, 276 pp.

Yi Y, Kim H., Boehm RA., Webb ZD., Choi J., Wang HC., Murcia-Delso J., Hrynyk TD., and Bayrak O. 2022. “3D Strut-and-Tie Modeling for Design of Drilled Shaft Footings,” Report No. FHWA/TX-21/0-6953-1, Center for Transportation Research, University of Texas at Austin, Austin, Texas.

Yi, Y., H. Kim, T. D. Hrynyk, J. Murcia-Delso, and O. Bayrak. Forthcoming. 2024. “Numerical Parametric Study on Structural Response of Drilled Shaft Footings subjected to Concentric Axial Force.” Journal of Structural Engineering. 150 (10), 04024132.

Appendix A. Drawing for Tx-girder specimens

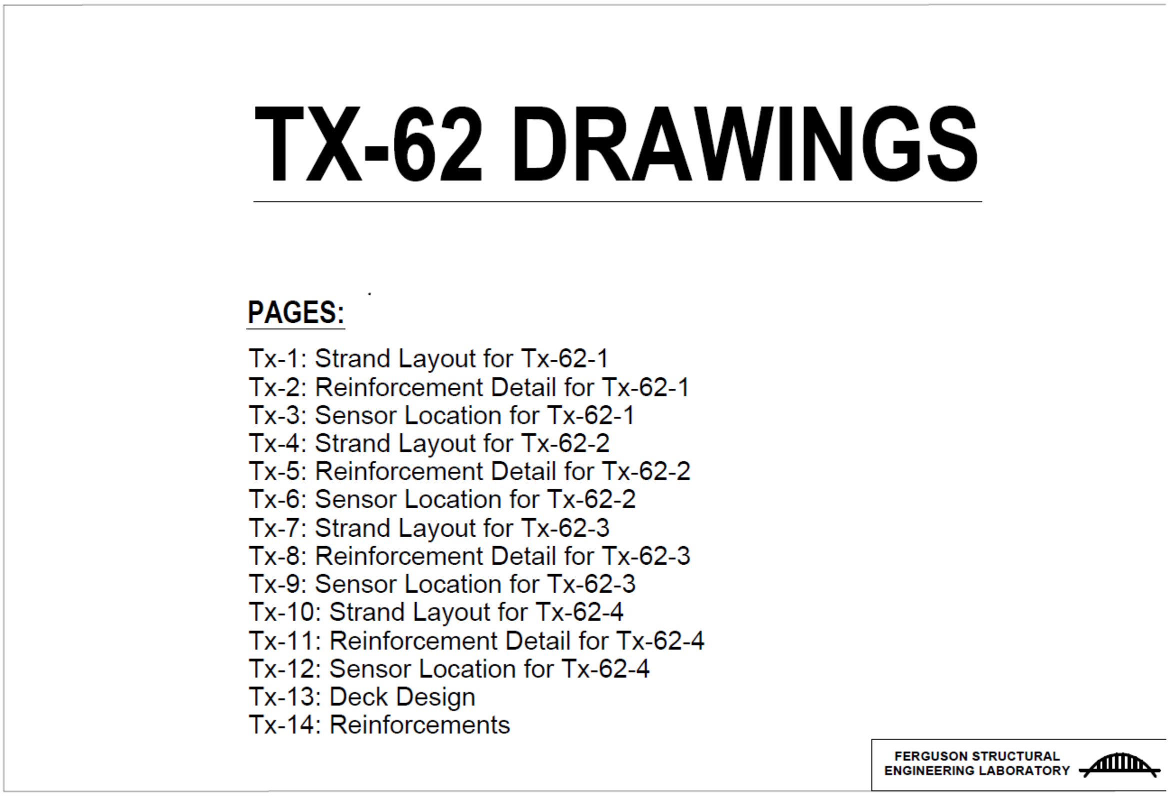

TX-62 DRAWINGS

PAGES:

Tx-1: Strand Layout for Tx-62-1
Tx-2: Reinforcement Detail for Tx-62-1
Tx-3: Sensor Location for Tx-62-1
Tx-4: Strand Layout for Tx-62-2
Tx-5: Reinforcement Detail for Tx-62-2
Tx-6: Sensor Location for Tx-62-2
Tx-7: Strand Layout for Tx-62-3
Tx-8: Reinforcement Detail for Tx-62-3
Tx-9: Sensor Location for Tx-62-3
Tx-10: Strand Layout for Tx-62-4
Tx-11: Reinforcement Detail for Tx-62-4
Tx-12: Sensor Location for Tx-62-4
Tx-13: Deck Design
Tx-14: Reinforcements

FERGUSON STRUCTURAL
ENGINEERING LABORATORY

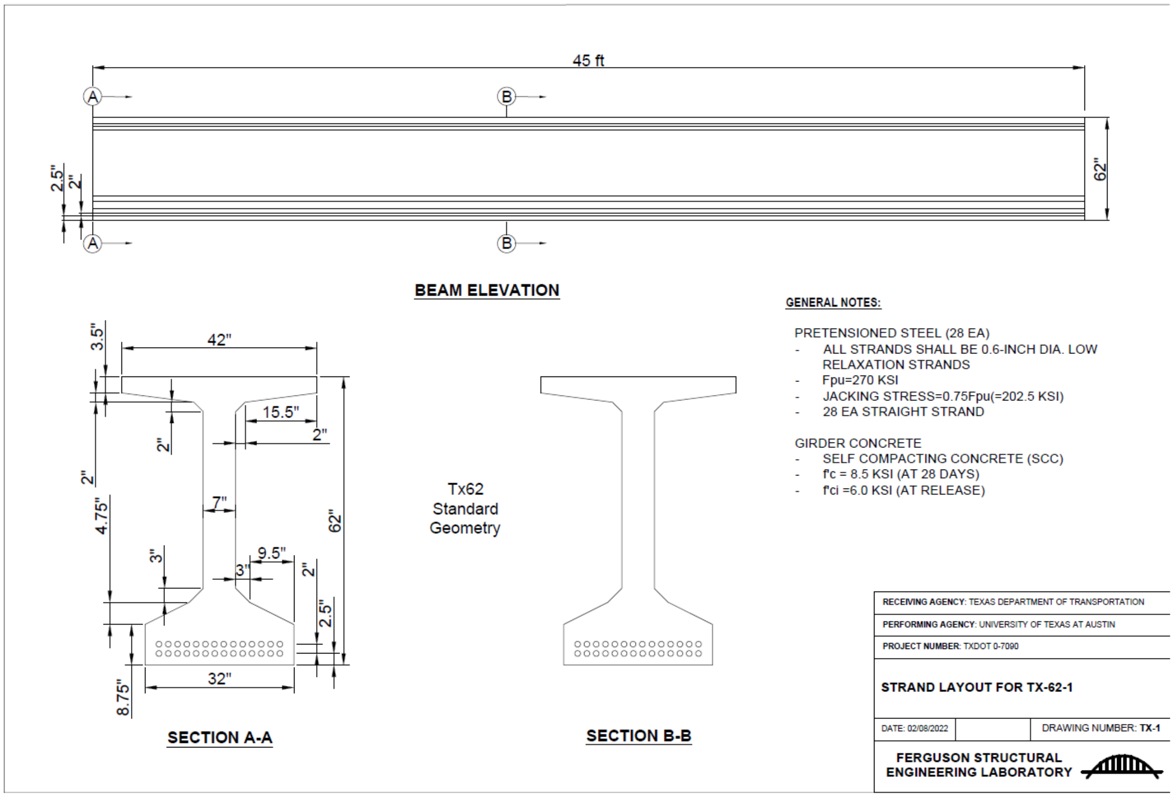

GENERAL NOTES:

PRETENSIONED STEEL (28 EA)
- ALL STRANDS SHALL BE 0.6-INCH DIA. LOW RELAXATION STRANDS
- Fpu=270 KSI
- JACKING STRESS=0.75Fpu(=202.5 KSI)
- 28 EA STRAIGHT STRAND

GIRDER CONCRETE
- SELF COMPACTING CONCRETE (SCC)
- f'c = 8.5 KSI (AT 28 DAYS)
- f'ci =6.0 KSI (AT RELEASE)

RECEIVING AGENCY: TEXAS DEPARTMENT OF TRANSPORTATION
PERFORMING AGENCY: UNIVERSITY OF TEXAS AT AUSTIN
PROJECT NUMBER: TXDOT 0-7090

STRAND LAYOUT FOR TX-62-1

DATE: 02/08/2022
DRAWING NUMBER: **TX-1**

FERGUSON STRUCTURAL
ENGINEERING LABORATORY

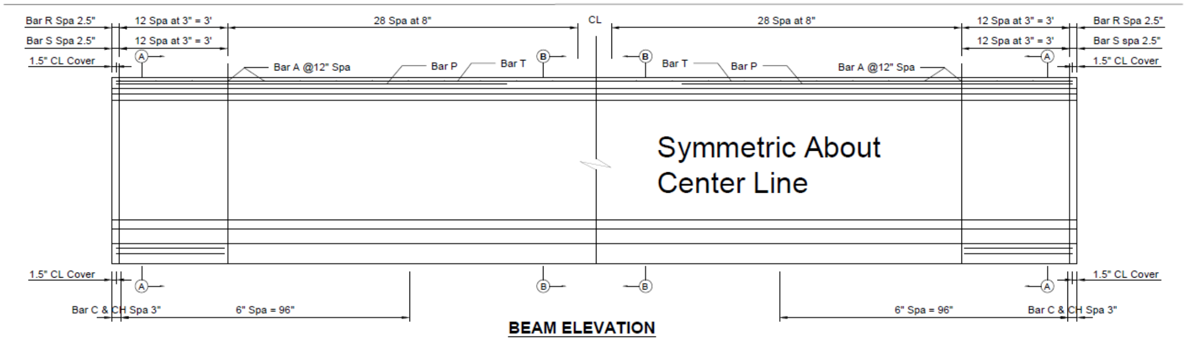

BEAM ELEVATION

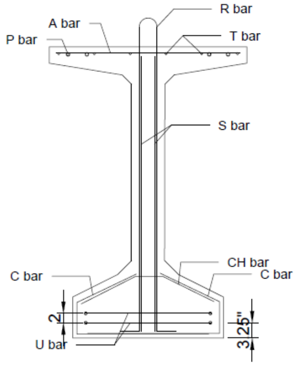

SECTION A-A

Tx62
Standard
Rebar
Layout

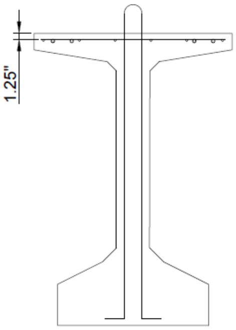

SECTION B-B

GENERAL NOTES:

EVERY TYPE OF REINFORCEMENT
- GRADE 60 (YIELD STRENGTH = 60 KSI) FOR TOTAL LENGTH OF THE BEAM

RECEIVING AGENCY: TEXAS DEPARTMENT OF TRANSPORTATION
PERFORMING AGENCY: UNIVERSITY OF TEXAS AT AUSTIN
PROJECT NUMBER: TXDOT 0-7090

REINFORCEMENT DETAIL FOR TX-62-1

DATE: 02/08/2022 | DRAWING NUMBER: **TX-2**

FERGUSON STRUCTURAL ENGINEERING LABORATORY
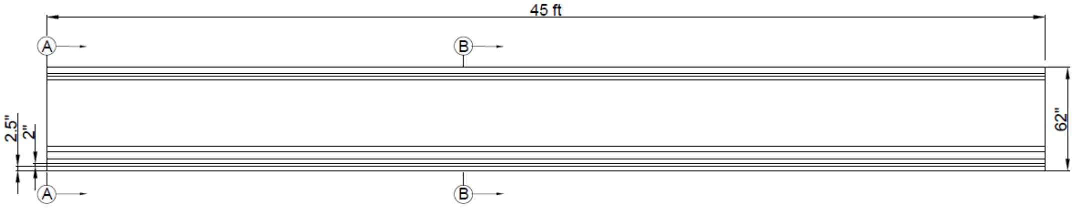
BEAM ELEVATION

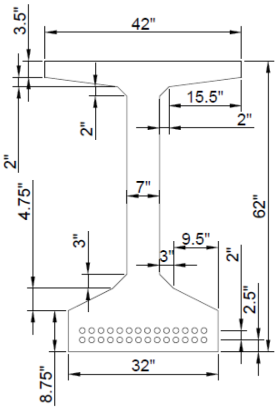

SECTION A-A

Tx62
Standard
Geometry

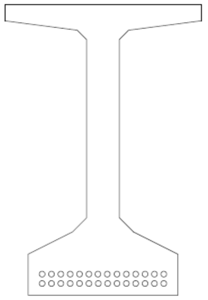

SECTION B-B

GENERAL NOTES:

PRETENSIONED STEEL (28 EA)
- ALL STRANDS SHALL BE 0.6-INCH DIA. LOW RELAXATION STRANDS
- Fpu=270 KSI
- JACKING STRESS=0.75Fpu(=202.5 KSI)
- 28 EA STRAIGHT STRAND

GIRDER CONCRETE
- SELF COMPACTING CONCRETE (SCC)
- f'c = 8.5 KSI (AT 28 DAYS)
- f'ci =6.0 KSI (AT RELEASE)

RECEIVING AGENCY: TEXAS DEPARTMENT OF TRANSPORTATION
PERFORMING AGENCY: UNIVERSITY OF TEXAS AT AUSTIN
PROJECT NUMBER: TXDOT 0-7090

STRAND LAYOUT FOR TX-62-2

DATE: 02/08/2022 | DRAWING NUMBER: **TX-7**

FERGUSON STRUCTURAL ENGINEERING LABORATORY

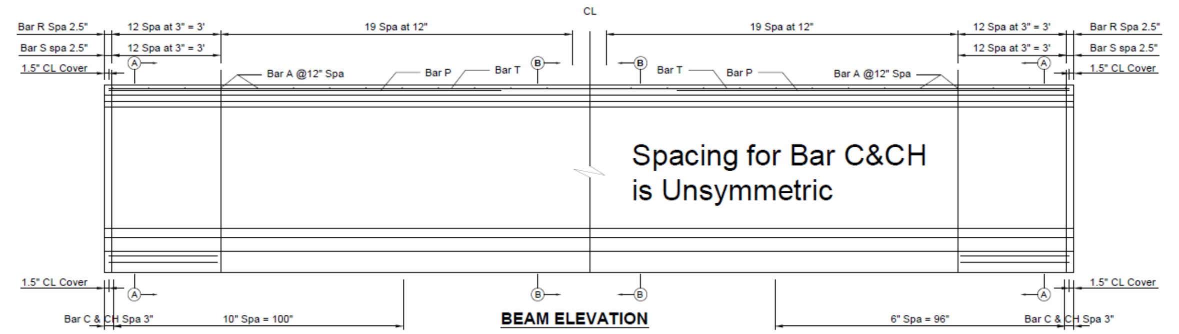

BEAM ELEVATION

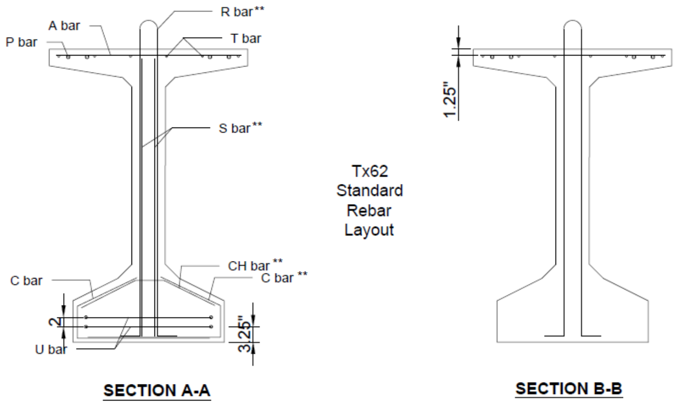

SECTION A-A

SECTION B-B

GENERAL NOTES:

BAR A,P,T,U
- GRADE 60 (YIELD STRENGTH = 60 KSI) FOR TOTAL LENGTH OF THE BEAM

** BAR C,CH,R,S
- GRADE 100 (YIELD STRENGTH = 100 KSI) FOR TOTAL LENGTH OF THE BEAM

RECEIVING AGENCY: TEXAS DEPARTMENT OF TRANSPORTATION
PERFORMING AGENCY: UNIVERSITY OF TEXAS AT AUSTIN
PROJECT NUMBER: TXDOT 0-7090

REINFORCEMENT DETAIL FOR TX-62-2

DATE: 02/08/2022 | DRAWING NUMBER: **TX-8**

FERGUSON STRUCTURAL ENGINEERING LABORATORY

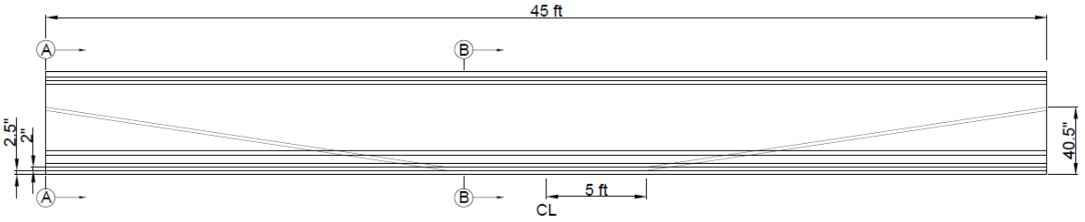

BEAM ELEVATION

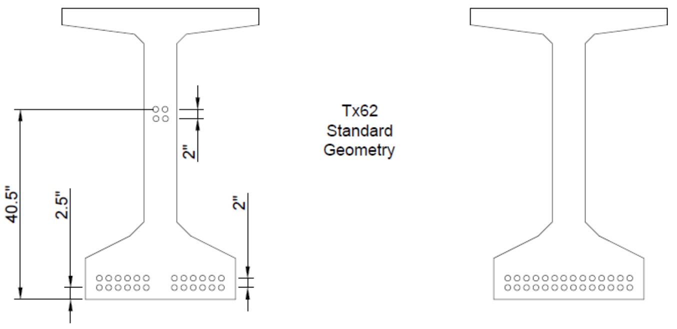

SECTION A-A

SECTION B-B

GENERAL NOTES:

PRETENSIONED STEEL (28 EA)
- ALL STRANDS SHALL BE 0.6-INCH DIA. LOW RELAXATION STRANDS
- Fpu=270 KSI
- JACKING STRESS=0.75Fpu(=202.5 KSI)
- 24 EA STRAIGHT STRAND + 4 EA HARPED STRAND

GIRDER CONCRETE
- SELF COMPACTING CONCRETE (SCC)
- f'c = 8.5 KSI (AT 28 DAYS)
- f'ci =6.0 KSI (AT RELEASE)

RECEIVING AGENCY: TEXAS DEPARTMENT OF TRANSPORTATION
PERFORMING AGENCY: UNIVERSITY OF TEXAS AT AUSTIN
PROJECT NUMBER: TXDOT 0-7090

STRAND LAYOUT FOR TX-62-3

DATE: 02/08/2022 | DRAWING NUMBER: **TX-4**

FERGUSON STRUCTURAL ENGINEERING LABORATORY

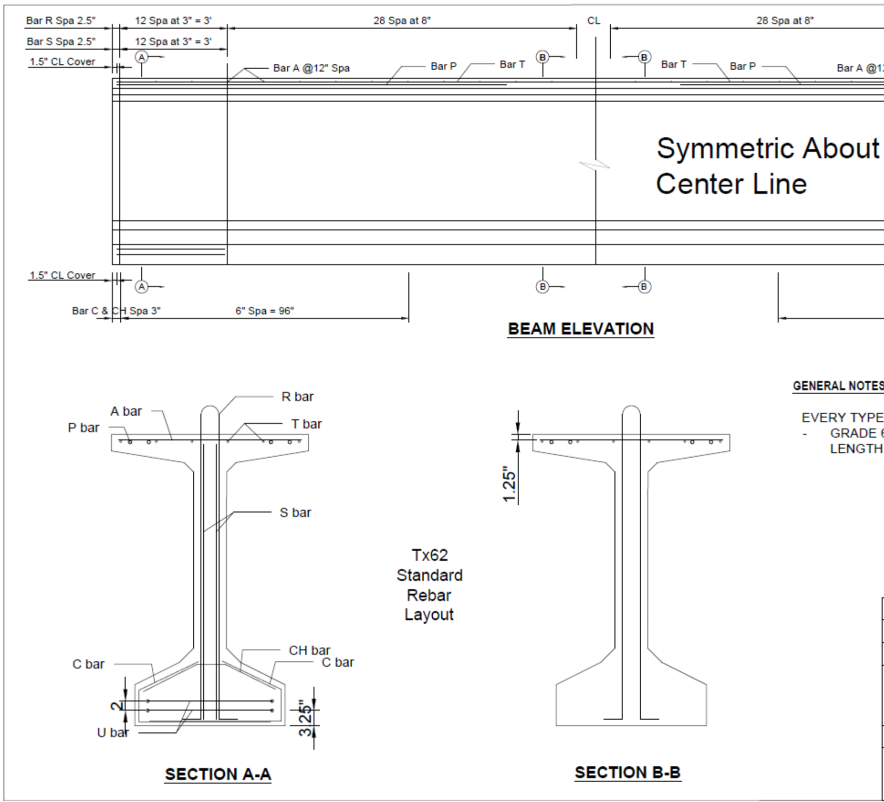

GENERAL NOTES:

EVERY TYPE OF REINFORCEMENT
- GRADE 60 (YIELD STRENGTH = 60 KSI) FOR TOTAL LENGTH OF THE BEAM

RECEIVING AGENCY: TEXAS DEPARTMENT OF TRANSPORTATION
PERFORMING AGENCY: UNIVERSITY OF TEXAS AT AUSTIN
PROJECT NUMBER: TXDOT 0-7090

REINFORCEMENT DETAIL FOR TX-62-3

DATE: 02/08/2022 | DRAWING NUMBER: **TX-5**

FERGUSON STRUCTURAL ENGINEERING LABORATORY

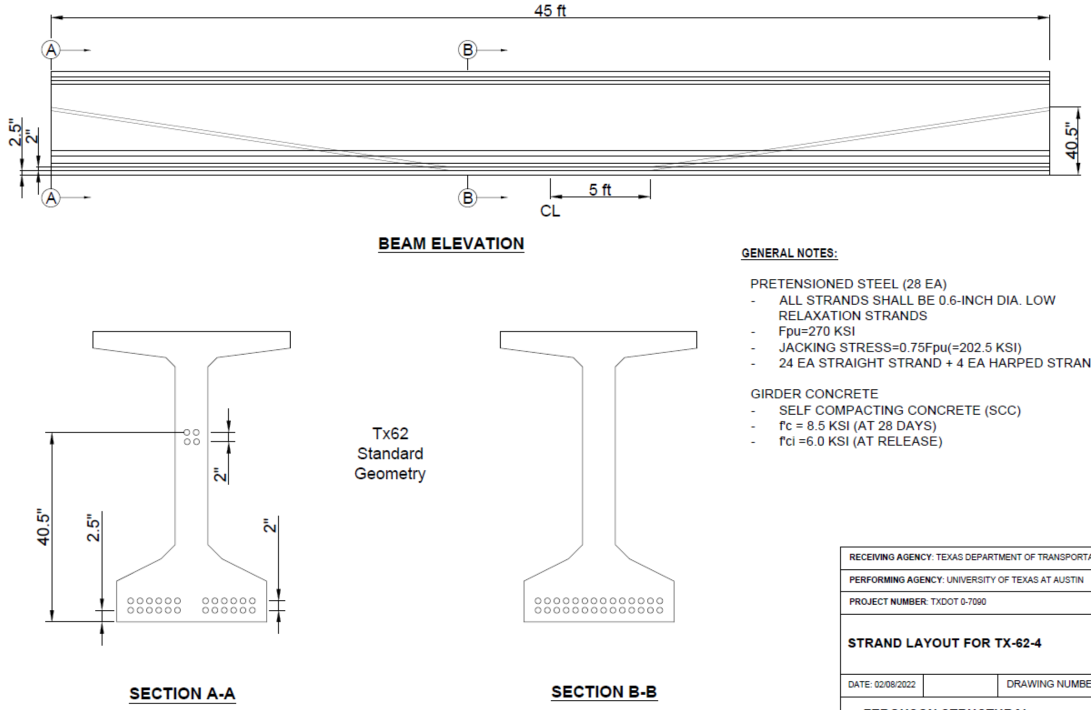

GENERAL NOTES:

PRETENSIONED STEEL (28 EA)
- ALL STRANDS SHALL BE 0.6-INCH DIA. LOW RELAXATION STRANDS
- Fpu=270 KSI
- JACKING STRESS=0.75Fpu(=202.5 KSI)
- 24 EA STRAIGHT STRAND + 4 EA HARPED STRAND

GIRDER CONCRETE
- SELF COMPACTING CONCRETE (SCC)
- f'c = 8.5 KSI (AT 28 DAYS)
- f'ci =6.0 KSI (AT RELEASE)

RECEIVING AGENCY: TEXAS DEPARTMENT OF TRANSPORTATION
PERFORMING AGENCY: UNIVERSITY OF TEXAS AT AUSTIN
PROJECT NUMBER: TXDOT 0-7090

STRAND LAYOUT FOR TX-62-4

DATE: 02/08/2022 | DRAWING NUMBER: **TX-10**

FERGUSON STRUCTURAL ENGINEERING LABORATORY

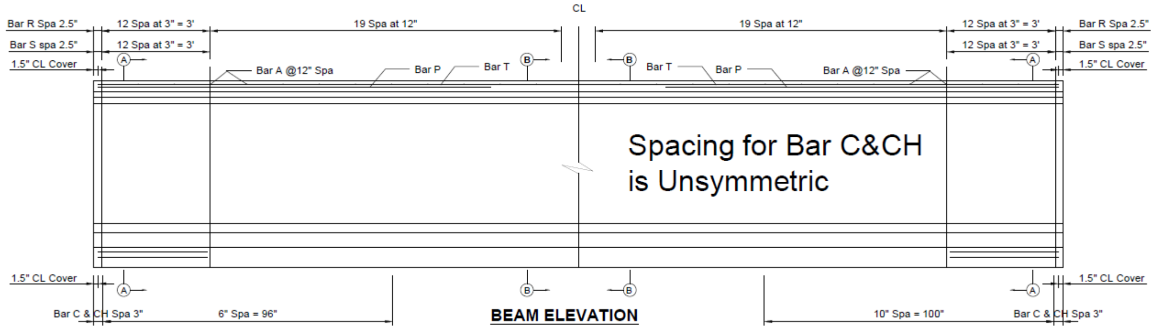

Spacing for Bar C&CH is Unsymmetric

BEAM ELEVATION

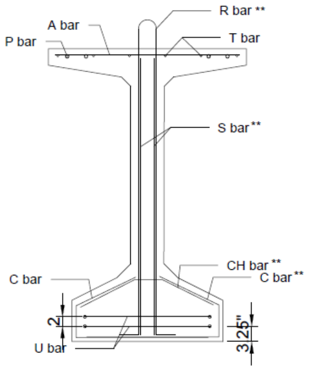

SECTION A-A

Tx62
Standard
Rebar
Layout

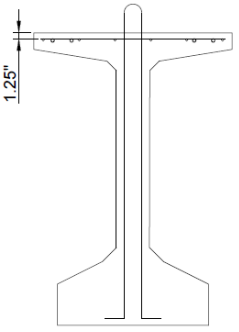

SECTION B-B

GENERAL NOTES:

BAR A,P,T,U
- GRADE 60 (YIELD STRENGTH = 60 KSI) FOR TOTAL LENGTH OF THE BEAM

** BAR C,CH,R,S
- GRADE 100 (YIELD STRENGTH = 100 KSI) FOR TOTAL LENGTH OF THE BEAM

RECEIVING AGENCY: TEXAS DEPARTMENT OF TRANSPORTATION		
PERFORMING AGENCY: UNIVERSITY OF TEXAS AT AUSTIN		
PROJECT NUMBER: TXDOT 0-7090		
REINFORCEMENT DETAIL FOR TX-62-4		
DATE: 02/08/2022		DRAWING NUMBER: **TX-11**
FERGUSON STRUCTURAL ENGINEERING LABORATORY		

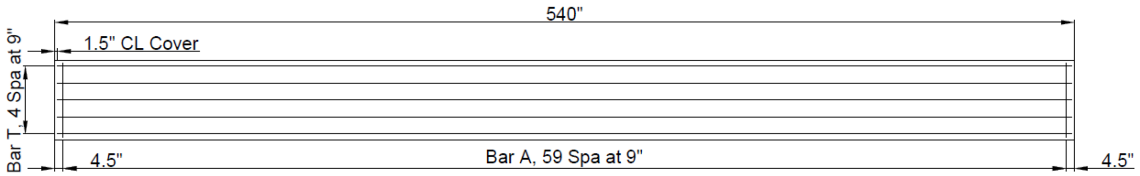

DECK PLAN

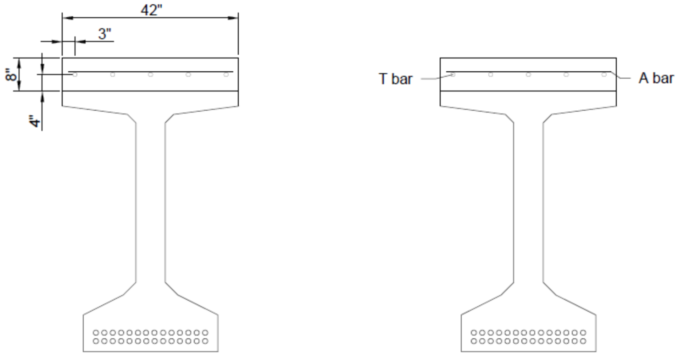

TYPICAL TRANSVERSE SECTION

GENERAL NOTES:

DECK CONCRETE
- SELF COMPACTING CONCRETE (SCC)
- f'c = 4.0 KSI (AT 28 DAYS)

RECEIVING AGENCY: TEXAS DEPARTMENT OF TRANSPORTATION		
PERFORMING AGENCY: UNIVERSITY OF TEXAS AT AUSTIN		
PROJECT NUMBER: TXDOT 0-7090		
DECK DESIGN		
DATE: 02/08/2022		DRAWING NUMBER: **TX-13**
FERGUSON STRUCTURAL ENGINEERING LABORATORY		

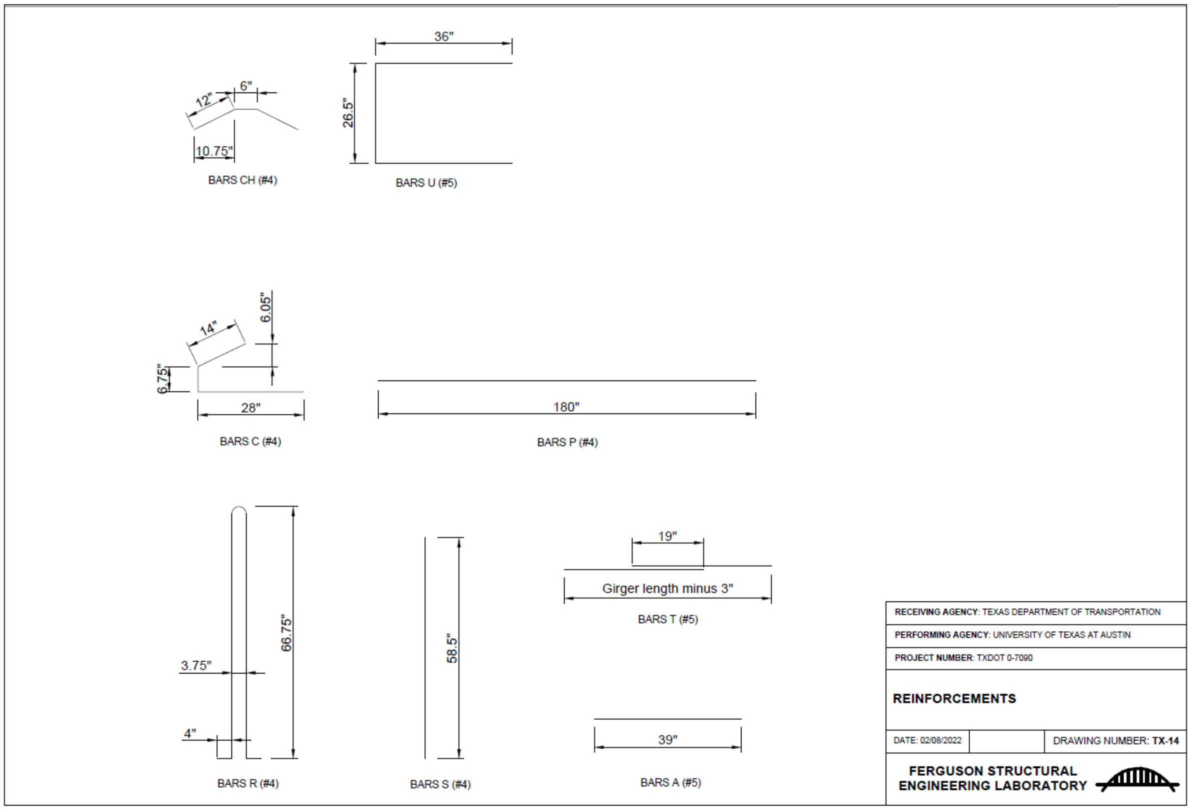

Appendix B. Drawing for Box beam specimens

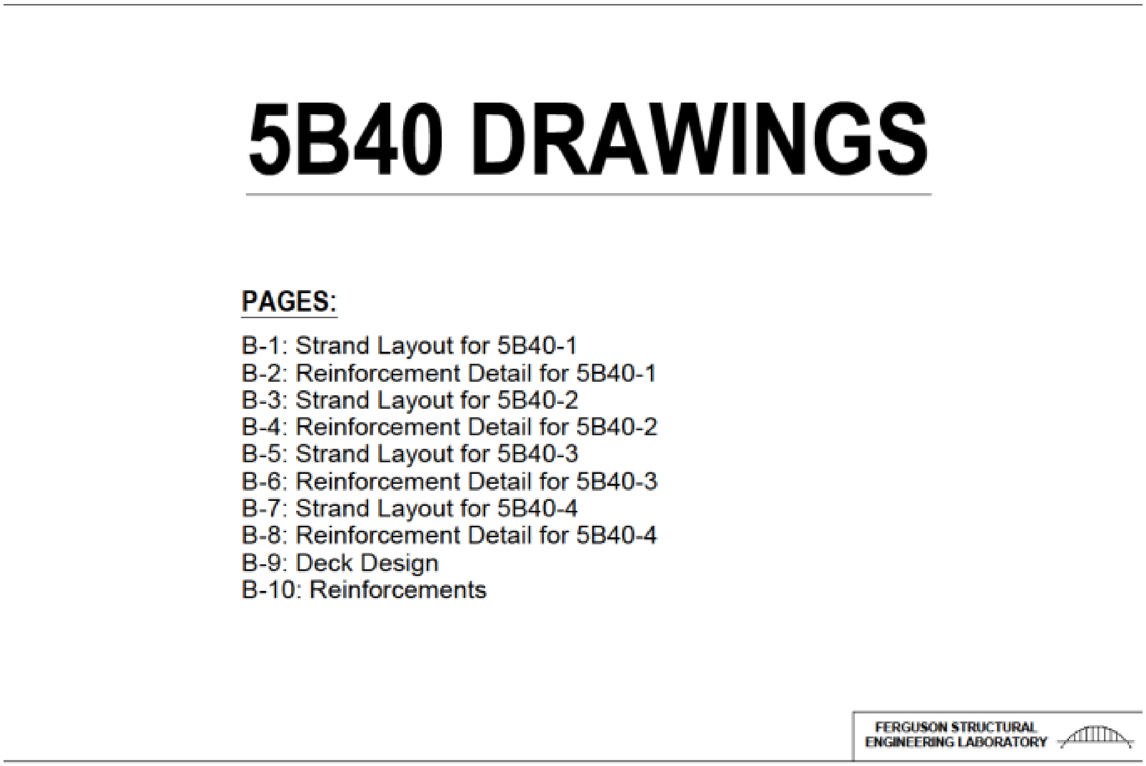

5B40 DRAWINGS

PAGES:

B-1: Strand Layout for 5B40-1
B-2: Reinforcement Detail for 5B40-1
B-3: Strand Layout for 5B40-2
B-4: Reinforcement Detail for 5B40-2
B-5: Strand Layout for 5B40-3
B-6: Reinforcement Detail for 5B40-3
B-7: Strand Layout for 5B40-4
B-8: Reinforcement Detail for 5B40-4
B-9: Deck Design
B-10: Reinforcements

FERGUSON STRUCTURAL
ENGINEERING LABORATORY

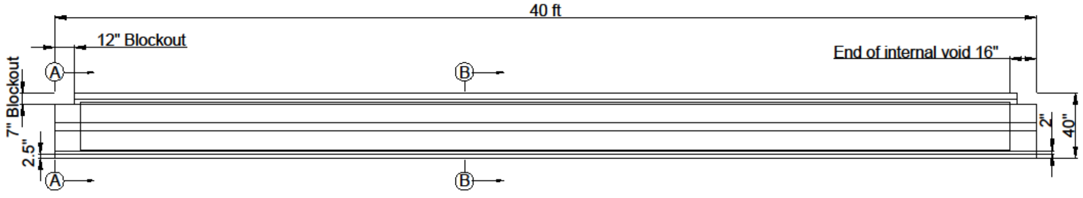

BEAM ELEVATION

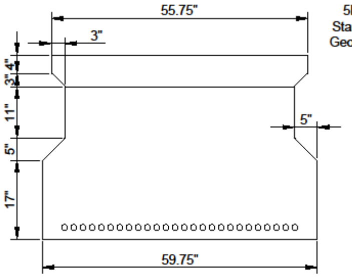

SECTION A-A

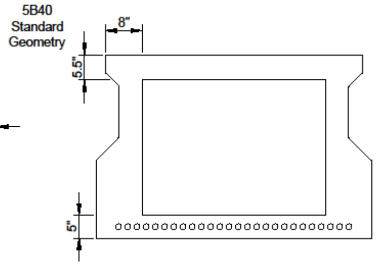

SECTION B-B

GENERAL NOTES:

PRETENSIONED STEEL (26 EA)
- ALL STRANDS SHALL BE 0.6-INCH DIA. LOW RELAXATION STRANDS
- Fpu=270 KSI
- JACKING STRESS=0.75Fpu(=202.5 KSI)
- 26 EA STRAIGHT FULLY BONDED STRAND

GIRDER CONCRETE
- SELF COMPACTING CONCRETE (SCC)
- f'c = 8.5 KSI (AT 28 DAYS)
- f'ci =6.0 KSI (AT RELEASE)

RECEIVING AGENCY: TEXAS DEPARTMENT OF TRANSPORTATION

PERFORMING AGENCY: UNIVERSITY OF TEXAS AT AUSTIN

STRAND LAYOUT FOR 5B40-1

DRAWING NUMBER: **B-1**

FERGUSON STRUCTURAL ENGINEERING LABORATORY

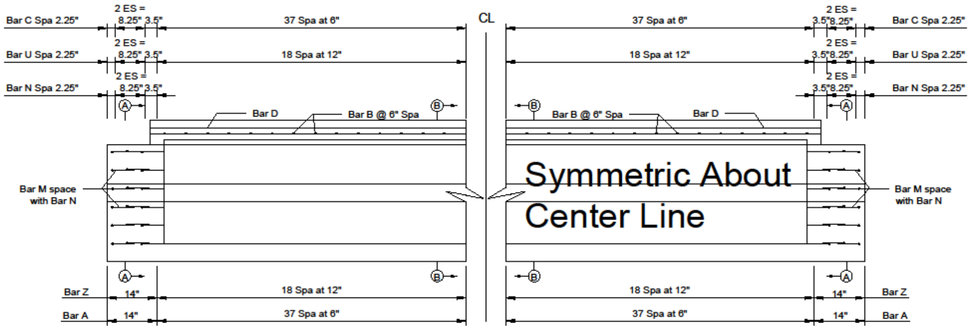

BEAM ELEVATION

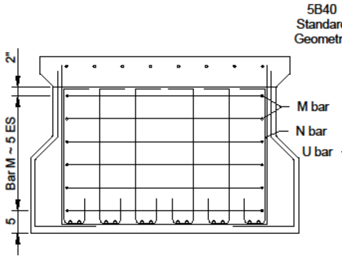

SECTION A-A

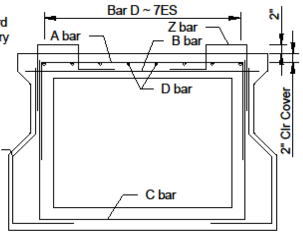

SECTION B-B

GENERAL NOTES:

EVERY TYPE OF REINFORCEMENT
- GRADE 60 (YIELD STRENGTH = 60 KSI) FOR TOTAL LENGTH OF THE BEAM

RECEIVING AGENCY: TEXAS DEPARTMENT OF TRANSPORTATION

PERFORMING AGENCY: UNIVERSITY OF TEXAS AT AUSTIN

REINFORCEMENT DETAIL FOR 5B40-1

DRAWING NUMBER: **B-2**

FERGUSON STRUCTURAL ENGINEERING LABORATORY

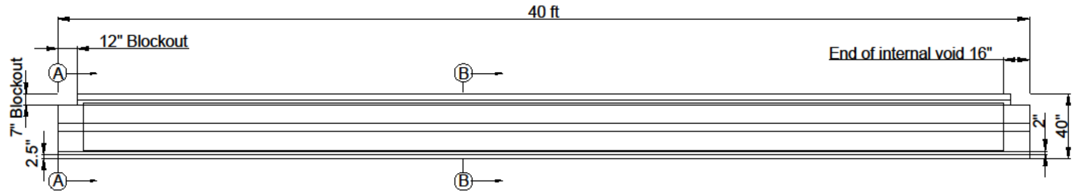

BEAM ELEVATION

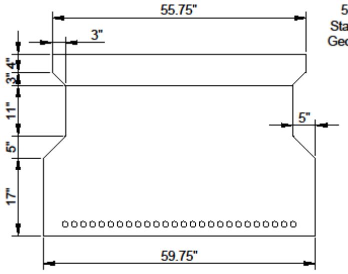

SECTION A-A

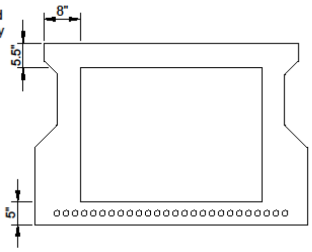

SECTION B-B

GENERAL NOTES:

PRETENSIONED STEEL (26 EA)
- ALL STRANDS SHALL BE 0.6-INCH DIA. LOW RELAXATION STRANDS
- Fpu=270 KSI
- JACKING STRESS=0.75Fpu(=202.5 KSI)
- 26 EA STRAIGHT FULLY BONDED STRAND

GIRDER CONCRETE
- SELF COMPACTING CONCRETE (SCC)
- f'c = 8.5 KSI (AT 28 DAYS)
- f'ci =6.0 KSI (AT RELEASE)

RECEIVING AGENCY: TEXAS DEPARTMENT OF TRANSPORTATION
PERFORMING AGENCY: UNIVERSITY OF TEXAS AT AUSTIN

STRAND LAYOUT FOR 5B40-2

DRAWING NUMBER: B-3

FERGUSON STRUCTURAL ENGINEERING LABORATORY

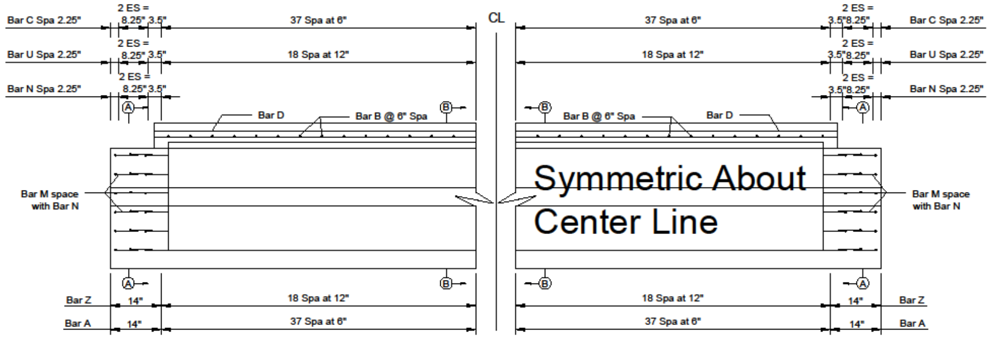

BEAM ELEVATION

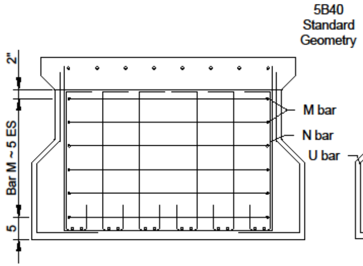

SECTION A-A

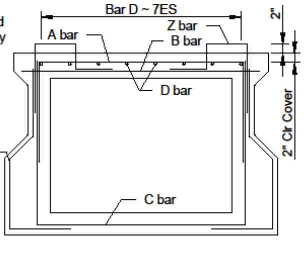

SECTION B-B

GENERAL NOTES:

EVERY TYPE OF REINFORCEMENT
- GRADE 60 (YIELD STRENGTH = 60 KSI) FOR TOTAL LENGTH OF THE BEAM

RECEIVING AGENCY: TEXAS DEPARTMENT OF TRANSPORTATION
PERFORMING AGENCY: UNIVERSITY OF TEXAS AT AUSTIN

REINFORCEMENT DETAIL FOR 5B40-2

DRAWING NUMBER: B-4

FERGUSON STRUCTURAL ENGINEERING LABORATORY

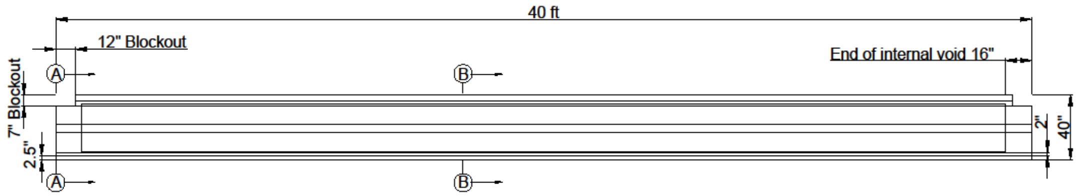

BEAM ELEVATION

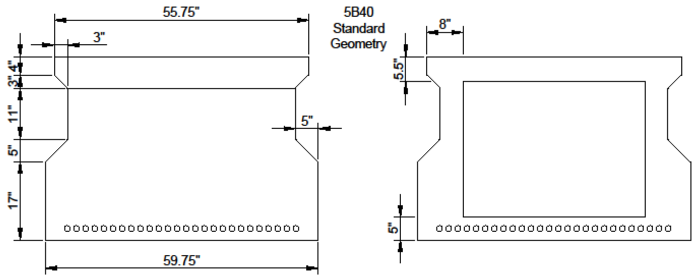

SECTION A-A

SECTION B-B

GENERAL NOTES:

PRETENSIONED STEEL (26 EA)
- ALL STRANDS SHALL BE 0.6-INCH DIA. LOW RELAXATION STRANDS
- Fpu=270 KSI
- JACKING STRESS=0.75Fpu(=202.5 KSI)
- 26 EA STRAIGHT FULLY BONDED STRAND

GIRDER CONCRETE
- SELF COMPACTING CONCRETE (SCC)
- f'c = 8.5 KSI (AT 28 DAYS)
- f'ci =6.0 KSI (AT RELEASE)

RECEIVING AGENCY: TEXAS DEPARTMENT OF TRANSPORTATION

PERFORMING AGENCY: UNIVERSITY OF TEXAS AT AUSTIN

STRAND LAYOUT FOR 5B40-3

DRAWING NUMBER: **B-5**

FERGUSON STRUCTURAL
ENGINEERING LABORATORY

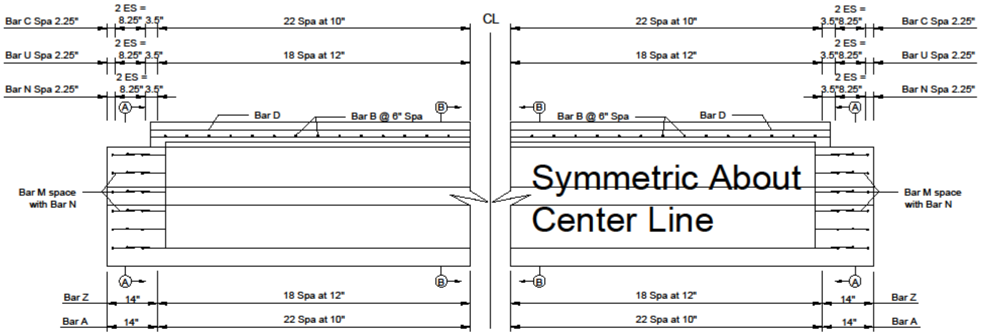

BEAM ELEVATION

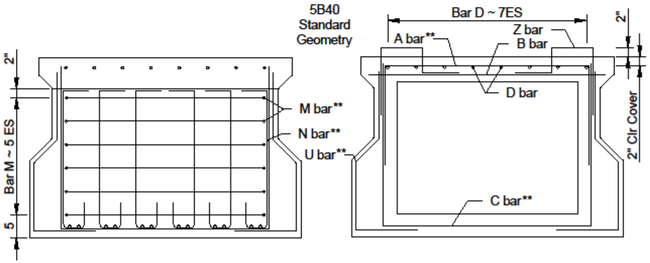

SECTION A-A

SECTION B-B

GENERAL NOTES:

BAR B,D,Z
- GRADE 60 (YIELD STRENGTH = 60 KSI) FOR TOTAL LENGTH OF THE BEAM

BAR A,C,M,N,U
- GRADE 100 (YIELD STRENGTH = 100 KSI) FOR TOTAL LENGTH OF THE BEAM

RECEIVING AGENCY: TEXAS DEPARTMENT OF TRANSPORTATION

PERFORMING AGENCY: UNIVERSITY OF TEXAS AT AUSTIN

REINFORCEMENT DETAIL FOR 5B40-3

DRAWING NUMBER: **B-6**

FERGUSON STRUCTURAL
ENGINEERING LABORATORY

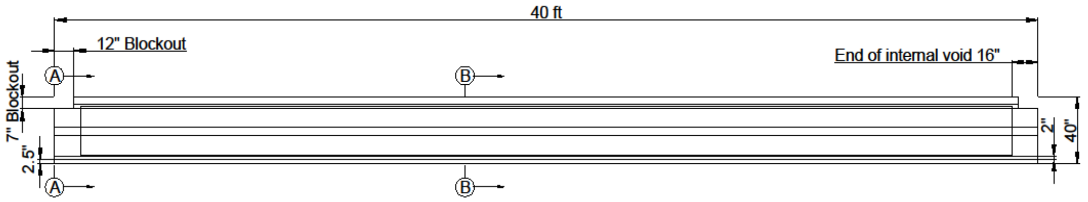

BEAM ELEVATION

GENERAL NOTES:

PRETENSIONED STEEL (26 EA)
- ALL STRANDS SHALL BE 0.6-INCH DIA. LOW RELAXATION STRANDS
- Fpu=270 KSI
- JACKING STRESS=0.75Fpu(=202.5 KSI)
- 26 EA STRAIGHT FULLY BONDED STRAND

GIRDER CONCRETE
- SELF COMPACTING CONCRETE (SCC)
- f'c = 8.5 KSI (AT 28 DAYS)
- f'ci =6.0 KSI (AT RELEASE)

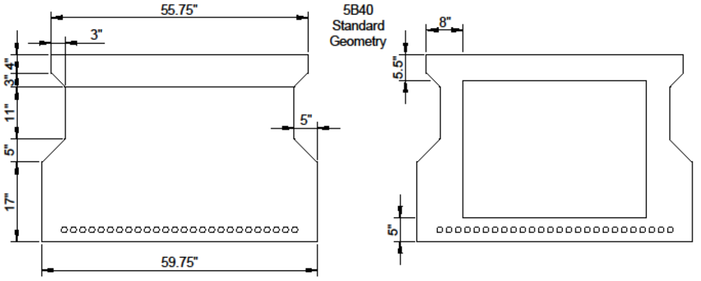

SECTION A-A

SECTION B-B

RECEIVING AGENCY: TEXAS DEPARTMENT OF TRANSPORTATION
PERFORMING AGENCY: UNIVERSITY OF TEXAS AT AUSTIN

STRAND LAYOUT FOR 5B40-4

DRAWING NUMBER: B-7

FERGUSON STRUCTURAL
ENGINEERING LABORATORY

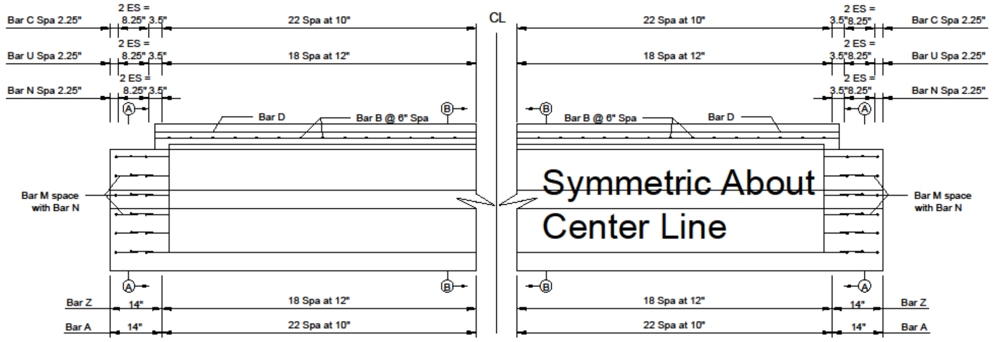

BEAM ELEVATION

GENERAL NOTES:

BAR B,D,Z
- GRADE 60 (YIELD STRENGTH = 60 KSI) FOR TOTAL LENGTH OF THE BEAM

BAR A,C,M,N,U
- GRADE 100 (YIELD STRENGTH = 100 KSI) FOR TOTAL LENGTH OF THE BEAM

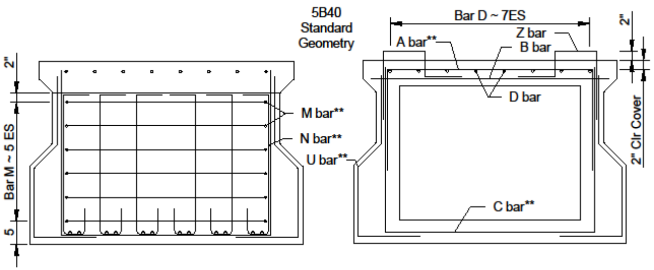

SECTION A-A

SECTION B-B

RECEIVING AGENCY: TEXAS DEPARTMENT OF TRANSPORTATION
PERFORMING AGENCY: UNIVERSITY OF TEXAS AT AUSTIN

REINFORCEMENT DETAIL FOR 5B40-4

DRAWING NUMBER: B-8

FERGUSON STRUCTURAL
ENGINEERING LABORATORY

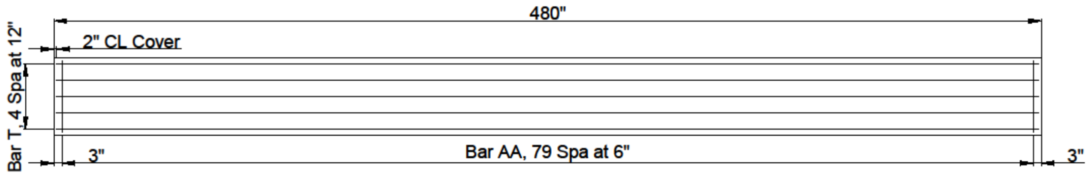

DECK PLAN

GENERAL NOTES:

DECK CONCRETE
- SELF COMPACTING CONCRETE (SCC)
- f'c = 4.0 KSI (AT 28 DAYS)

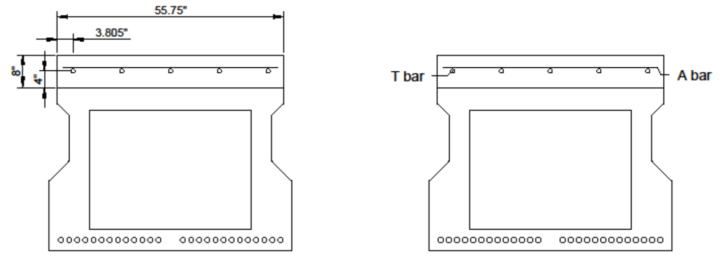

TYPICAL TRANSVERSE SECTION

RECEIVING AGENCY: TEXAS DEPARTMENT OF TRANSPORTATION
PERFORMING AGENCY: UNIVERSITY OF TEXAS AT AUSTIN

DECK DESIGN

DRAWING NUMBER: B-9

FERGUSON STRUCTURAL ENGINEERING LABORATORY

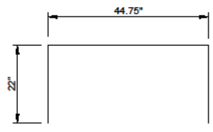

BARS A (#4)

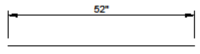

BARS B (#4)

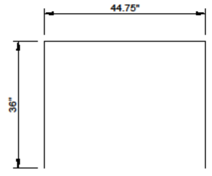

BARS C (#4)

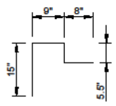

BARS Z (#4)

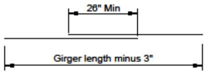

BARS D (#5)

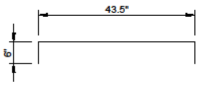

BARS M (#4)

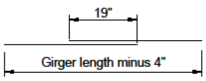

BARS T (#5)

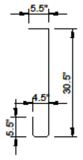

BARS N (#4)

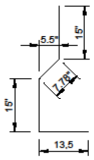

BARS U (#4)

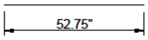

BARS AA (#5)

RECEIVING AGENCY: TEXAS DEPARTMENT OF TRANSPORTATION
PERFORMING AGENCY: UNIVERSITY OF TEXAS AT AUSTIN

REINFORCEMENTS

DRAWING NUMBER: B-10

FERGUSON STRUCTURAL ENGINEERING LABORATORY

Appendix C. Calculation Process for Bridge Deck

5XB28

1) Current rebar layout

(1) Transverse reinforcement (Current TxDOT layout of Gr.60: #5@6")

- **Flexural strength**

Flexural strength calculated considering resistance factor of 0.90 in accordance with AASTHO LRFD (2020), Article 5.5.4.2.

Positive section (Bottom): Flexural strength is 16.78 kip-ft > 5.84 kip-ft (OK)

Negative section (Top): Flexural strength is 16.54 kip-ft > 3.64 kip-ft (OK)

- **Rebar Spacing Check**

The minimum rebar spacing was calculated following Equation (3-2).

Positive section (Bottom): Required rebar spacing is 23.6 in. > 6 in. (OK)

Negative section (Top): Required rebar spacing is 46.4 in. > 6 in. (OK)

The maximum rebar spacing was calculated following *AASHTO LRFD (2020), Article 5.10.3.2*.

Spacing of the reinforcement in slabs shall not be greater than the lesser of the following: 1.5 times the thickness of the member; or 18.0 in.

In this case, the maximum spacing is 12 in.> 6 in. (OK)

(2) Longitudinal reinforcement (Current TxDOT layout of Gr.60: Bottom-5#5@9"btw girder, Top-#4@9")

- **Bottom**

Check the required spacing to use #5 as bottom longitudinal reinforcement is calculated using Equation (5-1).

$220/\sqrt{7} = 83\ percent$, thus use 67 % of transverse reinforcement.

Required area of reinforcement = $0.67 \times \left(0.31 \times \frac{12}{6}\right) = 0.42\ in^2/ft$

Current area of reinforcement= $0.31 \times \frac{12}{9} = 0.41\ in^2/ft \approx 0.42\ in^2/ft$ (OK)

- **Top**

Calculate the required area of reinforcement following Equation (5-2).

Current area of top longitudinal reinforcement= $0.20 \times \frac{12}{9} = 0.267\ in^2/ft$

Required area of reinforcement= $\frac{1.30 \times 12 \times 8}{2(12+8) \times 60} = 0.052\ in^2/ft < 0.267\, in^2/ft$ (OK)

2) High-strength rebar layout

(1) Transverse reinforcement

Grade 80

Try to reduce as much as strength ratio= $0.620 \times \frac{60}{80} = 0.465\ in^2/ft$ → #5@8"

- **Flexural strength**

Positive section (Bottom): Flexural strength is 16.57 ≈ 16.78 kip-ft

Negative section (Top): Flexural strength is 16.55 ≈ 16.54 kip-ft

- **Rebar Spacing Check**

Positive section (Bottom): Required rebar spacing is 26.8 in. > 8 in. (OK)

Negative section (Top): Required rebar spacing is 33.6 in. > 8 in. (OK)

The maximum spacing is 12.0 in.> 8 in. (OK)

Grade 100

Try to reduce as much as strength ratio= $0.620 \times \frac{60}{100} = 0.465\ in^2/ft$ → #5@10"

- **Flexural strength**

Positive section (Bottom): Flexural strength is 16.41 ≈ 16.78 kip-ft

Negative section (Top): Flexural strength is 16.55 ≈ 16.54 kip-ft

- **Rebar Spacing Check**

Positive section (Bottom): Required rebar spacing is 21.1 in. > 10 in. (OK)

Negative section (Top): Required rebar spacing is 25.9 in. > 10 in. (OK)

The maximum spacing is 12.0 in.> 10 in. (OK)

2) Longitudinal reinforcement

Grade 80

- **Bottom**

Try to reduce as much as strength ratio= $0.41 \times \frac{60}{80} = 0.31\ in^2/ft$ → 4#5@12"btw girder

Required area of reinforcement = $0.67 \times \left(0.31 \times \frac{12}{8}\right) = 0.31\ in^2/ft$ (OK)

- **Top**

Try to reduce as much as strength ratio= $0.267 \times \frac{60}{80} = 0.200\ in^2/ft$ → #4@12"

Required area of reinforcement= $\frac{1.30\times12\times8}{2(12+8)\times80} = 0.039\, in^2/ft < 0.200\, in^2/ft$ (OK)

Grade 100

- **Bottom**

Try to reduce as much as strength ratio= $0.41 \times \frac{60}{100} = 0.25\ in^2/ft$ → 4#4@10"btw girder

Required area of reinforcement = $0.67 \times \left(0.31 \times \frac{12}{10}\right) = 0.25\ in^2/ft$ (OK)

- **Top**

Try to reduce as much as strength ratio= $0.267 \times \frac{60}{100} = 0.160\ in^2/ft$ → #3@9"

Required area of reinforcement= $\frac{1.30\times12\times8}{2(12+8)\times100} = 0.031\, in^2/ft < 0.160\, in^2/ft$ (OK)

Tx62

1) Current rebar layout

(1) Transverse reinforcement (Current TxDOT layout of Gr.60: #4@9")

- **Flexural strength**

Flexural strength calculated considering resistance factor of 0.90 in accordance with AASTHO LRFD (2020), Article 5.5.4.2.

Negative section (Top): Flexural strength is 7.72 kip-ft > 4.72 kip-ft (OK)

- **Rebar Spacing Check**

The minimum rebar spacing was calculated following Equation (3-2).

Negative section (Top): Required rebar spacing is 15.9 in. > 9 in. (OK)

The maximum rebar spacing was calculated following *AASHTO LRFD (2020), Article 5.10.3.2*.

Spacing of the reinforcement in slabs shall not be greater than the lesser of the following: 1.5 times the thickness of the member; or 18.0 in.

In this case, the maximum spacing is 12.8 in.> 9 in. (OK)

(2) Longitudinal reinforcement (Current TxDOT layout of Gr.60: Top-#4@9")

Calculate the required area of reinforcement following Equation (5-2).

Current area of top longitudinal reinforcement= $0.20 \times \frac{12}{9} = 0.267\ in^2/ft$

Required area of reinforcement= $\frac{1.30 \times 12 \times 8.5}{2(12+8.5) \times 60} = 0.054\ in^2/ft < 0.267\, in^2/ft$ (OK)

2) High-strength rebar layout

(1) Transverse reinforcement

Grade 80

Try to reduce as much as strength ratio= $0.267 \times \frac{60}{80} = 0.20\ in^2/ft$ → #4@12"

- **Flexural strength**

Negative section (Top): Flexural strength is 7.72 ≈ 7.72 kip-ft

- **Rebar Spacing Check**

Negative section (Top): Required rebar spacing is 8 in. < 12 in. (NG)

Try to change rebar size and spacing: #3@6.5" (Flexural strength is 7.82 kip-ft)

Negative section (Top): Required rebar spacing is 10.6 in. > 6.5 in. (OK)

The maximum spacing is 12.8 in.> 6.5 in. (OK)

Grade 100

Try to reduce as much as strength ratio= $0.267 \times \frac{60}{100} = 0.160\ in^2/ft$ → #4@15"

- **Flexural strength**

Negative section (Top): Flexural strength is 7.69 ≈ 7.72 kip-ft

- **Rebar Spacing Check**

Negative section (Top): Required rebar spacing is 5.3 in. < 15 in. (NG)

The maximum spacing is 12.8 in. < 15 in. (NG)

Try to change rebar size and spacing: #3@6.5" (Flexural strength is 9.71 kip-ft)

- **Flexural strength**

Negative section (Top): Flexural strength is 10.09 > 8.34 kip-ft

- **Rebar Spacing Check**

Negative section (Top): Required rebar spacing is 7.74 in. > 6.5 in. (OK)

The maximum spacing is 12.8 in.> 6.5 in. (OK)

(2) Longitudinal Reinforcement

Grade 80

Try to reduce as much as strength ratio= $0.267 \times \frac{60}{80} = 0.200\ in^2/ft$ → #4@12"

Required area of reinforcement= $\frac{1.30\times12\times8.5}{2(12+8.5)\times80} = 0.039\, in^2/ft < 0.200\, in^2/ft$ (OK)

Grade 100

Try to reduce as much as strength ratio= $0.267 \times \frac{60}{100} = 0.160\ in^2/ft$ → #3@9"

Required area of reinforcement= $\frac{1.30\times12\times8.5}{2(12+8.5)\times100} = 0.031\, in^2/ft < 0.160\, in^2/ft$ (OK)

Appendix D. Calculation Process for Prestressed Girders

Tx62

1) Current rebar layout (Current TxDOT layout of Gr.60: #4@8")

(1) Shear resistance by transverse reinforcement

$$V_s = \frac{A_v f_y d_v (cot\theta + cot\alpha) sin\alpha}{s} = \frac{0.4 \times 60 \times 65.53 \times \cot{(38.66°)}}{8} = 246\ kip$$

$$\varepsilon_s = \frac{\left(\frac{|M_u|}{d_v} + |V_u - V_p| - A_{ps} f_{po}\right)}{E_s A_{ps}} = 0.00276 \rightarrow \theta = 29 + 3500\varepsilon_s = 38.66\ degree$$

(2) Transverse reinforcement limit

The minimum transverse reinforcement was calculated following Equation (5-4).

$$A_v = 0.4 \geq 0.0316\lambda\sqrt{f_c'}\frac{b_v s}{f_y} = 0.0316 \times 1 \times \sqrt{5} \times \frac{7 \times 8}{60} = 0.066 \text{ (OK)}$$

The minimum spacing of transverse reinforcement was calculated following Equation (5-5).

$$\begin{array}{r} v_u = \frac{297}{0.9 \times 7 \times 65.53} = 0.72 \geq 0.125 f_c' = 0.63 \\ s_{max} = 0.4 \times 65.53 = 26.2\ in. \rightarrow 12\ in. > 8\ in. \end{array} \text{(OK)}$$

2) High-strength rebar layout

Grade 80

$$s = \frac{A_v f_y d_v (cot\theta + cot\alpha) sin\alpha}{V_s} = \frac{0.4 \times 80 \times 65.53 \times \cot{(38.66°)}}{246} = 10.65\ in$$

$$A_v = 0.4 \geq 0.0316\lambda\sqrt{f_c'}\frac{b_v s}{f_y} = 0.0316 \times 1 \times \sqrt{5} \times \frac{7 \times 10.65}{80} = 0.066 \text{ (OK)}$$

$$\begin{array}{r} v_u = \frac{297}{0.9 \times 7 \times 65.53} = 0.72 \geq 0.125 f_c' = 0.63 \\ s_{max} = 0.4 \times 65.53 = 26.2\ in. \rightarrow 12\ in. > 10.65\ in. \end{array} \text{(OK)}$$

Grade 100

$$s = \frac{A_v f_y d_v (cot\theta + cot\alpha) sin\alpha}{V_s} = \frac{0.4 \times 100 \times 65.53 \times \cot{(38.66°)}}{246} = 13.32\ in$$

$$v_u = \frac{297}{0.9 \times 7 \times 65.53} = 0.72 \geq 0.125 f_c' = 0.63$$
(NG)
$$s_{max} = 0.4 \times 65.53 = 26.2\ in. \rightarrow 12\ in. > 13.32\ in.$$

Therefore, spacing of 12 in. was selected.

$$A_v = 0.4 \geq 0.0316 \lambda \sqrt{f_c'} \frac{b_v s}{f_y} = 0.0316 \times 1 \times \sqrt{5} \times \frac{7 \times 12}{100} = 0.059 \text{ (OK)}$$

5B40

1) Current rebar layout (Current TxDOT layout of Gr.60: #4@6")

(1) Shear resistance by transverse reinforcement

$$V_s = \frac{A_v f_y d_v (cot\theta + cot\alpha) sin\alpha}{s} = \frac{0.4 \times 60 \times 39.34 \times \cot(34°)}{6} = 233\ kip$$

$$\varepsilon_s = \frac{\left(\frac{|M_u|}{d_v} + |V_u - V_p| - A_{ps} f_{po}\right)}{E_s A_{ps}} = 0.00143 \rightarrow \theta = 29 + 3500 \varepsilon_s = 34\ degree$$

(2) Transverse reinforcement limit

The minimum transverse reinforcement was calculated following Equation (5-4).

$$A_v = 0.4 \geq 0.0316 \lambda \sqrt{f_c'} \frac{b_v s}{f_y} = 0.0316 \times 1 \times \sqrt{5} \times \frac{10 \times 6}{60} = 0.071 \text{ (OK)}$$

The minimum spacing of transverse reinforcement was calculated following Equation (5-5).

$$v_u = \frac{297}{0.9 \times 10 \times 39.34} = 0.84 \geq 0.125 f_c' = 0.63$$
(OK)
$$s_{max} = 0.4 \times 39.34 = 15.7\ in. \rightarrow 12\ in. > 8\ in.$$

2) High-strength rebar layout

Grade 80

$$s = \frac{A_v f_y d_v(cot\theta + cot\alpha)sin\alpha}{V_s} = \frac{0.4 \times 80 \times 39.34 \times \cot(34°)}{233} = 8.0\ in$$

$$A_v = 0.4 \geq 0.0316\lambda\sqrt{f_c'}\frac{b_v s}{f_y} = 0.0316 \times 1 \times \sqrt{5} \times \frac{10\times8.0}{80} = 0.071 \text{ (OK)}$$

$$\begin{matrix} v_u = \frac{297}{0.9\times7\times39.34} = 0.84 \geq 0.125f_c' = 0.63 \\ s_{max} = 0.4 \times 39.34 = 15.7\ in. \rightarrow 12\ in. > 8\ in. \end{matrix} \quad \text{(OK)}$$

Grade 100

$$s = \frac{A_v f_y d_v(cot\theta + cot\alpha)sin\alpha}{V_s} = \frac{0.4 \times 100 \times 39.34 \times \cot(34°)}{233} = 10.0\ in$$

$$A_v = 0.4 \geq 0.0316\lambda\sqrt{f_c'}\frac{b_v s}{f_y} = 0.0316 \times 1 \times \sqrt{5} \times \frac{10\times10.0}{100} = 0.071 \text{ (OK)}$$

$$\begin{matrix} v_u = \frac{297}{0.9\times7\times39.34} = 0.84 \geq 0.125f_c' = 0.63 \\ s_{max} = 0.4 \times 39.34 = 15.7\ in. \rightarrow 12\ in. > 10\ in. \end{matrix} \quad \text{(OK)}$$

Appendix E. Calculation Process for Bent Cap

Inverted T bent (Moment frame)

1) Longitudinal ties

(1) Bottom chord

- **Current**

Factored load: $F_u = 1842.7$ kip

Tie capacity: $\Phi f_y A_{st} = F_u \rightarrow A_{st} = \frac{F_u}{\Phi f_y} = \frac{1842.7}{0.9\times 60} = 34.12\ in^2$

Required number of #11 bars: $n = \frac{34.12}{1.56} = 21.9$ → 22-#11 (Grade 60)

- **High-strength rebar**

Grade 80: $A_{st} = \frac{F_u}{\Phi f_y} = \frac{1842.7}{0.9\times 80} = 25.59\ in^2, n = \frac{25.59}{1.56} = 16.4$ → 17-#11

Grade 100: $A_{st} = \frac{F_u}{\Phi f_y} = \frac{1842.7}{0.9\times 100} = 20.47\ in^2, n = \frac{20.47}{1.56} = 13.1$ → 14-#11

(2) Top chord

- **Current**

Tie AB

Factored load: $F_u = 331.4$ kip

Tie capacity: $\Phi f_y A_{st} = F_u \rightarrow A_{st} = \frac{F_u}{\Phi f_y} = \frac{331.4}{0.9\times 60} = 6.14\ in^2$

Nodal check at node C

- Concrete capacity: $f_{cu} = mvf_c' = 1 \times 0.7 \times 5 = 3.5\ ksi$

$\Phi F_n = \Phi\left(f_{cu}A_{cn} + f_y A_{st}\right) = 0.7(3.5 \times 9.2 \times 40 + 60A_{st}) \geq F_u, \therefore\ A_{st} \geq 22.41\ in^2$

Required number of #11 bars: $n = \frac{22.41}{1.56} = 14.4$ → 15-#11 (Grade 60)

- **High-strength rebar**

Grade 80: $A_{st} \geq \frac{\frac{F_u}{\Phi} - f_{cu}A_{cn}}{f_y} = \frac{\frac{1842.7}{0.7} - 3.5\times 9.2\times 40}{80} = 16.81\ in^2, n = \frac{16.81}{1.56} = 10.8$ → 11-#11

Grade 100: $A_{st} \geq \frac{\frac{F_u}{\Phi} - f_{cu}A_{cn}}{f_y} = \frac{\frac{1842.7}{0.7} - 3.5\times9.2\times40}{80} = 13.44\ in^2, n = \frac{13.44}{1.56} = 8.6 \rightarrow$ 9-#11

2) Vertical ties

Tie EK

- **Current**

Factored load: $F_u = 923.7$ kip

Tie capacity: $\Phi f_y A_{st} = F_u \rightarrow A_{st} = \frac{F_u}{\Phi f_y} = \frac{923.7}{0.9\times60} = 17.11\ in^2$

Required number of double #6 stirrups: $n = \frac{17.11}{4\times0.44} = 9.72$

Required stirrups spacing: $s = \frac{62}{9.72} = 6.4\ in$

- **High-strength rebar**

Grade 80: $A_{st} = \frac{923.7}{0.9\times80} = 12.83\ in^2, n = \frac{12.83}{4\times0.44} = 7.29, s = \frac{62}{7.29} = 8.5\ in$

Grade 100: $A_{st} = \frac{923.7}{0.9\times100} = 10.26\ in^2, n = \frac{10.26}{4\times0.44} = 5.83, s = \frac{62}{5.83} = 10.6\ in$

Tie CI

- **Current**

Factored load: $F_u = 513.8$ kip

Tie capacity: $\Phi f_y A_{st} = F_u \rightarrow A_{st} = \frac{F_u}{\Phi f_y} = \frac{513.8}{0.9\times60} = 9.51\ in^2$

Required number of #6 stirrups: $n = \frac{9.51}{2\times0.44} = 10.81$

Required stirrups spacing: $s = \frac{62}{10.81} = 5.7\ in$

- **High-strength rebar**

Grade 80: $A_{st} = \frac{513.8}{0.9\times80} = 7.14\ in^2, n = \frac{7.14}{2\times0.44} = 8.11, s = \frac{62}{8.11} = 7.6\ in$

Grade 100: $A_{st} = \frac{513.8}{0.9\times100} = 5.71\ in^2, n = \frac{5.71}{2\times0.44} = 6.49, s = \frac{62}{6.49} = 9.6\ in$

Tie BH

- **Current**

  Factored load: $F_u = 518.9$ kip

  Tie capacity: $\Phi f_y A_{st} = F_u \rightarrow A_{st} = \frac{F_u}{\Phi f_y} = \frac{518.9}{0.9\times 60} = 9.61\ in^2$

  Required number of #6 stirrups: $n = \frac{9.61}{2\times 0.44} = 10.92$

  Required stirrups spacing: $s = \frac{103.5}{10.92} = 9.5\ in$

- **High-strength rebar**

  Grade 80: $A_{st} = \frac{518.9}{0.9\times 80} = 7.21\ in^2, n = \frac{7.21}{2\times 0.44} = 8.19, s = \frac{103.5}{8.19} = 12.6\ in$

  Grade 100: $A_{st} = \frac{518.9}{0.9\times 100} = 5.77\ in^2, n = \frac{5.77}{2\times 0.44} = 6.55, s = \frac{103.5}{6.55} = 15.8\ in$

3) Ledge reinforcement

Tie C_sF_s

- **Current**

  Factored load: $F_u = 198.4$ kip

  Tie capacity: $\Phi f_y A_{st} = F_u \rightarrow A_{st} = \frac{F_u}{\Phi f_y} = \frac{198.4}{0.9\times 60} = 3.67\ in^2$

  Required number of #6 bars: $n = \frac{3.67}{0.44} = 8.35$

  Required stirrups spacing: $s = \frac{62}{8.35} = 7.4\ in$

- **High-strength rebar**

  Grade 80: $A_{st} = \frac{198.4}{0.9\times 80} = 2.76\ in^2, n = \frac{2.76}{0.44} = 6.26, s = \frac{62}{6.26} = 9.9\ in$

  Grade 100: $A_{st} = \frac{198.4}{0.9\times 100} = 2.20\ in^2, n = \frac{2.20}{0.44} = 5.01, s = \frac{62}{5.01} = 12.4\ in$

Inverted T bent (Simply support)

1) Longitudinal ties

(1) Bottom chord

- **Current**

Factored load: $F_u = 2602.7$ kip

Tie capacity: $\Phi f_y A_{st} = F_u \rightarrow A_{st} = \frac{F_u}{\Phi f_y} = \frac{2602.7}{0.9 \times 60} = 48.20\ in^2$

Required number of #11 bars: $n = \frac{48.20}{1.56} = 30.9$ → 31-#11 (Grade 60)

- **High-strength rebar**

Grade 80: $A_{st} = \frac{F_u}{\Phi f_y} = \frac{2602.7}{0.9 \times 80} = 36.15\ in^2, n = \frac{36.15}{1.56} = 23.2$ → 24-#11

Grade 100: $A_{st} = \frac{F_u}{\Phi f_y} = \frac{2602.7}{0.9 \times 100} = 28.92\ in^2, n = \frac{28.92}{1.56} = 18.5$ → 19-#11

Top chord

- **Current**

Nodal check at node C

- Concrete capacity: $f_{cu} = m v f_c' = 1 \times 0.7 \times 5 = 3.5\ ksi$

$$\Phi F_n = \Phi\left(f_{cu} A_{cn} + f_y A_{st}\right) = 0.7(3.5 \times 12.7 \times 40 + 60 A_{st}) \geq F_u, \therefore\ A_{st} \geq 32.34\ in^2$$

Required number of #11 bars: $n = \frac{32.34}{1.56} = 20.7$ → 21-#11 (Grade 60)

- **High-strength rebar**

Grade 80: $A_{st} \geq \frac{\frac{F_u}{\Phi} - f_{cu} A_{cn}}{f_y} = \frac{\frac{1842.7}{0.7} - 3.5 \times 12.7 \times 40}{80} = 24.25\ in^2\ n = \frac{24.25}{1.56} = 15.5$ → 16-#11

Grade 100: $A_{st} \geq \frac{\frac{F_u}{\Phi} - f_{cu} A_{cn}}{f_y} = \frac{\frac{1842.7}{0.7} - 3.5 \times 12.7 \times 40}{80} = 19.40\ in^2, n = \frac{19.40}{1.56} = 12.4$ → 13-#11

2) Vertical ties

Tie GO

- **Current**

  Factored load: $F_u = 917.8$ kip

  Tie capacity: $\Phi f_y A_{st} = F_u \rightarrow A_{st} = \frac{F_u}{\Phi f_y} = \frac{917.8}{0.9\times 60} = 17.00\ in^2$

  Required number of double #6 stirrups: $n = \frac{17.0}{4\times 0.44} = 9.66$

  Required stirrups spacing: $s = \frac{50.5}{9.66} = 5.2\ in$

- **High-strength rebar**

  Grade 80: $A_{st} = \frac{917.8}{0.9\times 80} = 12.75\ in^2, n = \frac{12.75}{4\times 0.44} = 7.24, s = \frac{50.5}{7.24} = 7.0\ in$

  Grade 100: $A_{st} = \frac{917.8}{0.9\times 100} = 10.20\ in^2, n = \frac{10.20}{4\times 0.44} = 5.79, s = \frac{50.5}{5.79} = 8.7\ in$

Tie CK

- **Current**

  Factored load: $F_u = 507.5$ kip

  Tie capacity: $\Phi f_y A_{st} = F_u \rightarrow A_{st} = \frac{F_u}{\Phi f_y} = \frac{507.5}{0.9\times 60} = 9.40\ in^2$

  Required number of #6 stirrups: $n = \frac{9.40}{2\times 0.44} = 10.68$

  Required stirrups spacing: $s = \frac{50.5}{10.68} = 4.7\ in$

- **High-strength rebar**

  Grade 80: $A_{st} = \frac{507.5}{0.9\times 80} = 7.05\ in^2, n = \frac{7.05}{2\times 0.44} = 8.01, s = \frac{50.5}{8.01} = 6.3\ in$

  Grade 100: $A_{st} = \frac{507.5}{0.9\times 100} = 5.64\ in^2, n = \frac{5.64}{2\times 0.44} = 6.41, s = \frac{50.5}{6.41} = 7.9\ in$

Tie AI

- **Current**

  Factored load: $F_u = 542.5$ kip

  Tie capacity: $\Phi f_y A_{st} = F_u \rightarrow A_{st} = \frac{F_u}{\Phi f_y} = \frac{542.5}{0.9\times60} = 10.05\ in^2$

  Required number of #6 stirrups: $n = \frac{10.05}{2\times0.44} = 11.42$

  Required stirrups spacing: $s = \frac{75}{11.42} = 6.6\ in$

- **High-strength rebar**

  Grade 80: $A_{st} = \frac{542.5}{0.9\times80} = 7.53\ in^2, n = \frac{7.53}{2\times0.44} = 8.56, s = \frac{75}{8.56} = 8.8\ in$

  Grade 100: $A_{st} = \frac{542.5}{0.9\times100} = 6.03\ in^2, n = \frac{6.03}{2\times0.44} = 6.85, s = \frac{75}{6.85} = 10.9\ in$

3) Ledge reinforcement

Tie C_sF_s

- **Current**

  Factored load: $F_u = 225.5$ kip

  Tie capacity: $\Phi f_y A_{st} = F_u \rightarrow A_{st} = \frac{F_u}{\Phi f_y} = \frac{225.5}{0.9\times60} = 4.18\ in^2$

  Required number of #6 bars: $n = \frac{4.18}{0.44} = 9.49$

  Required stirrups spacing: $s = \frac{50.5}{9.49} = 5.3\ in$

- **High-strength rebar**

  Grade 80: $A_{st} = \frac{225.5}{0.9\times80} = 3.13\ in^2, n = \frac{3.13}{0.44} = 7.12, s = \frac{50.5}{7.12} = 7.1\ in$

  Grade 100: $A_{st} = \frac{225.5}{0.9\times100} = 2.51\ in^2, n = \frac{2.51}{0.44} = 5.69, s = \frac{50.5}{5.69} = 8.9\ in$

IH610 buslane-Bent 5

1) Longitudinal ties

(1) Bottom chord

- **Current**

  Grade 60: 7-#11

  Tie capacity: $F_u = f_y A_{st} = 60 \times 7 \times 1.56 = 655.2\ kip$

- **High-strength rebar**

  Grade 80: $A_{st} = \frac{F_u}{f_y} = \frac{655.2}{80} = 8.19\ in^2, n = \frac{8.19}{1.56} = 5.3$ → 6-#11

  Grade 100: $A_{st} = \frac{F_u}{f_y} = \frac{655.2}{100} = 6.55\ in^2, n = \frac{6.55}{1.56} = 4.2$ → 5-#11

(2) Top chord

- **Current**

  Grade 60: 48-#11

  Tie capacity: $F_u = f_y A_{st} = 60 \times 48 \times 1.56 = 4{,}492.8\ kip$

- **High-strength rebar**

  Grade 80: $A_{st} = \frac{F_u}{f_y} = \frac{4492.8}{80} = 56.16\ in^2, n = \frac{18.61}{1.56} = 36.0$ → 36-#11

  Grade 100: $A_{st} = \frac{F_u}{f_y} = \frac{4492.8}{100} = 44.93\ in^2, n = \frac{14.89}{1.56} = 28.8$ → 29-#11

2) Vertical ties

- **Current**

  Dbl. #6 btw girders at 4.8 in. (30 ES in 12 ft-0.5 in.) and #6 at center at 10 in. (6 ES in 5 ft)

  Tie capacity: $F_{u1} = f_y A_{st1} = 60 \times 30 \times (4 \times 0.44) = 3{,}168\ kip$

  $$F_{u2} = f_y A_{st2} = 60 \times 6 \times (2 \times 0.44) = 316.8\ kip$$

- **High-strength rebar**

  Grade 80: $A_{st1} = \frac{F_{u1}}{f_y} = \frac{3168}{80} = 39.60\ in^2, n = \frac{39.60}{4 \times 0.44} = 22.5$, $s = \frac{144.5}{22.5} = 6.4\ in$

$$A_{st2} = \frac{F_u2}{f_y} = \frac{316.8}{80} = 3.96\ in^2, n = \frac{3.96}{2\times0.44} = 4.5, \text{s} = \frac{60}{4.5} = 13.3\ in$$

Grade 100: $A_{st1} = \frac{F_{u1}}{f_y} = \frac{3168}{100} = 31.68\ in^2, n = \frac{31.68}{4\times0.44} = 18.0, \text{s} = \frac{144.5}{18.0} = 8.0\ in$

$$A_{st2} = \frac{F_u2}{f_y} = \frac{316.8}{100} = 3.17\ in^2, n = \frac{3.17}{2\times0.44} = 3.6, \text{s} = \frac{60}{3.6} = 16.7\ in$$

(3) Ledge

- **Current**

#7 btw girders at 4.8 in. (30 ES in 12 ft-0.5 in.) and #7 at center at 5 in. (12 ES in 5 ft)

Tie capacity: $F_{u1} = f_y A_{st1} = 60 \times 30 \times 0.6 = 1{,}080\ kip$

$$F_{u2} = f_y A_{st2} = 60 \times 12 \times 0.6 = 432\ kip$$

- **High-strength rebar**

Grade 80: $A_{st1} = \frac{F_{u1}}{f_y} = \frac{1080}{80} = 13.50\ in^2, n = \frac{13.50}{0.6} = 22.5, \text{s} = \frac{144.5}{22.3} = 6.4\ in$

$$A_{st2} = \frac{F_u2}{f_y} = \frac{432}{80} = 5.40\ in^2, n = \frac{5.40}{0.6} = 9.0, \text{s} = \frac{60}{9.0} = 6.7\ in$$

Grade 100: $A_{st1} = \frac{F_{u1}}{f_y} = \frac{1080}{100} = 10.80\ in^2, n = \frac{10.80}{0.6} = 18.0, \text{s} = \frac{144.5}{18.0} = 8.0\ in$

$$A_{st2} = \frac{F_u2}{f_y} = \frac{432}{100} = 4.32\ in^2, n = \frac{4.32}{0.6} = 7.2, \text{s} = \frac{60}{7.2} = 8.3\ in$$

(4) Crack control reinforcement

- **Horizontal reinforcement (#7 rebar)**

$$A_h = 0.003 b_w s_h, s_h = \frac{A_h}{0.003 b_w} = \frac{2 \times 0.6}{0.003 \times 45} = 8.9\ in$$

- **Vertical reinforcement**

Dbl. #6: $A_v = 0.003 b_w s_v, s_v = \frac{A_v}{0.003 b_w} = \frac{4\times0.44}{0.003\times45} = 13.0\ in$

Sgl. #6: $A_v = 0.003 b_w s_v, s_v = \frac{A_v}{0.003 b_w} = \frac{2\times0.44}{0.003\times45} = 6.5\ in$

IH610 buslane-Bent 11

1) Longitudinal ties

(1) Bottom chord

- **Current**

  Grade 60: 84-#11

  Tie capacity: $F_u = f_y A_{st} = 60 \times 84 \times 1.56 = 7{,}862.4\ kip$

- **High-strength rebar**

  Grade 80: $A_{st} = \frac{F_u}{f_y} = \frac{7862.4}{80} = 98.28\ in^2, n = \frac{98.28}{1.56} = 63.0$ → 63-#11

  Grade 100: $A_{st} = \frac{F_u}{f_y} = \frac{7862.4}{100} = 78.62\ in^2, n = \frac{78.62}{1.56} = 50.4$ → 51-#11

(2) Top chord

- **Current**

  Grade 60: 16-#11

  Tie capacity: $F_u = f_y A_{st} = 60 \times 16 \times 1.56 = 1{,}497.6\ kip$

- **High-strength rebar**

  Grade 80: $A_{st} = \frac{F_u}{f_y} = \frac{1497.6}{80} = 18.72\ in^2, n = \frac{18.72}{1.56} = 12.0$ → 12-#11

  Grade 100: $A_{st} = \frac{F_u}{f_y} = \frac{1497.6}{100} = 14.98\ in^2, n = \frac{14.989}{1.56} = 9.6$ → 10-#11

2) Vertical ties

(1) Sectional method

- **Current**

  Dbl. #6 at max. 5 in., (165 ES in 68 ft-6 in.)

$$\varepsilon_s = \frac{\left(\frac{|M_u|}{d_v} + V_u\right)}{E_s A_s} = 0.00053 \rightarrow \theta = 29 + 3500\varepsilon_s = 30.9\ degree$$

$$V_s = \frac{A_v f_y d_v (cot\theta + cot\alpha) sin\alpha}{s} = 2{,}955\ kip$$

- **High-strength rebar**

Grade 80: $s = \frac{A_v f_y d_v (cot\theta + cot\alpha) sin\alpha}{V_s} = 6.5\ in$

Grade 100: $s = \frac{A_v f_y d_v (cot\theta + cot\alpha) sin\alpha}{V_s} = 7.9\ in$

(2) STM

- **Current**

  Dbl. #6 at max. 5 in., (165 ES in 68 ft-6 in.)

  Tie capacity: $F_u = f_y A_{st1} = 60 \times 165 \times (4 \times 0.44) = 17{,}424\ kip$

- **High-strength rebar**

  Grade 80: $A_{st} = \frac{F_u}{f_y} = \frac{17424}{80} = 217.80\ in^2$, $n = \frac{217.80}{4 \times 0.44} = 123.8$, $s = \frac{822}{123.8} = 6.6\ in$

  Grade 100: $A_{st} = \frac{F_u}{f_y} = \frac{17424}{100} = 174.24\ in^2$, $n = \frac{174.24}{4 \times 0.44} = 99.0$, $s = \frac{822}{99.0} = 8.3\ in$

3) Ledge

- **Current**

  #7 at max. 5 in., (76 ES in 31 ft-2.75 in.)

  Tie capacity: $F_u = f_y A_{st} = 60 \times 76 \times 0.6 = 2{,}736\ kip$

- **High-strength rebar**

  Grade 80: $A_{st} = \frac{F_{u1}}{f_y} = \frac{2736}{80} = 34.20\ in^2$, $n = \frac{34.20}{0.6} = 57.0$, $s = \frac{374.75}{57.0} = 6.6\ in$

  Grade 100: $A_{st} = \frac{F_{u1}}{f_y} = \frac{2736}{100} = 27.36\ in^2$, $n = \frac{27.36}{0.6} = 45.6$, $s = \frac{374.75}{45.6} = 8.2\ in$

4) Crack control reinforcement

- **Horizontal reinforcement (#7 rebar)**

$$A_h = 0.003 b_w s_h, s_h = \frac{A_h}{0.003 b_w} = \frac{2 \times 0.6}{0.003 \times 45} = 8.9\ in$$

- **Vertical reinforcement**

$$A_v = 0.003 b_w s_v, s_v = \frac{A_v}{0.003 b_w} = \frac{4 \times 0.44}{0.003 \times 45} = 13.0\ in$$

Appendix F. Calculation Process for Drilled Shaft Footing

I-2 footing specimen (TxDOT Project 0-6953)

1) STM

(1) Bottom mat rebar

- **Current**

Dimension and properties in Figure 5-32.

$$f_c' = 5\ ksi\ , f_y = 60\ ksi$$

$$L_1 = L_2 = 96\ in., S_1 = S_2 = 64\ in., w_c = 32\ in., H = 32\ in.$$

$$d' = 0.9H - (c_b + d_b) = 0.9 \times 32 - (4 + 1) = 23.8\ in.$$

$$z' = \sqrt{(S_1/2 - w_c/4)^2 + (S_2/2 - w_c/4)^2} = 34.65\ in.$$

$$\theta = \tan^{-1}(d'/z') = 34.49\ \text{degree}, \alpha = \tan^{-1}\left(\frac{S_1/2 - w_c/4}{S_2/2 - w_c/4}\right) = 45\ degree$$

Ties EF and GH

Tie capacity: $T_x = f_y A_{st} = 60 \times 7 \times 2 \times 0.79 = 664\ kip$

Failure load: $P_{tie,x} = \frac{4T_x tan\theta}{sin\alpha} = 2579\ kip$

Ties FG and EH

Tie capacity: $T_y = f_y A_{st} = 60 \times 7 \times 2 \times 0.79 = 664\ kip$

Failure load: $P_{tie,y} = \frac{4T_y tan\theta}{cos\alpha} = 2579\ kip$

- **High-strength rebar**

Grade 80: $A_{st} = \frac{P_{tie} sin\alpha}{4 f_y tan\theta} = 8.30\ in^2, n = \frac{8.43}{2 \times 0.79} = 5.3$ → 11-2#8 in each direction

Grade 100: $A_{st} = \frac{P_{tie} sin\alpha}{4 f_y tan\theta} = 6.64\ in^2, n = \frac{6.74}{2 \times 0.79} = 4.2$ → 9-2#8 in each direction

(2) Side surface reinforcement

The required side surface reinforcement was calculated following Equations (5-2) and (3-11). I-2 specimen was designed to satisfy the requirement of side surface reinforcement following the minimum crack control reinforcement of 0.3% for STM design. Therefore, the reinforcement ratio of 0.3% was assumed to maintain in this calculation.

- **Current**

  Horizontal side face reinforcement

$$A_s = 0.44\ in^2/ft \geq \frac{1.30bh}{2(b+h)f_y} = \frac{1.30\times96\times32}{2(96+32)\times60} = 0.26\ in^2/ft \text{ (OK)}$$

$$\rho_s = \frac{A_s}{s}\frac{Perimeter}{A_g}\frac{f_y}{60} = \frac{0.11}{3}\frac{2(96+32)}{96\times32}\frac{60}{60} = 0.3\%$$

  Vertical side face reinforcement

$$A_s = 0.88\ in^2/ft \geq \frac{1.30bh}{2(b+h)f_y} = \frac{1.30\times96\times96}{2(96+96)\times60} = 0.52\ in^2/ft \text{ (OK)}$$

$$\rho_s = \frac{A_s}{s}\frac{Perimeter}{A_g}\frac{f_y}{60} = \frac{0.44}{6}\frac{96\times4}{96^2}\frac{60}{60} = 0.3\%$$

- **High-strength rebar**

  Grade 80

  Horizontal side face reinforcement

$$s = \frac{A_s}{\rho_s}\frac{Perimeter}{A_g}\frac{f_y}{60} = \frac{0.11}{0.003}\frac{2(96+32)}{96\times32}\frac{80}{60} = 4.1\ in. \rightarrow \text{5-\#3@4"}$$

  Vertical side face reinforcement

$$s = \frac{A_s}{\rho_s}\frac{Perimeter}{A_g}\frac{f_y}{60} = \frac{0.44}{0.003}\frac{96\times4}{96^2}\frac{80}{60} = 8.2\ in. \rightarrow \text{10-\#6@8"}$$

  Grade 100

  Horizontal side face reinforcement

$$s = \frac{A_s}{\rho_s}\frac{Perimeter}{A_g}\frac{f_y}{60} = \frac{0.11}{0.003}\frac{2(96+32)}{96\times32}\frac{100}{60} = 5.1\ in. \rightarrow \text{4-\#3@5"}$$

  Vertical side face reinforcement

$$s = \frac{A_s}{\rho_s}\frac{Perimeter}{A_g}\frac{f_y}{60} = \frac{0.44}{0.003}\frac{96\times4}{96^2}\frac{100}{60} = 10.2\ in. \rightarrow \text{8-\#6@10"}$$

2) Sectional method

(1) Bottom mat rebar

- **Current**

  Dimension and properties in Figure 5.2.

  The flexural strength at section was calculated using strain compatibility method.

  Flexural strength is 2,968 kip-ft (Grade 60 14-2#8@6")

- **High-strength rebar**

  Grade 80

  Try to reduce as much as strength ratio= $\frac{28\times0.79\times60}{80} = 16.59\ in^2$ → 11-2#8 in each direction

  Flexural strength is 3,101 kip-ft > 2,968 kip-ft (OK)

  Grade 100

  Try to reduce as much as strength ratio= $\frac{28\times0.79\times60}{100} = 13.27\ in^2$ → 9-2#8 in each direction

  Flexural strength is 3,167 kip-ft > 2,968 kip-ft (OK)

(2) Side surface reinforcement

The required side surface reinforcement is the same way following Equations (5-2) and (3-11). In addition, the required side surface reinforcement of 0.18% was used in this calculation.

- **Current**

  Horizontal side face reinforcement

$$\rho_s = \frac{A_s}{s}\frac{Perimeter}{A_g}\frac{f_y}{60} = \frac{0.11}{3}\frac{2(96+32)}{96\times32}\frac{60}{60} = 0.3\%$$

  Vertical side face reinforcement

$$\rho_s = \frac{A_s}{s}\frac{Perimeter}{A_g}\frac{f_y}{60} = \frac{0.44}{6}\frac{96\times4}{96^2}\frac{60}{60} = 0.3\%$$

- **High-strength rebar**

  Grade 80

  Horizontal side face reinforcement

$$s = \frac{A_s}{\rho_s}\frac{Perimeter}{A_g}\frac{f_y}{60} = \frac{0.11}{0.0018}\frac{2(96+32)}{96\times 32}\frac{80}{60} = 6.8\ in. \rightarrow \text{4-\#3@6"}$$

Vertical side face reinforcement

$$s = \frac{A_s}{\rho_s}\frac{Perimeter}{A_g}\frac{f_y}{60} = \frac{0.44}{0.0018}\frac{96\times 4}{96^2}\frac{80}{60} = 13.6\ in. \rightarrow \text{7-\#6@13"}$$

Grade 100

Horizontal side face reinforcement

$$s = \frac{A_s}{\rho_s}\frac{Perimeter}{A_g}\frac{f_y}{60} = \frac{0.11}{0.0018}\frac{2(96+32)}{96\times 32}\frac{100}{60} = 8.5\ in. \rightarrow \text{3-\#3@8"}$$

Vertical side face reinforcement

$$s = \frac{A_s}{\rho_s}\frac{Perimeter}{A_g}\frac{f_y}{60} = \frac{0.44}{0.0018}\frac{96\times 4}{96^2}\frac{100}{60} = 16.7\ in. \rightarrow \text{6-\#6@16"}$$

II-7 footing specimen

1) STM

(1) Bottom mat rebar

- **Current**

Dimension and properties in Figure 5-35.

$$f_c' = 5\ ksi\ , f_y = 60\ ksi$$

$$L_1 = 96\ in., L_2 = 132\ in., S_1 = 64\ in., S_2 = 100.25\ in., w_c = 32\ in., H = 40\ in.$$

$$d' = 0.9H - (c_b + d_b) = 0.9 \times 40 - (4 + 1.128) = 30.87\ in.$$

$$z' = \sqrt{(S_1/2 - w_c/4)^2 + (S_2/2 - w_c/4)^2} = 48.48\ in.$$

$$\theta = \tan^{-1}(d'/z') = 32.49\ \text{degree}, \alpha = \tan^{-1}\left(\frac{S_1/2 - w_c/4}{S_2/2 - w_c/4}\right) = 29.67\ degree$$

Ties EF and GH

Tie capacity: $T_x = f_y A_{st} = 60 \times 11 \times 2 \times 1 = 1320\ kip$

Failure load: $P_{tie,x} = \frac{4T_x tan\theta}{sin\alpha} = 6793\ kip$

Ties FG and EH

Tie capacity: $T_y = f_y A_{st} = 60 \times 8 \times 2 \times 1 = 960\ kip$

Failure load: $P_{tie,y} = \frac{4T_y tan\theta}{cos\alpha} = 2814\ kip$

- **High-strength rebar**

Grade 80

$A_{st} = \frac{P_{tie,x} sin\alpha}{4 f_y tan\theta} = 16.50\ in^2, n = \frac{16.50}{2\times1} = 8.3$ → 17-2#9 in x direction

$A_{st} = \frac{P_{tie,y} cos\alpha}{4 f_y tan\theta} = 12.00\ in^2, n = \frac{12.00}{2\times1} = 6.0$ → 12-2#9 in y direction

Grade 100

$A_{st} = \frac{P_{tie,x} sin\alpha}{4 f_y tan\theta} = 13.20\ in^2, n = \frac{13.20}{2\times1} = 6.6$ → 14-2#9 in y direction

$A_{st} = \frac{P_{tie,y} cos\alpha}{4 f_y tan\theta} = 9.60\ in^2, n = \frac{9.60}{2\times1} = 4.8$ → 10-2#9 in y direction

(2) Side surface reinforcement

The required side surface reinforcement was calculated following Equations (5-2) and (3-11). I-2 specimen was designed to satisfy the requirement of side surface reinforcement following the minimum crack control reinforcement of 0.3% for STM design. Therefore, the reinforcement ratio of 0.3% was assumed to maintain in this calculation.

- **Current**

Horizontal side face reinforcement

x direction: $A_s = 0.62\ in^2/ft \geq \frac{1.30bh}{2(b+h)f_y} = \frac{1.30\times132\times40}{2(132+40)\times60} = 0.33\ in^2/ft$ (OK)

y direction: $A_s = 0.62\ in^2/ft \geq \frac{1.30bh}{2(b+h)f_y} = \frac{1.30\times96\times40}{2(96+40)\times60} = 0.31\ in^2/ft$ (OK)

$$x\ direction: \rho_s = \frac{A_s}{s}\frac{Perimeter}{A_g}\frac{f_y}{60} = \frac{0.31}{6}\frac{2(132+40)}{132\times40}\frac{60}{60} = 0.3\%$$

$$y\ direction: \rho_s = \frac{A_s}{s}\frac{Perimeter}{A_g}\frac{f_y}{60} = \frac{0.31}{6}\frac{2(96+40)}{96\times40}\frac{60}{60} = 0.4\%$$

Vertical side face reinforcement

$x\ direction\text{: } A_s = 1.06\ in^2/ft \geq \frac{1.30bh}{2(b+h)f_y} = \frac{1.30\times96\times132}{2(96+132)\times60} = 0.60\ in^2/ft$ (OK)

$y\ direction\text{: } A_s = 1.01\ in^2/ft \geq \frac{1.30bh}{2(b+h)f_y} = \frac{1.30\times132\times96}{2(132+96)\times60} = 0.60\ in^2/ft$ (OK)

$$x\ direction\text{: } \rho_s = \frac{A_s}{s}\frac{Perimeter}{A_g}\frac{f_y}{60} = \frac{0.44}{5}\frac{2(96+132)}{96\times132}\frac{60}{60} = 0.3\%$$

$$y\ direction\text{: } \rho_s = \frac{A_s}{s}\frac{Perimeter}{A_g}\frac{f_y}{60} = \frac{0.44}{5.25}\frac{2(132+96)}{132\times96}\frac{60}{60} = 0.3\%$$

- **High-strength rebar**

Grade 80

Horizontal side face reinforcement

$s_x = \frac{A_s}{\rho_s}\frac{Perimeter}{A_g}\frac{f_y}{60} = \frac{0.31}{0.003}\frac{2(132+40)}{132\times40}\frac{80}{60} = 9.0\ in.$ → 4-#5@9.0"

$s_y = \frac{A_s}{\rho_s}\frac{Perimeter}{A_g}\frac{f_y}{60} = \frac{0.31}{0.003}\frac{2(96+40)}{96\times40}\frac{80}{60} = 9.8\ in.$ → 4-#5@9.5"

Vertical side face reinforcement

$s_x = \frac{A_s}{\rho_s}\frac{Perimeter}{A_g}\frac{f_y}{60} = \frac{0.44}{0.003}\frac{2(96+132)}{96\times132}\frac{80}{60} = 7.0\ in.$ → 17-#6@7.0"

$s_y = \frac{A_s}{\rho_s}\frac{Perimeter}{A_g}\frac{f_y}{60} = \frac{0.44}{0.003}\frac{2(132+96)}{132\times96}\frac{80}{60} = 7.0\ in.$ → 12-#6@7.0"

Grade 100

Horizontal side face reinforcement

$s_x = \frac{A_s}{\rho_s}\frac{Perimeter}{A_g}\frac{f_y}{60} = \frac{0.31}{0.003}\frac{2(132+40)}{132\times40}\frac{100}{60} = 11.2\ in.$ → 3-#5@11.0"

$s_y = \frac{A_s}{\rho_s}\frac{Perimeter}{A_g}\frac{f_y}{60} = \frac{0.31}{0.003}\frac{2(96+40)}{96\times40}\frac{100}{60} = 12.2\ in.$ → 3-#5@12.0"

Vertical side face reinforcement

$s_x = \frac{A_s}{\rho_s}\frac{Perimeter}{A_g}\frac{f_y}{60} = \frac{0.44}{0.003}\frac{2(132+96)}{132\times96}\frac{100}{60} = 8.8\ in.$ → 14-#6@8.5"

$s_y = \frac{A_s}{\rho_s}\frac{Perimeter}{A_g}\frac{f_y}{60} = \frac{0.44}{0.003}\frac{2(96+132)}{96\times132}\frac{100}{60} = 8.8\ in.$ → 10-#6@8.5"

2) Sectional method

(1) Bottom mat rebar

- **Current**

  Dimension and properties in Figure 5.2.

  The flexural strength at section was calculated using strain compatibility method.

  x direction: flexural strength is 7,298 kip-ft (Grade 60 22-2#9@5.25")

  y direction: flexural strength is 5,308 kip-ft (Grade 60 16-2#9@5")

- **High-strength rebar**

  Grade 80

  Try to reduce as much as strength ratio= $\frac{44\times1\times60}{80} = 33.0\ in^2$ → 17-2#9 in x direction

  Flexural strength is 7,504 kip-ft > 7,298 kip-ft (OK)

  Try to reduce as much as strength ratio= $\frac{32\times1\times60}{80} = 24.0\ in^2$ → 12-2#9 in y direction

  Flexural strength is 5,308 kip-ft ≈ 5,308 kip-ft (OK)

  Grade 100

  Try to reduce as much as strength ratio= $\frac{44\times1\times60}{100} = 26.4\ in^2$ → 14-2#9 in x direction

  Flexural strength is 7,709 kip-ft > 7,298 kip-ft (OK)

  Try to reduce as much as strength ratio= $\frac{32\times1\times60}{100} = 19.2\ in^2$ → 10-2#9 in y direction

  Flexural strength is 5,514 kip-ft >5,308 kip-ft (OK)

(2) Side surface reinforcement

The required side surface reinforcement is the same way following equations (5.1) and (5.2). In addition, the required side surface reinforcement of 0.18% was used in this calculation.

- **Current**

  Current side surface is the same as above chapter.

- **High-strength rebar**

Grade 80

Horizontal side face reinforcement

$$s_x = \frac{A_s}{\rho_s}\frac{Perimeter}{A_g}\frac{f_y}{60} = \frac{0.31}{0.0018}\frac{2(132+40)}{132\times40}\frac{80}{60} = 15.0\ in. \rightarrow \text{2-\#5@15"}$$

$$s_y = \frac{A_s}{\rho_s}\frac{Perimeter}{A_g}\frac{f_y}{60} = \frac{0.31}{0.0018}\frac{2(96+40)}{96\times40}\frac{80}{60} = 16.3\ in. \rightarrow \text{2-\#5@16"}$$

Vertical side face reinforcement

$$s_x = \frac{A_s}{\rho_s}\frac{Perimeter}{A_g}\frac{f_y}{60} = \frac{0.44}{0.0018}\frac{2(96+132)}{96\times132}\frac{80}{60} = 11.7\ in. \rightarrow \text{11-\#6@11.0"}$$

$$s_y = \frac{A_s}{\rho_s}\frac{Perimeter}{A_g}\frac{f_y}{60} = \frac{0.44}{0.0018}\frac{2(132+96)}{132\times96}\frac{80}{60} = 11.7\ in. \rightarrow \text{8-\#6@11.0"}$$

Grade 100

Horizontal side face reinforcement

$$s_x = \frac{A_s}{\rho_s}\frac{Perimeter}{A_g}\frac{f_y}{60} = \frac{0.31}{0.0018}\frac{2(132+40)}{132\times40}\frac{100}{60} = 18.7\ in. \rightarrow \text{2-\#5@18.0"}$$

$$s_y = \frac{A_s}{\rho_s}\frac{Perimeter}{A_g}\frac{f_y}{60} = \frac{0.31}{0.0018}\frac{2(96+40)}{96\times40}\frac{100}{60} = 20.3\ in. \rightarrow \text{2-\#5@18.0"}$$

AASHTO LRFD (2020), Article 5.10.3.2 limits the spacing of the reinforcement in slabs shall not be greater than the lesser of the following: 1.5 times the thickness of the member; or 18.0 in. The maximum rebar spacing for II-7 specimen is 18.0 in.

Vertical side face reinforcement

$$s_x = \frac{A_s}{\rho_s}\frac{Perimeter}{A_g}\frac{f_y}{60} = \frac{0.44}{0.0018}\frac{2(132+96)}{132\times96}\frac{100}{60} = 14.7\ in. \rightarrow \text{9-\#6@14.0"}$$

$$s_y = \frac{A_s}{\rho_s}\frac{Perimeter}{A_g}\frac{f_y}{60} = \frac{0.44}{0.0018}\frac{2(96+132)}{96\times132}\frac{100}{60} = 14.7\ in. \rightarrow \text{6-\#6@14.0"}$$